JOHANNES GUTENBERG UNIVERSITÄT MAINZ

MAX PLANCK INSTITUTE FOR POLYMER RESEARCH

Hydrogen Bonding Dynamics in Liquids

Dissertation zur Erlangung des Grades

DOKTOR RERUM NATURALIUM (DR.RER.NAT.)

im Promotionsfach Chemie

am Fachbereich 09
Chemie, Pharmazie, Geographie und Geowissenschaften
der Johannes Gutenberg Universität-Mainz

Lucas Julian GUNKEL
geboren in Lahnstein

Mainz, März 2025

1. Gutachter:

[redacted]

2. Gutachter:

[redacted]

Tag der mündlichen Prüfung: 08.05.2025

Declaration of Authorship

Hiermit erkläre ich Gunkel, Lucas Julian, dass ich die vorliegende Arbeit mit dem Titel: "Hydrogen Bonding Dynamics in Liquids" selbstständig verfasst und keine anderen als die angegebenen Quellen und Hilfsmittel (dazu zählen auch KI-basierte Anwendungen oder Werkzeuge) benutzt habe. Sämtliche wörtlichen oder sinngemäßen Übernahmen und Zitate sind kenntlich gemacht und nachgewiesen (dies gilt auch für Texte, die durch generative KI, wie Chat GPT erzeugt wurden). Ich versichere, dass ich keine Hilfsmittel verwendet habe, deren Nutzung die Prüferin oder der Prüfer explizit ausgeschlossen hat. Im Anhang „Nutzung KI-Tools“ habe ich die verwendeten KI-Tools dokumentiert. Mit Abgabe der vorliegenden Leistung übernehme ich die Verantwortung für das eingereichte Gesamtprodukt. Ich verantworte damit auch jegliche KI-generierten Inhalte, die ich in meine Arbeit übernommen habe. Die Richtigkeit übernommener (KI- generierter) Aussagen und Inhalte habe ich nach bestem Wissen und Gewissen geprüft. Mir ist bekannt, dass ein Verstoß gegen die genannten Punkte prüfungsrechtliche Konsequenzen hat und insbesondere dazu führen kann, dass die Promotionsleistung als mit „nicht bestanden“ bewertet wird. Die Einschreibung kann für bis zu zwei Jahre widerrufen werden, wenn Studierende zweimal oder häufiger bei Prüfungsleistungen täuschen (§ 69 Abs. 4 und 5 HochSchG)

Zusätzlich habe ich diese Arbeit in der ersten Person Plural verfasst (wir andstatt ich bzw. im Englischen *we* anstelle von *I*) für bessere Lesbarkeit, sowie der Anerkennung der spezifizierten Beiträge, welche die Coautoren der publizierten Kapitel beigetragen haben. Die genauen Beiträge aller Coautoren sind in Kapitel "Publications Covered in this Thesis" auf Seite ix aufgelisted.

Lucas Julian GUNKEL
Mainz, März 2025

FB09 Fachbereich
Chemie, Pharmazie, Geographie
und Geowissenschaften

JG|U

Versicherung

für das Gesuch um Zulassung zur Promotion im Fachbereich 09 an der Johannes Gutenberg-Universität Mainz

Hiermit versichere ich _____ gemäß § 10 Abs. 3d
Name, Vorname

der Promotionsordnung vom 24.07.2007:

☐ Ich habe die jetzt als Dissertation vorgelegte Arbeit selbst angefertigt und alle benutzten Hilfsmittel (Literatur, Apparaturen, Material) in der Arbeit angegeben.[1]

☐ Ich hatte die jetzt als Dissertation vorgelegte Arbeit als Prüfungsarbeit für folgende Prüfungen eingereicht.

_____
(Bezeichnung der Prüfung)

_____
(Bezeichnung und Ort der Prüfungsstelle)

☐ Ich hatte weder die jetzt als Dissertation vorgelegte Arbeit noch Teile davon bei einer anderen Fakultät bzw. einem anderen Fachbereich als Dissertation eingereicht.

_____ _____
Datum Unterschrift

[1] Eine ausführlichere Eigenständigkeitserklärung finden Sie auf der Webseite des Fachbereichs 09 zu Promotion und Habilitationen. Diese ist insbesondere zu nutzen sofern Regelungen bzgl. der Nutzung von KI mit der betreuenden Person getroffen worden sind oder KI für die Verfassung der Arbeit verwendet wurde.
Die Eigenständigkeitserklärung muss mit eingereicht werden, muss aber nicht zwingend in die Arbeit eingebunden sein.

Acknowledgements

Publications Covered in this Thesis

The three publications outlined below are reproduced in chapters 6, 7 and 8 with minor changes. The methods sections of these publications have been edited and moved to chapter 5. Otherwise the formatting of these publications have been altered to fit into the format of this thesis. Names highlighted in bold are first authors or shared first authors.

Chapter 6:

Gunkel, L.; **Ehrhard, A. A.**; Krevert, C. S.; Marekha, B. A.; Bonn, M.; Grechko, M.; Hunger, J. *Nature Communications* **2024**, *15*, 1–9.[1]
DOI: 10.1038/s41467-024-54804-y

L.G., A.A.E., and J.H. conceptualized the study. **L.G.**, A.A.E., M.B., M.G., and J.H. developed the methodology and analysis. **L.G.**, A.A.E., C.S.K., B.A.M., and J.H. performed the experiments and computations. J.H. supervised the project. **L.G.** and A.A.E. wrote the original draft and **L.G.**, A.A.E., C.S.K., B.A.M., M.B., M.G., and J.H. revised and edited the manuscript. **L.G.** and A.A.E. contributed equally.

Chapter 7:

Caporaletti, F.; **Gunkel, L.**; Fernández-Ibáñez, M. Á.; Hunger, J.; Woutersen, S. *Angewandte Chemie International Edition* **2024**, *63*.[2]
DOI: 10.1002/anie.202416091

F.C., J.H. and S.W. conceptualized the study. F.C. performed linear IR and TRIR measurements, **L.G.** performed linear IR and 2DIR measurements, J.H. performed DRS measurements and DFT calculations. J.H. and S.W. supervised the project. F.C., **L.G.**, J.H. and S.W. wrote the original manuscript. F.C., **L.G.**, J.H., S.W. and M.A.F.I. revised and edited the manuscript. F.C. and **L.G** contributed equally.

Chapter 8:

Krevert, C. S.; **Gunkel, L.**; Sutter, J.; Meyer, R.; Schneider, P.; Nagata, Y.; Hunger, J. *The Journal of Physical Chemistry B* **2024**, *128*, 10688–10698.[3]
DOI: 10.1021/acs.jpcb.4c04760

C.S.K and J.H. designed the research project. C.S.K. prepared the samples. C.S.K. and P.S. measured the linear IR spectra; C.S.K. and **L.G.** measured the 2D IR data. C.S.K. analyzed and interpreted the spectroscopic data. J.S. performed the DFT calculations. R.M. prepared the 13C-labeled peptide sample. Y.N. performed the MD simulations. Y.N. and **L.G.** evaluated the simulation data. All authors discussed the results. C.S.K., **L.G.** and J.H. wrote the manuscript. C.S.K. and **L.G.** contributed equally.

Other publications:

Krevert, C. S.; Gunkel, L.; Haese, C.; Hunger, J. *Communications Chemistry* **2022**, *5*, 173.[4]
DOI: 10.1038/s42004-022-00789-y
Seki, T.; Yu, X.; Zhang, P.; Yu, C. C.; Liu, K.; Gunkel, L.; Dong, R.; Nagata, Y.; Feng, X.; Bonn, M. *Chem* **2021**, *7*, 2758–2770.[5]
DOI: 10.1016/j.chempr.2021.07.016
Ehrhard, A. A.; Gunkel, L.; Jäger, S.; Sell, A. C.; Nagata, Y.; Hunger, J. *ACS Catalysis* **2022**, *12*, 12689–12700.[6]
DOI: 10.1021/acscatal.2c03382

Contents

Chapter 1

Abstract

Liquids may appear disordered compared to the structured nature of crystals, but this is only true when considering long-range order. Unlike ideal gases, most liquids exhibit local order due to molecular interactions, ranging from dipole-dipole to electrostatic interactions. For example, water forms an extensive hydrogen bond network or molecular liquids such as alcohols can form aggregates. Understanding intermolecular forces, especially hydrogen bonding, is crucial for insights into phenomena like water's density anomalies. This thesis addresses three topics within the framework of hydrogen bonding in liquids, with a particular focus on the dynamics of these bonds. We employ linear and two-dimensional infrared spectroscopy (2DIR) alongside ab initio molecular dynamics (AIMD) simulations to explore bonding in liquids.

In the first project, we employ linear and two dimensional infrared (2DIR) spectroscopy to investigate the correlation of the donating hydrogen bonds of water. Water has previously been proposed to form asymmetric hydrogen bonds based on X-ray absorption studies. This supposed asymmetry has been controversially discussed. Our results provide experimental evidence for dynamic anti correlations instead of static asymmetric hydrogen bonds. We use 2DIR spectroscopy to isolate the inhomogeneous contributions to the lineshape for pure and isotopically dilute (HOD in H_2O) D_2O in dimethylformamide (DMF). Through the dilution in DMF each water molecule only forms two donating hydrogen bonds to the solvent. This allows us to distinguish between symmetric and asymmetric stretching modes for D_2O. Comparison with density functional theory calculations (DFT) show, that the about twice broader inhomogeneous lineshape of HOD can be explained by an anti correlated distribution of hydrogen bonds. Furthermore analysis of the crosspeaks for D_2O give direct experimental evidence for the anti correlation. We find that this anti correlation quickly decays (< 500 fs). Furthermore similar experiments on urea also show this anti correlation, albeit less pronounced. This confirms that these short lived anti correlations are not special for water but rather expected for all XH_2 containing molecules.[1]

In the second project we investigate the solvent properties of the fluorinated

mono alcohol hexafluoroisopropanol (HFIP). HFIP is a solvent that is widely used in synthetic chemistry as well as chemical biology. It has been shown to open up novel reaction pathways and to increase the reaction speed of several reactions. This increase in reaction speed has been coined a "booster effect". We investigate the dynamic origins of the booster effect of HFIP, via vibrational and dielectric spectroscopy of HFIP and its non fluorinated counterpart isopropanol (IP). With polarization controlled time resolved IR spectroscopy (TRIR) we found that individual HFIP molecules show a slower reorientation than IP, even though linear IR spectroscopy suggests weaker hydrogen bonds between HFIP molecules compared to IP. 2DIR spectroscopy shows slower hydrogen bonding dynamics for HFIP. Using dielectric relaxation spectroscopy (DRS), we find faster collective reorientation of HFIP, suggesting a smaller average cluster size. Titration experiments with a hydrogen bond accepting substrate (diethylether) reveal that HFIP forms much stronger hydrogen bonds with the substrate than IP. Together our findings suggest that HFIP forms smaller clusters than IP, and thus has more terminal OH groups as potential hydrogen bond donors. The slower hydrogen bond dynamics and reorientation of HFIP can stabilize the hydrogen bonded clusters, and thus make solvent substrate interactions more likely.[2]

The last projects is about specific ion effects on peptides. The strucure of peptides depends on the solvation environment. Ions can affect peptides directly through electrostatic interactions as well as indirectly through disruption of the solvent environment. We investigate the effects of Ca^{2+} on the dipeptide L-alanyl-L-alanine (2Ala). Calcium is located on the protein denaturation side of the Hofmeister series. We in particular focus on the competition between the two potential binding sites with the carboxylate group and the amide carbonyl group. With linear and 2DIR spectroscopy we find a blueshifted shoulder for the carboxylate peak as well as a small redshift for the amide carbonyl. Experiments with ^{13}C labeled 2ALa reveal that the shoulder is connected with Ca^{2+} interaction at the carboxylate group. Ab initio MD simulations show that Ca^{2+} binds to the carboxylate and to a lesser degree at the amide CO. This is consistent with an increasing lifetime of the amide CO peak found from 2DIR spectroscopy with increasing salt concentration. At the carboxylate we only find Ca^{2+} only monodentate bonded. Vibrational density of states (VDOS) show that this is consistent with a spectral blueshift. Additionally we find configurations of two Ca^{2+} bound mono dentally to the two carboxylate oxygens. This configuration leads to an additional blueshift. Our results highlight the importance of taking competition between different binding sites into account, when designing model systems for peptide interactions.[3]

Chapter 2

German Abstract

Verglichen mit der strukturierten Natur von Kristallen mögen Flüssigkeiten ungeordnet erscheinen, das trifft aber nur zu, wenn man die Ordnung über große Distanzen betrachtet. Im Gegensatz zu idealen Gasen weisen die meisten Flüssigkeiten eine lokale Ordnung auf, die auf molekulare Wechselwirkungen zurückzuführen ist, die von Dipol-Dipol- bis zu elektrostatischen Wechselwirkungen reichen. So bildet Wasser beispielsweise ein ausgedehntes Wasserstoffbrückenbindungsnetz oder molekulare Flüssigkeiten wie Alkohole können Aggregate bilden. Das Verständnis der zwischenmolekularen Kräfte, insbesondere der Wasserstoffbrückenbindungen, ist entscheidend für den Einblick in Phänomene wie die Dichteanomalien von Wasser. Diese Arbeit befasst sich mit drei Themen im Rahmen der Wasserstoffbrückenbindungen in Flüssigkeiten, wobei ein besonderer Schwerpunkt auf der Dynamik dieser Bindungen liegt. Wir setzen lineare und zweidimensionale Infrarotspektroskopie (2DIR) zusammen mit ab initio Molekulardynamik (AIMD) Simulationen ein, um die Bindungen in Flüssigkeiten zu untersuchen.

Im ersten Projekt setzen wir lineare und zweidimensionale Infrarotspektroskopie (2DIR) ein, um die Korrelation der spendenden Wasserstoffbrückenbindungen von Wasser zu untersuchen. Auf der Grundlage von Röntgenabsorptionsstudien wurde bisher angenommen, dass Wasser asymmetrische Wasserstoffbrückenbindungen bildet. Diese vermutete Asymmetrie wurde kontrovers diskutiert. Unsere Ergebnisse liefern experimentelle Beweise für dynamische Anti-Korrelationen anstelle von statischen asymmetrischen Wasserstoffbrückenbindungen. Wir verwenden 2DIR-Spektroskopie, um die inhomogenen Beiträge zur Linienform für reines und isotopenverdünntes (HOD in H_2O) D_2O in Dimethylformamid (DMF) zu isolieren. Durch die Verdünnung in DMF bildet jedes Wassermolekül nur noch zwei Donor Wasserstoffbrückenbindungen zum Lösungsmittel aus, was uns erlaubt, zwischen symmetrischen und asymmetrischen Streckungsmoden für D_2O zu unterscheiden. Der Vergleich mit Dichtefunktionaltheorie-Rechnungen (DFT) zeigt, dass die etwa doppelt so breite inhomogene Linienform von HOD durch eine antikorrelierte Verteilung der Wasserstoffbrückenbindungen erklärt werden kann. Darüber hinaus liefert die Analyse der Kreuzpeaks für D_2O einen direkten experimentellen Beweis für die Anti-Korrelation. Wir stellen fest, dass diese Anti-Korrelation schnell abklingt (< 500 fs). Außerdem zeigen ähnliche Experimente mit Harnstoff ebenfalls diese

Anti-Korrelation, wenn auch weniger ausgeprägt. Dies bestätigt, dass diese kurzlebigen Anti-Korrelationen nicht speziell für Wasser gelten, sondern für alle XH_2-haltigen Moleküle zu erwarten sind.[1]

Im zweiten Projekt untersuchen wir die Lösungsmitteleigenschaften des fluorierten Monoalkohols Hexafluorisopropanol (HFIP). HFIP ist ein Lösungsmittel, das sowohl in der synthetischen Chemie als auch in der chemischen Biologie weit verbreitet ist. Es hat sich gezeigt, dass es neue Reaktionswege eröffnet und die Reaktionsgeschwindigkeit verschiedener Reaktionen erhöht. Diese Erhöhung der Reaktionsgeschwindigkeit wurde als „Booster-Effekt" bezeichnet. Wir untersuchen den dynamischen Ursprung des Booster-Effekts von HFIP mittels Schwingungs- und dielektrischer Spektroskopie von HFIP und seinem nicht fluorierten Gegenstück Isopropanol (IP). Mit Hilfe polarisationskontrollierter zeitaufgelöster IR-Spektroskopie (TRIR) fanden wir heraus, dass einzelne HFIP-Moleküle eine langsamere Reorientierung zeigen als IP, obwohl die lineare IR-Spektroskopie auf schwächere Wasserstoffbrückenbindungen zwischen HFIP-Molekülen im Vergleich zu IP schließen lässt. 2DIR-Spektroskopie zeigt eine langsamere Wasserstoffbrückenbindungsdynamik für HFIP. Mit Hilfe der dielektrischen Relaxationsspektroskopie (DRS) finden wir eine schnellere kollektive Reorientierung von HFIP, was auf eine geringere durchschnittliche Clustergröße schließen lässt. Titrationsexperimente mit einem Wasserstoffbrückenbindungsakzeptor Substrat (Diethylether) zeigen, dass HFIP viel stärkere Wasserstoffbrückenbindungen mit dem Substrat bildet als IP. Zusammengenommen deuten unsere Ergebnisse darauf hin, dass HFIP kleinere Cluster als IP bildet und somit mehr endständige OH-Gruppen als potenzielle Wasserstoffbrückenbindungsdonatoren aufweist. Die langsamere Wasserstoffbrückenbindungsdynamik und Umorientierung von HFIP kann die wasserstoffgebundenen Cluster stabilisieren und damit Wechselwirkungen mit dem Lösungsmittel wahrscheinlicher machen.[2]

Das letzte Projekt befasst sich mit den spezifischen Auswirkungen von Ionen auf Peptide. Die Struktur von Peptiden hängt von der Solvatationsumgebung ab. Ionen können Peptide sowohl direkt durch elektrostatische Wechselwirkungen als auch indirekt durch Störung der Lösungsmittelumgebung beeinflussen. Wir untersuchen die Auswirkungen von Ca^{2+} auf das Dipeptid L-Alanyl-L-Alanin (2Ala). Calcium befindet sich auf der Seite der Denaturierung von Proteinen in der Hofmeister-Reihe. Wir konzentrieren uns insbesondere auf die Konkurrenz zwischen den beiden potentiellen Bindungsstellen mit der Carboxylatgruppe und der Amidcarbonylgruppe. Mit linearer IR und 2DIR-Spektroskopie finden wir eine blauverschobene Schulter für den Carboxylat-Peak sowie eine kleine Rotverschiebung für die Amidcarbonylgruppe. Experimente mit ^{13}C-markiertem 2ALa zeigen, dass die Schulter mit

der Ca^{2+}-Wechselwirkung an der Carboxylatgruppe verbunden ist. Ab-initio-MD-Simulationen zeigen, dass Ca^{2+} an die Carboxylatgruppe und in geringerem Maße an das Amid-CO bindet. Dies stimmt mit der zunehmenden Lebensdauer des Amid-CO-Peaks überein, die bei der 2DIR-Spektroskopie mit steigender Salzkonzentration festgestellt wurde. Am Carboxylat finden wir nur Ca^{2+}, das nur monodental gebunden ist. Die Schwingungsdichte der Zustände (VDOS) zeigt, dass dies mit einer spektralen Blauverschiebung vereinbar ist. Zusätzlich finden wir Konfigurationen mit zwei Ca^{2+}, die monodental an die beiden Carboxylatsauerstoffatome gebunden sind. Diese Konfiguration führt zu einer zusätzlichen Blauverschiebung. Unsere Ergebnisse zeigen, wie wichtig es ist, bei der Entwicklung von Modellsystemen für Peptidinteraktionen die Konkurrenz zwischen verschiedenen Bindungsstellen zu berücksichtigen.[3]

Chapter 3

Introduction

3.1 Liquid Dynamics Through the Lense of Vibrational Spectroscopy

On a superficial level liquids may look rather unordered compared to the rigid repeating structure of crystals. This, however, is only true looking at long range ordering. Most liquids differ from ideal gases through local order at short ranges. Interactions between molecules can range from dipole-dipole interactions like vander-Waals interactions to electrostatic Coulomb interactions. The most obvious example of the local order in liquids can be seen by the hydration shell of water as seen from the radial distribution function of water, where the first hydration shell is still rather ordered, and gets consecutively less well defined from the second to third hydration shell. Beyond a distance of three molecules the radial distribution function shows no further peaks, meaning there is no long-range correlation.[7] A different example of ordering in liquids is the formation of aggregates in molecular liquids. While water forms an extended hydrogen-bonded network[8, 9], less polar liquids such as alcohols form molecular aggregates and transient chains in bulk solution.[10, 11] In particular, the sizes of these aggregates have been proposed to vary from alcohol to alcohol depending on factors like C-chain length, steric accessibility or halogenation.[10] Furthermore, the size of these aggregates has effects on the solvent properties.[2, 10] This local ordering is highly dependent on the intermolecular forces, in particular electrostatic hydrogen bonding determines the local association of molecules. Understanding not only the strengths and binding geometries but also the dynamical behavior of hydrogen bonds in liquids is critical to gaining deeper insights into fundamental behaviors such as the anomalous behaviors of water in regards to density, solvent properties for organic synthesis, or ion interactions with peptides in solution.

Vibrational spectroscopy is an obvious tool, for investigating hydrogen bonds, because the vibrational frequency of an oscillator depends on its immediate surroundings, especially H-bonds.[12, 13] While diatomic molecules only show a single stretching vibration, polyatomic molecules show a variety of different molecular vibrations comprised of combinations of fundamental vibrations. Fundamental vibrations are, for example, stretching or bending vibrations. A hydrogen bond leads to a

red-shifted response for a stretch vibration and the magnitude of the redshift scales with the strength of the hydrogen bond, as schematically shown in figure 3.1 a.[14] This is most easily seen from the comparison of the gas phase and liquid phase linear IR spectra of water. In the liquid phase, the spectrum shows, a broad OH stretching mode at 3000-3600 cm^{-1}.[15–19] The gas phase spectrum shows besides peaks from small clusters in the bonded OH region (3000-3600 cm^{-1}), a much narrower peak at 3700 cm^{-1} corresponding to water monomers.[20]

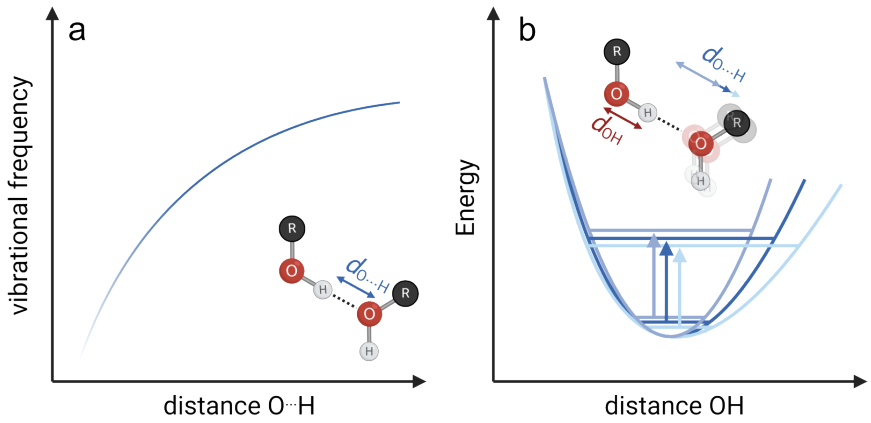

FIGURE 3.1: a) Schematic of the relationship between hydrogen bond distance and vibrational frequency. b) Schematic drawing of how fluctuations in the solvation shell of an oscillator leads to fluctuations of the vibrational frequency.

While linear vibrational spectroscopy is extremely useful for understanding liquids, everything is seen as a time and ensemble average. Therefore all information on the dynamic nature of hydrogen bonds in liquids is lost. To access this dynamical information, nonlinear spectroscopic methods, such as pump-probe spectroscopy or two-dimensional infrared spectroscopy (2DIR), are required. The potential of a molecular vibration can be described by an anharmonic oscillator, as schematically shown in figure 3.1. This model describes strong repulsions for short atomic distances and bond breaking at long distances. Dynamical changes in the solvation shell of a molecule lead to frequency fluctuations.[21] These changes include hydrogen bond stretching, compression, bending, formation or breaking and effectively stretch or compress the anharmonic potential and thus alter the instantaneous vibrational frequency, as schematically shown in figure 3.1 b.[21]

This, in turn, means that all previously mentioned changes to the hydrogen bonds are in principle encoded in the frequency autocorrelation function, which is indirectly accessible via 2DIR spectroscopy. This means that 2DIR opens up the possibility to study time-dependent phenomena such as spectral diffusion (change of oscillator frequency with time), anisotropy decay (reorientation of molecules) and the lifetime of the excited state, not only for water but also for a variety of different liquids and probes. In particular, OH/NH stretch, OD/ND stretch and C=O stretch have been widely used as vibrational probes. However, while not as widely used also the HOH bending mode has shown promising results as a vibrational probe.[22]

This thesis focuses on three major areas of liquid dynamics, which are introduced in the following chapters.

3.2 The Structure and Dynamics of Liquid Water

Water is a special liquid as it is simultaneously one of the most ubiquitous substances on earth and is essential for life as we know it, yet many of its key properties are surprisingly little understood. However, in many cases, these anomalies make water useful as a building block for life.[23] The most obvious example is the density anomaly of water. Where most other liquids contract as they cool down and eventually freeze water has its density maximum at 4°C. This behavior is critical for the survival of life on earth. Lakes freeze from the top and form an insulating layer of ice that allows deeper waters to remain warmer and liquid even at much lower air temperatures, ensuring aquatic life's survival throughout colder periods. The details of this behavior and other anomalies, such as a nonlinear heat capacity-temperature relationship are still points of discussion. This and other open questions show that understanding the structure of liquid water in detail is crucial for many scientific fields.[24]

Due to its importance, the investigation of the structure of water reaches back far into history but Wilhelm Röntgen's 1892 study "Ueber die Constitution des flüssigen Wassers" is generally considered one of the earliest attempts.[25, 26] Harris Chadwell proposed in 1928 in the review "The Molecular Structure of Water" [27] that water consists of two distinguishable substances and changing the temperature leads to a shift in the equilibrium between the two fractions, explaining the anomalous behavior of water. In their 1969 book "The structure and properties of water", Eisenberg and Kauzmann dismissed this two-liquid model in favor of a wide distribution of molecular environments.[26, 28] A new version of the two liquids model emerged in the 1990's and now generally refers to a mixture of low-density (LDL) and high-density (HDL) liquid water.[29, 30] Since its reemergence, two-phase liquid water, has been controversially discussed and has not yet been resolved.[31–35]

In the 1930's, following works on the structure of ice[36, 37] and diffraction data of liquid water by Amaldi[38], Bernal and Fowler proposed [39] a distorted tetrahedral structure for liquid water, where water forms two donating and two accepting hydrogen bonds of similar strength, as shown in figure 3.2.

In 2004, Wernet and co-workers proposed, based on X-ray diffraction and X-ray absorption experiments, that liquid water forms one strong accepting and donating hydrogen bond, suggesting a highly asymmetric hydrogen bonding environment.[40] This picture suggests that water forms ring- or chain-like structures in liquid. Wernets paper once again sparked interest in the structure of liquid water.[31, 41–43] The asymmetric water picture was mostly based on X-Ray and theoretical studies, but Leetmaa and coworkers showed that this picture does not fit with IR

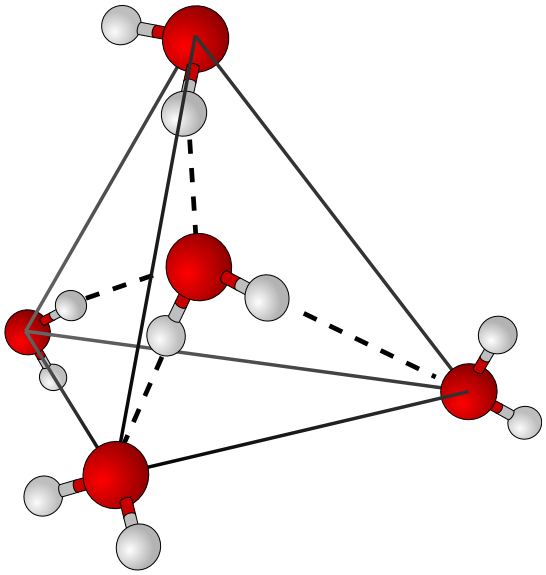

FIGURE 3.2: Schematic drawing of waters in a tetrahedral environment as first proposed by Bernal and Fowler.[39]

and Raman data.[44] In recent years, there seems to be some convergence on a picture where the majority of water molecules are in a rather symmetrical tetrahedral environment, but there is a significant number of water molecules in a highly asymmetric environment. These asymmetric water molecules are however not a separate static phase but only appear transiently.[13, 14, 45, 46] The hydrogen bond network of water undergoes continuous rearrangements such as breaking and formation of hydrogen bonds. These rearrangements are accessible with 2DIR spectroscopy.[47, 48] For pure water in particular the frequency-frequency correlation function shows a recurrence at $\sim$200 fs as a result of an underdamped oscillation of the hydrogen bond.[47, 49] Additionally correlations with a lifetime of $\sim$1 ps, such as collective rearrangements, contribute to the overall dynamics.[15, 47, 50]

In the project presented in Chapter 6 we utilize 2DIR spectroscopy to investigate the supposed transient asymmetry of water. For this, we dilute water with dimethylformamide (DMF), so that each water molecule only forms two donating hydrogen bonds to neighboring DMF molecules, to better resolve the coupled symmetric and asymmetric stretching modes of D_2O.

3.3 Alcohol aggregates in bulk liquid

The second project focuses on the liquid structure of bulk alcohols. In bulk liquid form, alcohols have been shown to form aggregates in the form of chains of bonded molecules.[10, 11, 51–53] The size of these chains depends on the alcohol, with longer carbon tails of the alcohols leading to overall shorter and a greater number of chains.[2, 10] The size of these aggregates has been shown to influence their solvent properties.[10] In particular, the acidity of the terminal OH group is influenced by

the length of the hydrogen-bonded chain. Furthermore, the size of aggregates also affects how many free and bonded OH groups are present in the liquid.[10].

In this project, we investigate the fluorinated mono alcohol hexafluoroisopropanol (HFIP). HFIP has become a widely used solvent in a variety of fields from synthetic chemistry to chemical biology.[54] In synthetic chemistry, a so-called "booster effect" has been reported.[10] This means that not only does HFIP as a solvent speed up various chemical reactions compared to other common solvents,[55–58] but it also opens up completely novel reaction pathways that show promise in green chemistry.[59] Despite the wide usage of HFIP the "booster effect" is not fully understood. Berkessel and coworkers have shown that HFIP forms strong hydrogen bonds to substrates and has a much higher affinity to interact with a substrate than with itself.[10] The exact mechanisms of the low affinity and the dynamics of hydrogen bonds in liquid are not yet understood. We investigate HFIP in comparison with its non-fluorinated counterpart. We employ time-resolved polarization-controlled infrared spectroscopy (TRIR) to investigate the reorientation of individual alcohol molecules. Using two-dimensional infrared spectroscopy (2DIR), we investigate the hydrogen bonding dynamics in bulk alcohols. Finally, we use dielectric relaxation spectroscopy (DRS) to learn about collective reorientation and aggregate sizes.

3.4 Ion Peptide Interactions

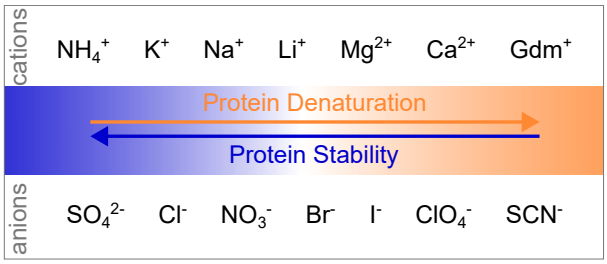

FIGURE 3.3: Hofmeister series for cations(top) and anions (bottom). The series goes from left to right from protein stabilization do destabilization in aqueous solution.

The three-dimensional structure of peptides and proteins is highly dependent on their environment. Hydrogen bonding to solvent molecules, such as water, influences the structure.[60] Besides the solvent also the presence of salt plays a crucial role through electrostatic interactions and disruption of both the hydrogen bonds between peptide and solvent, as well as solvent-solvent hydrogen bonds.[61] Various ions are generally classified as either structure makers or structure breakers based on their effects on the structure of bulk water. Lewis acidic cations such as Ca^{2+}, Mg^{2+} or Li^+ are structure makers, while ions with a lower acidity, such as Cs^+, Rb^+ or K^+, are structure breakers.[61] The relative acidity compared to water determines whether water binds to the ions (structure makers) or not (structure breakers).[61] The effects of ions on solvated peptides have been studied since Franz Hofmeister's 1888 publication "Zur Lehre von der Wirkung der Salze".[62] Based

upon Hofmeister's findings the Hofmeister series ranks ions based on their effect on the stabilization of proteins in aqueous solutions.[62–65] On the left-hand side of the series, ions such as ammonium or sulfate lead to a stabilization of proteins in solution, while ions on the opposite site of the series, such as guanidinium or thiocyanate, destabilize proteins.[66, 67] These specific ion effects on proteins have been subject to extensive studies in recent years.[3, 4, 68–70] Due to the complexity of protein structures, analyzing the ion interactions at specific functional groups can prove difficult. Thus, studies generally use model systems for peptides, such as N-methylacrylamide (NMA)[68, 69, 71] or butyramid[72] for the peptide bond or carboxylate groups for the C-terminus and carboxylate side chains[73]. Therefore, the competition between potential binding sites is not taken into account. We use L-Alanylalanine (2Ala) as a small model peptide to study the competitive specific ion effects. 2Ala has a peptide bond as well as a C and N terminus on which interactions with cations and anions may take place. We focus on the interactions of calcium with 2Ala. Calcium is an important agent in many biological processes such as biological signaling or as cofactors in enzymes[74–76] We employ FTIR and 2DIR spectroscopy as well as Born-Oppenheimer molecular dynamics (BOMD) simulations to understand the binding geometry of calcium to small peptides.

Chapter 4

Theoretical Background

4.1 Fundamentals of Spectroscopy

4.1.1 Introduction to Vibrational Spectroscopy

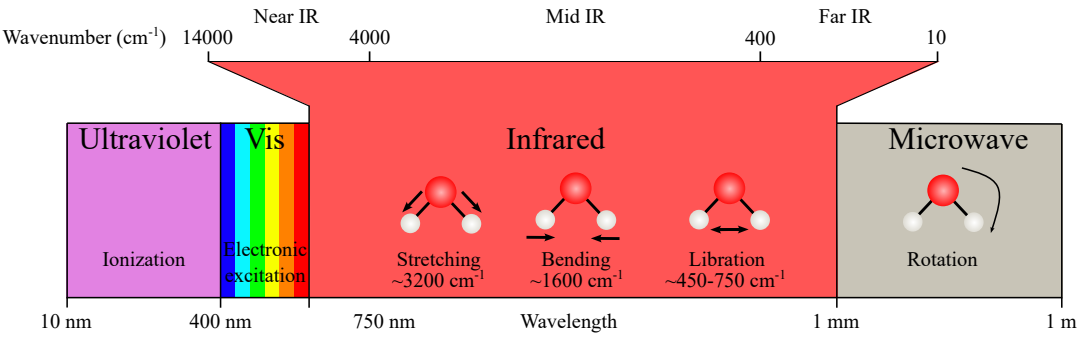

FIGURE 4.1: Schematic overview over the electromagnetic spectrum.[77]

The infrared spectrum stretches a range from about 10 cm^{-1} to 14000 cm^{-1} and is generally separated into three distinct frequency ranges.

- far-infrared (FIR) $\approx$ 10-400 cm^{-1}
- mid-infrared (MIR) $\approx$ 400-4000 cm^{-1}
- near-infrared (NIR) $\approx$ 4000-14000 cm^{-1}

The near-IR extends to roughly the highest frequency absorption of water. The mid-IR range encompasses most molecular vibrations like stretching and bending vibrations. And finally the far-IR spectrum has both information on low frequency molecular motions such as librations as well as intermolecular modes such has hydrogen bonds. As most vibrational modes fall into the mid-IR range, this thesis focuses on mid-IR frequencies.[77]

4.1.2 Light-Matter Interactions: Maxwell's equations

Electromagnetic radiation has, as the name implies, both an electric component E and a magnetic component H. In the case of linear polarized light, as shown in figure 4.2, these two oscillating fields are orthogonal to each other and have a sinusoidal shape. They can be described by[78, 79]:

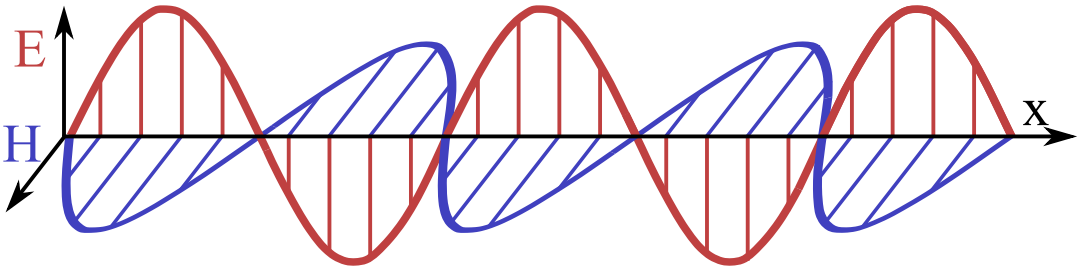

FIGURE 4.2: Schematic drawing of linear polarized light with the electric field in z- the magnetic field in y- and the wave propagation in x-direction.[78]

$$E = A\sin(2\pi\nu t - kx) \tag{4.1}$$

$$H = A\sin(2\pi\nu t - kx) \tag{4.2}$$

with the amplitude A, the frequency $2\pi\nu$ and the wave vector k. Since k is the same for both fields they propagate in phase.[78] To understand light-matter interactions we start with Maxwell's equations, that describe the relationships of electric and magnetic fields with charges.[80]:

$$\vec{\nabla}\cdot\vec{D} = \mathrm{div}\vec{D} = \rho_\mathrm{f} \tag{4.3}$$

$$\vec{\nabla}\cdot\vec{B} = \mathrm{div}\,\vec{B} = 0 \tag{4.4}$$

$$\vec{\nabla}\times\vec{E} = \mathrm{rot}\vec{E} = \frac{\partial\vec{B}}{\partial t} \tag{4.5}$$

$$\vec{\nabla}\times\vec{H} = \mathrm{rot}\vec{H} = j + \frac{\partial\vec{D}}{\partial t} \tag{4.6}$$

Equation 4.3 is also known as Gauss's law and relates the distribution of electric charges to the resulting electric field. The electric displacement field $\vec{D}$ is an auxiliary field taking effects from polarization $\vec{P}$ and the electric field $\vec{E}$ into account and ρ_f is the free electric charge density. The displacement field also depends on the relative permittivity ϵ^* of the propagating medium, which is a complex property.[80, 81]

$$\vec{D} = \epsilon_0\vec{E} + \vec{P} = \epsilon^*\epsilon_0\vec{E} \tag{4.7}$$

with the polarization $\vec{P}$ and the vacuum permittivity ϵ_0. The second of Maxwell's equations (equation 4.4) is Gauss's law for magnetism and it states that magnetic monopoles do not exist.[80, 82] The third Maxwell equation (equation 4.5) is Faraday's law of induction. It describes the change of an electric field upon changes to the magnetic field. And the last of Maxwell's equations (4.6) is the Ampère-Maxwell

law. The magnetizing field $\vec{H}$ is an auxiliary field described by equation 4.8 and j the current density.

$$\vec{H} = \frac{1}{\mu_0}\vec{B} - \vec{M} \tag{4.8}$$

With the magnetization $\vec{M}$ and the vacuum permeability μ_0. It describes how magnetic fields relate to electric current.[80, 82]

4.1.3 Polarization and Absorption

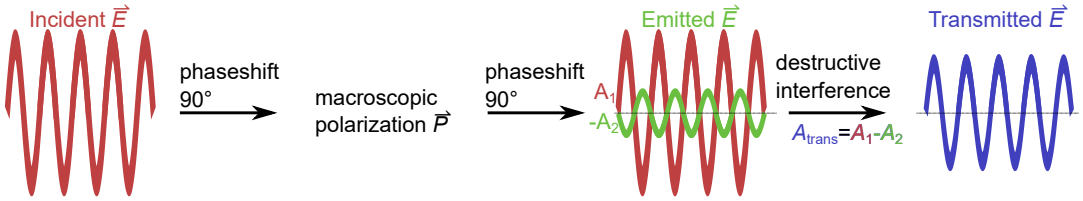

FIGURE 4.3: Schematic overview of linear absorption.

The displacement field $\vec{D}$ as described in equation 4.7 relates the electric field to the macroscopic polarization $\vec{P}$. Rearranging equation 4.7 yields a description of the macroscopic polarization in a medium caused by interaction with an electric field with the angular frequency ω.[81]

$$\vec{P}(\omega) = \epsilon_0 \vec{E}(\epsilon^* - 1) = \epsilon_0 \chi_e^*(\omega)\vec{E}. \tag{4.9}$$

The response of the electrons and nuclei to an oscillating electric field can be modeled with the Lorentz oscillator. Here, the electron is imagined to be connected by a hypothetical to the nucleus. After displacement, the spring undergoes a damped oscillation until the system is back to equilibrium. This damped oscillation is driven by an electric field. This model can be expressed in a classical equation of motion.[83]

$$-q\vec{E} = m_e \frac{\partial^2 \vec{r}}{\partial t^2} + m_e \gamma \frac{\partial \vec{r}}{\partial t} + m_e \omega_0^2 \vec{r} \tag{4.10}$$

where the first term on the right side is the accelerating force with the electron mass m_e and the displacement from the equilibrium position $\vec{r}$, the second term is a frictional force with the damping constant γ and the third term is the restoring force of the spring with the resonance frequency ω_0. The term on the left side is the electric force driving the oscillation with the charge q.[83]

The time domain equation can be converted through a Fourier transformation (see chapter 5.4) and solved for the displacement $\vec{r}$ to equation 4.11.[83]

$$\vec{r}(\omega) = -\frac{q}{m_e}\frac{\vec{E}(\omega)}{\omega_0^2 - \omega^2 - i\omega\gamma}. \tag{4.11}$$

The displacement of the charge induces an electric dipole moment $\vec{\mu}$.[81, 83]

$$\vec{\mu}(\omega) = -q\vec{r}(\omega) = \alpha(\omega)\vec{E}(\omega) \tag{4.12}$$

with the Lorentz polarizability $\alpha(\omega)$ a measure of how difficult it is for charges to be displaced. Comparing equation 4.11 and equation 4.12 gives us an expression for the Lorentz polarizability.[83]

$$\alpha(\omega) = \frac{q^2}{m_e}\frac{1}{\omega_0^2 - \omega^2 - i\omega\gamma}. \tag{4.13}$$

The macroscopic polarization $\vec{P}$ can be calculated as the ensemble average $\langle ... \rangle$ of the dipole moment.[81]

$$\vec{P}(\omega) = N\langle\vec{\mu}(\omega)\rangle = \frac{Nq^2}{m_e}\frac{\vec{E}(\omega)}{\omega_0^2 - \omega^2 - i\omega\gamma}. \tag{4.14}$$

where N is the number of atoms per unit volume. Substituting equation 4.9 into equation 4.14 and solving for the complex electric susceptibility χ_e^* gives the following expression:[81, 83, 84]

$$\chi_e^*(\omega) = \frac{\omega_p^2}{\omega_0^2 - \omega^2 - i\omega\gamma} \tag{4.15}$$

with the plasma frequency $\omega_p = \sqrt{\frac{Nq^2}{m\epsilon_0}}$. We can split complex electric susceptibility $\chi_e^*(\omega)$ in its real χ_e' and imaginary part χ_e''.[85]:

$$\chi_e^*(\omega) = \chi_e' + \chi_e'' = \frac{\omega_p^2(\omega_0^2 - \omega^2)}{(\omega_0^2 - \omega^2)^2 + (\omega\gamma)^2} + i\frac{\omega_p^2\omega\gamma}{(\omega_0^2 - \omega^2)^2 + (\omega\gamma)^2} \tag{4.16}$$

We can then write the complex susceptibility in polar form:

$$\chi_e^*(\omega) = |\chi_e(\omega)|e^{i\phi_{\chi e}(\omega)}. \tag{4.17}$$

The magnitude $|\chi_e(\omega)|$ and complex phase $\phi_{\chi e}$ are given by:[81, 85]

$$|\chi_e(\omega)| = \sqrt{\chi_e'^2 + \chi_e''^2} \tag{4.18}$$

$$\phi_{\chi e}(\omega) = \arctan\left(\frac{\chi_e''(\omega)}{\chi_e'(\omega)}\right) = \arctan\left(\frac{\omega\gamma}{\omega_0^2 - \omega^2}\right). \tag{4.19}$$

From equation 4.19 it follows that if $\omega \to \omega_0$ the denominator in the argument of the arc tangent becomes zero and $\frac{\omega\gamma}{\omega_0^2 - \omega^2} \to \infty$ and the phase difference between incident field and Polarization therefore becomes $\frac{\pi}{2}$[85].

This means as schematically shown in figure 4.3 that the induced macroscopic polarization $\vec{P}$ in the sample has a 90° phase shift compared to the incident field $\vec{E}_{inc}$ and the emitted field $\vec{E}_{emit}$ has another 90° phase shift compared to $\vec{P}$. The emitted field thus has a 180° phase shift compared to the incident field, meaning that

both fields destructively interfere, resulting in a transmitted field with the phase of the incident field. The amplitude becomes the difference between the amplitudes of $\vec{E}_{\text{inc}}$ and $\vec{E}_{\text{emit}}$. The absorbance A is then defined as the negative logarithm of the ratio of measured intensity of the transmitted field to the incident field[21, 78]:

$$A = -\log\left(\frac{I_{\text{trans}}}{I_{\text{inc}}}\right). \tag{4.20}$$

with the Intensity being proportional to the square of the electric field $I \propto E^2$.[78]

4.1.4 Harmonic and Anharmonic Oscillator

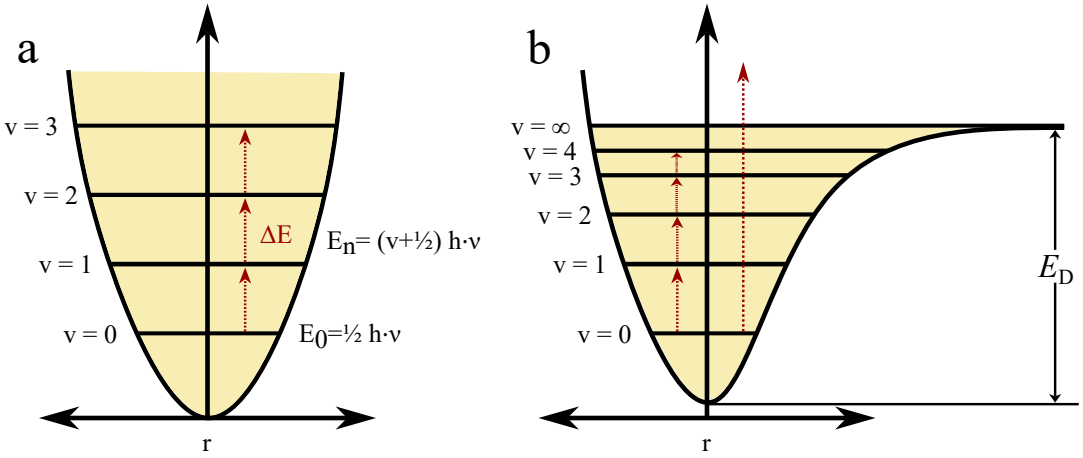

FIGURE 4.4: Schematic drawing of a) a harmonic oscillator and b) an anharmonic oscillator.[79]

The simplest model for the vibration of a diatomic molecule is two weights bound by a spring. In this case, the restoring force of the spring F can be described by Hooke's law as shown in the last term in the Lorentz oscillator model (equation 4.10).[79]:

$$F = -\frac{\mathrm{d}V(r)}{\mathrm{d}r} = -\omega_0^2 mr = -kr \tag{4.21}$$

with the potential energy V, the force constant k ($k = \omega_0^2 m$) and the displacement r. The potential energy is then the first derivative of the restoring force[79]:

$$V(x) = \frac{1}{2}kr^2. \tag{4.22}$$

When looking at the spring model through a classical lense $V(x)$ can take arbitrary values. In quantum mechanics, this is however not true, and only quantized values are possible. The Schrödinger equation for the harmonic oscillator allows for the calculation of the quantized energies E_{HO}[86]:

$$\hat{H}_{\text{HO}}\Psi = E_{\text{HO}}\Psi \tag{4.23}$$

where Ψ is the wave function and $\hat{H}_{HO}$ is the Hamilton operator for the quantum mechanical harmonic oscillator[86]:

$$\hat{H}_{HO} = \frac{\hbar^2}{2\mu}\frac{d^2}{dr^2} + \frac{1}{2}kr^2 \tag{4.24}$$

with the reduced mass of the nuclei μ. The Schrödinger equation then becomes:

$$\frac{\mathrm{d}^2\Psi}{\mathrm{d}r^2} + (\frac{2\mu E}{\hbar^2} - \frac{\mu k r^2}{\hbar^2})\Psi = 0. \tag{4.25}$$

When equation 4.25 is solved the energy of the harmonic oscillator comes out to[79, 86]:

$$E = h\nu(v + \frac{1}{2}). \tag{4.26}$$

The vibrational quantum number v can only take whole number values (v = 0, 1, 2, ...), hence the quantization. The vibrational frequency ν is given by:

$$\nu = \frac{1}{2\pi}\sqrt{\frac{k}{\mu}}. \tag{4.27}$$

This also shows that E can not be zero, and the lowest possible value for E is $\frac{1}{2}h\nu$ the zero point energy. For a transition between vibrational states to be infrared active, the general selection rule is that only transitions where the electric dipole moment changes are allowed. The molecule in question does not need to have a permanent dipole, but a change in dipole has to happen for a transition to be IR-active. An example of an IR-inactive vibrational mode would be the stretching vibration of a homonuclear diatomic molecule such as Cl_2. Therefore this particular mode does not lead to an absorption when exposed to IR light. The selection rule for transitions in the harmonic approximation is $\Delta v = \pm 1$. This means that higher-order transitions (e.g. $0 \rightarrow 2$), such as overtones, are forbidden in the harmonic approximation. The thermal energy at room temperature corresponds to about $kT/hc \approx 200\mathrm{cm}^{-1}$, and therefore most molecules are in their vibrational ground state (for mid-IR vibrational modes), which means that fundamental transitions make up the majority of observed transitions.[79]

The harmonic approximation however does not reproduce certain key features of real oscillations, first and foremost, that bonds dissociate given large displacements. The potential energy curve flattens at the dissociation energy E_D and the force constant tends towards 0. Additionally, the two masses repel each other when approaching, causing the potential to be steeper than the harmonic approximation at negative displacements. This deviation from the harmonic approximation can be described as the anharmonic oscillator, which is displayed in figure 4.4b. The anharmonicity of the potential energy curve lifts the selection rules of the harmonic oscillator so that overtones become allowed transitions, even though in most cases

they only have weak intensities. The Morse potential can be used as a simplified functional form of the anharmonic oscillator:[79, 86]

$$V(x) = E_{\mathrm{D}} \cdot (1 - e^{-ar})^2 \tag{4.28}$$

where a is a constant that controls the width of the potential.[79, 86]

4.1.5 Normal Modes

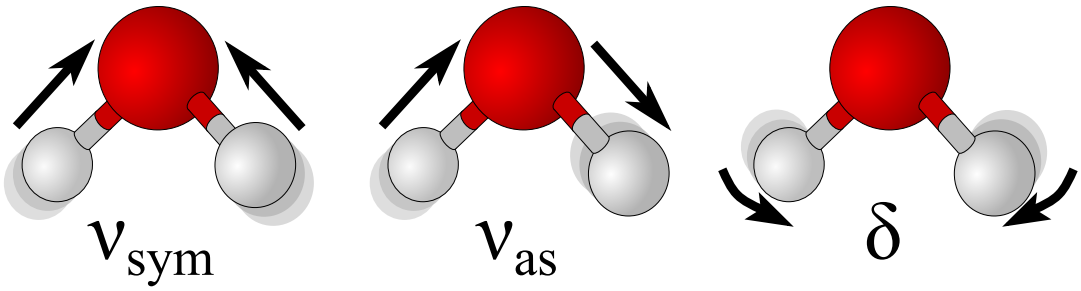

FIGURE 4.5: Schematic illustration of the three normal modes of water: symmetric stretching (ν_{sym}), asymmetric stretching (ν_{as}) and the bending mode (δ).

While diatomic molecules only show one kind of vibration, larger polyatomic molecules show a multitude of different stretching, bending, and other types of vibrations. To specify the positions of all N atoms $3N$ coordinates are needed. Three possible displacements correspond to the translation of the whole molecule in x,y and z directions. To fully describe the orientation of a linear molecule in space, two angles are needed, and in the nonlinear case, an additional angle is needed to describe the orientation along the direction specified by the other two angles. Thus, the total number of independent vibrational modes of a N-atomic molecule is $3N - 6$ or $3N - 5$ for linear molecules. For water as a triatomic nonlinear molecule this comes out to three normal modes, as shown in figure 4.5. The symmetric stretching mode ν_{sym}, the asymmetric stretching mode ν_{as} and the bending mode δ. However, normal modes are only in special cases (such as CO_2) purely stretching/bending modes and in most cases they have contributions from multiple different motions, such as the amide-II mode, which has contributions from both N-H in-plane bending and C-N stretching.[79, 87]

4.1.6 Vibrational Coherence and Eigenstates

The theoretical framework presented in this section is based on the scope outlined in reference [21].

The time-independent Schrödinger equation for a harmonic oscillator (equation 4.23) can be used to calculate the eigenstates $|n\rangle$ of the Hamiltonian for an isolated molecules $\hat{H}_0$.

$$\hat{H}_0|n\rangle = E_{\mathrm{n}}|n\rangle \tag{4.29}$$

To now describe the interactions of the molecule with a laser pulse, the time-dependent Schrödinger equation is required.

$$i\hbar\frac{\partial}{\partial t}|\Psi\rangle = \hat{H}|\Psi\rangle \tag{4.30}$$

with the corresponding Hamilton operator $\hat{H}$.

$$\hat{H} = \hat{H}_0 - \hat{\mu}E \tag{4.31}$$

where $\hat{\mu}$ is the dipole operator and $\vec{E}(t)$ is the electric field of a laser pulse interacting with the molecule. In the absence of a laser pulse $\hat{H}_0$ is time-independent, and the solution of equation 4.30 becomes:

$$|\Psi\rangle = \sum_{\mathrm{n}} c_{\mathrm{n}} e^{\frac{-iE_{\mathrm{n}}t}{\hbar}}|n\rangle \tag{4.32}$$

where c_{n} is a coefficient corresponding to the eigenstate $|n\rangle$. The interaction with a laser pulse can now be modeled by combining equations 4.30 and 4.32.

$$\frac{\partial}{\partial t}c_{\mathrm{m}}(t) = -\frac{i}{\hbar}\sum_{\mathrm{n}} c_{\mathrm{n}}(t) e^{\frac{-i(E_{\mathrm{n}}-E_{\mathrm{m}})t}{\hbar}}\langle m|\hat{\mu}(t)|n\rangle \tag{4.33}$$

where $\langle n|\hat{\mu}|m\rangle$ is the transition dipole moment $\hat{\mu}_{\mathrm{nm}}$.

$$\hat{\mu}_{\mathrm{nm}} = \langle n|\hat{\mu}|m\rangle = \frac{d\mu}{dx}\langle n|\hat{x}|m\rangle \tag{4.34}$$

with the coordinate x along which the vibration takes place. The change of the static dipole upon compression or stretching $\frac{d\mu}{dx}$ is proportional to the absorption intensity, and $\langle n|\hat{x}|m\rangle$ gives rise to the $\Delta\nu = \pm 1$ selection rule, as the integral vanishes if this rule is not fulfilled in the harmonic approximation. In a two-level system, the transition from vibrational ground state $|0\rangle$ to first excited state $|1\rangle$ has the transition frequency $\omega_{01} = \frac{(E_1 - E_0)}{\hbar}$. Equation 4.33 in the two-level case yields two coupled equations for the time evolution of both states.

$$\begin{aligned}\frac{\partial}{\partial t}c_1(t) &= +\frac{i}{\hbar}c_0(t)e^{-i\omega_{01}t}\langle 1|\hat{\mu}|0\rangle\vec{E}(t)\\ \frac{\partial}{\partial t}c_0(t) &= +\frac{i}{\hbar}c_1(t)e^{+i\omega_{01}t}\langle 0|\hat{\mu}|1\rangle\vec{E}(t)\end{aligned} \tag{4.35}$$

Equation 4.35 can be solved to find the state of the system is after interacting with the laser pulse. The solution of the time dependent Schrödinger equation will be a wavefunction consisting of a linear combination of eigenstates $|0\rangle$ and $|1\rangle$.

$$|\Psi\rangle(t) = c_0 e^{-\frac{iE_0 t}{\hbar}}|0\rangle + ic_1 e^{-\frac{iE_1 t}{\hbar}}|1\rangle \tag{4.36}$$

The molecule is vibrating with a 90° phase shift with respect to the laser pulse, and thus, if multiple molecules are excited, they are in phase with each other. Therefore in the sample, a macroscopic polarization $\vec{P}$ is induced that evolves in time

according to equation 4.36. The macroscopic polarization $\vec{P}$ can be calculated as the expectation value of the transition dipole.

$$\begin{aligned}\vec{P} &= \langle \mu \rangle = \langle \Psi(t) | \hat{\mu} | \Psi(t) \rangle \\ &= c_0 c_1 \langle 0 | \hat{\mu} | 1 \rangle \sin(\omega_{01} t) + c_0^2 \langle 0 | \hat{\mu} | 0 \rangle + c_1^2 \langle 1 | \hat{\mu} | 1 \rangle\end{aligned} \tag{4.37}$$

In equation 4.37 $\langle 0|\hat{\mu}|0\rangle$ and $\langle 1|\hat{\mu}|1\rangle$ have no time dependence and can thus not emit a field. Since the excited population is much smaller than the population in the ground state, $c_0 \approx 1$. From equation 4.33, it follows that $c_1 \propto \mu_{01}$. Thus equation 4.37 can be simplified to:

$$\begin{aligned}\vec{P} &= c_0 c_1 \mu_{01} \sin(\omega_{01} t) \\ \vec{P} &\propto \mu_{01}^2 \sin(\omega_{01} t)\end{aligned} \tag{4.38}$$

The laser pulse creates vibrational coherence through a linear combination of eigenstates that subsequently radiates an emitted field. In linear spectroscopy, the absorption solely stems from the destructive interference between the incident and the emitted field caused by vibrational coherence introduced by electromagnetic radiation between the ground and the first excited state.

4.1.7 Bloch Vectors and the Density Matrix

The theoretical framework presented in this section is based on the scope outlined in reference [21].

So far, we have only taken single molecules with a single vibrational frequency into account. In the condensed phase, however, multiple molecules are in different environments and therefore have slightly different vibrational frequencies. Considering two molecules with different vibrational frequencies, the induced macroscopic polarization can be written as:

$$P(t) = c_0^{(1)} c_1^{(1)} \mu_{01}^{(1)} \sin(\omega_{01}^{(1)} t) + c_0^{(2)} c_1^{(2)} \mu_{01}^{(2)} \sin(\omega_{01}^{(2)} t) \tag{4.39}$$

The electromagnetic radiation emitted from the polarizations of both molecules would initially interfere constructively, since they are still in phase but become out of phase after some time and destructively interfere. In an ensemble of molecules, this leads to a continuously decreasing signal as all oscillators become more and more out of phase. To describe the behavior of multiple excited molecules, we use Bloch vectors. The Bloch-vector for a single oscillator is defined with the following x,y and z components:

$$\begin{aligned}B_\mathrm{x} &= i(c_0(t) c_1^*(t) - c_0^*(t) c_1(t)) = c_0 c_1 \sin(\omega_{01} t) \\ B_\mathrm{y} &= c_0(t) c_0^*(t) - c_1(t) c_1^* \\ B_\mathrm{z} &= c_0(t) c_1^*(t) - c_0(t)^* c_1(t) = c_0 c_1 cos(\omega_{01} t).\end{aligned} \tag{4.40}$$

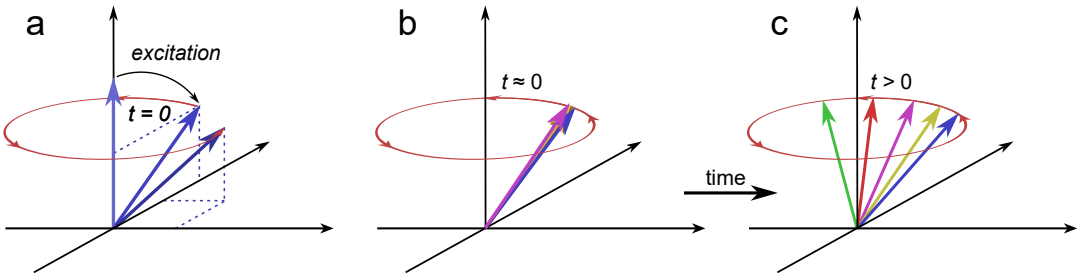

FIGURE 4.6: a) Before excitation the Bloch vector is parallel to the z-axis. After excitation, the Bloch vector is in the z-y plane and starts precessing around the z-axis. b) Bloch vectors of multiple molecules precess in phase at short times after laser excitation. c) After some time, the Bloch vectors dephase, leading to partial destructive interference.

Figure 4.6 a) shows schematically a Bloch-vector of a single oscillator and how it interacts with a laser pulse. Before the laser pulse arrives the oscillator is in its ground state ($c_0 = 1; c_1 = 0$) and the corresponding Bloch-vector is upright ($\mathrm{B}_x = 0$, $\mathrm{B}_y = 0$, $\mathrm{B}_z = 1$). After excitation at ($t = 0$) the vector is in the z-y plane at an angle that depends on the strength of the excitation. Due to the time dependence of the coefficients the vector precesses around the z-axis, which is ultimately responsible for the emitted signal field. The macroscopic polarization is proportional to the x component of the Bloch-vector $P(t) \propto B_\mathrm{x}$. The x and y components of the vector are referred to as the coherence and the derivation from $B_z = 1$ as the population.

If we look at the Bloch-vector representation for an ensemble of molecules at early times (Figure 4.6 b) we see that the molecules initially are in phase and therefore constructively interfere. Since all oscillators have slightly different precession frequencies, after some time, they become out of phase and partially destructively interfere. The macroscopic polarization becomes the sum of the projections on the x axis $\langle B_\mathrm{x} \rangle$:

$$\begin{aligned} P(t) &= \langle \mu \rangle = \langle B_\mathrm{x} \rangle \\ &= \sum_\mathrm{s} i p_\mathrm{s} (c_0^\mathrm{s}(t) c_1^{\mathrm{s}*}(t) - c_0^{\mathrm{s}*}(t) c_1^\mathrm{s}(t)) \\ &= i(\langle c_0(t) c_1^* \rangle - \langle c_0^*(t) c_1(t) \rangle) \end{aligned} \tag{4.41}$$

where p_s weighs the contributions of each wavefunction, and the brackets $\langle \cdots \rangle$ denote the ensemble average. Similarly, instead of treating the Bloch-vectors of all molecules individually, we can write the ensemble average x, y, and z components.

$$\begin{aligned} \langle B_\mathrm{x} \rangle &= i(\langle c_0(t) c_1^*(t) \rangle - \langle c_0^*(t) c_1(t) \rangle) \\ \langle B_\mathrm{y} \rangle &= \langle c_0(t) c_1^*(t) \rangle + \langle c_0^*(t) c_1(t) \rangle \\ \langle B_\mathrm{z} \rangle &= \langle c_0(t) c_0^*(t) \rangle - \langle c_1^*(t) c_1(t) \rangle \end{aligned} \tag{4.42}$$

From this, we know that there are multiple mechanisms that contribute to a diminishing macroscopic polarization and therefore signal with time. The first is pure dephasing, which is caused by a loss of phase in between the precession of oscillators Bloch vectors. This can have two different origins. First, considering a static

non-changing distribution of oscillators with different vibrational frequencies, the oscillators slowly dephase. The second case is the dynamic change of oscillator frequencies as a response to changes in the local oscillator environment (e.g. compression and stretching of the hydration shell).

Besides the pure dephasing, population relaxation also contributes to the diminishing signal with time. Starting from an excited state after laser excitation ($|\Psi\rangle = c_0|0\rangle + ic_1|1\rangle$) through energy transfer, the system will eventually fall back to the ground state $|0\rangle$.

The components of the Bloch vector are related to the elements of the density matrix ρ. The density matrix is a matrix describing an quantum mechanical ensemble.

$$\rho = \begin{pmatrix} \rho_{00} & \rho_{01} \\ \rho_{10} & \rho_{11} \end{pmatrix} = \begin{pmatrix} \langle c_0(t)c_0^*(t)\rangle & -i\langle c_0(t)c_1^*(t)\rangle \\ i\langle c_1(t)c_0^*(t)\rangle & \langle c_1(t)c_1^*(t)\rangle \end{pmatrix}. \tag{4.43}$$

Comparing Equation 4.43 and 4.42 yields the following expressions for the ensemble-averaged Bloch vector components:

$$\begin{aligned} \langle B_x\rangle &= -(\rho_{01} + \rho_{10}) \\ \langle B_y\rangle &= i(\rho_{01} - \rho_{10}) \\ \langle B_z\rangle &= \rho_{00} - \rho_{11}. \end{aligned} \tag{4.44}$$

The difference of the diagonal components of the density matrix determines the z component of the Bloch-vector. This means that the diagonal elements of ρ are the respective populations. The off-diagonal elements of ρ are responsible for the precession of the Bloch-vector and are therefore linked to the coherences and, ultimately, to the emitted field. Without population relaxation and dephasing, the time dependence of the matrix elements becomes:

$$\begin{aligned} \rho_{00}(t) &= c_0^2 \\ \rho_{11}(t) &= c_1^2 \\ \rho_{01}(t) &= -ic_0c_1e^{i\omega_{01}t} \\ \rho_{10}(t) &= ic_0c_1e^{-i\omega_{01}t}. \end{aligned} \tag{4.45}$$

We find the diagonal elements to be constant and the off-diagonal elements display a constant harmonic behavior (Bloch-vector rotating around z). We include dephasing phenomenologically with an exponential decay with the homogeneous dephasing time T_2.

$$\begin{aligned} \rho_{01}(t) &= -ic_0c_1e^{i\omega_{01}t}e^{\frac{-t}{T_2}} \\ \rho_{10}(t) &= ic_0c_1e^{-i\omega_{01}t}e^{\frac{-t}{T_2}}. \end{aligned} \tag{4.46}$$

Population relaxation results in a decay of the ρ_{11} element and a repopulation of the ρ_{00} ground state with a time constant T_1.

$$\begin{aligned} \rho_{11}(t) &= \rho_{11}(0)e^{\frac{-t}{T_1}} \\ \rho_{00}(t) &= 1 - \rho_{11}(t). \end{aligned} \tag{4.47}$$

The homogeneous dephasing time T_2 and and population relaxation are related by the pure dephasing time T_2^*. This is because population relaxation also causes homogeneous dephasing even without pure dephasing.

$$\frac{1}{T_2} = \frac{1}{2T_1} + \frac{1}{T_2^*} \tag{4.48}$$

4.2 Nonlinear Spectroscopy

The theoretical framework presented in this section is based on the scope outlined in reference [21].

4.2.1 Pump-Probe Infrared Spectroscopy

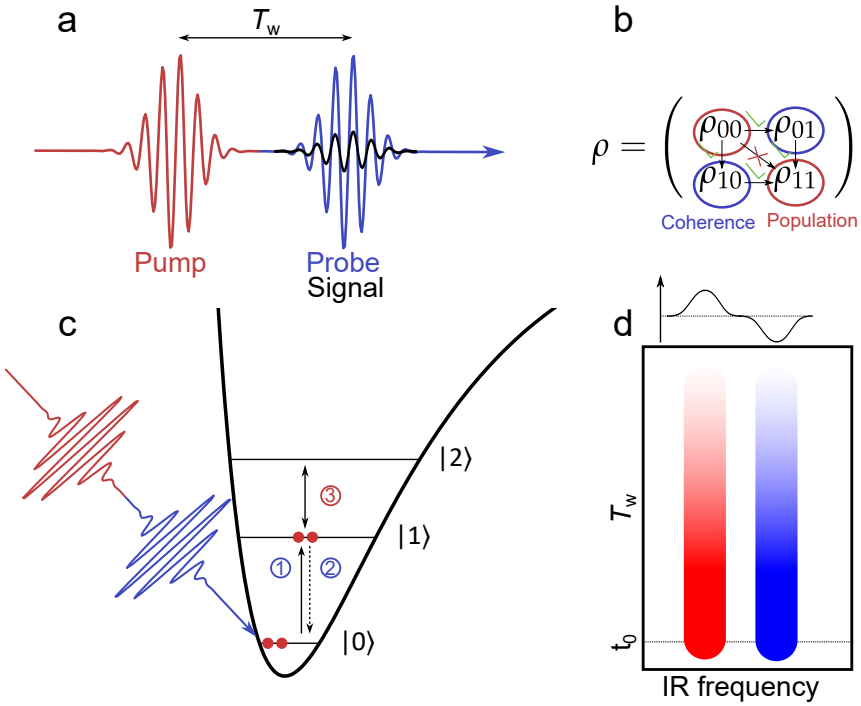

FIGURE 4.7: a) Pump probe pulse sequence. In pump probe geometry the signal is collinear with the probe pulse. b) The density matrix for a two-state system. c) Schematic of the possible interactions of the excited population with the probe pulse. d) Schematic drawing of a pump-probe spectrum.

Pump-probe IR spectroscopy is a nonlinear spectroscopy based on the quantum mechanical principles thus far discussed. We employ the pulse sequence displayed in figure 4.7 a, where an initial intense pump pulse creates a population in the first excited state $|1\rangle$. The density matrix shown in figure 4.7 b shows that a diagonal transition in the density matrix is not possible, and therefore, first coherence needs

to be created. This also means that two interactions with the laser pulse are required to actually obtain an excited population. This is achieved by a high-energy pump pulse that is much more intense than the following probe pulse. After a time delay called waiting time T_w the probe pulse arrives and three possible interactions can take place:
(1) The ground state bleach (GSB) appears because of the depleted population in $|0\rangle$. When the probe pulse arrives the coherence created is smaller than in the unpumped case. This leads to a negative signal at the ω_{01} transition frequency in the difference spectrum (unpumped minus pumped spectrum).
(2) Stimulated emission (SE). The population in $|1\rangle$ can undergo stimulated emission and transition to the ground state. This subsequently reduces the absorption and leads to a negative signal at ω_{01}. When talking about the negative peak in pump-probe or 2DIR spectroscopy, it is often only referred to as GSB even though it also includes SE contributions
(3) The excited state absorption (ESA) leads to a positive peak at the ω_{12} transition frequency. The probe laser pulse can create coherence between the first and second excited states resulting in linear absorption. No population in the second excited state is however generated.

In the harmonic approximation, the transition frequencies are equal $\omega_{01} = \omega_{12}$ and therefore positive and negative peaks would overlap and, depending on transition dipoles cancel each other out fully or partially. This means that the frequency difference of GSB and ESA peaks in the pump-probe spectrum, gives information on the anharmonicity of the anharmonic oscillator. From the decay of the peaks in the pump-probe spectrum, we can learn about the population relaxation of the system. Since the preferred relaxation pathways highly depend on the local environment of the oscillator, the change in population lifetime can give valuable insights into changes in the immediate environment of an oscillator.

4.2.2 Two Dimensional Infrared Spectroscopy (2DIR)

Two-dimensional infrared spectroscopy is an extension of pump-probe spectroscopy with the same underlying principles. Additionally to the frequency resolution of the probe axis, 2DIR also gives frequency resolution along the probe axis. This means that a narrow band pump pulse that also has a short pulse duration is needed, so as not to lose time resolution. This, however, conflicts with Heisenberg's energy-time uncertainty principle ($\Delta E \Delta t \geq \frac{\hbar}{2}$).[78] To circumvent this problem, we add an additional pump pulse to the pulse sequence (see figure 4.8). The two pump pulses have a time delay, the so-called coherence time τ, which is varied, and a time domain spectrum is recorded. After Fourier transformation, we obtain frequency resolution along the pump axis. In the pump probe geometry, the signal is collinear with the probe pulse, as the two pump pulses are collinear. In principle, the same interactions take place as for pump-probe spectroscopy, however, due to the additional resolution along the pump axis, additional features can be distinguished. The

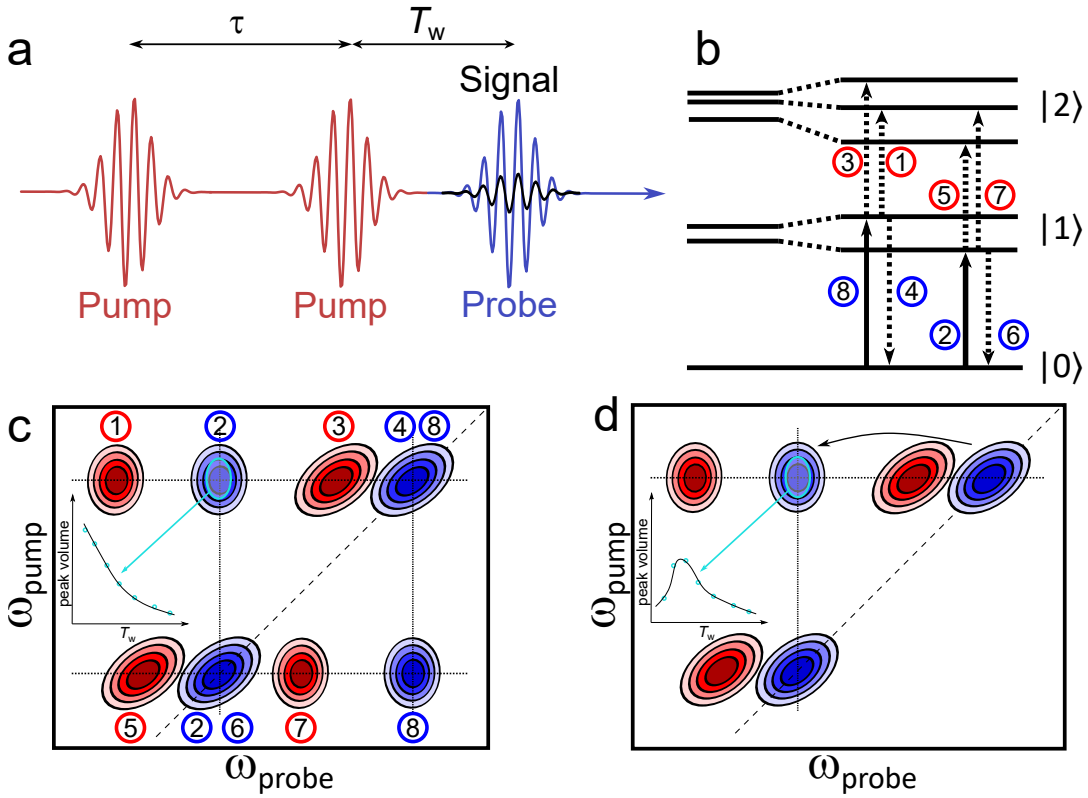

FIGURE 4.8: a) Pulse sequence used for 2DIR spectroscopy. In pump-probe geometry, the two pump pulses are collinear and therefore the signal is collinear with the probe pulse. b) Energy level diagram for two coupled oscillators with all possible transitions. c) Schematic drawing of a 2DIR spectrum of two coupled oscillators. The numbers link peaks in the spectrum to the transitions in b). The inset shows schematically the decay of a crosspeak caused by coupling. d) A schematic 2DIR spectrum of two oscillators that undergo downhill energy transfer. The inset shows a schematic behavior with time of an energy transfer cross peak.

pump-probe spectrum is essentially the 2D spectrum projected on the probe axis. Figure 4.8 b shows an energy level diagram of two coupled oscillators and the resulting 2D Spectrum is schematically shown in figure 4.8 c. The 2D spectrum allows for the resolution of crosspeaks as a result of coupling. Pumping the vibrational frequency of one oscillator will also cause a signal at the frequency of the second oscillator through coupling. This results in off-diagonal peaks forming a square shape together with the diagonal peaks.

These cross peaks are a useful tool for structural analysis as the presence of a cross peak can hint at two oscillators being in close proximity. Besides coupling, there are other mechanisms that can result in the appearance of cross peaks. Energy transfer from one to the other oscillator results in a cross peak. Figure 4.8 d shows a schematic 2D spectrum resulting from downhill energy transfer. A cross peak from energy transfer can be distinguished by the peak volume over time. For two coupled oscillators, the highest peak intensity is at t_0 following a decay (see inset figure 4.8 c) similar to what is expected for the diagonal peaks. For energy transfer, however, the cross peak intensity first increases to a maximum and is then followed by an exponential decay (see inset figure 4.8 d). Additionally, cross peaks at later waiting times can also appear due to heat dissipation into the sample, causing shifts of the peaks resulting in a negative and positive feature in the difference spectrum. Finally chemical exchange can also lead to cross-peak features as the oscillators inter convert on the timescale of the measurement.[88]

4.2.3 Spectral Diffusion

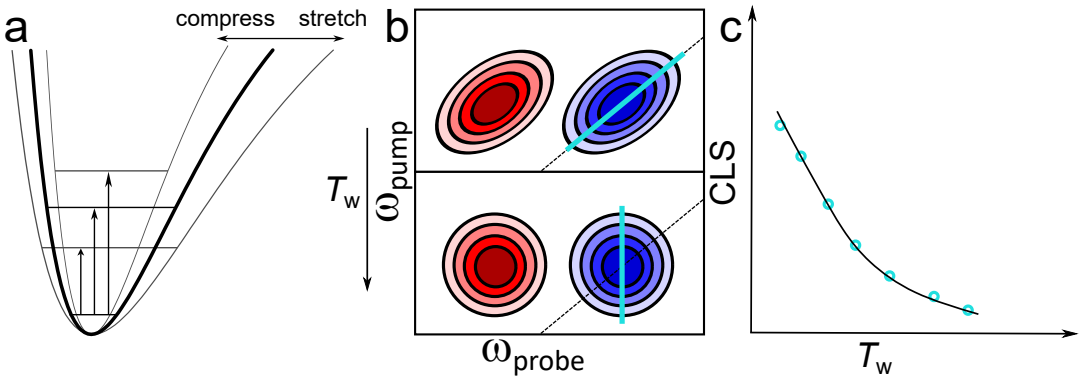

FIGURE 4.9: a) Schematic of an anharmonic oscillator stretching and compressing due to changes in the oscillator solvation shell, changing the instantaneous transition frequency. b) Schematic drawing of a 2DIR spectrum that undergoes spectral diffusion with time, and c) the corresponding center line slope dynamic.

As schematically shown in figure 4.8 c) and d) diagonal peaks can be elongated along the diagonal. This effect is called inhomogeneous broadening. With time the environment of a molecule fluctuates through deformation of the immediate surroundings, bond breaking or bond formation. This results in the compression

and stretching of the anharmonic oscillator of that molecule and therefore a fluctuation in instantaneous 0-1 transition frequency. This fluctuation encodes the spectral diffusion dynamics of the system. Spectral diffusion can, for example be caused by changes to the solvation shell or changes to the hydrogen bonding state of the molecule. 2DIR spectroscopy allows us to access the spectral diffusion dynamics via the tilt of the diagonal peaks. At early waiting times, not enough time has passed in which the oscillators could have changed their frequencies, therefore, there is a high correlation between where the oscillator was pumped and what frequency it had when being probed (see figure 4.9 b). This results in peaks elongated along the diagonal. The diagonal broadening for systems with a broad range of different micro environments at early waiting times is called inhomogeneous broadening. The anti-diagonal of the peak at early waiting times is only homogeneously broadened. At late waiting times, the initial frequency correlation is lost and the peaks become more upright in shape. This change in tilt is essentially a measure of the frequency frequency correlation function (FFCF) and can be accessed by the center line slope (CLS) method[89]. In cuts parallel to the probe axis, the position of the minimum is determined. The locations of the minima vs. the pump frequency are then fitted via linear regression. Because of the axis assignment convention abided by in this thesis (x-axis: probe and y-axis: pump) the actual observable is the inverse of the CLS. The decaying CLS with time can be fitted with one (or multiple, depending on the system) exponential functions as well as oscillations in special cases. Important to note is that the exponential has to decay to zero, as with infinite time, the correlation is completely lost. Changes in the CLS dynamics can give information on changes to the hydrogen bonding network and is therefore a useful tool when analyzing the dynamic nature of hydrogen bonds.

4.2.4 Kubo Lineshape Theory

We previously discussed the homogeneous and inhomogeneous contributions to a peak, but to better understand their origins, we will discuss lineshape theory. The transition frequency ω_{01} in a real system is not static but fluctuates with time, leading to dephasing. In equation 4.48 we only treat pure dephasing phenomenologically by including a decay with T_2. Now, we want to understand dephasing on a microscopic level. The time evolution of a density matrix of a single oscillator during the coherence time is described by equation 4.49

$$\frac{d\rho_{01}(t)}{dt} = -i\omega_{01}(t)\rho_{01}(t) \tag{4.49}$$

where now the transition frequency $\omega_{01}(t)$ is time dependent. Integration of equation 4.49 and considering the ensemble average yields:

$$\langle \rho_{01}(t) \rangle \propto \left\langle \exp(-i \int_0^t \omega_{01}(\tau) d\tau) \right\rangle . \tag{4.50}$$

Because the molecules in the ensemble dephase with time, the magnitude of the ensemble-averaged density matrix $\langle \rho_{01} \rangle$ decays with time. To simplify equation 4.50 we split the transition frequency into a static mean frequency and a time dependent-fluctuation $\delta\omega_{01}(t)$.

$$\omega_{01}(t) = \omega_{01} + \delta\omega_{01}(t). \tag{4.51}$$

Since the time average with a time-independent frequency disappears, we get the following expression:

$$\rho_{01}(t) \propto e^{-i\omega_{01}t} \left\langle \exp(-i \int_0^t \delta\omega_{01}(\tau) d\tau) \right\rangle. \tag{4.52}$$

If all possible states of ω_{01} are reached by time evolution, we can modify the ensemble average to a moving time average. This gives the frequency frequency correlation function (FFCF):

$$\langle \delta\omega_{01}(t)\delta\omega_{01}(0) \rangle = \frac{1}{T} \int_0^T \omega_{01}(\tau)\omega_{01}(\tau + t) d\tau \tag{4.53}$$

where T is the total length of the time trace. The FFCF can be normalized with the variance of the fluctuations $\langle \delta\omega_{01}^2 \rangle$ so that the value at $t = 0$ is one.

Kubo introduced an exponential ansatz for the FFCF [90]

$$\langle \delta\omega(t)\delta\omega(0) \rangle = \Delta\omega^2 e^{-\frac{|\tau|}{\tau_c}}. \tag{4.54}$$

The so-called Kubo lineshape function ($g(t)$) is obtained by integrating equation 4.54 twice.

$$g(t) = \Delta\omega^2 \tau_c^2 \left(e^{-\frac{t}{\tau_c}} + \frac{t}{\tau_c} - 1 \right). \tag{4.55}$$

In the homogeneous limit, fluctuations are very fast ($\Delta\omega\tau_c \ll 1$), and the Kubo lineshape function simplifies to:

$$g(t) = \Delta\omega^2 \tau_c t \equiv \frac{t}{T_2^*} \tag{4.56}$$

with a pure dephasing time $T_2^* = \frac{1}{\Delta\omega^2\tau_c}$. In the homogeneous limit this function can be approximated by a delta function and we obtain a Lorentzian lineshape with width ($\frac{1}{T_2^*}$).

$$A(\omega) \propto \frac{\frac{1}{T_2^*}}{(\omega - \omega_{01})^2 + \frac{1}{T_2^{*2}}}. \tag{4.57}$$

The linewidth in the fast modulation limit is actually narrower than the distribution of frequencies $\Delta\omega$. This process is called motional narrowing and is caused by the linear dependence of the width on the coherence time. Effectively, the fluctuations are so fast that only the average is observable.

On the opposite end of fluctuation speeds is the slow fluctuation or inhomogeneous limit ($\Delta\omega\tau_c \gg 1$). The frequency fluctuations are so slow that they are assumed to be static and the FFCF is constant ($\langle\delta\omega(t)\delta\omega(o)\rangle = \Delta\omega^2$) and the lineshape function becomes:

$$g(t) = \frac{\Delta\omega^2 t^2}{2}. \tag{4.58}$$

The absorption spectrum reduces to a Gaussian lineshape.

$$A(\omega) \propto e^{-\frac{\omega-\omega_{01}}{2\Delta\omega^2}}. \tag{4.59}$$

Typically even single-component systems are composed of fluctuations on multiple timescales, a fast (inertial) and a slow (diffusive) component. Thus, peaks in the 2DIR spectrum show a Voigt line shape along the diagonal. A Voigt profile is a convolution of a Lorentzian (inertial) and a Gaussian (diffusive) profile. Along the anti-diagonal only oscillators with a singular frequency are excited, therefore, only the fast fluctuations contribute to the line shape, and we obtain a Lorentzian line shape.

4.3 Classical Force Field Molecular Dynamics (FFMD)

Molecular Dynamics (MD) simulation is a computational technique where Newton's equations of motion are solved numerically for a set of molecules. For a simple atomic system, the classical equations of motions can be written as:[91]

$$f_i = m_i \frac{d^2 r_i}{dt^2} = -\frac{\partial}{\partial r_i} U(r_i) \tag{4.60}$$

where f_i is the force of an atom, r_i is its position and U_i is the potential. Conceptually for each propagation step of length δt the forces acting on each atom are calculated at t, followed by the calculation of the new positions at $t+$. Since atoms in the simulation box interact with other atoms, interactions between molecules have to be taken into account. These interactions are treated by a force field (ff). The force field is a set of parameters describing the bonded and non-bonded interactions and is derived from quantum mechanical calculations. The non-bonded pairwise interactions (like van-der-Waals interactions) are most commonly modeled by a Lennard-Jones Potential.[91, 92]

$$U^{\mathrm{LJ}}(r) = 4\epsilon \left[\left(\frac{\sigma}{r}\right)^{12} - \left(\frac{\sigma}{r}\right)^{6} \right] \tag{4.61}$$

where σ is the width and ϵ is the depth of the well. Electrostatic pairwise interactions are modeled by a Coulomb potential.

$$U^{\mathrm{Coulomb}}(r) = \frac{Q_1 Q_2}{4\pi\epsilon_0 r} \tag{4.62}$$

with the charges Q_1 and Q_2 and the vacuum permittivity ϵ_0.[91]

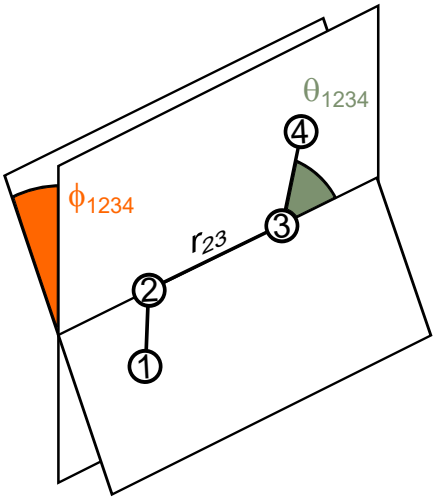

FIGURE 4.10: Illustration of a molecule with four atoms and the corresponding distance, angle and dihedral angle.

The bonding potentials are split in bond, angle and dihedral interactions, as displayed in figure 4.10 and are described by:[91]

$$\begin{aligned} U_{\text{intra}} = &\frac{1}{2}\sum_{\text{bonds}} k^r_{\text{ij}}(r_{\text{ij}} - r_{\text{c}})^2 \\ &+ \frac{1}{2}\sum_{\text{angle}} k^\theta_{\text{ijk}}(\theta_{\text{ijk}} - \theta_{\text{c}})^2 \\ &+ \frac{1}{2}\sum_{\text{dihedral}}\sum_{\text{m}} k^{\phi,m}_{\text{ijkl}}(1 + \cos(m\phi_{\text{ijkl}} - \phi_{\text{c}})) \end{aligned} \tag{4.63}$$

The bonds are modeled by a harmonic potential with the equilibrium distance r_{c}, the distance r_{ij} and the spring constant k^r_{ij}. The angle contributions describe bending motions between three connected atoms (i-j-k). This is also usually modeled with a harmonic potential around an equilibrium angle θ_{c}, the current angle θ_{ijk} and the spring constant k^θ_{ijk}. The dihedral interactions describe torsion angles between four connected atoms (i-j-k-l). It is defined as the angle between the unit normal of the two planes defined by the two angles θ_{ijk} and θ_{jkl} ($\cos(\phi_{\text{ijkl}}) = (r_{\text{ij}} \times r_{\text{jk}}) \cdot (r_{\text{jk}} \times r_{\text{kl}})$). Usually, the dihedral interactions involve an expansion in periodic functions of the order $m = 1, 2, ...$[91]

4.3.1 The Velocity Verlet Algorithm

A full description and calculation of all molecular parameters would be very expensive, therefore different algorithms try to reduce necessary calculations. These include the original Verlet algorithm[93, 94], the leapfrog algorithm[95], and the velocity Verlet algorithm[96], that we will discuss in more detail. For a system with N atoms with the coordinates $r^N = (r_1, r_2, ...r_N)$, the momenta $p^N = (p_1, p_2, ...p_N)$ and the potential energy $U(r^N)$, the velocity Verlet algorithm can then be written as:

$$p_i\left(t+\frac{1}{2}\delta t\right) = p_i(t) + \frac{1}{2}\delta t f_i(t) \tag{4.64}$$

$$r_i(t+\delta t) = r_i(t) + \frac{\delta t p_i(t+\frac{1}{2}\delta t)}{m_i} \tag{4.65}$$

$$p_i(t+\delta t) = p_i(t+\frac{1}{2}\delta t) + \frac{1}{2}\delta t f_i(t+\delta t) \tag{4.66}$$

To propagate the system by one step, first the momentum and velocity at half of the step are calculated (equation 4.64). From there, the positions at the full step are calculated (equation 4.65). After that the forces $f_i(t+\delta t)$ are calculated, and then finally, the momentum/velocity for the full step is calculated (equation 4.66). Generally, calculating the force is the most expensive step. Therefore the velocity Verlet algorithm can reduce computational costs by reducing the necessary force calculation to once per step.

4.3.2 Periodic Boundary Conditions

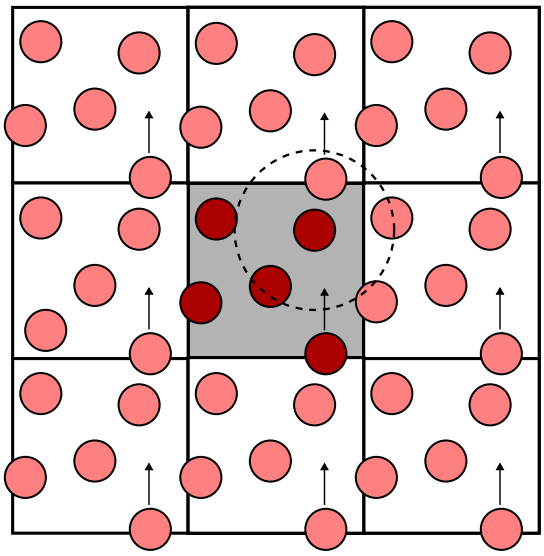

FIGURE 4.11: Illustration of periodic boundary conditions in a MD simulation. When an atom leaves the original simulation box, a copy will reenter the original box on the opposite side at the same speed.[92]

The number of atoms that can be included in a MD simulation is very limited and therefore most of those atoms are at the surface. Considering 1000 atoms arranged in a cube with $10 \times 10 \times 10$ atoms. In this case, 488 atoms are at the surface, and increasing the number of atoms still leads to a significant fraction of surface molecules. To accurately calculate bulk properties periodic boundary conditions (PBC) are used. This means that if an atom leaves the simulation box it will reenter from the opposite side with the same velocity and direction. Therefore, atoms on one side of the simulation box can interact with copies of atoms on the other side of the simulation box.

This means that only bulk atoms are present. For long range interactions the atom will only interact with the closest image of another atom. It is important to note that the simulation box needs to be larger than the longest potential interactions. [91, 92]

4.3.3 Statistical Ensembles

In the simulation, a statistical ensemble needs to be specified. This ensemble describes which properties are kept constant and what properties are free. The most commonly used ensemble is the canonical (NVT) ensemble. Here, the number of particles N, the volume V and the temperature T are kept constant. On the other hand, the chemical potential μ, the pressure p and the energy E are free to vary. The constant volume and the constant number of particles is achieved by default but keeping the temperature static requires a thermostat. The simplest way of implementing a thermostat is to periodically randomize the velocities of the particles weighted by the Boltzmann distribution for the desired temperature.[97] A different option is the Nose-Hoover thermostat[98]. In the Nose-Hoover thermostat, a dynamic friction variable ζ is introduced to calculate the momentum.

$$\frac{dp_{\mathrm{i}}}{dt} = f_{\mathrm{i}} - \zeta p_{\mathrm{i}}. \tag{4.67}$$

The friction coefficient changes based of the ratio on set temperature to actual temperature, and either slows atoms down or speeds them up. Other commonly used statistical ensembles are shown in table 4.1.[99]

TABLE 4.1: Overview of commonly used statistical ensembles.

Ensemble	Given parameters	Dynamic parameters
canonical	N, V, T	μ, p, E
micro canonical	N, V, E	μ, p, T
grand canonical	μ, V, T	N, p, E
isothermal-isobaric	N, p, T	μ, V, E

4.3.4 Radial Distribution Functions (RDF)

The radial distribution function (RDF) $g(r)$ is given by equation 4.68.[100]

$$g(r) = \lim_{dr \to 0} \frac{p(r)}{4\pi(\frac{N_{\mathrm{pairs}}}{V})r^2 dr} \tag{4.68}$$

with the particle pair distance r, the average number of atom pairs found at distances in between r and $r + dr$ $p(r)$, the volume V and the number of unique pairs of atoms N_{pairs}. In case of an ideal gas, the denominator becomes $p(r)$ and the radial distribution function becomes one for all distances $g(r) = 1$. The denominator also normalizes the RDF to the bulk density, and therefore, for long distances $g(r) \approx 1$. The number of atom pairs found between r and $r + dr$ can be calculated with equation 4.69:[100]

$$p(r) = \frac{1}{N_{\text{frame}}} \sum_{i}^{N_{\text{frame}}} \sum_{\text{j}\in\text{sel}_1} \sum_{\text{k}\in\text{sel}_2;\text{k}\neq\text{j}} \delta(r - r_{\text{ijk}}). \tag{4.69}$$

with the Dirac delta function $\delta(x)$

$$\delta(x) = \begin{cases} 0, x \neq 0 \\ \infty, x = 0 \end{cases} \tag{4.70}$$

where sel_1 and sel_2 are the selection criteria for the sets of atoms. For example sel_1 could be name: O and sel_2 name: H. Then the RDF would represent the O-H distances. The number of simulation frames in the trajectory is N_{frame} and r_{ijk} is the distance from atom j to atom k in frame i. Since only finite sampling is possible due to the time steps of the simulation, the continuous function in equation 4.69 turns into a histogram.[100]

$$p(r) = \frac{1}{N_{\text{frame}}} \sum_{i}^{N_{\text{frame}}} \sum_{\text{j}\in\text{sel}_1} \sum_{\text{k}\in\text{sel}_2;\text{k}\neq\text{j}} \sum_{\text{all}} d_\kappa(r; r_{\text{ijk}}) \tag{4.71}$$

where κ indexes the bins of the histogram and d_x references wether atoms are in the bin.

$$d_\kappa(r_{\text{ijk}}) = \begin{cases} (\Delta r)^{-1} & \text{if } r_\kappa \leq r < r_\kappa + \Delta r \text{ and } r_\kappa \leq r_{\text{ijk}} < r_\kappa + \Delta r \\ 0 & \text{else} \end{cases} \tag{4.72}$$

with the width of the bins Δr and the minimum distance for each bin $r_\kappa = r_0 + \kappa\Delta r$, where r_0 is the lower bound of the histogram. Because of periodic boundary conditions r_{ijk} is the shortest distance between j and any mirror image of i. In this case the the maximum distance sampled by the histogram should be chosen as smaller than half the box length a to exclude counting multiple mirror images of k.[100]

4.4 Ab Initio Molecular Dynamics (AIMD)

Classical MD treats the system as fully classical and only the force field parameters are derived from quantum calculations. This means that the force field has to be specifically parameterized for all specific interactions that can occur in the system. Typically, more general force fields (AMBER[101, 102], CHARMM[103, 104] or OPLS-AA[105]) are parametrized on a variety of different molecules, however, the force field is very likely not specifically parameterized for the exact desired system, which can lead to inaccuracies. The alternative is to parameterize a force field for the specific problem at hand. This however requires a lot of effort. Another drawback of classical force fields is that covalent bonds are modeled by a harmonic potential, meaning that bond breaking and formation is impossible.[99] A solution

to these problems comes with ab initio MD (AIMD). The basic idea of AIMD is to not rely on a pre-parameterized force field but rather calculate the forces acting on the atoms from electronic structure calculations during the simulation. This however means that AIMD is much more expensive than FFMD and therefore the systems in general have to be smaller and the simulated time be shorter. Instead of modeling interatomic forces with a force field, AIMD aims to solve the time-dependent Schrödinger equation (equation 4.30) of the system. With the Hamilton operator:

$$\hat{H} = -\sum_{\mathrm{I}} \frac{\hbar^2}{2M_{\mathrm{I}}} \nabla_{\mathrm{I}}^2 + \hat{H}_{\mathrm{e}}(\{r_{\mathrm{i}}\}, \{R_{\mathrm{I}}\}) \tag{4.73}$$

where $\{r_{\mathrm{i}}\}$ are the electronic and $\{R_{\mathrm{I}}\}$ the nuclear degrees of freedom, M_{I} is the mass of the Ith nucleus and $\hat{H}_{\mathrm{e}}$ is the electronic Hamilton operator.[99]

4.4.1 Born-Oppenheimer MD (BOMD)

Since calculating the exact solution to the Schrödinger equation is impossible, approximations are required. In the Born-Oppenheimer approximation[106], it is assumed that since the nuclei are orders of magnitude heavier than the electrons and thy are, therefore, much slower. The nuclei can then be assumed to be static for the calculation of the potential. Therefore, the time-independent Schrödinger equation can be used to calculate the potential of the nuclei.[99]

$$\hat{H}_{\mathrm{el}}(r, R)\psi_{\mathrm{n}}(r, R) = E_{\mathrm{n}}(R)\psi_{\mathrm{n}}(r, R) \tag{4.74}$$

with the electronic Hamilton operator

$$\hat{H}_{\mathrm{el}}(r, R) = \hat{T}_{\mathrm{e}} + \hat{U}_{\mathrm{en}} + \hat{U}_{\mathrm{ee}} + \hat{U}_{\mathrm{nn}} \tag{4.75}$$

where $\hat{T}_e$ is the kinetic energy operator for the electrons, $\hat{U}_{\mathrm{en}}$ is the electron nucleus attraction, $\hat{U}_{\mathrm{ee}}$ is the electron-electron repulsion and $\hat{U}_{\mathrm{nn}}$ is the nucleus-nucleus repulsion. Then, the nuclear Schrödinger equation χ_{k} can be formed.[99]

$$\left[\hat{T}(R) + E_{\mathrm{n}}(R)\right] \chi_{\mathrm{n}} = i\hbar \frac{\partial}{\partial t} \chi_{\mathrm{n}} \tag{4.76}$$

In the classic approximation, this can be expressed in the form of Newtons equations of motion:

$$M_{\mathrm{I}} \frac{d^2 R_{\mathrm{I}}}{dt^2} = -\nabla_{\mathrm{I}} E_{\mathrm{n}} \tag{4.77}$$

In Born-Oppenheimer MD, the potential of the electrons acting on the nuclei E_{n} is calculated for every simulation step and the system is then subsequently propagated with equation 4.77.[99]

4.4.2 Vibrational Density of States (VDOS)

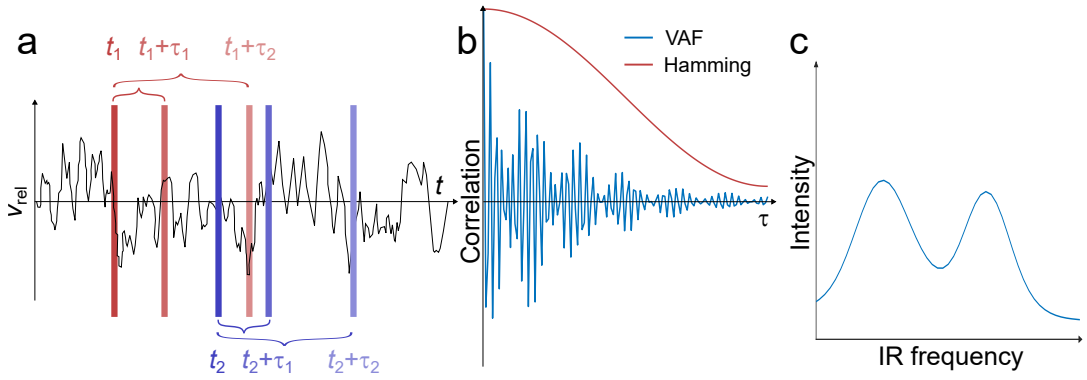

FIGURE 4.12: a) Relative velocity over time with a schematic illustration of the velocity autocorrelation function (VAF). b) To the velocity auto correlation function (blue) a Hamming window is applied. After Fourier transformation of the VAF the vibrational density of states (VDOS) shown in c) is obtained.

The vibrational density of states (VDOS) is essentially a spectrum without taking transition dipole moments into account. Therefore, it is useful to observe trends in e.g. peak shifts upon changes to the system however it does not predict peak intensities well. The VDOS is calculated through the velocity autocorrelation function (VAF).[107]

$$\mathrm{VAF}(t,\tau) = \frac{\langle \vec{v}_{\mathrm{rel}}(t+\tau)\vec{v}_{\mathrm{rel}}(t)\rangle}{\langle \vec{v}_{\mathrm{rel}}(t)^2\rangle} \tag{4.78}$$

Functionally, the relative velocity ($\vec{v}_{\mathrm{rel}} = \vec{v}_{\mathrm{i}} - \vec{v}_{\mathrm{k}}$) of a bond between atoms i and j at time t_1 is correlated with the relative velocity at $t_1 + \tau_1$. This is repeated for one t for all τ and then summed up over all t as schematically shown in figure 4.12 a. Then the function is normalized by the mean square of the relative velocity. The corresponding VAF is displayed in figure 4.12 b. Before fast Fourier transformation, a window function (in this case, Hamming window) is applied to avoid spectral leakage. The resulting VDOS is shown in figure 4.12 c.

Chapter 5

Methods and Materials

The sections of Methods and Materials are reproduced from the publications [1], [2] and [3], with minor changes. The sections are modified to fit the format of the thesis.

5.1 Methods and Materials for Chapter 6[1]

5.1.1 Sample preparation

Deuteriumoxide (D_2O, 99.9 atom% D), urea (ACS reagent), and urea-d4 (98 atom% D) were purchased from Sigma-Aldrich and used without further purification. Dimethylsulfoxide (DMSO, 99.7+%, extra dry) and (DMF, 99.8%, extra dry) were purchased from Arcos Organics. The solvents DMF and DMSO were stored over 4 Å molecular sieve (Carl Roth), which was dried in a vacuum oven prior to use. H_2O with a specific resistivity of 18.2 MΩcm at 25 °C was obtained from a Synergy purification system (Merck). 10% D_2O/90% H_2O and 100% D_2O solutions of water in DMF were prepared volumetrically with a constant mole fraction of water of 5%. For the 10% D_2O/90% H_2O mixture, HOD molecules comprise the major fraction of isotopically substituted species: a binomial distribution of isotopes results in 1% D_2O, 18% HOD, and 81% H_2O. Urea/urea-d4 mixtures (30% urea-d4 and 100% urea-d4) were prepared by weight in glass vials using an analytical balance. After isotopic equilibration the 30% urea-d4 corresponds to ∼1% urea-d4, ∼8% urea-d3, ∼26% urea-d2, ∼41% urea-d1, and ∼24% urea. The total urea mole fraction was kept constant at 2.8%. To minimize water contamination for the urea/urea-d4 mixtures in DMSO, samples were prepared in an Ar-filled glovebox. To ensure isotopic equilibration, samples were prepared at least 24 h prior to experiments (see Supplementary Fig. 6.15). All samples were held between two CaF_2 windows separated by a Teflon spacer (urea-d4 100%: 100 μm; urea-d4 30%: 300 μm; 10% D_2O: 200 μm and 100% D_2O: 50 μm). To avoid uptake of moisture for urea in DMSO, the sample cells were assembled and filled in a glovebox.

5.1.2 Infrared Absorption Spectroscopy

Infrared spectra were recorded in transmission using a Bruker Vertex 70 IR spectrometer, with a resolution of 4 cm^{-1} at frequencies ranging from 400 cm^{-1} to 4000

cm^{-1}. The spectrometer was purged with dried air during measurement.

5.1.3 Two-Dimensional Infrared Spectroscopy

2D-IR experiments were based on 800 nm pulses (7 W, 35 fs, 1 kHz) from a Ti: sapphire-based regenerative amplifier (Coherent Astrella). A fraction of these pulses (pulse energy 2.7 mJ) was used to pump an optical parametric amplifier (Coherent Topas Prime) togenerate signal and idler pulses. IR pulses at 4 μm (30μJ, 400 cm^1 FWHM) were generated via non-collinear difference frequency generation between the signal and idler beams in a GaSe crystal (Coherent, Topas). The 4 μm pulses are sent to a commercial 2D-IR spectrometer 2D-Quick IR (PhaseTech Spectroscopy, Inc.). The reflection at a wedged ZnSe window is used as a probe beam. Excitation pulses are generated from the residual IR beam in a pulse shaper, in which the IR beam is diffracted from a grating (200 l/mm), collimated by a parabolic mirror, and guided through an acousto-optic modulator (AOM). The beam is diffracted from the AOM and focused by a second parabolic mirror on a second grating (200 l/mm). The waiting time (T_w) of the excitation pulses, relative to the probe pulse, is controlled using a translational stage, and the polarization of the excitation beam is set to 45°, relative to the probe beam using a half-wave plate. Pump and probe pulses are focused by a parabolic mirror and overlapped at the sample position. After re-collimation with a second parabolic mirror, the probe beam components perpendicular/parallel to the pump pulse are transmitted/ reflected through/from a wire grid polarizer, spectrally dispersed (SP2156 imaging spectrograph, Princeton Instruments, 30 l/mm grating), and detected (128 × 128-pixel mercury cadmium telluride array detector), to obtain the signals perpendicular ($\Delta\alpha_\perp(\tilde{\nu}_{\text{probe}})$) and parallel ($\Delta\alpha_\parallel(\tilde{\nu}_{\text{probe}})$) to the excitation polarization, respectively, as a function of detection frequency, $\tilde{\nu}_{\text{probe}}$, in the frequency domain. The excitation frequency, $\tilde{\nu}_{\text{pump}}$, is resolved in the time domain by generating two pump pulses that are delayed by t_1 using the pulse shaper. The resulting pulses have a pulse length of ∼90 fs. A rotating frame at 2400 cm^{-1} was used to reduce the number of time steps[108] and the raw data (700 fs at increments of 35 fs) were apodized using a Hamming window and zero-padded to 128 data points before Fourier transformation to the frequency domain (excitation frequency resolution of ∼4 cm^{-1}). For better comparability, signals were Fourier-filtered analogously along the probe axis. All 2D-IR spectra were corrected for the frequency-dependent pump pulse intensity. From these data sets, isotropic 2D-IR spectra, $\Delta\alpha_{\text{iso}}(\tilde{\nu}_{\text{pump}}, \tilde{\nu}_{\text{probe}})$, which are free of orientational dynamics, were constructed using the Eq. 5.1:

$$\Delta\alpha_{\text{iso}}(\tilde{\nu}_{\text{pump}}, \tilde{\nu}_{\text{probe}}) = \frac{\Delta\alpha_\parallel(\tilde{\nu}_{\text{pump}}, \tilde{\nu}_{\text{probe}}) + 2\Delta\alpha_\perp(\tilde{\nu}_{\text{pump}}, \tilde{\nu}_{\text{probe}})}{3} \tag{5.1}$$

Figures 6.2b–e and 6.5a, b in the main manuscript show $\Delta\alpha_{\text{iso}}(\tilde{\nu}_{\text{pump}}, \tilde{\nu}_{\text{probe}})$ data, Figs. 6.4a, b and 6.5d show $\Delta\alpha_\perp(\tilde{\nu}_{\text{pump}}, \tilde{\nu}_{\text{probe}})$.

5.1.4 DFT calculations

All calculations were performed using Orca 4.1.1 [109] (BLYP[110, 111] -D3(BJ)[112, 113] /def2-TZVPP[114, 115] level of theory). Geometries of one water (urea) molecule, donating two (four) H-bonds to two DMF (four DMSO) molecules embedded in a polarizable continuum[116] (DMF or DMSO) were optimized, with two hydrogen bond distances $H_{water}\cdots O_{DMF}$ ($H_{urea}\cdots O_{DMSO}$) of water (one amine group) constrained to 1.5–2.4 Å at increments of 0.1 Å (water) and to 1.5–2.4 Å at increments of 0.1 Å (urea). Coupled OD stretching frequencies of water were obtained using D_2O and uncoupled stretching frequencies using HOD. For urea, coupled N-D stretching vibrations were calculated for one of urea's amine groups of urea-d2t2, with the hydrogen-bonding distances to the ND_2 groups being varied. Uncoupled N-D frequencies, were obtained based on urea-h1d1t2. All frequencies discussed in the manuscript are based on harmonic normal mode frequencies and were interpolated using spline interpolation. As anharmonic corrections exhibit a linear correlation with harmonic frequencies[117], we scale the thus obtained harmonic frequencies by a constant scaling factor for each mode such that the harmonic frequencies at the energetic minimum match the experimental center frequencies.

5.2 Methods and Materials for Chapter 7 [2]

5.2.1 Materials

1,1,1,3,3,3-hexafluoroisopropanol (HFIP, spectroscopy grade, $> 99.9\,\%$, Fisher Scientific) and isopropanol (Optima LC/MS Grade, $> 99.9\,\%$, Fisher Scientific). Deuterated HFIP-d2 and isopropanol were purchased from Eurisotop (99.00% D, water content $< 0.3\%$). Diethylether ($\geq 99.5\%$) was purchased from Carl Roth and Chloroform ($99 + \%$) was purchased by Acros Organics. All chemicals were used without further purification. Deuterated samples were handled under an inert Argon atmosphere.

5.2.2 Linear Infrared spectroscopy

Transmission infrared spectra were recorded using a Bruker Vertex 70 IR spectrometer, with a resolution of 4 cm^{-1} between 400 cm^{-1} to 4000 cm^{-1}. During measurement the spectrometer was flushed with dried air. Linear spectra of isotopically dilute alcohols were measured using a 50¯m spacer and measurements in chloroform were conducted using a 200¯m spacer.

5.2.3 Infrared pump-probe spectroscopy

Mid-IR vibrational pump-probe spectroscopy was used to measure the decay of the vibrational anisotropy of the OD-stretch vibration of isotoped-diluted solutions of HFIP and isopropanol. The femtosecond IR pulses (5 μJ) used in the experiments

were characterized by a center frequency of 2500 cm^{-1}, duration ∼180 fs (FWHM) and spectral width of 150 cm^{-1} (FWHM) and were generated by a series of nonlinear frequency-conversion processes pumped by a commercial Ti:sapphire regenerative amplifier (for details see Ref. huertaviga2010). The probe and reference beams were generated by splitting off a small portion (a few %) of the IR light with a wedged CaF_2 window, while the transmitted light provided the pump beam. The measurements were performed on isotopically diluted samples (D/H=0.1) to avoid coupling between molecular oscillators [118–120]. The bandwidth of the pump and probe beams was $\sim$ 150cm^{-1}, large enough to avoid the influence of spectral diffusion on the anistropy measurements. The liquid samples were loaded into 200μm thick cells equipped with CaF_2 windows.

5.2.4 Two-dimensional Infrared (2D-IR) spectroscopy

The setup is described in more detail in our previous work.[4, 121] Briefly, we used 800 nm laser pulses (5.6 W, 35 fs, 1 kHz) from a regenerative amplifier (Coherent Astrella) to generate 4000 nm IR pulses (25 μJ, 400 nm full width at half maximum) with an optical parametric amplifier (Topas Prime, Coherent) and noncollinear difference frequency generation (NDFG). The IR pulses are guided into a commercial 2D-IR spectrometer (2D Quick IR, Phasetech Inc.). A small fraction of the IR pulses is split off as the probe pulse. We generated pump pulse pairs, delayed by 0 fs to 700 fs at increments of 35 fs, using a pulse shaper based on an acousto-optic modulator (AOM). The pump frequency was resolved by Fourier transformation of these time-domain data. A rotating frame at 2300 cm^{-1} was used to reduce the measuring time. Before Fourier transformation, the data was zero padded to 128 data points and a Hamming window was applied. Pump and probe pulses were focused and overlapped in the samples, which were held between CaF_2 windows separated by 100 μm teflon spacers. We use a pump probe geometry yielding absorptive 2D-IR spectra.[21] The probe frequency was resolved in the frequency domain by dispersing the probe pulses onto a 128 x 128 mercury cadmium telluride (MCT) array detector. All spectra were recorded with parallel polarized excitation and detection pulses. For better comparability, signals were Fourier-filtered analogously along the probe axis.

5.2.5 Dielectric relaxation spectroscopy

Complex permittivity spectra $\hat{\varepsilon}(\nu) = \varepsilon'(\nu) - i\varepsilon''(\nu)$, where ε' is the dielectric permittivity and ε'' the dielectric loss, were measured as function of field frequency, ν, using a frequency domain reflectometer using flanged open-ended coaxial probes [122–124]. Frequencies at $0.07 \leq \nu/\mathrm{GHz} \leq 0.52$ were covered using coaxial probes made from SMA hermetic feedthroughs and frequencies $0.53 \leq \nu/\mathrm{GHz} \leq 43$ using coaxial probes based on 1.85 mm feedthroughs connected to a vector network analyzer (VNA, Anritsu MS4647A). Spectra at $57 \leq \nu/\mathrm{GHz} \leq 125$ were recorded using

a 1 mm connector coaxial probe connected to an external frequency converter (Anritsu 3744A mmW) in combination with the VNA [125]. The reflection coefficient at the coaxial-probe/sample interface was calibrated using air, conductive silver paint, and water as references [126]. Spectra were recorded from 5 mL of the sample in a glass vial in contact with the coaxial probes.

5.2.6 Density functional theory calculations

To estimate the differences in hydrogen-bond strengths formed by the two alcohols, we determined interaction energies for HFIP and isopropanol donating hydrogen-bonds to HFIP, isopropanol, and diethylether using density functional theory (DFT) calculations with the ORCA program package (version 5.0.4) [109]. All calculations were performed at the B3LYP[110, 127–129], 6-311++G(d,p) [130] level of theory. The solvent was accounted for using the CPCM solvation model[131–134] using chloroform as solvent. To determine the interaction energies we optimized the geometry of the dimers. Subsequently, we displaced the two molecules and performed a second geometry optimization with the distance of the two oxygen atoms (the O of the hydrogen-bond donating OH group and the hydrogen-bond accepting O) constrained to 30 Å. The interaction energy was taken as the difference in the single point energies of both geometry optimizations, which includes electronic and solvation contributions.

5.3 Methods and Materials for Chapter 8 [3]

5.3.1 Sample Preparation

Calcium chloride ($CaCl_2$) was purchased from Sigma-Aldrich (anhydrous powder, $\geq$ 97 %). $CaCl_2$ was dried in vacuo at 200 °C for two hours and stored in an Ar-filled glove box. *L*-alanyl-*L*-alanine (2Ala), *N*-methylacetamide (NMA), L-alanine (1Ala), and D_2O were purchased from Sigma-Aldrich and used without further purification. We synthesized isotope-labeled 2Ala using a procedure described in the Supplementary Information (Supplementary Figures 1-3). All solutions were prepared in 1 mL volumetric flasks. For all experiments reported in the main manuscript, the concentration of 2Ala was kept constant at 250 mM. Solutions of NMA and 1Ala were prepared at 125 mM. The concentration of $CaCl_2$ was increased from 1 to 5 M at increments of 1 M.
For IR experiments, samples were contained between two CaF_2 windows (2 mm thickness; 2.54 cm diameter) separated by a 25 µm Teflon spacer for solutions of 2Ala (50 µm for solutions of 1Ala and NMA measurements).

5.3.2 Linear IR Measurements

Linear infrared absorption spectra were recorded using a Bruker Vertex 70 spectrometer in transmission geometry at frequencies ranging from 400 to 4000 cm^{-1} with a

resolution of 4 cm^{-1}. The sample compartment of the spectrometer was continuously purged with purified, dry air. Linear IR absorption spectra were reordered prior to the 2D IR experiments.

5.3.3 2D IR Measurements

800 nm pulses (35 fs pulse duration, 1 kHz repetition rate, 7 mJ pulse energy) from a regenerative amplified laser system (Coherent, Astrella) were used to pump an optical parametric amplifier (Topas Prime, Coherent) with an NDFG (non-collinear difference frequency generation) stage to generate IR pulses (6 µm wavelength, 18 µJ pulse energy, 400 cm^{-1} FWHM, $\sim$ 100 fs pulse duration). The IR pulses were guided to a commercial 2D IR spectrometer (2D Quick IR, Phasetech Inc.).[135, 136] A detailed description of the experimental setup (including the acousto-optic modulator to generate pump pulse pairs), in which the modulation of an infrared probe pulse transmitted through the sample by excitation of the sample is monitored as a function of time, can be found elsewhere.[4, 121]
The excitation frequency has been resolved in the time domain using pump pulse pairs delayed by 0 to 2555 fs (35 fs increments, with a rotating frame at 1400 cm^{-1}). Frequency-dependent modulation of the probe beam was detected by dispersing the probe beam onto a 128 x 128 mercury cadmium telluride (MCT) array detector. Prior to Fourier transformation of the time-domain data at each detection frequency, the time-domain data were zero-padded to 128 data points and filtered with a Hamming window. The 2D IR spectra of pure 2Ala in D_2O have been taken from ref. [4] and reevaluated for the present study.

5.3.4 *Ab initio* MD Simulations

We performed Born Oppenheimer MD simulations using the CP2K code.[137] We used the revPBE[138] exchange-correlation functional together with the empirical van der Waals correction scheme using Grimme's D3(0)[112] correction. We used the mixed Gaussian and plane wave approach.[139] Atomic orbitals were described using the DZVP-GTH basis set. Core electrons were described using norm conserving Goedecker-Teter-Hutter pseudopotentials.[140] The time step was set to 0.8 fs, and all simulations were performed at 350 K in the NVT ensemble using a canonical velocity rescaling thermostat.[141] The simulation boxes contained 60 water, 6 $CaCl_2$, and 1 2Ala in a (13.3 Å)^3 box, which corresponds to a $\sim$5 M $CaCl_2$ solution. Nine simulation runs with different initial geometries were recorded. Each simulation run was equilibrated for $\sim$24 ps and trajectories were recorded every 8 fs for $\sim$124 ps per simulation run, resulting in a total trajectory of 1.1 ns. Radial distribution functions (RDF) have been calculated using *VMD: Visual molecular dynamics*.[100, 142] The vibrational density of states (VDOS) was calculated based on the CO bond velocities.

5.3.5 Single Point DFT calculations

Vibrational frequencies of 2Ala and an acetate ion with different Ca^{2+} binding motifs were calculated using density functional theory (DFT) calculations with the ORCA program package (version 5.0.4).[109] Geometry optimizations were performed at the PBE,[143] def2-TZVPP [114] level of theory. The atom-pairwise dispersion correction with Becke-Johnson damping (D3BJ) was applied.[112, 113] Calculations were performed with a conductor-like polarizable continuum model with the dielectric properties of water. CHELPG partial charges were obtained using the Multiwfn package.[144, 145] All single point DFT calculations are shown in the Supplementary Information.

5.4 Fourier Transform and the Frequency Domain Spectrum

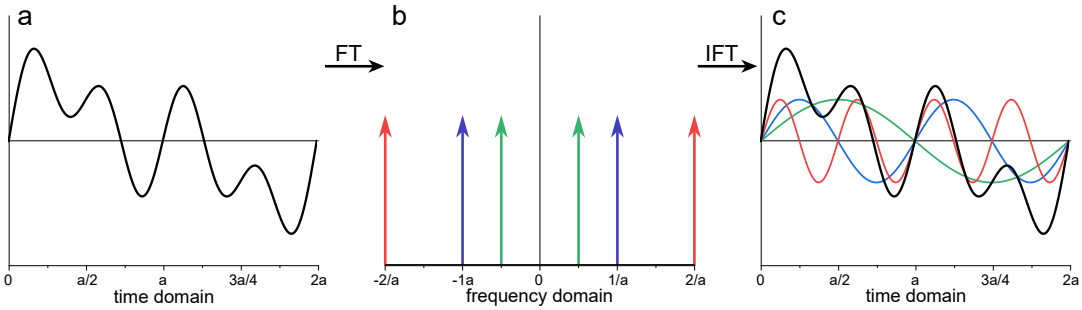

FIGURE 5.1: a) Time domain signal with unknown components. b) Fourier transform of the unknown signal reveals three spectral components as delta functions at their corresponding frequency. c) Inverse Fourier transform of the separated components reveals the three sine waves producing the original signals.

Figure 4.3 shows a time domain picture of the linear absorption process. However to obtain the linear absorption spectrum we must convert from time domain to frequency domain using a Fourier transformation (FT).[146]

$$F(y) = \frac{1}{\sqrt{2\pi}} \int_{-\infty}^{\infty} f(x) e^{-iy \cdot x} \mathrm{d}x. \tag{5.2}$$

Figure 5.1 a shows a signal comprised of multiple sine functions with unknown frequencies. A Fourier transform yields delta functions at the frequencies (and negative frequencies) of the sinusoidal components (see figure 5.1 b). This allows us to then separate the components, and for example apply a filter function to remove the high frequency component. An inverse Fourier transform then converts back to the time domain.[86, 146]

Figure 5.2 shows some important functions for spectroscopy and their Fourier transformed form. The Fourier transform of a sine (or cosine; Figure 5.2 a) wave is a delta function at the the corresponding frequency ($\delta(\pm\omega)$; Figure 5.2 b), a sinc function ($\frac{sin(x)}{x}$; Figure 5.2 c) converts to a rectangular function (Figure 5.2 d), a Gaussian function (Figure 5.2 e) converts to another Gaussian function (Figure 5.2 f) and a

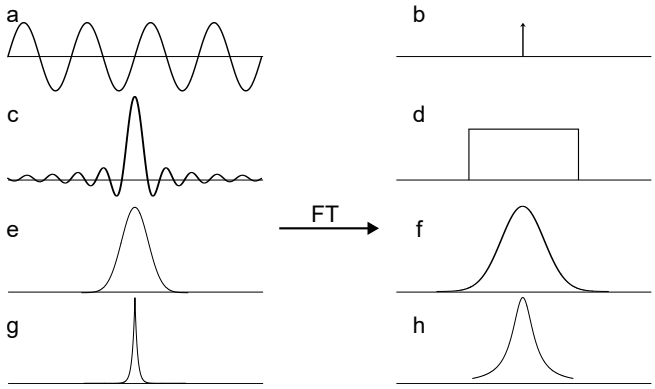

FIGURE 5.2: Overview of functions and their Fourier transforms:a) sine wave, b) Dirac delta function, c) sinc function, d) rectangular function, e) and f) Gaussian functions, g) double exponential function and h) Lorentzian function.

double exponential function (Figure 5.2 g) converts to a Lorentzian function (Figure 5.2 h). In all cases these also apply in the reverse as the inverse Fourier transform is functionally the same as the Fourier transform.[86, 146]

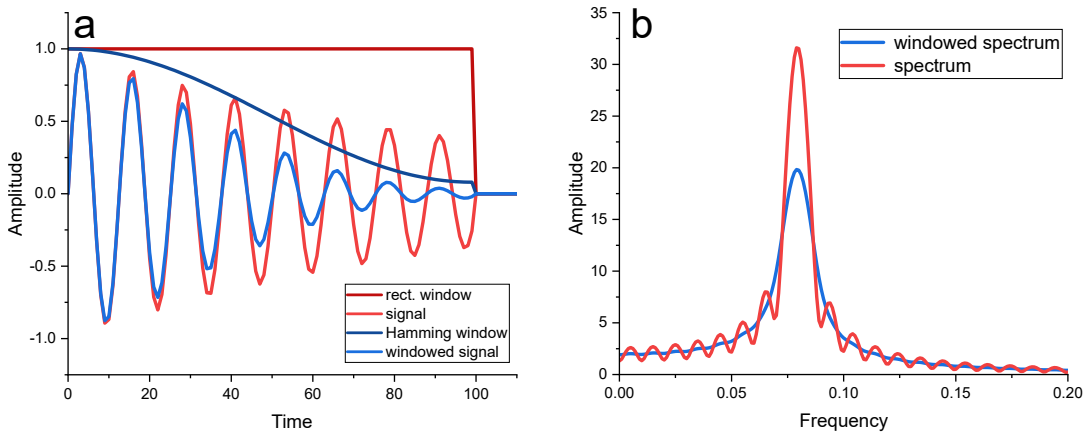

FIGURE 5.3: a) Exemplary convoluted signal (light red) consisting of a sine wave, an exponential decay and a rectangular function (dark red). After applying the Hamming window (dark blue) the windowed signal is obtained (light blue). b) Spectra resulting from the FFT of the original signal (red) and the windowed signal (blue).

The example in Figure 5.1 shows how useful the FT is in spectroscopy, however this simplified picture does apply for real measurements. The sine components are always damped in reality and the sine wave is thus multiplied with an exponential decay. Therefore, instead of a delta function at the center frequency ω_c we obtain a Lorentzian function shifted with the center frequency ω_c. Additionally as equation 5.2 shows we integrate over all real numbers meaning for this pure case we would need to measure the damped sine wave until infinity. Because the signal is only measured for a certain time the damped sine wave is essentially multiplied by a rectangular function. Therefore, upon Fourier transformation we obtain an additional sinc wave component. This phenomenon is called the spectral leakage and leads to a distortion of the true lineshape. This can be seen exemplary in figure 5.3 b, where the spectrum shows distinct features of a sinc function. [147] To circumvent

this artefact a window function is applied to the data, giving more weight to early data points than late data points. Figure 5.3 a shows a damped sine wave multiplied by a rectangular window (light red). After discrete Fourier transformation we obtain the spectrum (light red line in Figure 5.3 b) which shows artefacts due to spectral leakage. Multiplying the signal with a window function (light blue in Figure 5.3 a) can reduces spectral leakage effects. Here we use a Hamming window function (Equation 5.3 with $a_0 \approx 0.54$) as shown in dark blue (Figure 5.3 a)).[147]

$$a_0 + (1 - a_0) * \cos\left(\pi \frac{n}{N}\right) \qquad \text{with} \quad 0 \leq n \leq N \tag{5.3}$$

The resulting spectrum after discrete Fourier transformation can be seen in Figure 5.3 b (light blue line), where the spectral leakage is removed.

Chapter 6

Dynamic anti-correlations of water hydrogen bonds

Gunkel, L.; **Ehrhard, A. A.**; Krevert, C. S.; Marekha, B. A.; Bonn, M.; Grechko, M.; Hunger, J. *Nature Communications* **2024**, *15*, 1–9.[1]
DOI: 10.1038/s41467-024-54804-y

L.G., A.A.E., and J.H. conceptualized the study. L.G., A.A.E., M.B., M.G., and J.H. developed the methodology and analysis. L.G., A.A.E., C.S.K., B.A.M., and J.H. performed the experiments and computations. J.H. supervised the project. L.G. and A.A.E. wrote the original draft and L.G., A.A.E., C.S.K., B.A.M., M.B., M.G., and J.H. revised and edited the manuscript. L.G. and A.A.E. contributed equally.

6.1 Abstract

Water is characterized by strong intermolecular hydrogen bonds (H-bonds) between molecules. The two hydrogen atoms in one water molecule can form H-bonds of dissimilar length. Although intimately connected to water's anomalous properties, the details and the origins of the asymmetry have remained elusive. We study water's H-bonds using the O-D stretching vibrations as sensitive reporters of H-bonding of D_2O and HOD in dimethylformamide. Broader inhomogeneous linewidths of the OD band of HOD compared to the symmetric and asymmetric OD stretching modes of D_2O together with density functional theory calculations provide evidence for markedly anti-correlated H-bonds: water preferentially forms one weak and one strong H-bond. Coupling peaks in the spectra for D_2O directly demonstrate anti-correlated H-bonds and these anti-correlations are modulated by thermal motions of water on a sub-picosecond timescale. Experimentally inferred H-bond distributions suggest that the anti-correlations are a direct consequence of the H-bonding potential of XH_2 groups, which we confirm for the ND_2 group of urea. These structural and dynamic insights into H-bonding are essential for understanding the relationship between the H-bonded structure and phase behavior of water.

6.2 Introduction

The peculiar properties of water have been ascribed to its intermolecular interactions: strong and directional hydrogen bonds (H-bonds), which determine its three-dimensional structure. Albeit controversially discussed[42, 148], the traditional picture of liquid water forming a symmetric coordination structure (Fig 6.1a)[149] has been challenged by X-ray spectroscopy[40, 43]. Indeed, molecular dynamics simulations have shown that symmetric/tetrahedral coordination cannot capture all structural details of liquid water[45, 46, 150, 151]. Transient deviations from on-average symmetric coordination are intimately connected to local correlations of the H-bond strengths[33, 45, 46] and asymmetric coordination geometries with, e.g., one water molecule forming two strong and two weak H-bonds result in ring- or chain-like structures of water[42, 150, 151]. Such motifs have been suggested to have profound implications for the phase behavior of water[33] and may explain some of the anomalous properties of water at reduced temperatures, such as a density maximum at 277 K or a nonlinear temperature-dependence of the heat capacity[152, 153]. Also, at ambient temperatures, where the H-bonded structure determines water's performance as solvent[154], asymmetric coordination geometries exist[31, 155], yet, thermal fluctuations seem to limit the spatial extent of such structural correlations[156]. However, experimental evidence on the exact details of the H-bond symmetry, such as the origin of the asymmetry, correlation of H-bond lengths, and their evolution, is lacking.

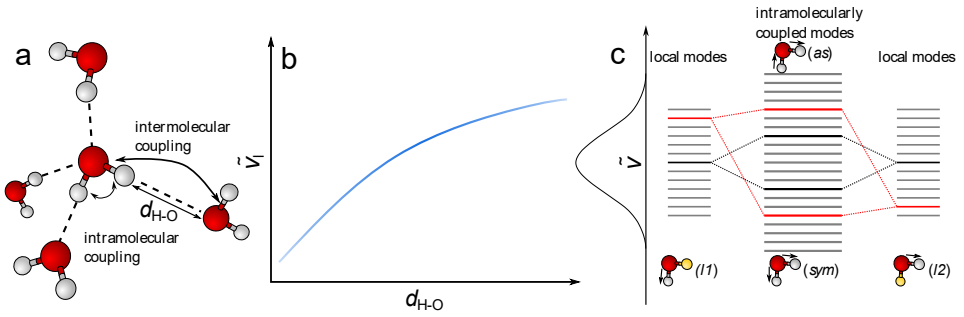

FIGURE 6.1: **a** Schematic illustration of a (distorted) tetrahedral coordination geometry of water, with arrows indicating intra- and intermolecular coupling of O-H oscillators. The H-bond distance d_{H-O} markedly affects the resonance frequency of a single O-H oscillator, as schematically depicted in (**b**), giving rise to a broad distribution of O-H stretching frequencies in water. The experimentally observed O-H stretching linewidth (depicted as vertical Gauss distribution in **c**) is further affected by vibrational coupling, as illustrated for intramolecular coupling in (**c**). Reproduced from [1].

The frequencies and linewidths of O-H stretching vibrations reflect the length and symmetry of water's H-bonds[13]. The frequency of a single (local) O-H stretching oscillator depends on H-bonding distance d_{H-O} (Fig 6.1b)[157]. A water molecule has two local O-H stretching modes (*l1*, *l2*), which interact to form symmetric (*sym*) and asymmetric (*as*) vibrations. The instantaneous frequencies of *sym* and *as* depend on the instantaneous frequencies of *l1* and *l2*, thus on the H-bond distances

of the two O-H groups, and on the coupling strength (Fig 6.1c). These different factors governing the instantaneous frequencies of *sym*, *as*, *l1* and *l2* make also the linewidths of coupled and uncoupled modes to differ. In turn, the correlation of H-bonds can be probed via the lineshapes of *sym* and *as*. However, O-H stretching frequencies in neat H_2O—and similarly O-D stretching frequencies in D_2O—are also affected by intermolecular coupling with O-H groups of surrounding molecules (Fig 6.1a)[19, 158]. This coupling gives rise to vibrational excitons—O-H stretching modes delocalized over several molecules[19, 158–160]. This delocalized character of the O-H stretching band in neat water impedes the direct correlation of spectral and structural information. To eliminate delocalization, we dilute water in dimethylformamide (DMF), isolating water molecules from each other[49, 161–164].

The broadening of the distribution of O-H stretching frequencies due to varying H-bond length is represented by inhomogeneous broadening. To reveal this broadening, we use two-dimensional infrared (2D-IR) spectroscopy[21]. In conjunction with density functional theory (DFT) calculations, we show that the linewidths of the coupled and local O-D stretching modes of isolated water in DMF indeed contain the correlation of H-bond lengths. Coupling peaks in the spectra reveal that the two H-bonds of a D_2O molecule are anti-correlated, but this anti-correlation persists for only a few hundred femtoseconds. Comparison of experimentally inferred H-bond distributions to the DFT-calculated H-bonding potential indicates that anti-correlations are intrinsic to the H-bonding potential of XD_2 groups. We verify this hypothesis with experiments on the ND_2 groups of urea. As such, our results evidence a strong, yet rapidly randomized, H-bond anti-correlation for molecular entities that can donate two H-bonds. Our observations suggest that these anti-correlations also exist in neat water, which implies a dynamic picture with short-lived asymmetric water molecules rather than persistent chain- or ring-like structures.

6.3 Results and Discussion

To elucidate the H-bonding of water, we measure the O-D stretching vibration of 5 mol% of water in DMF, where water-water H-bonds are negligible[161]. We characterize the distribution of O-D stretching frequencies of isolated O-D groups in DMF solution using isotopically diluted water containing ∼1% D_2O, ∼81% H_2O, and ∼18% HOD molecules. The corresponding local O-D stretching mode (*l*) of predominantly HOD molecules, is centered at 2580 cm^{-1} with a linewidth (full width at half maximum, FWHM) of ∼94 cm^{-1} (Fig 6.2a, see also Supplementary Note 6.5.1, Supplementary Fig. 6.6, and Supplementary Table 6.1). Conversely, for D_2O in DMF, intramolecular coupling of O-D oscillators produces the symmetric stretching band at ∼ 2540 cm^{-1} and the asymmetric stretching band at ∼ 2640 cm^{-1} (Fig 6.2a). Notably, *as* and *sym* have an appreciably narrower linewidth (FWHM of ∼78 cm^{-1}) than the local mode *l*.

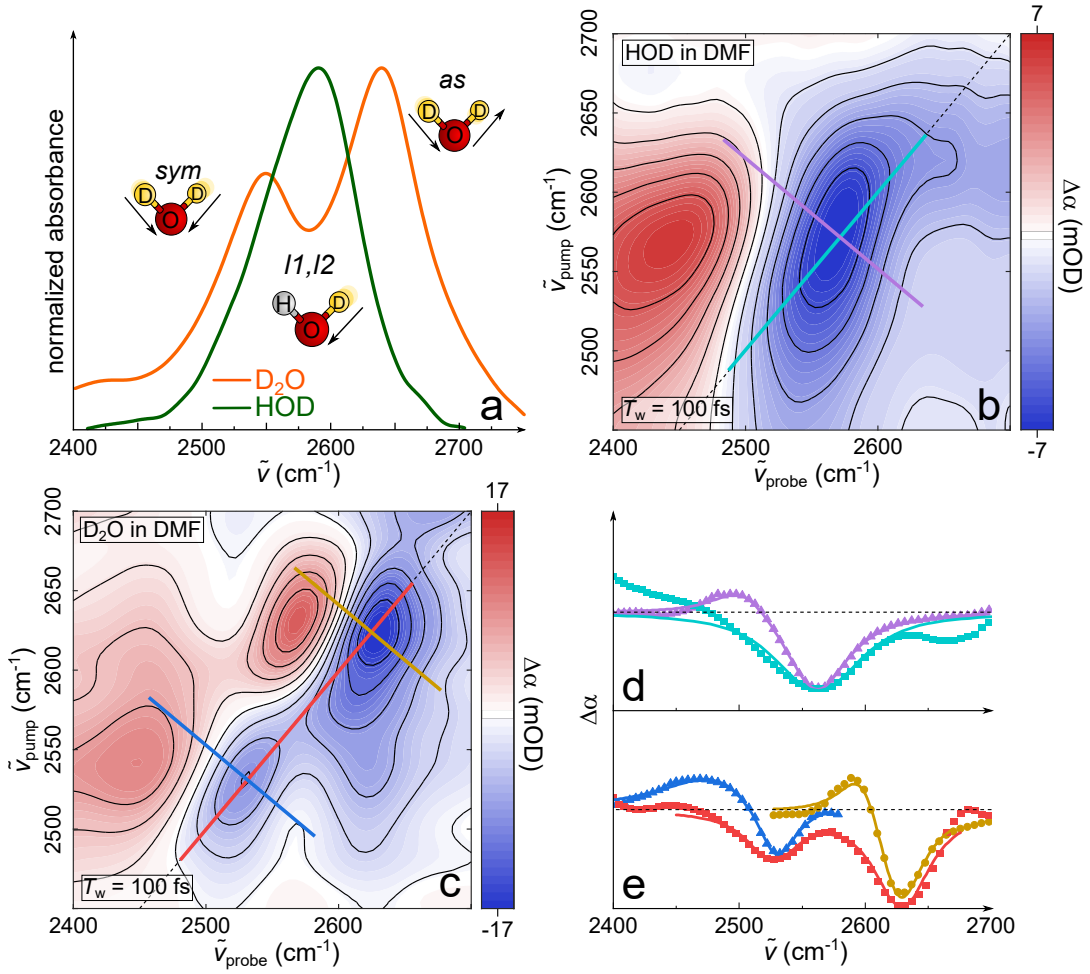

FIGURE 6.2: **a** Solvent-background subtracted, normalized IR absorption spectra of 5 mol% water in DMF: D_2O (orange) and HOD (green). Isotropic 2D-IR spectra at waiting time T = 100 fs of (**b**) HOD in DMF (10% D_2O in H_2O) and (**c**) D_2O in DMF. Note that distortions of the 2D-IR lineshape in (**b**) at $\tilde{\nu}_{\mathrm{pump}} \approx 2650\mathrm{cm}^{-1}$ presumably result from residual D_2O. Diagonal and anti-diagonal profiles along the lines indicated in the 2D spectra (**b**, **c**, colored lines) are displayed for HOD in (**d**) and for D_2O in (**e**). Symbols in (**d**, **e**) show experimental data and solid lines show fits (for details, see Supplementary Note 6.5.2). Dotted line represents $\Delta\alpha = 0$. Note that the linewidths of the diagonal signals in (**d**, **e**) differ from the widths in (**a**) due to the different experimental sensitivities to the transition dipole[21]. Reproduced from [1].

To disentangle the homogeneous and inhomogeneous broadening contributions [165] to the linear spectra (Fig 6.2a), we perform 2D-IR spectroscopy experiments. Conceptually, in a 2D-IR experiment, a subset of vibrational modes resonant with a pump frequency ($\tilde{\nu}_{\mathrm{pump}}$) is excited and the response of these oscillators is probed over a broad detection frequency range ($\tilde{\nu}_{\mathrm{probe}}$) by a probe pulse[21]. The response typically contains positive signals from induced absorption due to the excited state absorption, and negative signals due to ground state bleaching and stimulated emission at the fundamental transition. Variation of $\tilde{\nu}_{\mathrm{pump}}$ results in a two-dimensional spectrum reflecting the correlation between excited and detected vibrational frequencies. For inhomogeneously broadened bands the bleaching signal is elongated along the diagonal, with an adjacent, red-shifted induced absorption, as shown for HOD in DMF in Fig 6.2b. The widths of these signals perpendicular to the diagonal are determined solely by homogeneous broadening[21] and the diagonal width is given by homogeneous and inhomogeneous broadening. For D_2O in DMF, two pairs of bleaching/induced absorption signals are present for *sym* and *as* at the diagonal (Fig 6.2c). Additionally, we observe an off-diagonal bleaching signal at ($\tilde{\nu}_{\mathrm{pump}} \approx$ 2540 cm^{-1}/$\tilde{\nu}_{\mathrm{pump}} \approx$2640 cm^{-1}), indicating coupling between *sym* and *as*. The coupling signal above the diagonal ($\tilde{\nu}_{\mathrm{pump}} \approx$ 2640 cm^{-1}/$\tilde{\nu}_{\mathrm{pump}} \approx$ 2540 cm^{-1}) presumably overlaps with the induced absorption of *as* and, thus, is not visible in the spectrum. These off-diagonal signals will be discussed in more detail below.

For a quantitative discussion of the linewidths, we infer the homogenous linewidth by fitting a sum of two Lorentzians of opposite signs to the anti-diagonal cuts (Fig 6.2d, e), yielding homogeneous linewidths of 6 cm^{-1} (*l*), 41 cm^{-1} (*sym*), and 47 cm^{-1} (a*s*) (see Supplementary Note 6.5.2 and Supplementary Table 6.2). These homogeneous linewidths are likely overestimated due to ultrafast spectral diffusion dynamics. Nevertheless, they show that the differing line widths in Fig 6.2a stem partly from differing homogeneous broadening. With these homogeneous widths, we deconvolve the inhomogeneous and homogeneous contributions to the diagonal widths: We constrain the homogeneous width to the values from the anti-diagonals and model the diagonal cuts with a Voigt profile (a Gaussian inhomogeneous distribution convolved with the Lorentzian homogeneous band[21, 166, 167]) to derive the inhomogeneous broadening (Fig 6.2d, e, for details see Supplementary Note 6.5.2 and Supplementary Tables 6.2–6.5). The thus obtained purely inhomogeneous width of the local O-D stretching mode of HOD ($\Gamma_{\mathrm{G,l}} = 38\mathrm{cm}^{-1}$) is about twofold broader than the inhomogeneous widths of *sym* and *as* ($\Gamma_{\mathrm{G,sym}} = 20\mathrm{cm}^{-1}$,$\Gamma_{\mathrm{G,as}} = 18\mathrm{cm}^{-1}$). As such, although D_2O and HOD experience very similar H-bonding environments, coupling of the two O-D stretching modes in D_2O results in a narrower distribution of frequencies for *as* and *sym* as compared to *l*, which is the predominant cause for the differing widths in Fig 6.2a.

To understand the origin of these different inhomogeneous widths, we calculated normal mode frequencies under the harmonic approximation for different H-bond geometries using DFT. We specifically address the effect of coupling on the harmonic

normal mode frequencies by calculating the frequencies for l, sym, and as using H/D isotope exchange: We optimized the geometry of a water molecule donating two H-bonds to two DMF molecules, with the H-bond lengths ($H/D_{water} - O_{DMF}$ distance) constrained to typical H-bonding distances[161] ranging from 1.5 to 2.4 Å. The resulting frequency maps for $D^{(1)}$-O-$D^{(2)}$, $D^{(1)}$-O-$H^{(2)}$, and $H^{(1)}$-O-$D^{(2)}$ molecules as a function of $H/D_{water} - O_{DMF}$ distances d_1 and $d_2$for both H/D atoms of water, where super- and subscripts denote the two light atoms of water, are displayed in Fig 6.3a. This allows us to assess the effect of (thermal) fluctuations of H-bond lengths on the vibrational frequencies of sym, $\tilde{\nu}_{sym}$, the local modes of O-D(1)/O-D(2), $\tilde{\nu}_{l1}/\tilde{\nu}$l2, and of *as*, $\tilde{\nu}_{as}$. In particular, we consider three limiting cases of H-bond fluctuations: (i) directly correlated ($d_1 = d_2$, Fig 6.3b), (ii) anti-correlated ($d_1 + d_2 = 3.8$ Å, Fig 6.3c), and (iii) uncorrelated ($d_2 = 1.9$ Å, Fig 6.3d) H-bond distances.

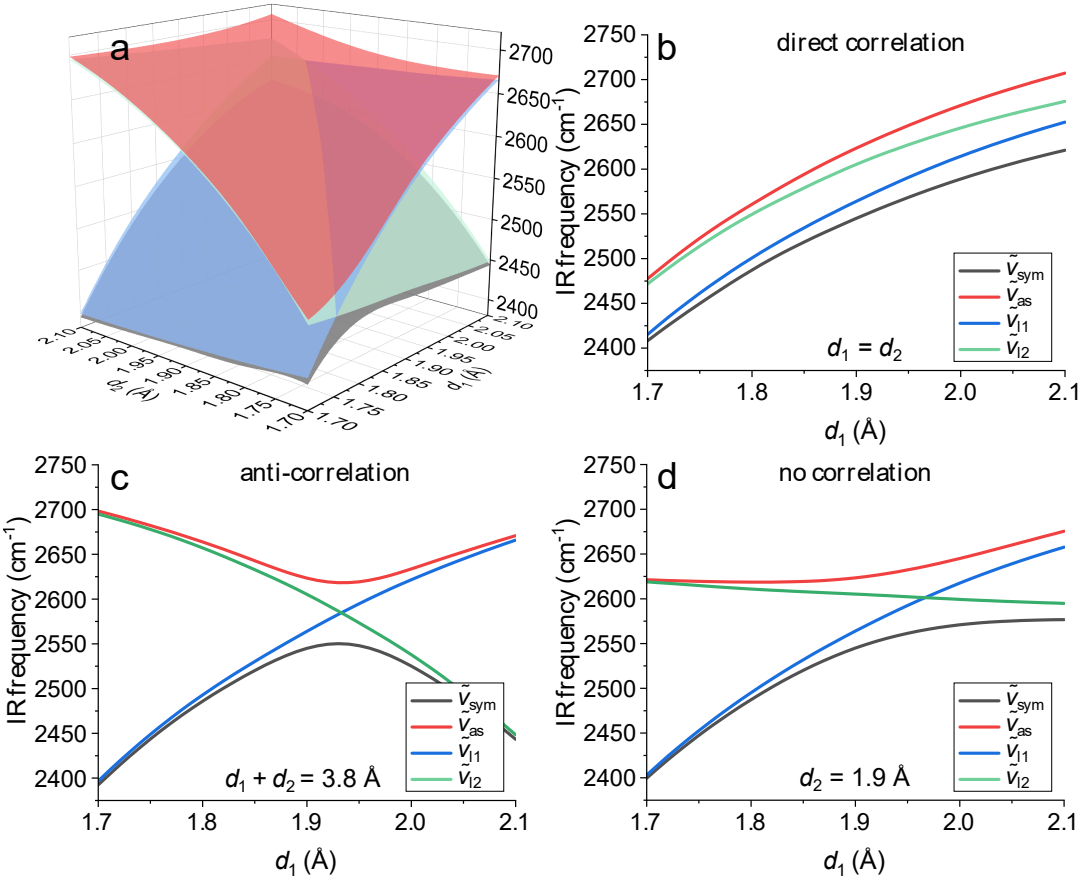

FIGURE 6.3: **a** Vibrational frequency maps for the symmetric $\tilde{\nu}_{sym}$(gray), local $\tilde{\nu}_{l1}$(blue), $\tilde{\nu}_{l2}$ (green), and asymmetric $\tilde{\nu}_{as}$(red) O-D stretching modes as a function of H-bond distances d_1 and d_2, as obtained from the harmonic frequencies of relaxed surface scans using DFT calculations. **b** Diagonal cut at $d_1 = d_2$ through the frequency maps representing directly correlated H-bonds, (**c**) anti-diagonal cut at $d_1 + d_2 = 3.8$ representing anti-correlated H-bonds, and (**d**) cut at $d_2 = 1.9$ representing uncorrelated H-bond distances. Reproduced from [1].

These limiting cases show that and simply scale with H bond distances d_1 and d_2, respectively (see also Fig 6.1b). When and are dissimilar, the frequencies of the 'coupled' modes and are close to those of the local modes or (see e.g., $d_1 < 1.8$ Å

or $d_1 > 2.0$ Å in Fig 6.3c, d). For H-bond configurations for which $d_1 \approx d_2$, coupling of the local modes and results in a separation of frequencies for the coupled modes $\tilde{\nu}_{sym}$ and $\tilde{\nu}_{as}$ (Figs. 3b and 1.8 Å $< d_1 <$ 2.0 Å in Fig 6.3c, d). Therefore, all frequencies show a similar dependence on for case (i) of directly correlated H-bonds. For cases (ii) anti-correlated and (iii) uncorrelated H-bonds, coupling gives rise to avoided crossings[168], and makes $\tilde{\nu}_{sym}$ and $\tilde{\nu}_{as}$ to not just scale with d_1. Consequently, for a given range of thermally accessible H-bond distances d_1, coupling results in a narrower distribution of $\tilde{\nu}_{sym}$ and $\tilde{\nu}_{as}$ as compared to $\tilde{\nu}_{l1}$ and $\tilde{\nu}_{l2}$ for (ii) and (iii). Conversely, for (i), the range of thermally accessible frequencies is similar for all vibrations. As the spread of H-bond geometries underlies the inhomogeneous linewidth of these modes, (ii) anti-correlated and (iii) uncorrelated H-bond geometries can qualitatively explain the experimentally observed reduced $\Gamma_{G,sym}$ and $\Gamma_{G,as}$, relative to $\Gamma_{G,l}$. For instance, assuming thermally accessible H-bond distances ranging from 1.8 Å to 2.0 Å, the data in Fig 6.3 suggest the resulting inhomogeneous linewidths of *sym* and *as* to be $\sim$2 and $\sim$4 times, respectively, narrower than that of *l* (HOD). Hence, while the comparison between calculated and experimental linewidths cannot discriminate between (ii) and (iii), we exclude directly correlated fluctuations of H-bond distances.

Although it is challenging to discriminate between (ii) and (iii) solely based on the frequencies of the three modes as a function of H-bond lengths, both limiting cases can be discerned by considering the relation between the DFT-calculated frequencies $\tilde{\nu}_{sym}$ and $\tilde{\nu}_{as}$: For (ii) the slopes of $\tilde{\nu}_{sym}(d_1)$ and $\tilde{\nu}_{as}(d_1)$ have opposite sign (Fig 6.3c): upon increasing d_1, $\tilde{\nu}_{sym}$ increases (decreases) and $\tilde{\nu}_{as}$ decreases (increases) for $d_1 \leq 1.9$ Å ($d_1 \geq 1.9$ Å). Conversely, for (iii) $\tilde{\nu}_{sym}(d_1)$ and $\tilde{\nu}_{as}(d_1)$ have positive or zero slopes throughout (Fig 6.3d).

Hence, for anti-correlated distances d_1 and d_2 (ii), the frequencies $\tilde{\nu}_{sym}$ and $\tilde{\nu}_{as}$ are anti-correlated, while for uncorrelated distances (iii) $\tilde{\nu}_{sym}$ and $\tilde{\nu}_{as}$ are correlated. The correlation between $\tilde{\nu}_{sym}$ and $\tilde{\nu}_{as}$ can be directly interrogated with 2D-IR spectroscopy as coupling between *sym* and *as* gives rise to the cross-peak ($\tilde{\nu}_{pump} \approx 2540\text{cm}^{-1}$ / $\tilde{\nu}_{pump} \approx 2620\text{cm}^{-1}$) in Fig 6.2c and the line shape of the cross-peak provides information on the correlations of H-bonding distances, analogously to earlier studies by Hochstrasser and coworkers[169–171] on different molecular systems. Due to the relative orientation of the transition dipoles of *sym* and *as* ($\sim$90–105°), such cross-peaks are more intense (relative to the diagonal signals) for perpendicular excitation and probing polarizations (Fig 6.4a, b)[21]. The presence of the cross-peak at early times (T_w, delay between pump and probe pulses) and evolution of its intensity similar to the diagonal signals evidences that the cross-peak is due to coupling (Supplementary Note 6.5.3, Supplementary Table 6.6, and Supplementary Figs. 6.7 & 6.8)[21]. To identify frequency-frequency (anti-)correlations, we calculate the signal-weighted local Pearson correlation coefficient (Supplementary Note 6.5.4). At T_w = 100 fs (for other waiting times, see Supplementary Fig. 6.9) these coefficients are positive for the diagonal signals, as expected for inhomogeneously broadened

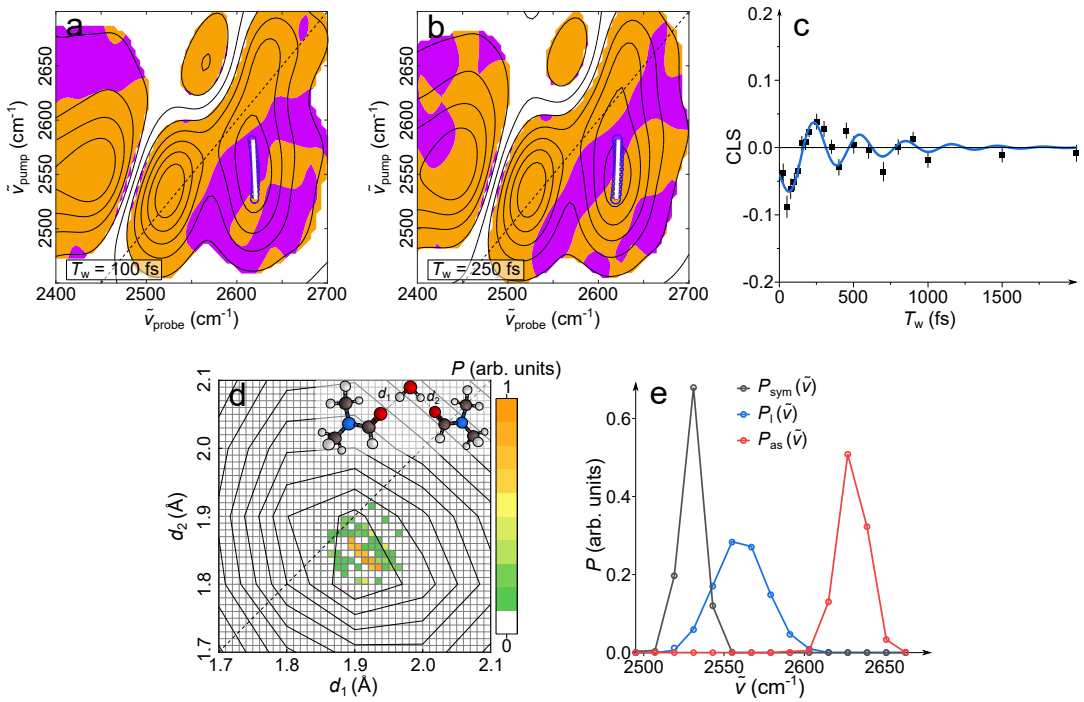

FIGURE 6.4: Perpendicular (<XXZZ>) 2D-IR spectrum of D_2O in DMF at (**a**) T_w = 100 fs and (**b**) T_w = 250 fs. Contour lines show signal intensities, orange and purple areas indicate spectral regions with positive and negative local Pearson correlation coefficients, respectively. Open blue symbols indicate the center-line position of the off-diagonal peak and the solid white line the center line. **c** Center-line slope dynamics, CLS(T_w) of the off-diagonal peak. Symbols show experimental data and error bars show the uncertainty of the slope obtained from linear regression of the center points. The solid line shows a fit using a sum of a damped oscillation (∼310 fs oscillation period, 470 fs damping time) and an exponential decay (50 fs decay time). The error bars are the standard errors of the linear regression of the center lines. **d** Fitted H-bond conformation distribution $P(d_1, d_2)$ of D_2O in DMF (pixel map) obtained from minimizing deviations between the experimental, discretized inhomogeneous distribution of frequencies $P_i(\tilde{\nu})$ (symbols in **e**) and the calculated distribution using $P(d_1, d_2)$ together with the frequency maps in Fig. 6.3a (solid lines in **e**). Contour lines in (**d**) show lines of equal population probability following the Boltzmann distribution (at 295 K) of H-bond conformations of D_2O + 2 DMF as obtained from the DFT-calculated total energy. Reproduced from [1].

bands. Conversely, the off-diagonal peak at $\tilde{\nu}_{\mathrm{pump}} \approx 2540\ \mathrm{cm}^{-1}$ / $\tilde{\nu}_{\mathrm{probe}} \approx 2620\ \mathrm{cm}^{-1}$ is dominated by negative correlation coefficients, suggesting anti-correlated $\tilde{\nu}_{\mathrm{sym}}$ and $\tilde{\nu}_{\mathrm{as}}$ (Fig 6.4a). Similarly, the center line slope (CLS) [172] of 0.05 for the cross-peak at T_{w} = 100 fs demonstrates anti-correlations between $\tilde{\nu}_{\mathrm{sym}}$and $\tilde{\nu}_{\mathrm{as}}$[172]. The data in Fig 6.3 show that this anti-correlation of $\tilde{\nu}_{\mathrm{sym}}$ and $\tilde{\nu}_{\mathrm{as}}$ signifies anti-correlated H-bond distances d_1 and d_2. Therefore, the cross-peak provides direct evidence for anti-correlated H-bond distances.

The frequency-frequency anti-correlations are however rather short-lived and are at e.g., T_{w} = 250 fs much less pronounced. The CLS at T_{w} = 250 fs is even slightly positive (Fig 6.4b, for other waiting times see Supplementary Fig. 6.9). Quantitatively, the waiting-time dependent CLS(T_{w}) of the cross-peak (Fig 6.4c) rapidly decays to ∼0, indicating that thermal fluctuations rapidly randomize the anti-correlation between and. Remarkably, CLS(T_{w}) appears to decay with marked oscillatory dynamics. It has previously been reported that such oscillatory dynamics may stem from coherence transfer within the time interval between the two excitation pulses in the time-domain 2D-IR experiment[173, 174]. This scenario is, however, rendered unlikely for the present system because (i) we find no evidence for oscillations in the 2D-IR signal intensities (Supplementary Fig. 6.8), (ii) 2D-IR spectra with suppressed coherence transfer from as to sym[175] exhibit the same oscillatory CLS dynamics (Supplementary Fig. 6.10), and (iii) also the CLS dynamics of the diagonal peak for l exhibit oscillatory dynamics with the same oscillation period (Supplementary Fig. 6.11). As such, these observations suggest that the oscillations of the frequency-frequency correlations in Fig 6.4c rather originate from a modulation of the CLS due to the inherent dynamics of water, which is also supported by molecular dynamics simulations[49]. In fact, the data in Fig 6.4c are well-described as a damped oscillation with an oscillation period of ∼310 fs and a ∼50 fs exponential decay (Fig 6.4c, Supplementary Note 6.5.5, and Supplementary Table 6.7), qualitatively similar to predictions by simulations for water in acetonitrile[49]. These timescales are close to the characteristic timescales of the H-bond stretching vibration for neat water at ∼200 cm^{-1} and water's libration band at ∼650 cm^{-1} (∼530 cm^{-1} for D_2O)[**Seki2020a**, 156, 176, 177], which are expected to be similar for D_2O in DMF (see Supplementary Note 6.6). These intrinsic dynamics of water also modulate the decay of the CLS of the diagonal peaks (see Supplementary Note 6.6.1 and Supplementary Fig. 6.11). As these lower-frequency H-bond stretching vibrations and librations are thermally excited at ambient conditions, the observed CLS dynamics show that the thermally excited low-frequency modes modulate H-bond anti-correlations.

To elucidate the origin of the H-bond anti-correlation, we estimate the distribution of H-bond conformations, $P(d_1, d_2)$, (Fig 6.4d) by simultaneously using the information from all vibrational modes *l*, *sym*, *as*. Therefore, we take the purely inhomogeneous distribution of frequencies, $P_{\mathrm{i}}(\tilde{\nu})$, using the center frequencies and the purely inhomogeneous linewidths ($\Gamma_{\mathrm{G,i}}$) obtained from analysis of the diagonal

and anti-diagonal lineshapes in Fig 6.2 (see Supplementary Note 6.5.2 and Supplementary Tables 6.2–6.3) together with the frequencies of all modes as a function of H-bond geometry (frequency maps in Fig 6.3a). For numerical treatment, we discretize at intervals of 15 cm^{-1} (Fig 6.4e, symbols) and the population of H-bond geometries at intervals of 0.01 Å (Fig 6.4d). Starting from random distributions of H-bond conformations $P(d_1, d_2)$, we optimize $P(d_1, d_2)$ such that the distributions $P_i(\tilde{\nu})$ calculated from the conformation distribution and the maps in Fig 6.3a match the discretized, purely inhomogeneous distribution of frequencies, $P_i(\tilde{\nu})$ in Fig 6.4e (details on the numerical accuracy are given in Supplementary Note 6.7 and Supplementary Fig. 6.12). The distribution of H-bond distances thus obtained are shown in Fig 6.4d. We note that the slight displacement of the maximum of the distribution in Fig 6.4d from the diagonal (symmetric H-bond distances) results from the simplified representation of water in DMF by only one water molecule and two DMF molecules in the DFT calculations used to obtain the frequency maps in Fig 6.3a (dispersive interactions between two DMF molecules lead to symmetry breaking, see Supplementary Fig. 6.13). Nevertheless, the distribution of H-bond conformations in Fig 6.4d confirms anti-correlated H-bond distances d_1 and d_2: $P(d_1, d_2)$ is elongated along the anti-diagonal, similar to results from molecular dynamics simulations of water[14].

To pinpoint the origin of the anti-correlated H-bond distances, we compare $P(d_1, d_2)$ (pixel plot, Fig 6.4d) to the distribution expected from the total energy of the DFT calculations (contour plot, Fig 6.4d). Assuming a Boltzmann distribution, anti-correlated H-bonds are also predicted solely based on the DFT-calculated energy of D_2O + 2 DMF: the shape of the Boltzmann distribution obtained from DFT (contour lines in Fig 6.4d) and the estimated distribution $P(d_1, d_2)$ (pixel plot in Fig 6.4d) agree well. The differing widths of both distributions are likely due to neglecting repulsive interactions with other molecules and overestimation of the homogeneous linewidth. Irrespective of these different widths, both distributions show that the energetically most favorable H-bond distance for one H-bond markedly depends on the H-bond distance of the other H-bond—the H-bonds are anti-correlated.

In fact, one might expect such distributions for any molecular group that can donate two H-bonds (XH_2): the H-bonding potential for such XH_2 fragments typically exhibits a global minimum at both H-bond equilibrium distances, with adjacent minimum energy paths for dissociation of one H-bond (see Supplementary Fig. 6.13). The resulting Boltzmann distributions of such potentials result in an anti-correlated distribution of H-bond distances d_1 and d_2. Thus, we hypothesize that the anti-correlated H-bond distances for D_2O in DMF are intrinsic to the H-bonding potential of XH_2 groups. Conversely, anti-correlated H-bonds are not unique to D_2O (+2 DMF) but common to XH_2 groups.

To test this hypothesis, we performed analogous experiments for the $N(H/D)_2$ groups of urea in dimethylsulfoxide (DMSO), for which the differences in linewidths of *l* and *as*, *sym* in the absorption spectra are even more pronounced (see Supplementary Fig. 6.14) as compared to D_2O in DMF. 2D-IR spectra demonstrate that

the symmetric (2420 cm^{-1}) and asymmetric (2560 cm^{-1}) N-D stretching modes (Fig 6.5a) are weakly inhomogeneously broadened. Conversely, for a 30% (D) 70% (H) isotopic mixture *l* at 2480 cm^{-1} is clearly inhomogeneously broadened (Fig 6.5b). Analysis of the 2D-IR lineshapes suggests the inhomogeneous linewidth of *l* with $\Gamma_{G,l} = 44$ cm^{-1} is ∼50% broader than of *as* with $\Gamma_{G,as} = 31$ cm^{-1} (Supplementary Tables 6.4, 6.5). The extremely narrow linewidth of *sym* ($\Gamma_{G,sym} = 14 cm^{-1}$) is presumably due to spectral distortion by a Fermi-resonance (see also Supplementary Note 6.7.1 and Supplementary Figs. 6.14, 6.15). Nevertheless, the H-bond distributions, fitted analogously to D_2O from solely $\Gamma_{G,l}$ and $\Gamma_{G,as}$ (i.e., omitting $\Gamma_{G,sym}$) and the corresponding frequency maps for urea + 4 DMSO (Supplementary Fig. 6.16), also exhibit anti-correlated H-bond distances (Fig 6.5c). The center of this distribution is displaced from a symmetric H-bond geometry ($d_1 = d_2$), likely due to the inequivalence of the two deuterium atoms of the ND_2 group. Similar to our findings for D_2O, the elliptical distribution of H-bond geometries can again be traced to the H-bonding potential of the ND_2 group (Fig 6.5c). Further, local correlation maps of the cross-peak at $\tilde{\nu}_{pump} \approx 2420$ cm^{-1}/ $\tilde{\nu}_{probe} \approx 2580$ cm^{-1} in Fig 6.5d evidence anti-correlated $\tilde{\nu}_{sym}$ and $\tilde{\nu}_{as}$. For urea-d4 also the cross-peak at $\tilde{\nu}_{pump} \approx 2580$ cm^{-1}/ $\tilde{\nu}_{probe} \approx 2430$ cm^{-1} can be isolated. Yet, overlap with the induced absorption of as distorts its lineshape and negative frequency-frequency correlations are not present for the entire signal. Overall, our key observations evidencing anti-correlated H-bonds are present for D_2O in DMF and urea in DMSO. As such, the data in Fig 6.5 support the notion that anti-correlated H-bonds are generic to H-bonding XD_2/XH_2 moieties.

6.4 Conclusions

We find the H-bond distances of the two H-bond donating deuterium atoms of D_2O and urea's ND_2 groups are anti-correlated: D_2O and urea's ND_2 group preferentially donate one strong and one weak H-bond. This anti-correlation is encoded in the inhomogeneous linewidths of the decoupled and coupled O/N-D stretching modes and in frequency-frequency correlations between the asymmetric and symmetric modes. Comparison to DFT calculations suggests that these anti-correlations stem from the H-bonding potential. Opposed to water in DMF, intermolecular coupling impedes spectroscopic detection of such anti-correlation in neat water[158], yet the H-bonding potentials for isolated water in DMF closely resemble the potential in neat water[178, 179]. As such, similar H-bond conformations are likely present in liquid water. In fact, similar information on the H-bond correlations, herein obtained from the O-D cross-peaks, is in principle also contained in the O-D—O-H frequency correlations of a water molecule. Thus, using two different isotopic labels may make this methodology also applicable to pure water.

The anti-correlations are short-lived at ambient conditions and randomize in <500 fs—in line with predictions for water[156]. Our results highlight that H-bond

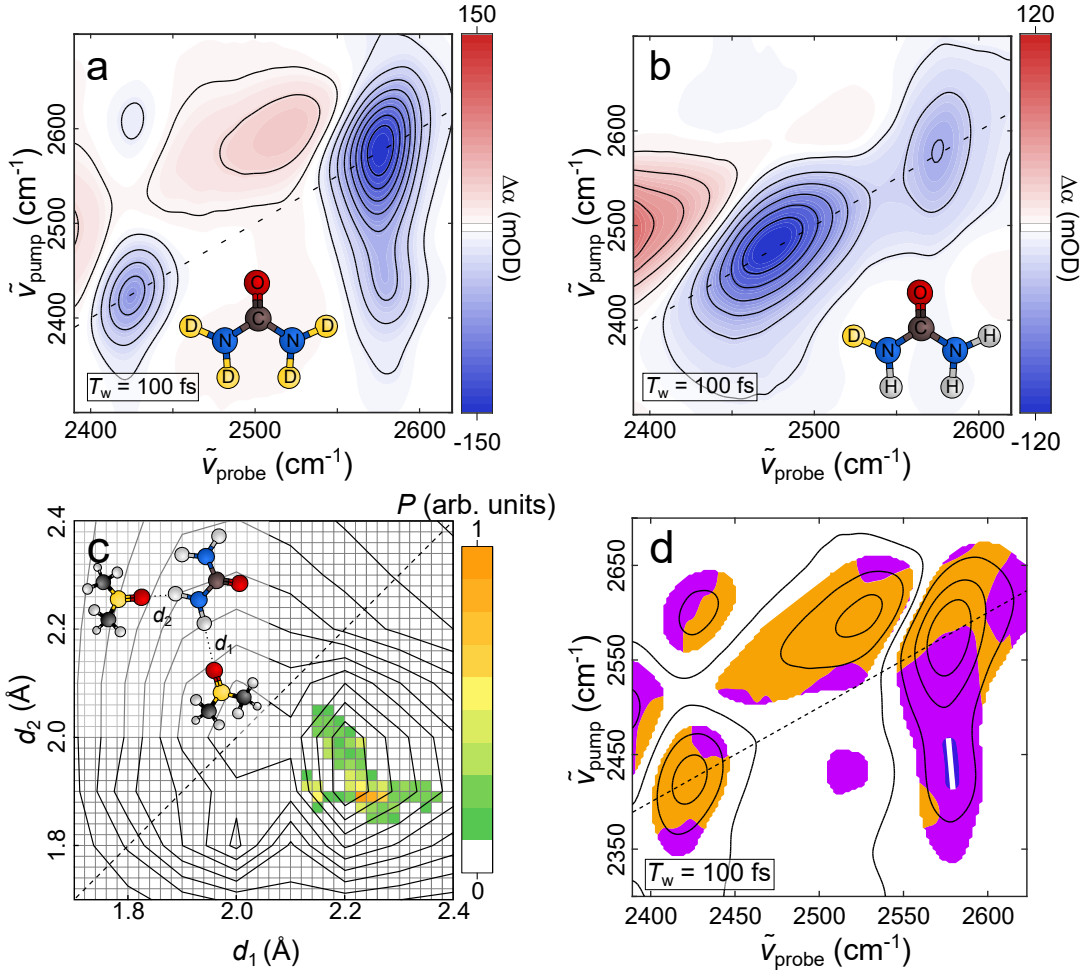

FIGURE 6.5: **a** Isotropic 2D-IR spectrum of urea-d4 in DMSO at T_w = 100 fs. **b** Isotropic 2D-IR spectrum of a 30%D/70%H isotopic mixture of urea, corresponding to ∼1% urea-d4, ∼8% urea-d3, ∼26% urea-d2, ∼41% urea-d1, and ∼24% urea, in DMSO at T_w = 100 fs. **c** H-bond conformation distribution $P(d_1, d_2)$ of urea in DMSO (pixel map) obtained analogously to Fig 6.4d together with contours representing equal probability of the DFT energy-based Boltzmann distribution. **d** Perpendicular (<XXZZ>) 2D-IR spectrum of urea-d4 in DMSO. Contour lines show signal intensities, orange and purple areas indicate spectral regions with positive and negative local Pearson correlation coefficients, respectively. Open blue symbols indicate the center-line position of the off-diagonal peak and the solid white line shows the center line. Reproduced from [1].

asymmetry in water is not simply a statistical process. The static distribution of H-bonds and its dynamics are key to understanding the relation between H-bonded structure and the phase behavior of water. The dynamics are governed by low-frequency motions (H-bond stretching vibration and libration), and the formation of structurally different subphases of water must therefore be encoded in these low-frequency signatures. Our findings also have implications for understanding water as solvent, as the H-bonded structure and the spatial distribution of H-bonds around solutes and their lifetime may help understand water's ability to efficiently hydrate solutes.

6.5 Supplementary Notes

6.5.1 Modelling of the linear IR absorption spectra of D_2O in DMF

To estimate the linewidths of the vibrational bands in the IR absorption spectra, we modelled the spectra of D_2O in DMF by a sum of three Gaussian bands to account for the overtone of the D_2O bending vibration, the symmetric O-D stretching band, and the asymmetric O-D stretching mode. The spectra of HOD in DMF were modelled with a single Gaussian band. The experimental spectra and the fits are displayed in Supplementary Figure 6.6 and the fit parameters are listed in Supplementary Table 6.1.

6.5.2 Lorentz and Voigt modelling of the 2D-IR slices

To model the antidiagonal cuts (Figure 6.2d and 6.2e in the main manuscript) and determine the homogeneous linewidths, we use a combination of two Lorentzian bands, $l(\tilde{\nu})$:

$$l(\tilde{\nu}) = A_{\mathrm{ESA,i}} \cdot \frac{1}{(\tilde{\nu} - \tilde{\nu}_{\mathrm{c,ESA,i}})^2 + \left(\frac{\Gamma_{\mathrm{L,ESA,i}}}{2}\right)^2} + A_{\mathrm{GSB,i}} \cdot \frac{1}{(\tilde{\nu} - \tilde{\nu}_{\mathrm{c,GSB,i}})^2 + \left(\frac{\Gamma_{\mathrm{L,GSB,i}}}{2}\right)^2} \quad (6.1)$$

with $A_{\mathrm{ESA,i}}$ and $A_{\mathrm{GSB,i}}$ (with i = *l*, *sym*, *as* for local, symmetric, and asymmetric stretching mode) the amplitudes of the bleaching signal and the excited state absorption, respectively. $\tilde{\nu}_{\mathrm{c,ESA,i}}$ and $\tilde{\nu}_{\mathrm{c,GSB,i}}$ are the resonance frequencies of the ground state bleaching signal and of the excited state absorption, respectively. To reduce the parameter space, we assume the full widths at half maximum $\Gamma_{\mathrm{L,ESA,i}}$ and $\Gamma_{\mathrm{L,GSB,i}}$, of both signals to be the same. This assumption cannot be made for the symmetric stretching mode of D_2O since the ESA peak here contains contributions of the symmetric stretching mode and the cross-peak. Therefore, in this case $\Gamma_{\mathrm{L,ESA,s}}$ and $\Gamma_{\mathrm{L,GSB,s}}$ are both adjustable parameters. To model the diagonal cuts, we fit a Voigt profile, $v(\tilde{\nu})$ – a convolution of a Gaussian profile f_2 representing the purely inhomogeneous distribution with a Lorentz band f_1 – to the data with $\Gamma_{\mathrm{L,GSB,i}}$ constrained to the value obtained from fitting Supplementary Eq. 6.1 to the antidiagonal cuts.

$$v(\tilde{\nu}) = (f_1 * f_2)(\tilde{\nu}) \tag{6.2}$$

where:

$$f_1(\tilde{\nu}) = \frac{A_\mathrm{i}}{2\pi} \frac{\Gamma_\mathrm{L,GSB,i}}{(\tilde{\nu} - \tilde{\nu}_\mathrm{c})^2 + (\frac{\Gamma_\mathrm{L,GSB,i}}{2})^2}, \quad f_2(\tilde{\nu}) = \sqrt{\frac{4\ln 2}{\pi}} \frac{\frac{4\ln 2}{\Gamma_\mathrm{G,i}^2}\tilde{\nu}^2}{\Gamma_\mathrm{G,i}} \tag{6.3}$$

with the amplitude of the Lorentz component A_i and $\Gamma_\mathrm{G,i}$ the purely inhomogeneous width of the Gaussian distribution. These fits are shown in Figure 6.2 of the main manuscript and the obtained parameters are listed in Supplementary Tables 6.2-6.5.

6.5.3 Population dynamics

The homogeneous broadening discussed above and in the main manuscript has contributions from population lifetime:[165] longer-lived vibrations give rise to narrower bands. Additionally, accelerated population relaxations for certain modes may indicate different relaxation pathways, such as Fermi resonances.[180, 181] Thus, we quantify the population relaxation via the temporal evolution of the on-diagonal bleaching signals of the different vibrational modes as function of waiting time T_w. We model the integrated 2D-IR signals assuming that the contribution of the excited state decays with a relaxation time $\tau_\mathrm{i}1$ and that the dissipation of the vibrational energy in the course of the relaxation leads to a small and persistent modulation of the oscillator (transient signal due to heat):[6]

$$V(T_\mathrm{w}) = V_\mathrm{exc} \cdot e^{\frac{-T_\mathrm{w}}{\tau_i}} + V_\mathrm{heat} \cdot (1 - e^{\frac{-T_\mathrm{w}}{\tau_i}}) \tag{6.4}$$

with V_exc and V_heat the magnitude of the contributions of the excitation and the heat, respectively. We integrate the peaks in the shaded areas shown in Supplementary Figure 6.7. We use elliptical integration areas and the tilt of the ellipse is taken from the tilt of the CLS at T_w = 100 fs. Supplementary Figure 6.8 shows the resulting fits and the thus obtained lifetimes are listed in Supplementary Table 6.6. For water we find similar lifetimes for the symmetric and the asymmetric stretching mode. The local mode of HOD molecules shows an increased lifetime compared to the coupled modes. Together with the homogeneous linewidth of the local mode being broader than the linewidths of the coupled mode, these data suggest that population relaxation is not the predominant broadening mechanism.[165, 182] For urea we find similar lifetimes for symmetric stretch and asymmetric stretch and the local mode has almost half the lifetime compared to the coupled modes, consistent with the broader homogeneous linewidth of the local mode compared to the coupled stretching modes. The peak volumes of the cross-peaks relax with timescales (see Supplementary Figure 6.8) similar to the diagonal signals suggesting that the

cross-peaks are due to coupling, rather than due to energy transfer or chemical exchange for both D_2O and urea-d4.

6.5.4 Local Correlation Maps

For visualization of frequency-frequency correlations in the 2D-IR spectra, we calculate the local, signal-weighted Pearson correlation coefficient r. Therefore, we take an array of 5x5 pixels of the 2D-IR spectra, resulting in 25 data triples ($\tilde{\nu}_{\mathrm{probe}}$; $\tilde{\nu}_{\mathrm{pump}}$; $|S_{\perp}(\tilde{\nu}_{\mathrm{probe}}, \tilde{\nu}_{\mathrm{pump}}|)$. The correlation coefficient, r, for the center pixel of the 5x5 array is then determined as:

$$r = \frac{\mathrm{cov}(\tilde{\nu}_{\mathrm{probe}}, \tilde{\nu}_{\mathrm{pump}}, |S_{\perp}(\tilde{\nu}_{\mathrm{probe}}, \tilde{\nu}_{\mathrm{pump}})|)}{\sqrt{\mathrm{cov}(\tilde{\nu}_{\mathrm{probe}}, \tilde{\nu}_{\mathrm{probe}}, |S_{\perp}(\tilde{\nu}_{\mathrm{probe}}, \tilde{\nu}_{\mathrm{pump}})|) \cdot \mathrm{cov}(\tilde{\nu}_{\mathrm{probe}}, \tilde{\nu}_{\mathrm{pump}}, |S_{\perp}(\tilde{\nu}_{\mathrm{pump}}, \tilde{\nu}_{\mathrm{pump}})|)}} \tag{6.5}$$

with $\mathrm{cov}(x, y, w) = \frac{\sum_{i=1\ldots25}(x_{\mathrm{i}} - \overline{x}) \cdot (y_{\mathrm{i}} - \mathrm{y}) w_{\mathrm{i}}}{\sum_{i=1\ldots25} w_{\mathrm{i}}}$, $\overline{x} = \frac{\sum_{i=1\ldots25} x_{\mathrm{i}} w_{\mathrm{i}}}{\sum_{i=1\ldots25} w_{\mathrm{i}}}$, and $\overline{y} = \frac{\sum_{i=1\ldots25} y_{\mathrm{i}} w_{\mathrm{i}}}{\sum_{i=1\ldots25} w_{\mathrm{i}}}$. To visualize correlated ($r > 0$), anti-correlated ($r < 0$), or uncorrelated ($r = 0$) spectral regions, we display these coefficients in Figures 4a,b & 5d of the main manuscript and in Supplementary Figure 6.9, where the signals are smaller than 25% of the minimum signal or greater than 15% of the maximum signal.

6.5.5 CLS Fitting of Cross-Peaks

To determine the centerline position we fitted a Gauss profile to the bleaching or cross peak signal to slices parallel to the probe axis and the center of the Gaussian is taken as the center position. The CLS value is determined from a linear fit of these center points. We model the CLS dynamics of the cross-peak with a combination of a dampened oscillation and an exponential decay:

$$\begin{aligned} CLS(T_{\mathrm{w}}) = & A_{\mathrm{osc}} \cdot \sin\left(\left(\frac{T_{\mathrm{w}}}{\tau_{\mathrm{osc}}} + \phi\right) \cdot 2\pi\right) \cdot \exp(-\frac{T_{\mathrm{w}}}{\tau_{\mathrm{damp}}}) + \\ & A_{\mathrm{ex}} \cdot exp(-\frac{T_{\mathrm{w}}}{\tau_{\mathrm{ex}}}) + CLS_{\mathrm{offset}} \end{aligned} \tag{6.6}$$

with the amplitude of the oscillation A_{osc}, the oscillation period τ_{osc}, a phase shift ϕ, the damping constant τ_{damp}, the amplitude of the exponential decay A_{ex}, the lifetime of the exponential decay τ_{ex}, and the CLS offset CLS_{offset}. This fit is shown in Figure 6.4c of the main manuscript and the parameters are listed in Supplementary Table 6.7.

6.6 Estimation of Hydrogen Bond Stretching Mode

Liquid water shows broad absorption bands in the THz region at 50 cm^{-1} (hydrogen-bond bend), 200 cm^{-1} (hydrogen-bond stretch), and 650 cm^{-1} (librations).[176] For D_2O the libration band is red-shifted to 530 cm^{-1}.[177] Assuming the potential for

the DMF-D_2O hydrogen-bond is the same as for the H_2O-H_2O hydrogen-bonds in neat water, the frequency of the DMF-D_2O hydrogen bond stretch can be estimated from the reduced mass ratio to:

$$200\text{cm}^{-1} \cdot \frac{\sqrt{\frac{m_{H_2O} \cdot m_{H_2O}}{m_{H_2O}+m_{H_2O}}}}{\sqrt{\frac{m_{D_2O} \cdot m_{DMF}}{m_{D_2O}+m_{DMF}}}} \approx 151\text{cm}^{-1} \tag{6.7}$$

which corresponds to an oscillation period of ~ 220 fs.

6.6.1 CLS analysis of the diagonal peaks

The CLS of the diagonal peaks show a similar oscillatory pattern as the cross-peak. Moreover, the CLS of the diagonal peaks are reminiscent of what has been reported for H_2O in acetonitrile,[49] for which the CLS decayed on the 50 fs timescale as well as a recurrence at ~ 200 fs, attributed to underdamped low frequency intermolecular H-bond stretching.[49] The CLS dynamics of the diagonal peaks of the present study can be described with the same oscillatory and fast decay dynamics as the cross-peak, with and additional exponential decay (solid lines in Supplementary Figure 6.10), with the parameters τ_{osc}, τ_{damp}, and τ_{ex} constrained to the values obtained from the cross-peak dynamics (Supplementary Table 6.7). As such, also frequency-frequency correlations for the individual vibrational modes are modulated by the characteristic timescales of water libration and hydrogen bond stretching.

6.7 Fit stability of population fits

In Supplementary Figure 6.12 we show the numerical fit stability of the fits described in the main manuscript to obtain the H-bond conformation distributions in Figure 6.4d & 6.5c. Using a discretized 15x15 (D_2O) and 12x12 (urea) distribution of H-bond configurations $P(d_1, d_2)$, we calculate from these distributions the inhomogeneous distribution of frequencies (Figure 6.4e & Supplementary Figure 6.12c) using the frequency maps shown in Figure 6.3a and Supplementary Figure 6.16a. We optimize the $P(d_1, d_2)$ distributions by minimizing the deviations of the calculated inhomogeneous distributions from the experimentally determined inhomogeneous distributions (Supplementary Tables 6.3 & 6.3). We note that we thereby assume transition dipoles to be independent of frequency. Due to the large parameter space (225 parameters for D_2O and 144 parameters for urea) and due to numerical discretization errors of the frequency maps, the resulting $P(d_1, d_2)$ distributions are not uniquely determined. To estimate the numerical accuracy, we perform these fits ten times, seeded with random $P(d_1, d_2)$ values. In the main manuscript we show the average distributions obtained from these 10 fits (Figure 6.4d & 6.5c). The standard deviations within these 10 fits are displayed in Supplementary Figures 6.12a&b. Comparison of the data in Supplementary Figures 6.12a&b to the distributions in Figure 6.4d

& 6.5c shows that the obtained distributions can be determined sufficiently well to confirm the anticorrelated distributions.

6.7.1 Linear absorption spectra of urea

Supplementary Figure 6.14 shows solvent subtracted linear absorption spectra of urea in DMSO with varying isotopic composition at ND stretching frequencies. In the linear absorption spectrum for urea-d4 three peaks are present, the symmetric stretching vibration (*sym*) at 2420 cm^{-1}, the asymmetric stretching vibration (*as*) at 2560 cm^{-1}, and an additional mode at 2360 cm^{-1}. The 2360 cm^{-1} band has also been shown to be present in the solid state.[183] For urea-h4 in the solid state a band adjacent to the N-H stretching band at 3264 cm^{-1} has been ascribed to a combination band of the symmetrical NH_2 deformation and the CO stretching vibration.[184] However, at N-D stretching frequencies a hypothetical combination band of the ND_2 deformation and CO stretching band would be expected at >2600 cm^{-1} and can therefore not explain the 2360 cm^{-1} peak.[183] A contribution of ND_2 deformation modes is even less likely since there seems to be an approximate linear dependence of the peak intensity on the urea-d4 concentration, which is expected for ND stretching but not for ND_2 deformation modes. The linear dependence of the amplitude of this mode on the N-D concentration (Supplementary Figure 6.14) points to a Fermi resonance including a ND stretching vibration, which in turn leads to a distortion of the line shape of the symmetric stretching mode at 2420 cm^{-1}. Due to this distortion we do not consider the *sym* mode in the analysis in the main manuscript. In Supplementary Figure 6.15 we show the IR spectrum of urea-d4/urea (50% / 50%) in DMSO measured over a time period of 2 weeks after preparation. The solution was stored in a glovebox over this time period to avoid uptake of moisture during NH/ND exchange. We find a marked change of the IR spectrum during the first day (different shades of grey). The measured spectrum after two weeks (blue dashed line) is nearly identical to the spectrum after 1 day (red line). We conclude that the NH/ND exchange has reached equilibrium after 1 day. Therefore, all samples measured in this study were prepared at least one day prior to the experiment. The peak at $\sim$2360 cm^{-1} decreases with isotope exchange. As during exchange the amount of fully deuterated urea decreases, this observation supports the assignment of the 2360 cm^{-1} peak to a Fermi resonance.

6.8 Supplementary Figures

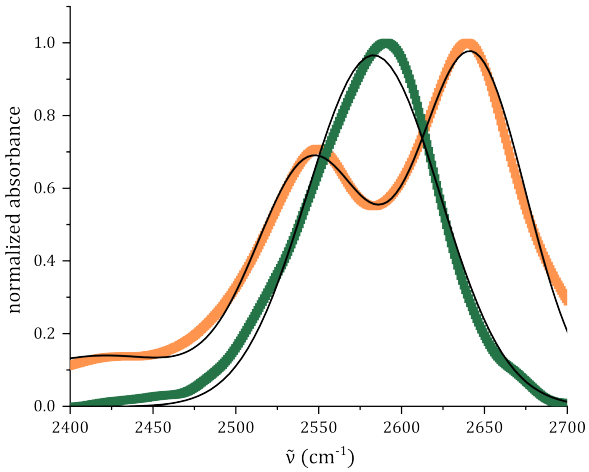

FIGURE 6.6: Normalized IR spectra of D_2O (orange symbols) and HOD (green symbols) in DMF with Gaussian fits (solid black lines). Reproduced from [1].

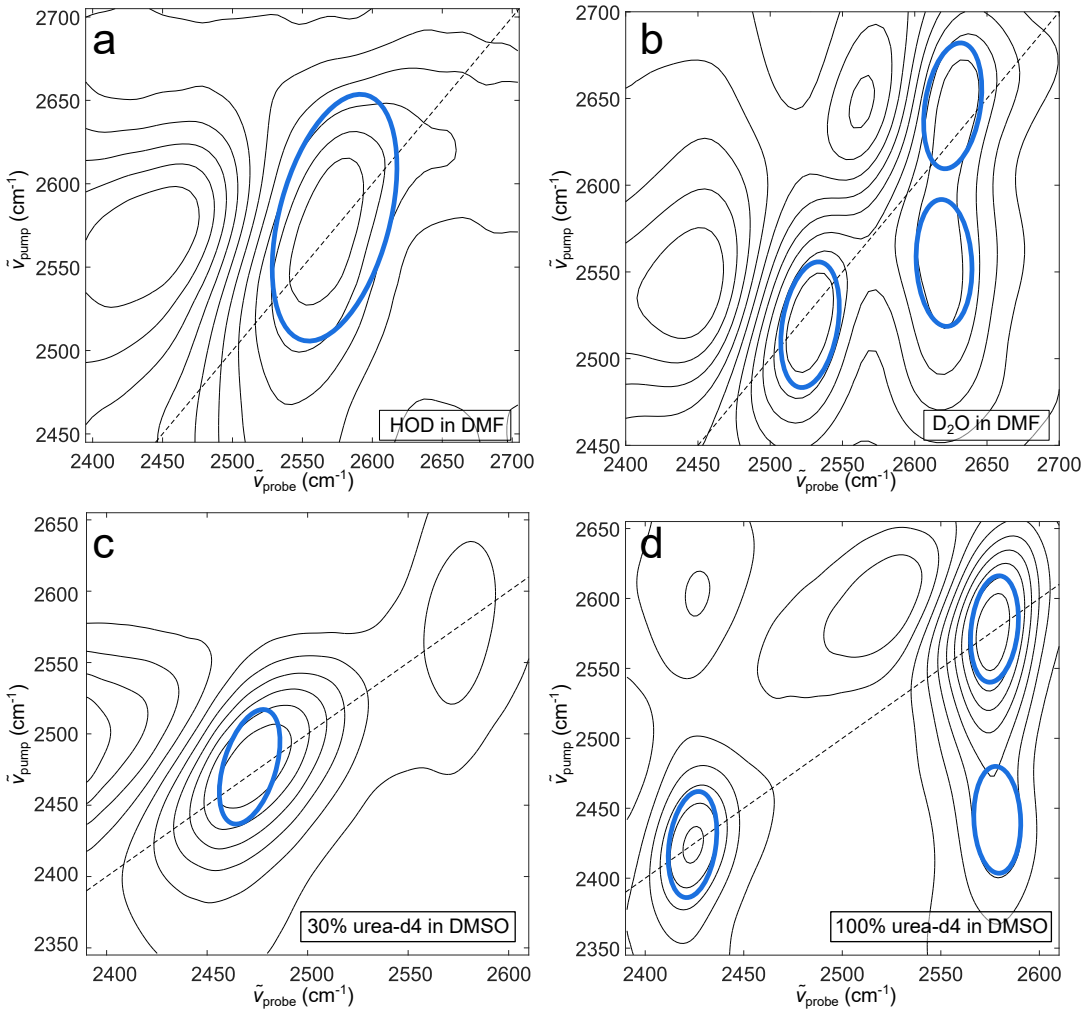

FIGURE 6.7: Isotropic 2D IR spectra at 100 fs of **a**) HOD in DMF, **b**) D_2O in DMF, **c**) 30% urea-d4 in DMSO and **d**) 100 % urea-d4 in DMSO with blue ellipses indicating the integration area for peak volume fitting in Supplementary Figure 6.8. Integration ellipses are rotated according to the tilt of the CLS at T_w = 100 fs. Reproduced from [1].

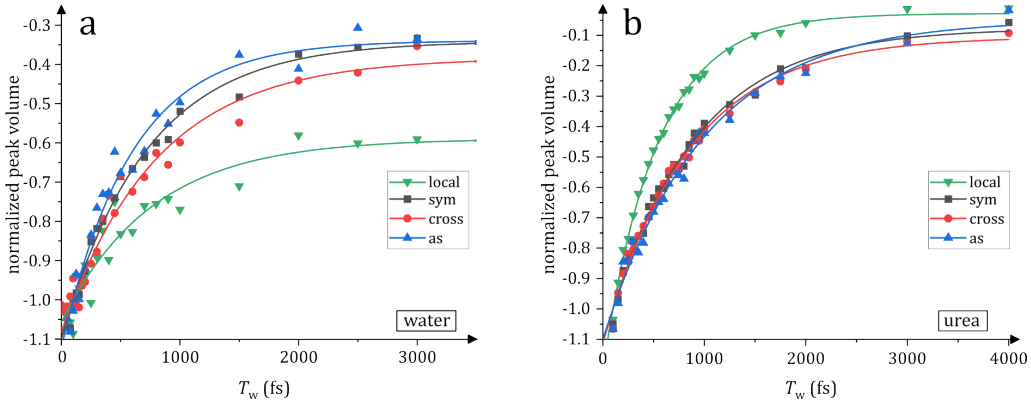

FIGURE 6.8: Normalized peak volumes of **a**) water and **b**) urea with the local mode (green), symmetric stretching (black), cross-peak (red), and asymmetric stretching (blue). Symbols show experimental data and solid lines show fits of Supplementary Eq. 6.4 to the data. Reproduced from [1].

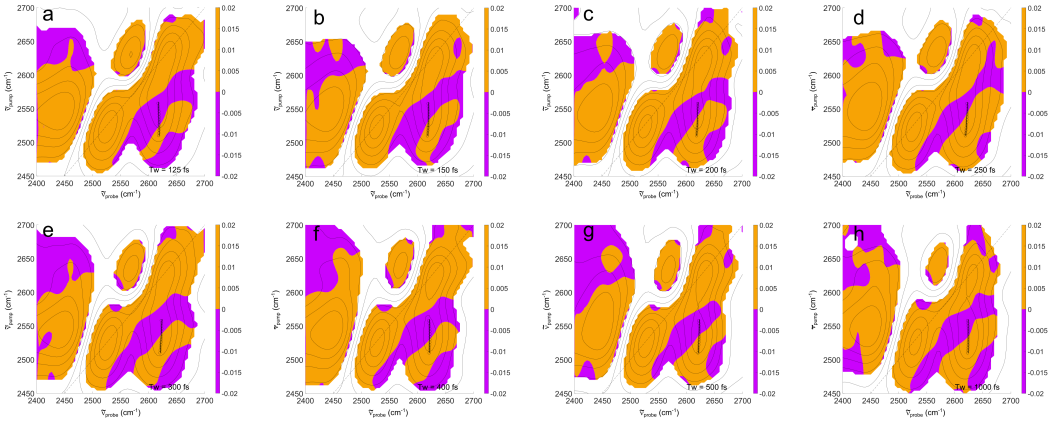

FIGURE 6.9: Waiting time dependent local correlation maps for D_2O for the perpendicular (<XXZZ>) 2D-IR spectra. **a**) 125 fs, **b**) 150 fs, **c**) 200 fs **d**) 250 fs, **e**) 300 fs, **f**) 400 fs, **g**) 500 fs and **h**) 1000 fs. Contour lines show signal intensities, orange and purple areas indicate spectral regions with positive and negative local Pearson correlation coefficients, respectively. Correlation coefficients are only shown where the signals are smaller than 25% of the minimum signal or greater than 15% of the maximum signal. Open blue symbols indicate the center position of the off-diagonal peak and the solid black line the center line. Reproduced from [1].

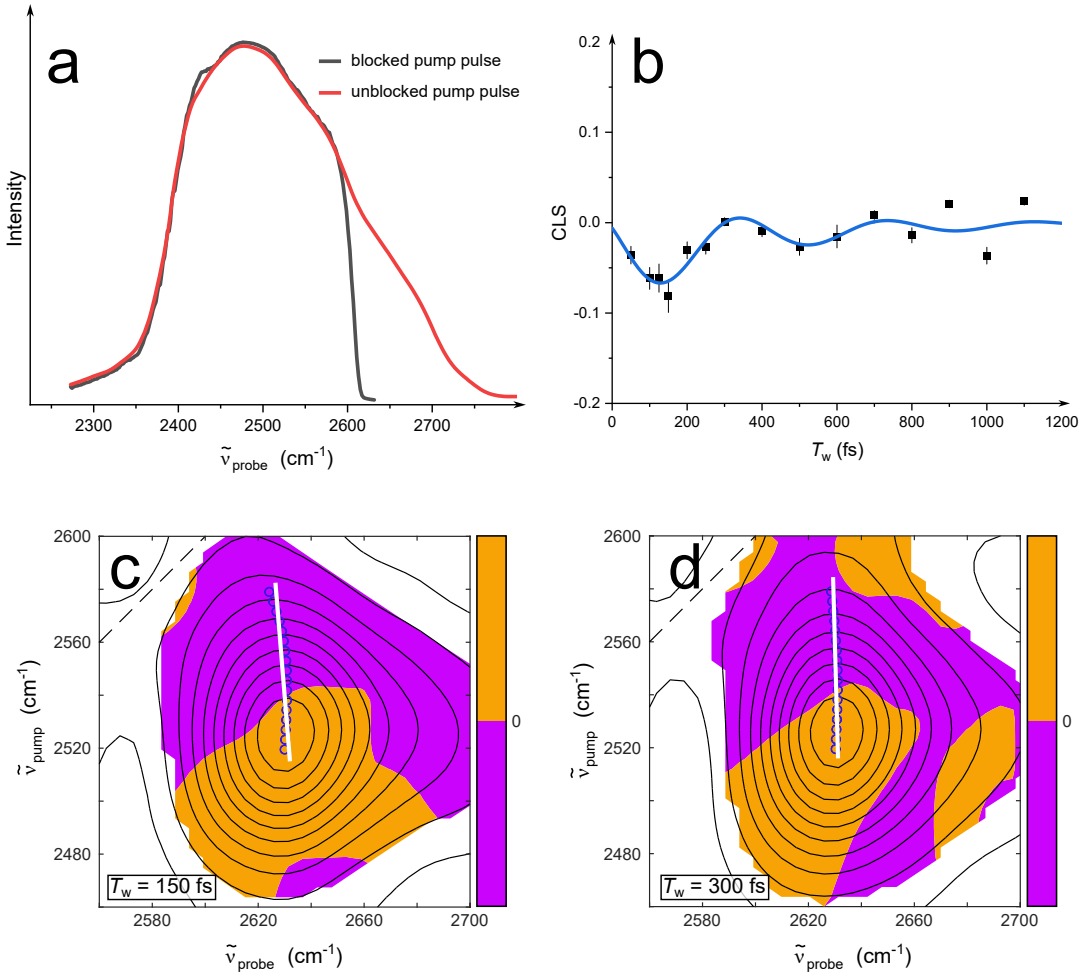

FIGURE 6.10: **a**) Pump pulse with high frequencies (> 2625 cm^{-1}) blocked. **b**) CLS of the crosspeak for D_2O in DMF using the high frequency blocked pump pulse in **a**). The error bars are the standard error of the linear regression of the center line. The CLS show the same oscillatory pattern as in the main text Figure 6.4c. This supports the notion that the oscillatory pattern in fact does not stem from coherence transfer between symmetric and asymmetric stretching modes. Perpendicular (<XXZZ>) 2D-IR spectrum of D_2O in DMF at **c**) T_w = 150 fs and **d**) T_w = 300 fs. Contour lines show signal intensities, orange and purple areas indicate spectral regions with positive and negative local Pearson correlation coefficients, respectively. Open blue symbols indicate the center-line position of the off-diagonal peak and the solid white line the center line. Reproduced from [1].

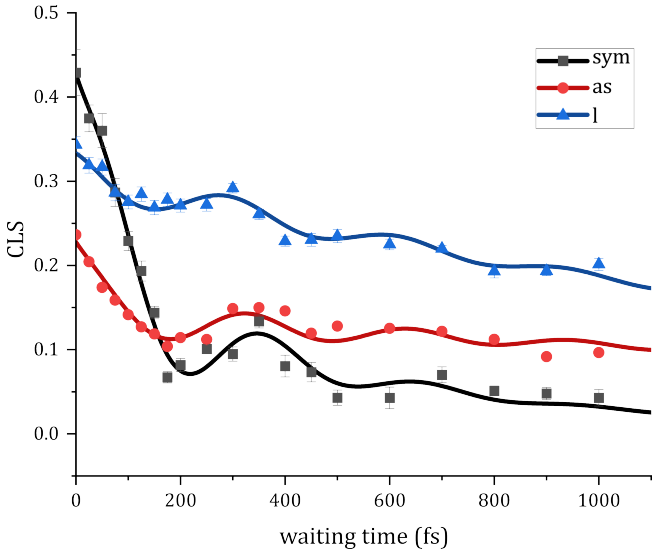

FIGURE 6.11: CLS of the diagonal peaks of the symmetric (black), asymmetric (red), and local mode (blue). The solid lines are fits using Supplementary Eq. 6.6 with an additional exponential decay. For these fits the characteristic times τ_{osc}, τ_{damp}, and τ_{ex} are constrained to the values obtained from the cross-peak fit (Supplementary Table 6.7). The error bars are the standard error of the linear regression of the center line. Reproduced from [1].

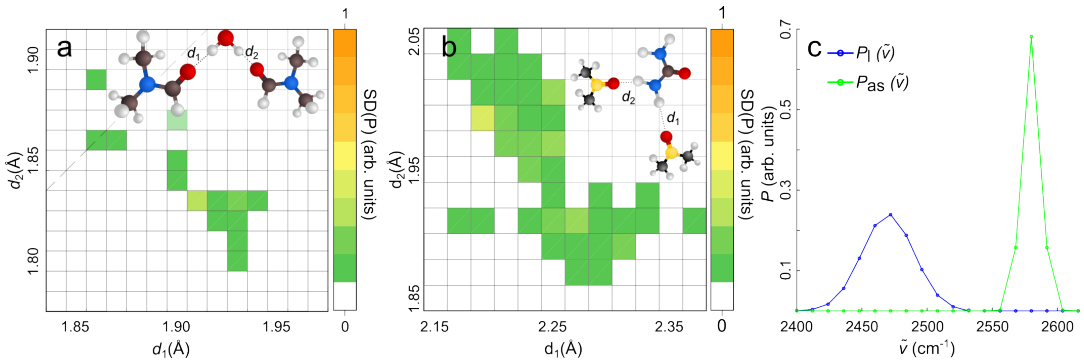

FIGURE 6.12: Standard deviation of the population fit $P(d_1, d_2)$ for **a**) D_2O in DMF and **b**) urea-d4 in DMSO, obtained from ten random initial populations. **c**) Inhomogeneous frequency distributions $P_i(\tilde{\nu})$ for urea in DMSO. Symbols show discretized experimental values and solid lines show the fits based on the distribution in Figure 6.5c and the frequency maps in Supplementary Figure 6.16. Reproduced from [1].

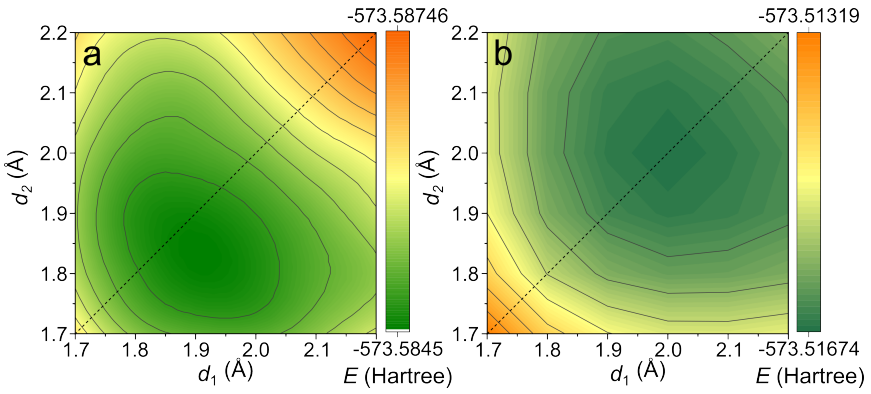

FIGURE 6.13: Total energy of a D_2O molecule bound to two DMF molecules as a function of H-bond distances with the adjacent minimum energy reaction paths for H-bond breaking, in addition to the global minimum at the equilibrium distance of the H-bonds with D3 dispersion correction and conductor-like polarizable continuum model (CPCM) in **a**) and without dispersion correction and CPCM in **b**). Comparison suggests that the asymmetry of the energy profile in **a**) most likely stems from DMF-DMF interactions. Reproduced from [1].

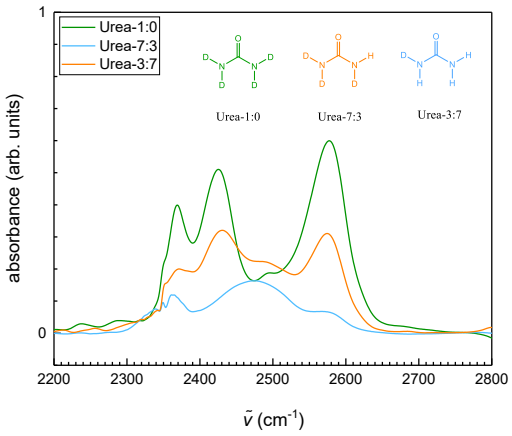

FIGURE 6.14: Solvent subtracted IR spectra of urea-d4/urea mixtures in DMSO at different mixing ratios: pure urea-d4 (green), 70 % urea-d4 (orange), and 30 % urea-d4 (blue). Reproduced from [1].

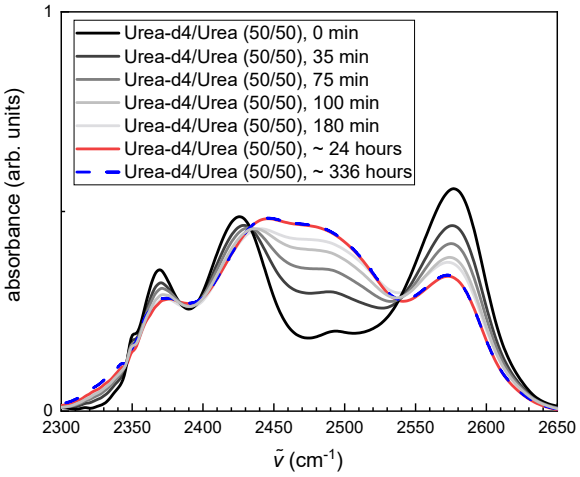

FIGURE 6.15: Solvent-subtracted IR absorption spectra of a urea-d4/urea (50% / 50%) mixture in DMSO as a function of time after mixing at a concentration of c(urea) + c(urea-d4) = 0.36 mol/kg. Reproduced from [1].

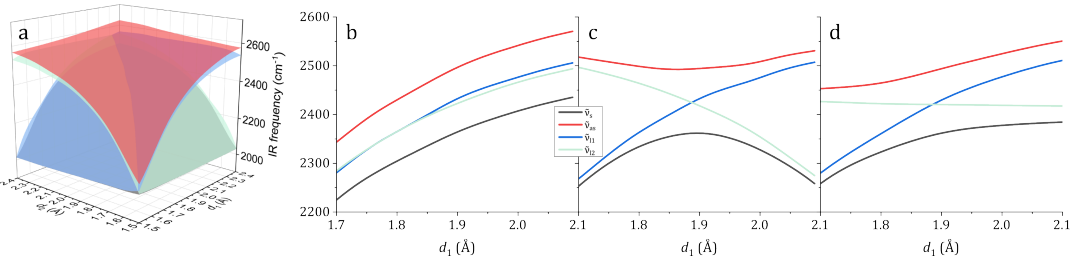

FIGURE 6.16: **a**) Frequency maps for the symmetric $\tilde{\nu}_{sym}$(grey), local $\tilde{\nu}_{l1}$ (light blue), $\tilde{\nu}_{l2}$ (light green), and asymmetric $\tilde{\nu}_{as}$ (red) ND stretching modes of urea+4 DMSO as a function of hydrogen-bond distances d_1 and d_2, as obtained from the harmonic frequencies of relaxed surface scans using DFT calculations. **b**) Diagonal cut at $d_1 = d_2$ through the frequency maps representing correlated H-bonds, **c**) antidiagonal cut at $d_1 + d_2 = 3.8$ Å representing anti-correlated H-bonds, and **d**) cut at $d_2 = 1.9$ Å representing uncorrelated H-bond distances. Reproduced from [1].

6.8.1 Supplementary Tables

TABLE 6.1: Fitting parameters of the Gaussian fits for the linear spectra displayed in Supplementary Figure 6.6. D_2O in DMF was fitted with three Gaussians accounting for the overtone of the DOD bending mode (δ^2), the symmetric stretching (*sym*), and the asymmetric stretching (*as*).

	D_2O in DMF (δ^2)	D_2O in DMF (*sym*)	D_2O in DMF (*as*)	HOD in DMF (*l*)
Γ_G(cm^{-1})	143	79	78	94
$\tilde{\nu}_c$(cm^{-1})	2414	2545	2640	2583
A_G	0.11	0.65	0.95	0.97

TABLE 6.2: Parameters obtained from fitting Supplementary Eq. 6.1 to the antidiagonal cuts of the 2D-IR spectra of D_2O and HOD in DMF.

	D_2O (*sym*) antidiagonal at 2538 cm^{-1}	D_2O (*as*) antidiagonal at 2635 cm^{-1}	HOD (*l*) antidia gonal at 2552 cm^{-1}
$A_{ESA,i}$ (mOD)	0.13	0.10	0.03
$A_{GSB,i}$ (mOD)	-0.08	-0.17	-0.09
$\tilde{\nu}_{c,ESA,i}(cm^{-1})$	2480	2600	2500
$\tilde{\nu}_{c,GSB,i}(cm^{-1})$	2530	2630	2560
$\Gamma_{L,ESA,i}(cm^{-1})$	104	47.1	63.0
$\Gamma_{L,GSB,i}(cm^{-1})$	40.7	47.1	63.0

TABLE 6.3: Fit parameters obtained from fitting Supplementary Eq. 6.2 to the diagonal slices of the 2D-IR spectra of D_2O and HOD in DMF.

	D_2O (*sym*) diagonal	D_2O (*as*) diagonal	HOD (*l*) diagonal
A_i mOD	-0.07	-0.15	-0.09
$\tilde{\nu}_{c,i}(cm^{-1})$	2530	2630	2560
$\Gamma_{L,GSB,i}(cm^{-1})$	40.7	47.1	63.0
$\Gamma_{G,i}(cm^{-1})$	20.2	17.5	38.0

TABLE 6.4: Parameters obtained from fitting Supplementary Eq. 6.1 to the antidiagonal slices of the 2D-IR spectra of urea in DMSO.

	urea-d4 (*sym*) antidiagonal at 2423 cm^{-1}	urea-d4 (*as*) antidiagonal at 2576 cm^{-1}	30% urea-d4 (*l*) antidiagonal at 2470 cm^{-1}
$A_{ESA,i}$ (mOD)	0.07	0.30	0.32
$A_{GSB,i}$ (mOD)	-0.22	-0.44	-0.57
$\tilde{\nu}_{c,ESA,i}(cm^{-1})$	2390	2540	2420
$\tilde{\nu}_{c,GSB,i}(cm^{-1})$	2420	2570	2470
$\Gamma_{L,GSB,i}(cm^{-1})$	23.3	31.5	42.0

TABLE 6.5: Parameters obtained from fitting Supplementary Eq. 6.2 to the antidiagonal slices of the 2D-IR spectra of urea in DMSO.

	urea-d4 (*sym*) diagonal	urea-d4 (*as*) diagonal	30% urea d-4 (*l*) diagonal
A_i (mOD)	-0.23	-0.46	-2.68
$\tilde{\nu}_{c,i}(cm^{-1})$	2420	2580	2470
$\Gamma_{L,GSB,i}(cm^{-1})$	23	31	42
$\Gamma_{G,i}(cm^{-1})$	14.1	16.5	46.9

TABLE 6.6: Signal decay times obtained from fitting Supplementary Eq. 6.4 to the integrated 2D-IR peaks.

	τ_{sym} (ps)	τ_{as} (ps)	τ_{cross} (ps)	τ_l (ps)
water	0.71 ± 0.06	0.59 ± 0.07	0.8 ± 0.1	0.8 ± 0.2
urea	0.83 ± 0.08	0.9 ± 0.2	1.0 ± 0.2	0.51 ± 0.02

TABLE 6.7: Parameters obtained from fitting Supplementary Eq. 6.6 to the CLS data of the cross-peak of D_2O in DMF.

A_{osc}	τ_{osc} (fs)	ϕ	τ_{damp}(fs)	A_{ex}	τ_{ex} (fs)	CLS_{offset}
-0.059	310	0.98	470	0.049	50	0.021

Chapter 7

Fast Collective Hydrogen-Bond Dynamics in Hexafluoroisopropanol Related to its Chemical Activity

Caporaletti, F.; **Gunkel, L.**; Fernández-Ibáñez, M. Á.; Hunger, J.; Woutersen, S. *Angewandte Chemie International Edition* **2024**, *63*.[2]
DOI: 10.1002/anie.202416091

F.C., J.H. and S.W. conceptualized the study. F.C. performed linear IR and TRIR measurements, L.G. performed linear IR and 2DIR measurements, J.H. performed DRS measurements and DFT calculations. J.H. and S.W. supervised the project. F.C., L.G., J.H. and S.W. wrote the original manuscript. F.C., L.G., J.H., S.W. and M.A.F.I. revised and edited the manuscript. F.C. and L.G contributed equally.

7.1 Abstract

Using fluorinated mono-alcohols, in particular hexafluoro-isopropanol (HFIP), as a solvent can enhance chemical reaction rates in a spectacular manner. Previous work has shown evidence that this enhancement is related to the hydrogen-bond structure of these liquids. Here, we investigate the hydrogen-bond dynamics of HFIP and compare it to that of its non-fluorinated analog, isopropanol. Ultrafast infrared spectroscopy experiments show that the dynamics of individual hydrogen-bonds is about twice as slow in HFIP as in isopropanol. Surprisingly, from dielectric spectroscopy we find the opposite behavior for the dynamics of hydrogen-bonded clusters: collective rearrangements are 3 times faster in HFIP than in isopropanol. This difference indicates that the hydrogen-bonded clusters in HFIP are smaller than in isopropanol. The differences in cluster size can be traced to changes in the hydrogen-bond donor and acceptor strengths upon fluorination. The smaller cluster size can boost reaction rates in HFIP by increasing the concentration of reactive, terminal OH-groups of the clusters, whereas the fast collective dynamics can increase the rate

of formation of hydrogen-bonds with the reactants. The longer lifetime of the individual hydrogen-bonds in HFIP can enhance the stability of the hydrogen-bonded clusters, and so increase the probability of reactant-solvent hydrogen-bonding.

7.2 Introduction

Fluorinated mono-alcohols, in particular hexafluoro-isopropanol (HFIP), can accelerate chemical reactions in spectacular ways, and many reactions take place only in these solvents [54, 185, 186]. In particular, when compared to its non-fluorinated analogue, isopropanol, HFIP shows superior performance as a reaction medium [187]. A well-known example are metal-catalyzed C−H functionalization reactions, where HFIP has become the most commonly used solvent [54, 185, 188]. HFIP also effectively stabilizes helical structures in proteins [185, 189]. Unraveling the molecular origins of the "booster effect" [10] of fluorinated alcohols is an active field of research. The "booster effect" has been suggested to be due to activation of reactants via solvation/protonation of reactants or stabilization of ionic species/transition states [185], depending on the chemical reaction. More generally, irrespective of the specific reaction mechanism, all activation pathways via solvation and protonation are intimately related to the hydrogen-bonding properties of HFIP. Based on combined *ab initio* calculations using the B3LYP density functional and NMR titration and reaction kinetics experiments, Berkessel *et al.*[10] have shown convincingly that the hydrogen-bonding properties of HFIP play a crucial role. In particular, aggregation of HFIP molecules into hydrogen-bonded clusters increases the hydrogen-bond donor ability of the terminal hydroxyl proton, and reaction-kinetics experiments show that 2–3 HFIP molecules are involved in the activation of the oxidant.[10] Thus, hydrogen-bonded clusters (rather than monomers) are crucial for the unique catalytic and solvolytic effects of HFIP. Whereas the hydrogen-bonding

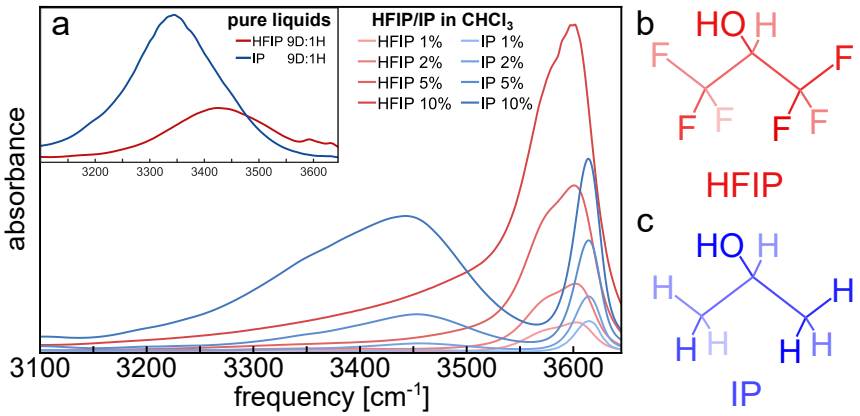

FIGURE 7.1: IR absorption spectra of increasing concentrations (in mol%) of HFIP (red) and isopropanol (blue) in chloroform. The spectra of the pure isotopically dilute (9D:1H) alcohols are shown in the inset. Chemical structures of (b) hexafluoroisopropanol (HFIP) and (c) isopropanol (IP). Reproduced from [2].

structure and energetics of HFIP has been studied experimentally and computationally,[10, 190–195] little is known about the dynamics of the hydrogen-bonds in fluorinated alcohols. Yet, the dynamics of the HFIP hydrogen-bonds is essential to understand activation of reactive intermediates via hydrogen-bonding.[196] Here, we explore the differences in hydrogen-bond dynamics of HFIP and its non-fluorinated counterpart (isopropanol) by combining ultrafast-infrared and GHz-dielectric spectroscopy. These methods provide complementary information on hydrogen-bond dynamics:[197, 198] time-resolved infrared spectroscopy probes the random orientational motion of individual OH groups,[11, 199–201] two-dimensional infrared (2D-IR) spectroscopy probes the distribution and fluctuations of the hydrogen-bonds, [6, 11, 21, 202–210] and dielectric spectroscopy can track the dynamics of collective rearrangements, in particular the orientational random motion of hydrogen-bonded aggregates[211–214]. We find that intermolecular hydrogen-bonds in liquid HFIP are weaker than in isopropanol. Surprisingly, whereas the hydrogen-bond fluctuations and the reorientation of individual OH groups (as probed by time-resolved infrared spectroscopy) are slower in HFIP than in isopropanol, the collective hydrogen-bond dynamics (probed by dielectric spectroscopy) is significantly faster. Our results indicate that in HFIP the hydrogen-bonded clusters are smaller and their collective rearrangements occur much faster than in isopropanol, whereas the individual hydrogen-bonds, whose dynamics is reflected in individual molecular re-arrangements, are longer lived. These differences can be explained by the subtle balance between hydrogen-bond donor and acceptor strength: HFIP is a stronger hydrogen-bond donor, and a weaker hydrogen-bond acceptor, than isopropanol, resulting in shorter, but longer-lived hydrogen-bonded clusters in HFIP. The resulting larger number of free hydrogen-bond donor groups in HFIP, which can donate stronger hydrogen-bonds, can enhance reaction rates observed in HFIP.

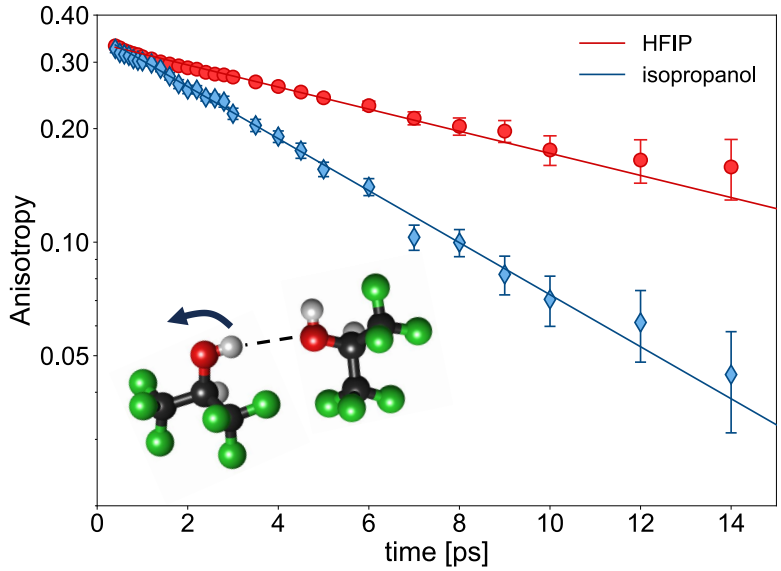

FIGURE 7.2: OD-Stretch anisotropy decay of hexafluoro-isopropanol (red circles) and isopropanol (cyan diamonds) measured at 2534 cm^{-1} and 2483 cm^{-1}, respectively. The samples were isotopically diluted (D/H=0.1) to avoid coupling between the molecular oscillators. The solid lines show a least-squares fit of a single exponential decay to the data. The inset shows the single-molecule re-orientation probed in these experiments. The error bars of $R(t)$ correspond to ± 1 standard deviation, and were estimated from the covariance matrix of the fitting procedure used to extract the re-orientational function from the anisotropy measurement. More details on the extraction procedure can be found in the Supporting Information. Reproduced from [2].

7.3 Results and discussion

To investigate hydrogen-bonding in HFIP and isopropanol we use the OH (or OD) stretching vibration of the alcohols, which is a sensitive probe of the hydrogen-bond strength.[215] To avoid excitonic-coupling effects[118, 216] we study isotopically diluted liquids (HFIP-OD in HFIP-OH, or vice versa). In the inset of Figure 7.1 we show the OH-stretch region of the IR spectra of isotope-diluted HFIP and isopropanol (see SI for the OD-stretch spectra). For HFIP, the spectrum exhibits weak peaks at $\sim$3590 cm^{-1} and $\sim$3630 cm^{-1} (OD: $\sim$2650 cm^{-1} and $\sim$2680 cm^{-1}, see Figure S1), which are due to the antiperiplanar and synclinal conformers of the non-hydrogen-bonded molecules.[190, 217] These non-hydrogen-bonded OH groups in the liquid are somewhat ($\sim$30 cm^{-1}) red-shifted as compared to the gas-phase [190], presumably due to weak interactions with the F atoms,[218, 219] but the OH-stretch frequency difference between antiperiplanar and synclinal is very similar in the liquid and gas phase.[190] The intense, red-shifted OH-stretching band centered at $\sim$3350 cm^{-1} in isopropanol and at $\sim$3420 cm^{-1} in HFIP is due to hydrogen-bonded OH groups. Since the redshift with respect to the non-hydrogen-bonded frequency is proportional the hydrogen-bond strength,[215] the difference in hydrogen-bonded OH-stretch frequency between HFIP and isopropanol indicates that HFIP forms weaker hydrogen-bonds with itself than does isopropanol. To confirm this,

we record spectra of the two alcohols dissolved in chloroform at increasing concentrations (Fig. 7.1). At low concentration, the spectra are dominated by the free OH peaks (at ∼3620 cm^{-1} for isopropanol and ∼3570 cm^{-1} and 3600 cm^{-1} for HFIP). With increasing concentration, isopropanol and HFIP show very different behaviour: for isopropanol, already at low concentrations a peak appears at ∼3450 cm^{-1}, which is due to hydrogen-bonded alcohol clusters,[220] while for HFIP the spectra are still dominated by the free OH peak even at the highest concentration. Thus, HFIP forms weaker hydrogen-bonds with itself than does isopropanol. This may seem counter intuitive, since the "booster effect" of HFIP is believed to be related to its ability to form strong hydrogen-bonds,[10, 190–194] but below we will see that there is in fact no contradiction.

To investigate the dynamics of individual hydrogen-bonds, we track the reorientation of the OD (or OH) groups in HFIP and isopropanol in real time, using ultrafast infrared spectroscopy[21, 118–120, 197, 198, 221]. In the experiments, a short (∼180 fs) infrared pulse excites ("tags") the stretching mode of a small fraction of the OD (or OH) bonds of the liquid. The infrared light is polarized, and preferentially excites OD (or OH) bonds that are aligned parallel to the polarization of the excitation pulse. This results in an anisotropic distribution of excited OD (or OH) bonds, which can be characterized by the so-called anisotropy parameter R (defined as $R = (\Delta A_{||} - \Delta A_{\perp})/(\Delta A_{||} + 2\Delta A_{\perp})$, where $\Delta A_{||,\perp}$ are the excitation-induced absorption changes for light polarized parallel and perpendicular to the excitation polarization). The random motion of the OD groups randomizes the anisotropic distribution, leading to a decay of the anisotropy, and the decay of R directly mirrors the correlation function of the OD random orientational motion.[21, 197, 198] In fact, $R(t)$ probes the dynamics of individual OH (or OD) groups.[197, 198]

We obtain $R(t)$ from the polarization-dependent absorption changes of the hydrogen-bonded OH (or OD) groups after correcting the data for a small thermal contribution using a procedure similar to that of ref.[222] (see SI for the details, Figs. S2-S6). Figure 7.12 shows the anisotropy decay of the OD groups of HFIP (red circles) and isopropanol (cyan diamonds), as observed in OD/OH dilute isotopic mixtures (the arrows in Fig. S1 indicate the frequencies at which the anisotropy decay was measured). The time dependence of $R(t)$ can be well described using a single-exponential decay, and we find that the decay time is ∼ twice as fast in isopropanol than in HFIP (a similar result is obtained for isotopically diluted HFIP-OH in HFIP-OD, see Fig. S7). Thus, despite the weaker hydrogen-bonds in HFIP (see Fig. 7.1), individual OD groups in HFIP reorient slower than in isopropanol.

The decay of $R(t)$ for hydrogen-bonded liquids can occur via different molecular mechanisms. At short timescales (< 0.5 ps) inertia-limited motions, such as librations, can result in a loss of orientational correlation.[223] Our data however show no evidence for a marked, fast $R(t)$ decay at short times. On longer timescales, molecular reorientation via angular jumps during which OH-groups exchange hydrogen-bond acceptors together with the rotation of intact hydrogen-bonds - the so-called

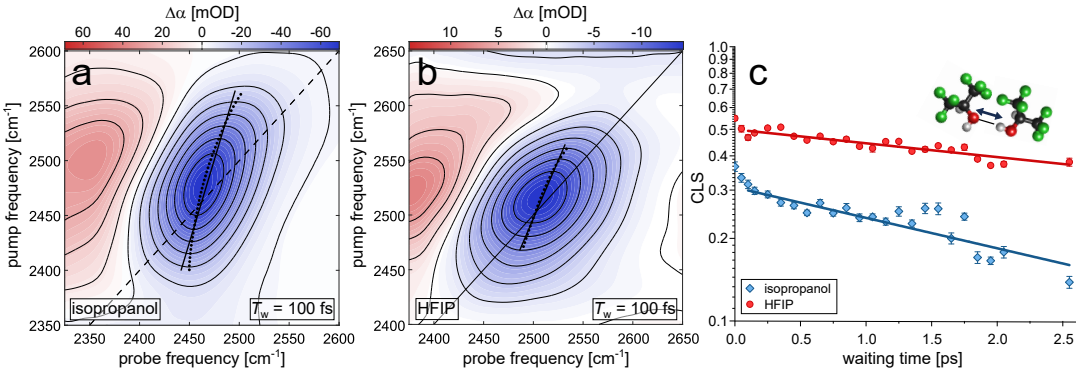

FIGURE 7.3: 2D-IR spectra (parallel pulse polarizations) at 100 fs for the OD-stretch band of a) isopropanol and b) HFIP (D/H=0.1). The black symbols show the minima of the bleaching signal at a given excitation frequencies together with a linear fit - the center line (solid). c) Time-dependent center line slope (CLS) for isopropanol (blue) and HFIP (red). The CLSs are the inverse slopes of the lines shown in panels a) and b). Symbols show experimental data and solid lines mono-exponential fits. . The inset illustrates the hydrogen-bond fluctuations probed by these experiments. Reproduced from [2].

frame orientation - give rise to the decay of the orientational memory.[223] For water, the loss of orientational correlation due to the jumps dominates the decay of $R(t)$ due to the large jump angle, while the frame orientation is somewhat slower. For alcohols, the orientation of intact hydrogen-bonds is even slower than in water (see discussion of the dielectric spectra below) and contributions due to the slower frame orientation to the $R(t)$ decay are very weak.[201] Moreover, due to the fast decay of the vibrational excitation for our samples on a $\sim$1 ps timescale, which limits our accessible time window for recording the $R(t)$ decays, the ultrafast infrared experiment is only weakly sensitive to slow dynamics. Hence, the observed decay of R is dominated by hydrogen-bond exchange dynamics. In this case, the reorientation dynamics are limited by the availability of potential hydrogen-bond acceptors to form a new hydrogen-bond after hydrogen-bond breaking, that is, the density of OH groups.[4, 223, 224] Indeed, liquid HFIP has a lower hydroxyl-group density (5.7 OH-groups/nm^3) than ispropanol (7.9 OH-groups/nm^3), which can explain the slower hydrogen-bond dynamics in the probed time-window. Similarly, steric congestion can also play an important role in slowing down exchange dynamics in HFIP, similarly to what has been observed in MD simulations of other monohydroxyl alcohols.[224] To resolve the exact molecular-level details underlying the detected orientational dynamics of the OH groups, molecular dynamics simulations would be required, and we hope that our results will stimulate work in this direction. Irrespective of the exact reorientation mechanism, our results indicate that individual hydrogen-bonds in HFIP, at the ps timescale, are less dynamic than those in isopropanol.

We further investigate the dynamics of individual hydrogen-bonds using two-dimensional infrared (2D-IR) spectroscopy [21] (the description of the experimental setup is available in ref.[4, 121]). In these pump-probe experiments, we vary the infrared exciting and probing frequencies, and measure the absorption change as

a function of both these frequencies [21]. The tilt of the contours (the "center line slope" or CLS) in the 2D-IR spectrum (Figure 7.3a,b; see Fig. S8 for other waiting times) shows to what extent the response depends on the excitation frequency, and the time dependence of this slope (Figure 7.3c) mirrors the correlation function of the fluctuations in the OD-stretch frequency,[21, 202] and hence of the fluctuations in the hydrogen-bond length [202]. We find that the slope at time zero is smaller in isopropanol than in HFIP (0.37 vs 0.55), which implies a more heterogeneous hydrogen-bond distribution in HFIP as compared to isopropanol [21]. The decay of the slope in the two liquids (Figure 7.3c) shows that the OD-stretch frequency fluctuations are somewhat slower in HFIP than in isopropanol (see Table 7.2 for the time constants; the uncertainties in this table are an underestimate of the actual uncertainties, since the statistically determined error bars on our data points are much smaller than the actual errors). These frequency fluctuations are due to breaking and re-formation of hydrogen-bonds (required for rotation of the OD bonds probed in the experiment of Fig. 7.12) and fluctuations in hydrogen-bond length and angle.[11] Thus, the CLS dynamics confirm that the hydrogen-bonds in HFIP are less dynamic than in isopropanol.

To probe the collective dynamics of hydrogen-bonded clusters in HFIP and isopropanol, we use dielectric spectroscopy. With this technique the molecular motion in response to an external, alternating electric field is monitored and the spectra are sensitive to both single and, especially, collective hydrogen-bond dynamics, thus providing a complementary view of on hydrogen-bond structure and dynamics. [197] It is important to stress that the collective dynamics of supramolecular structures in alcohols is expected to be significantly slower than the individual reorientation of HFIP molecules, as cooperative re-arrangements of more molecules are required.

The random orientational motions of electrical dipoles (either due to motion of individual molecules or of clusters) give rise to broad peaks in the dielectric-loss spectra $\varepsilon''(\omega)$ of a liquid, where the peak frequencies are determined by the characteristic time scales of these motions [225]. In mono-alcohols, the dielectric spectra in the MHz to GHz frequency region generally contain three distinct peaks. The two peaks at high frequencies are predominantly due to the fast rearrangements of individual molecules [226]. The peak at low frequency, despite different interpretations[213, 214, 227–235] is usually associated with the slower, collective rearrangements or dipolar cross- correlations arising from supramolecular structures: as the external electric field induces fluctuations of all molecules at the same time, the motion of an individual dipolar molecule is affected by both, the varying external field and the motion of dipoles in its direct vicinity (dipole-dipole correlations). As such, the lower-frequency dielectric peak mirrors the average size of hydrogen-bonded clusters (the lower its frequency, the larger the average cluster size/ dipole correlations).[213] Figure 7.4 shows the dielectric spectra of HFIP and

isopropanol. Both spectra can be well described by a combination of three (Debye-type) peaks, and from a least-squares-fit analysis (shown as the curves in Fig. 7.4; see SI and Ref. [122–126] for details) we obtain the time constants and amplitudes associated with each of the three peaks. The time constants are listed in Table 1 (see SI for the amplitudes). The dynamics on fast time scales, characterized by time constants τ_2 and τ_3, show the same trend as we observed in the time-resolved infrared experiments: both these relaxation times are shorter in isopropanol than in HFIP, indicating that individual hydrogen-bond rearrangements occur slower in HFIP than in isopropanol. The τ_2 and τ_{or} values are of similar magnitude, which suggests non-diffusive dynamics (in the limit of diffusive reorientational dynamics, the dielectric spectroscopy time should be 3 times slower than the time-resolved infrared time[236]). Such non-diffusive dynamics could arise from restricted dynamics, where the hydrogen-bonded structure imposes constraints on the angular degrees of freedom of the molecules, impeding reorientations with small angular increments.

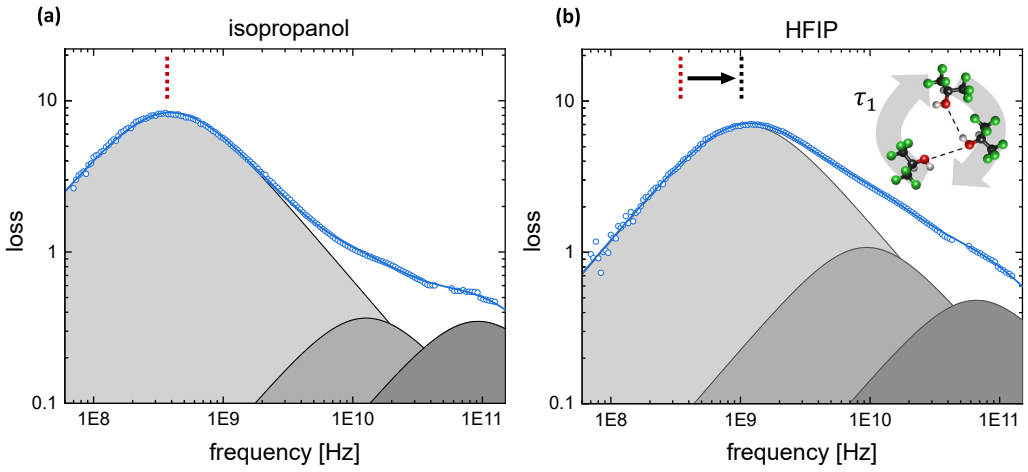

FIGURE 7.4: Dielectric-loss spectra of (a) isopropanol and (b) HFIP. Symbols show experimental data, solid lines show fits of a combination of three Debye peaks to the data (see SI for details). Shaded areas show the contributions of the individual Debye peaks to the spectrum. The minor offsets in the data at frequencies > 50 GHz are of instrumental origin due to the use of different coaxial probes and phase instabilities of the external frequency converter (see SI). The inset schematically illustrates the type of process probed by the low-frequency peak in these experiments. Reproduced from [2].

Whereas the time-resolved infrared and dielectric-spectroscopy experiments both show that individual hydrogen-bond rearrangements are slower in HFIP than in isopropanol, we find the opposite behavior for the collective dynamics: the most intense, low-frequency peak in the dielectric spectrum is at a much higher frequency for HFIP than for isopropanol (light-grey peak in Fig. 7.4), and the associated time constant τ_1 is nearly three times shorter for HFIP (Table 1). The shorter τ_1 time for

TABLE 7.1: Relaxation times τ_j obtained from least-squares fits to the time-resolved infrared, center line slopes, and dielectric-spectroscopy data. See SI for details of the data analysis.

	TRIR	2D-IR	Dielectric spectroscopy		
	τ_{or}/ps	τ_{CLS}/ps	τ_1 / ps	τ_2 / ps	τ_3 / ps
isopropanol	7 ± 1	3.9 ± 0.4	408 ± 5	12.6 ± 0.8	1.7 ± 0.2
HFIP	14 ± 1	8.6 ± 0.7	140 ± 11	17.5 ± 2.7	2.4 ± 0.3

the collective motion of HFIP clusters, as opposed to the slower dynamics of individual hydrogen-bonds in HFIP as compared to isopropanol, implies less cooperativity in the observed lower-frequency dielectric relaxation. These reduced correlations can be explained by significantly smaller hydrogen-bonded aggregates in HFIP than in isopropanol. The smaller cluster size is in line with findings for fluorinated and non-fluorinated tert-butanol [237] and is consistent with the higher strain (and hence, lower barrier for opening OH$\cdots$O hydrogen-bonds) in small ring-like clusters observed in the gas phase.[195] This difference in cluster size is confirmed by the larger spectral heterogeneity of the OD-stretch mode in the 2D-IR experiments (small aggregates have a larger proportion of terminal hydrogen-bonds, which differ in strength from the hydrogen-bonds in the interior of the aggregate, and this translates into a broader distribution of OD-stretch frequencies) [11, 220, 238, 239]. Similarly, more heterogeneous hydrogen-bonds giving rise to a broader distribution of vibrational lifetimes (Fig. S9) [239], and also the enhanced number of non-bonded OD groups in HFIP (Fig. 7.1) support reduced cluster sizes in HFIP.

7.4 Conclusions

Summarizing, our measurements indicate that compared to isopropanol, HFIP consists of smaller, faster-moving hydrogen-bonded clusters, in which the internal, somewhat weaker hydrogen-bonds are less dynamic. How are these differences between HFIP and isopropanol related to the difference in chemical activity of these two liquids? The weaker hydrogen-bonds in HFIP as compared to isopropanol may at first sight appear counter-intuitive, as fluorination of alcohols enhances the hydrogen-bond donor strength and, often equivalent, acidity [240–242]. However, fluorination also makes alcohols poorer hydrogen-bond acceptors [241, 242]. Indeed, density functional theory calculations of hydrogen-bonded dimers suggest that the interaction energy of 2 HFIPs and 2 isopropanols are comparable (see Fig. S10 while technical details are available in the supporting information and in Refs. [109, 110, 127–134]), whereas HFIP donating a hydrogen-bond to isopropanol is energetically much more favorable than isopropanol donating a hydrogen-bond to HFIP (Fig. S10). This notion is in line with previous NMR titration studies by Berkessel *et al.*[10]). Berkessel *et al.* have shown convincing evidence that the catalytic activity of HFIP is caused by hydrogen-bonded clusters in this solvent. Interestingly, their calculations show

that the hydrogen-bond donor capacity of a terminal HFIP molecule in a hydrogen-bonded cluster increases with cluster size, but that this effect already levels off at a cluster size of 3; and their chemical-kinetics experiments show that aggregates of only 2–3 monomers are responsible for the activation of the oxidant.[10] Our results suggest that HFIP consists of many small hydrogen-bonded clusters, which are sufficiently large and have a sufficiently long lifetime to efficiently boost chemical conversions, yet sufficiently small (smaller than in isopropanol) to posses a large number of available active terminal sites which can donate a hydrogen-bond to a reactant molecule.

These active terminal OH groups of HFIP can efficiently enhance chemical reaction rates by activating reactants via strong hydrogen-bond donation. The hydrogen-bonds donated to reactants by HFIP are in fact stronger than those donated by isopropanol, as we demonstrate for the hydrogen-bonds between the alcohols and the model reactant diethylether in chloroform solution, see Figure 7.5. The infrared spectra of 1 mol % HFIP or isopropanol are dominated by the non-hydrogen-bonded OH stretching bands at $\sim$3600 cm^{-1}. Upon addition of the hydrogen-bond acceptor diethylether, the OH stretching bands of hydrogen-bonded OH$\cdots$OEt$_2$ groups emerge at lower frequency: at $\sim$3450 cm^{-1} for isopropanol and $\sim$3200 cm^{-1} for HFIP, where the reversal in the hydrogen-bonded peak order with respect to Figure 1 (inset) should be noted. This marked difference in hydrogen-bonded OH-stretch frequencies shows that HFIP forms much stronger hydrogen-bonds to ether than does isopropanol. The difference in hydrogen-bond strength is further evidenced by the spectral amplitudes: non-bonded OH groups nearly fully vanish at 10 mol% diethylether for HFIP, while a large fraction of non-bonded OH groups are present for isopropanol (Fig. S11a). To quantify the binding strengths, we determine the degree of association from the spectral amplitudes as function of diethylether content (Fig. S11b–c, see SI for details). The data in Fig. S11c can be described by bimolecular association [243] with association constants $K_{\mathrm{ass}}(\mathrm{IP}) = 0.8\ \frac{\mathrm{L}}{\mathrm{mol}}$ and $K_{\mathrm{ass}}(\mathrm{HFIP}) = 3.9\ \frac{\mathrm{L}}{\mathrm{mol}}$, qualitatively consistent with DFT calculations (Fig. S10). Our experiments suggest about two times stronger hydrogen-bonding of HFIP to diethylether as compared to isopropanol.

Our spectroscopic results demonstrate that this subtle balance between the donor and acceptor strength results in less extended hydrogen-bonding in HFIP. As a consequence, (1) at ambient temperature the concentration of terminal (i.e., reactive, hydrogen-bond donating[10]) OH groups is larger in neat HFIP than in isopropanol; (2) due to the faster collective dynamics (i.e., the re-orientation of aggregates as a whole), these reactive terminal OH groups have a higher frequency of encounters with the reactant molecules; (3) the hydrogen-bonds within HFIP clusters are less dynamic (as evidenced from the slower OH-reorientation and CLS dynamics); finally, (4) the terminal OH groups of the HFIP clusters can donate strong hydrogen-bonds to the reactants. The latter can be seen from the linear absorption spectra and the DFT calculated hydrogen-bond strengths between the alcohols and diethylether,

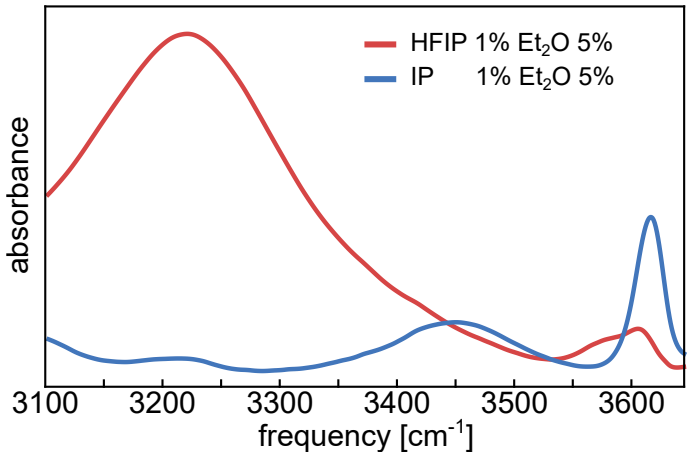

FIGURE 7.5: IR absorption spectra of mixed solutions in $CHCl_3$, containing 5 mol% Et_2O and 1 mol% HFIP or isopropanol. Note the reverse order of the $OH\cdots OEt_2$ hydrogen-bonded OH-stretch peaks of HFIP and isopropanol as compared to hydrogen-bonded peaks in the pure liquids, shown in the inset of Figure 1. Reproduced from [2].

which serves as a proxy for a large class of reactants.[10]

Thus, together with the structural booster effects reported by Berkessel *et al.*[10], our dynamical results complement the understanding of the enhanced reactivity in the solvent HFIP as compared to conventional alcohols such as isopropanol.

7.5 Acknowledgement

The authors thank Martina Knecht for recording the dielectric spectra. F.C. is a Chargé de Research of the Fonds de la recherche scientifique-FNRS.

7.6 Supporting Information

7.6.1 Fit parameters obtained from the dielectric spectra

The dielectric spectra can be well described by a combination of three (Debye-type) peaks, and from a least-squares-fit analysis using the fit function

$$\hat{\varepsilon}(\nu) = \sum_{j=1}^{3} \frac{\Delta\varepsilon_j}{1 + i2\pi\nu\tau_j} + \varepsilon_\infty, \tag{7.1}$$

where $\Delta\varepsilon_j$ are the relaxation strengths, τ_j the relaxation times, and ε_∞ is the high frequency limit of the permittivity. All fits were performed by minimizing the sum of the squared deviations on a logarithmic scale and error bars were obtained from the standard deviations of fitting at least six independently recorded spectra. The obtained fit parameters are listed in Table S1. While τ_j identifies the characteristic timescale of a relaxation mode, $\Delta\varepsilon_j$ is proportional to the number of dipoles reorientating at τ_j. The obtained fitting parameters are reported in Table 7.2.

TABLE 7.2: Fit parameters obtained from fitting eq. 1 to the experimental permittivity spectra: relaxation amplitudes $\Delta\varepsilon_j$; relaxation times τ_j, and infinite frequency permittivity, ε_∞.

	isopropanol	HFIP
$\Delta\varepsilon_1$	16.65 ± 0.06	13.66 ± 0.36
τ_1 / ps	408 ± 5	140 ± 11
$\Delta\varepsilon_2$	0.75 ± 0.06	2.2 ± 0.2
τ_2 / ps	12.6 ± 0.8	17.5 ± 2.7
$\Delta\varepsilon_3$	0.70 ± 0.05	0.98 ± 0.13
τ_3 / ps	1.7 ± 0.2	2.4 ± 0.3
ε_∞	2.43 ± 0.03	2.17 ± 0.05

7.6.2 Infrared absorption spectra of HFIP and isopropanol

Figure 7.6 shows the linear absorption spectra of OD/OH isotope-diluted isopropanol and HFIP. The OD-stretching band of HFIP is located at a higher frequency with respect to isopropanol. The small peaks at high frequencies have been assigned previously to free OH-groups[190, 217] of different conformers. The arrows indicate the frequencies at which we measured the single-molecule reorientation dynamics of HFIP and isopropanol.

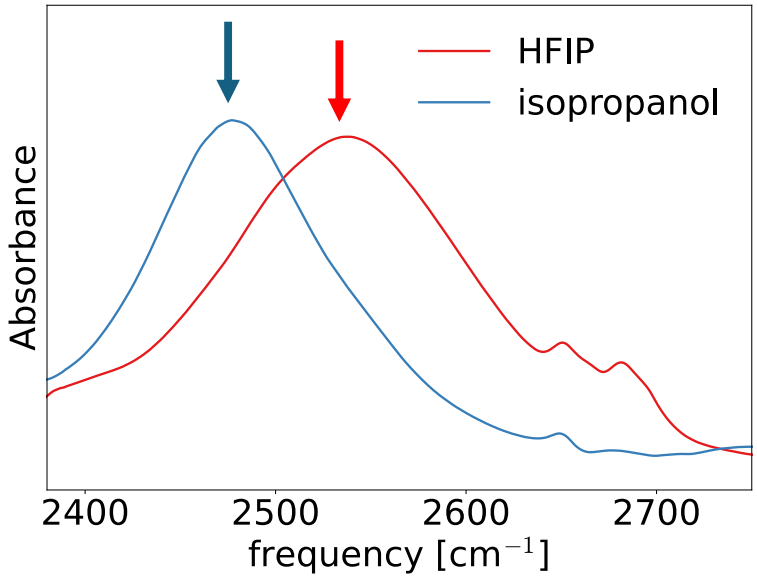

FIGURE 7.6: IR absorption spectra of isotope diluted (OD/OH=0.1) HFIP (red solid line) and isopropanol (blue solid line). The arrows indicate the central frequency of the broadband pulses used to measure the anisotropy decay. Reproduced from [2].

7.6.3 Analysis of transient absorption spectra to obtain the ani-sotropy

The rotational anisotropy is extracted starting from the parallel and perpendicular components of the transient absorption signal $\Delta\alpha_{||}$ and $\Delta\alpha_{\perp}$

$$R = \frac{\Delta\alpha_{||} - \Delta\alpha_{\perp}}{\Delta\alpha_{||} + 2\Delta\alpha_{\perp}}. \tag{7.2}$$

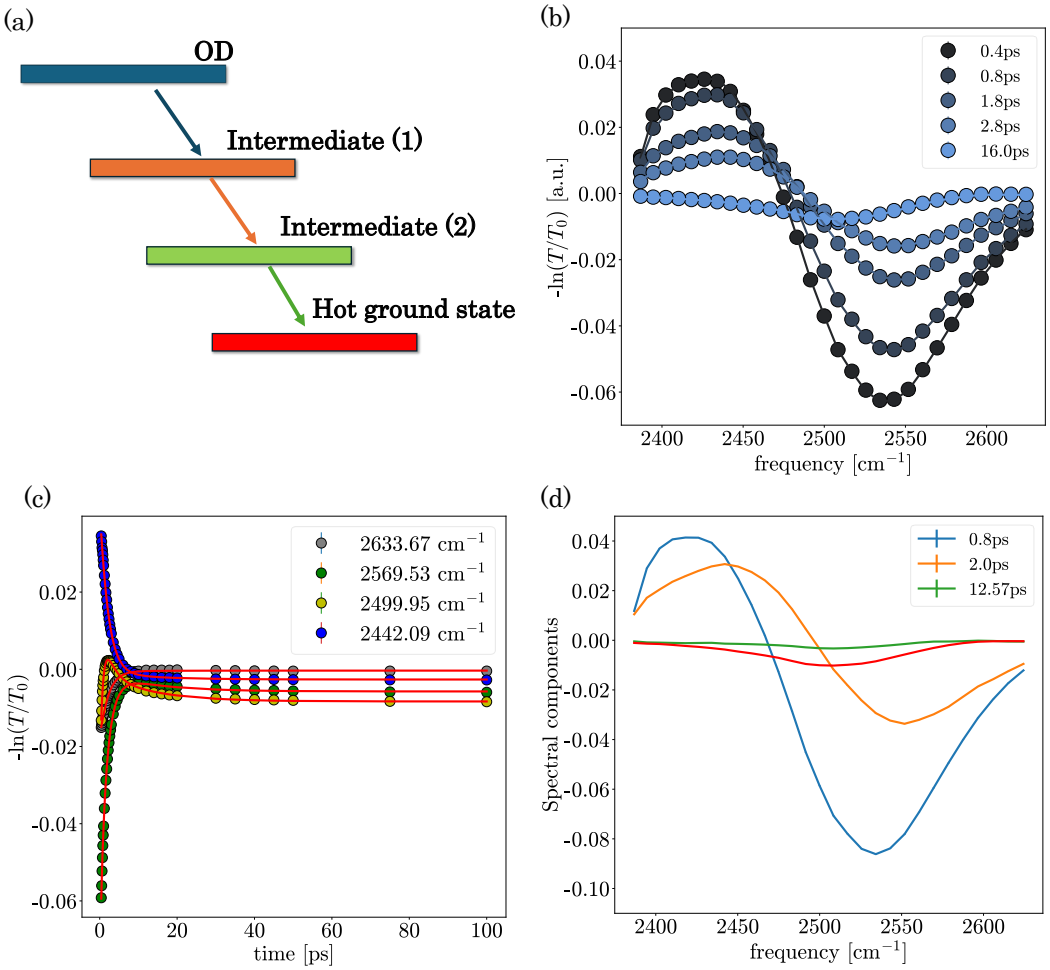

FIGURE 7.7: (a) Energy level diagram of the model that describes the vibrational relaxation of the OD stretch vibration of HFIP. (b) Isotropic absorption change as a function of frequency at different pump-probe delays. (c) Isotropic absorption change as a function of pump-probe delay at fixed frequencies. The curves in (b,c) show the result of the global-fitting procedure. (d) Spectral components of the vibrational levels extracted from the global fit. The red curve represents the hot ground state. Reproduced from [2].

The denominator of R is the isotropic signal

$$\Delta\alpha_{iso} = \frac{\Delta\alpha_{||} + 2\Delta\alpha_{\perp}}{3}. \tag{7.3}$$

$\Delta\alpha_{iso}$ is independent of molecular reorientation and purely reflects the relaxation of the vibrational excitation and the subsequent thermalization. Heating effects produced by the pump pulse give rise to an additional small contribution to the transient absorption, and as a consequence the anisotropy cannot be obtained directly from $\Delta\alpha_{||,\perp}$, but only after subtracting such thermal contribution, a correction procedure that is described in detail in refs.[222, 244]

Vibrational relaxation

The vibrational dynamics of the excited OD vibration of isotopically diluted mixtures of both HFIP and isopropanol has been modeled as a multi-step decay process, see Fig. 7.7(a). The first excited state decays first to an intermediate state, and finally, passing through an additional state, relaxes to a hot ground state. Modeling the data with only 1 intermediate state could not reproduce the data well. The time-dependent populations in this model are determined by the differential equations:

$$\frac{d}{dt}N_i(t) = k_{ij}N_j(t) \tag{7.4}$$

where $N_i(t)$ is the population, t is the delay between the pump and probe pulse, and k_{ij} are the relaxation rates defined by the kinetic model, in this case given by

$$k_{ij} = \begin{bmatrix} -k_1 & 0 & 0 & 0 \\ +k_1 & -k_2 & 0 & 0 \\ 0 & +k_2 & -k_3 & 0 \\ 0 & 0 & +k_3 & 0 \end{bmatrix} \tag{7.5}$$

where k_1 and k_2, k_3 are the decay rates of each state. Each vibrational state is characterized by a transient absorption spectrum $\sigma_i(\omega)$, and the total time-dependent isotropic absorption change is

$$\Delta\alpha_{iso}(t,\omega) = \sum_{i=1}^{N} \sigma_i(\omega)N_i(t) \tag{7.6}$$

where N is the total number of vibrational levels. The spectral components and the decay rates are finally obtained via a global least-squares fitting procedure on a weighted χ^2:

$$\chi^2 = \iint \left(\frac{\Delta\alpha_{iso}^{\text{experimental}}(t,\omega) - \Delta\alpha_{iso}^{\text{calc}}(t,\omega)}{\sigma(t,\omega)} \right)^2 d\omega dt \tag{7.7}$$

Fig. 7.7-(b) and (c) show the isotropic absorption change for HFIP, along with the obtained fitting curve. An excellent agreement between the experimental data and the model can be clearly observed. Fig. 7.7-(d) shows the spectral components of each excited states along with the characteristic lifetime. Similar results were obtained for isopropanol, see Fig. 7.8.

Table S2 lists the decay rates obtained from the global least-squares fits for HFIP and isopropanol. The excited-state decay rate $T_1 = 1/k_1$ is similar for the OD-vibration of HFIP and isopropanol and for the latter our value is in good agreement with the value of 0.990 ps reported previously.[11]

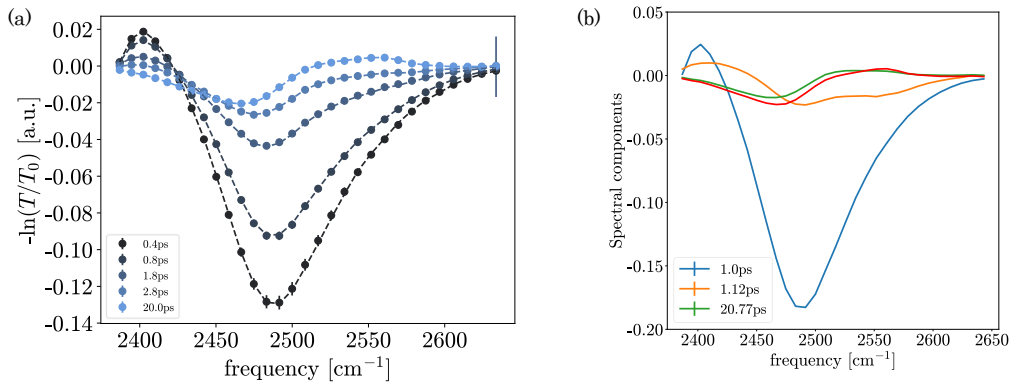

FIGURE 7.8: (a) Isotropic absorption change of the OD-stretch of isopropanol as a function of frequency at different pump-probe delays. The dashed lines are the curves obtained from the fitting procedure (b) Spectral components of the vibrational levels extracted from the fitting procedure. The red curve represents the hot ground state. Reproduced from [2].

TABLE 7.3: Time constants $T_i = 1/k_i$ associated to the vibrational dynamics of the OD-stretch mode of isopropanol and HFIP.

	Vibrational dynamics		
	T_1 / ps	T_2 / ps	T_3 / ps
isopropanol	1.0 ± 0.20	1.12 ± 0.1	20.8 ± 0.2
HFIP	0.8 ± 0.2	2.0 ± 0.1	12.6 ± 0.1

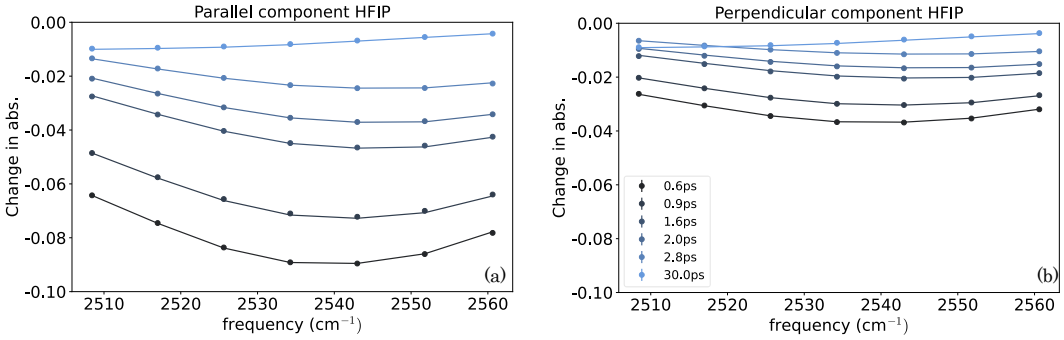

FIGURE 7.9: (a) Parallel ($\alpha_{||}$) and (b) perpendicular ($\alpha_{\perp}$) components of the absorption change measured in isotope diluted HFIP (D/H=0.1). The markers show the experimental data while the solid lines are the curves obtained by minimizing Eq. 7.11. Reproduced from [2].

Reorientation dynamics

The analysis of the isotropic transient absorption can be used to analyze the reorientational dynamics and, in particular, to subtract the heating contribution from the $\Delta A_{||,\perp}$ signals. We use a procedure similar to that of refs.[222, 244]. The parallel and perpendicular components of the transient absorption signal can be expressed in terms of $R(t)$ (see Eq. 7.2), and using Eq. 7.6, we have

$$\Delta\alpha_{||} = \sum_{i}^{N}[1 + 2R(t)]N_i(t)\sigma_i(\omega) \tag{7.8}$$

and

$$\Delta\alpha_{\perp} = \sum_{i}^{N}[1 - R(t)]N_i(t)\sigma_i(\omega) \tag{7.9}$$

where $R(t)$ is the time-dependent OH-anisotropy, which we model as

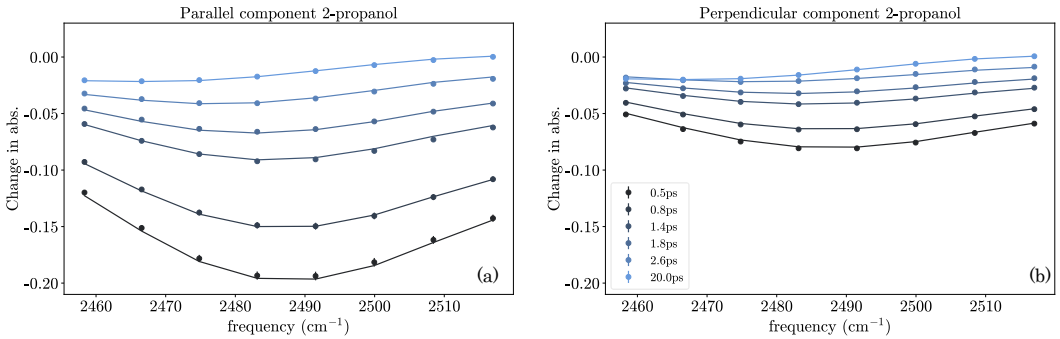

FIGURE 7.10: (a) Parallel ($\alpha_{||}$) and (b) perpendicular ($\alpha_{\perp}$) components of the absorption change measured in isotope diluted isopropanol (D/H=0.1). The markers show the experimental data while the solid lines are the curves obtained by minimizing Eq. 7.11. Reproduced from [2].

$$R(t) = Ae^{-t/\tau_{\text{or}}}, \tag{7.10}$$

where τ_{or} is the characteristic timescale of the OH-reorientation dynamics. A and τ_{or} are obtained by least-squares-fitting the parallel and perpendicular components via Eqs. 7.8 and 7.9 to the experimental data, specifically, by minimizing the function

$$\begin{aligned}\chi^2 = \int\int \Bigg[&\left(\frac{\delta\alpha_{||}(t,\omega) - \sum_i^N [1 + 2R_i]N_i(t)\sigma_i(\omega)}{\sigma^{||}(t,\omega)} \right)^2 \\ &+ \left(\frac{\delta\alpha_{\perp}(t,\omega) - \sum_i^N [1 - R_i]N_i(t)\sigma_i(\omega)}{\sigma^{\perp}(t,\omega)} \right)^2 \Bigg] d\omega dt\,.\end{aligned} \tag{7.11}$$

In the fitting procedure, both the spectral components $\sigma_i(\omega)$ and the population kinetics $N_i(t)$ are fixed to the values found from the analysis of the isotropic signal. The fits were performed in a frequency range centered at the bleach maximum, where the absorption change is largest. Examples of fitted parallel and perpendicular transient absorption signal are shown in Figures 7.9 and 7.10. Figure 7.11 shows the anisotropy that would be obtained from the uncorrected $\Delta A_{||,\perp}$, together with a calculated reconstruction of this data using the parameters obtained from the above global least-squares fit. This shows that even without correcting for thermal effects, a similar difference in dynamics between HFIP and isopropanol is observed as in Figure 2 of the main text.

The time-dependent anisotropy of HFIP and isopropanol (the experimental data

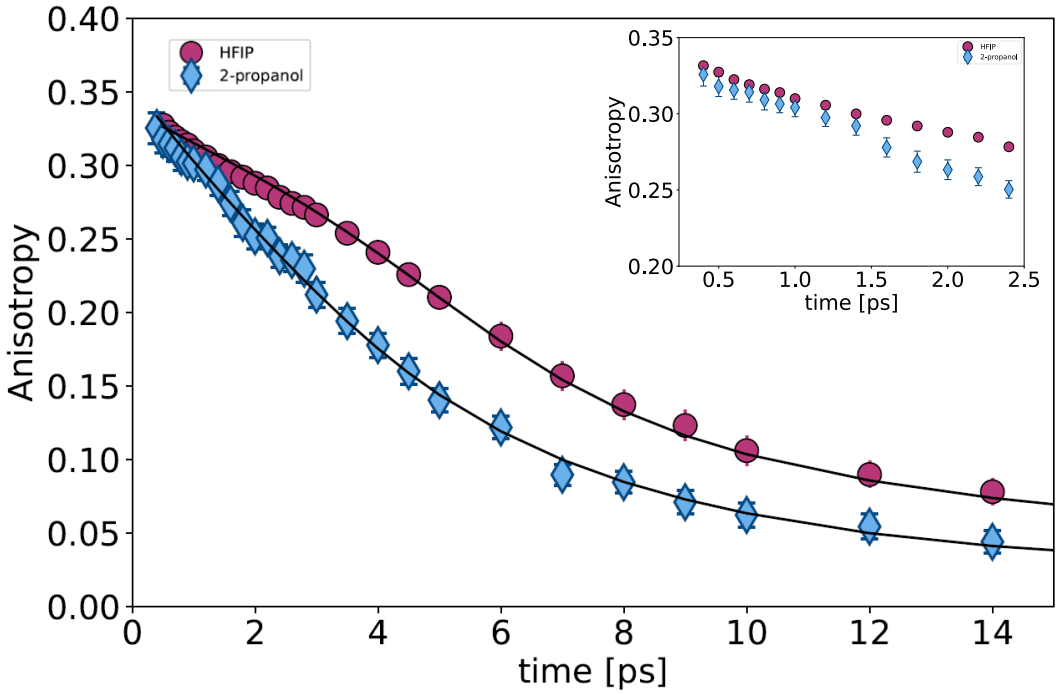

FIGURE 7.11: Total anisotropy as a function of delay time for HFIP and isopropanol isotope diluted solutions (D/H=0.1) at 2534 cm^{-1} and 2483 cm^{-1} respectively. The solid lines are fits to the experimental data via the model described in the supplementary information. The inset reports the first 2.5 ps of the anisotropy decay without further processing. Reproduced from [2].

shown in Fig. 2 of the main text) were obtained by subtracting the thermal components obtained from the analysis described above from the experimental data:

$$\Delta\alpha_{||}^{corr}(t,\omega) = \Delta\alpha_{||}(t,\omega) - [(1+2R_{HG}(t))\sigma_{HG}(\omega)N_{HG}(t)] \tag{7.12}$$

$$\Delta\alpha_{\perp}^{corr}(t,\omega) = \Delta\alpha_{\perp}(t,\omega) - [(1-R_{HG}(t))\sigma_{HG}(\omega)N_{HG}(t)] \tag{7.13}$$

where R_{HG}, $\sigma_{HG}(\omega)$ and $N_{HG}(t)$ are anisotropy, spectral component and population dynamics of the hot ground state. Finally, the time-dependent anisotropy is obtained as

$$R(t) = \frac{\Delta\alpha_{||}^{corr} - \Delta\alpha_{\perp}^{corr}}{\Delta\alpha_{||}^{corr} + 2\Delta\alpha_{\perp}^{corr}}\,. \tag{7.14}$$

7.6.4 Dynamics of isotopically diluted OH-groups

The reorientational dynamics of isopropanol and HFIP was also investigated in the inverted mix, that is, diluted HFIP-OH (isopropanol-OH) in HFIP-OD (isopropanol-OD). We used a dilution H/D=0.1. The anisotropy decays of the two molecules, extracted using the procedure detailed in the previous sections, show an analogous trend as observed in Fig. 2 of the main text. The obtained τ^{or} are in quantitative agreement with the results obtained in D/H=0.1 solutions (see table below)

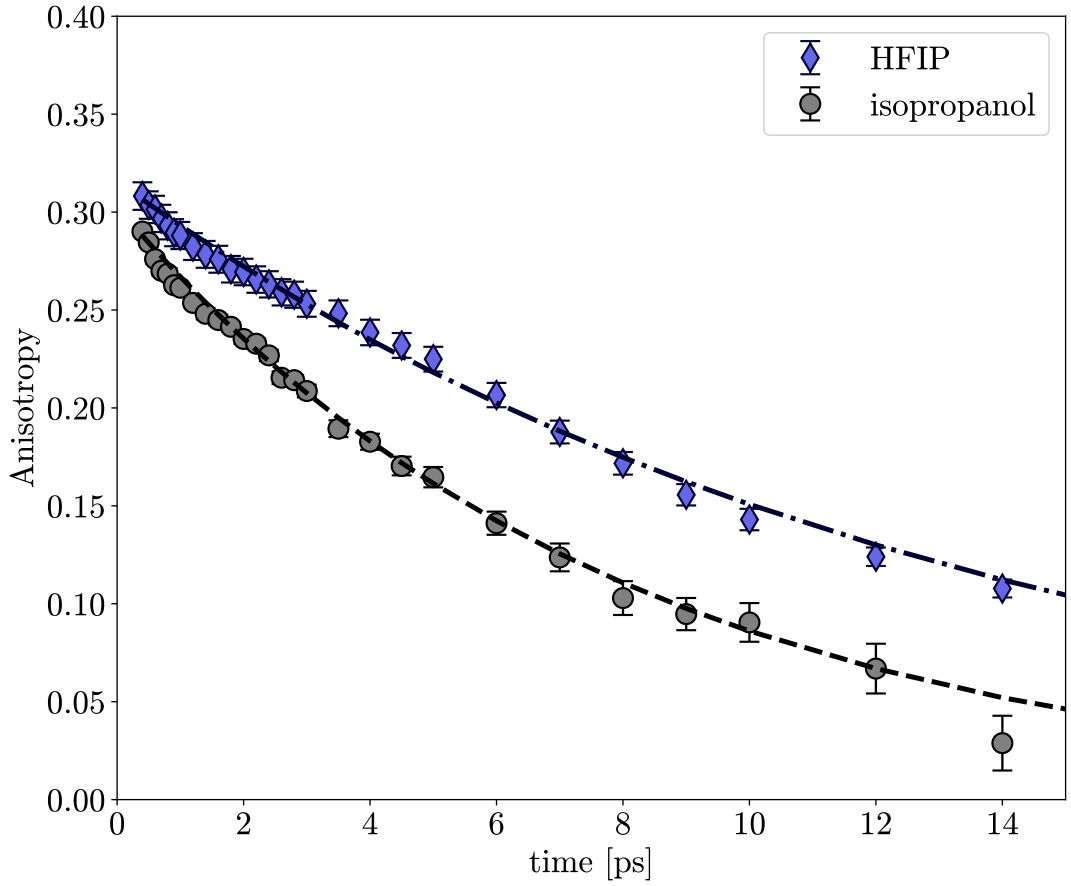

FIGURE 7.12: OH-Stretch anisotropy decay of hexafluoro-isopropanol (violet diamonds) and isopropanol (gray circles) measured at 3438 cm^{-1} and 3350 cm^{-1} respectively, i.e., at the center of the OH-stretch absorption band. The samples were isotopically diluted (H/D=0.1) to avoid coupling between the molecular oscillators. The solid lines show a least-squares fit of a single exponential decay to the data. Reproduced from [2].

TABLE 7.4: Relaxation times τ_{or} obtained from least-squares fits to the time-resolved infrared data measured on H/D=0.1 isotope diluted solutions.

OH-stretch anisotropy	τ_{or}/ps
isopropanol	7 ± 1
HFIP	13.5 ± 1.6

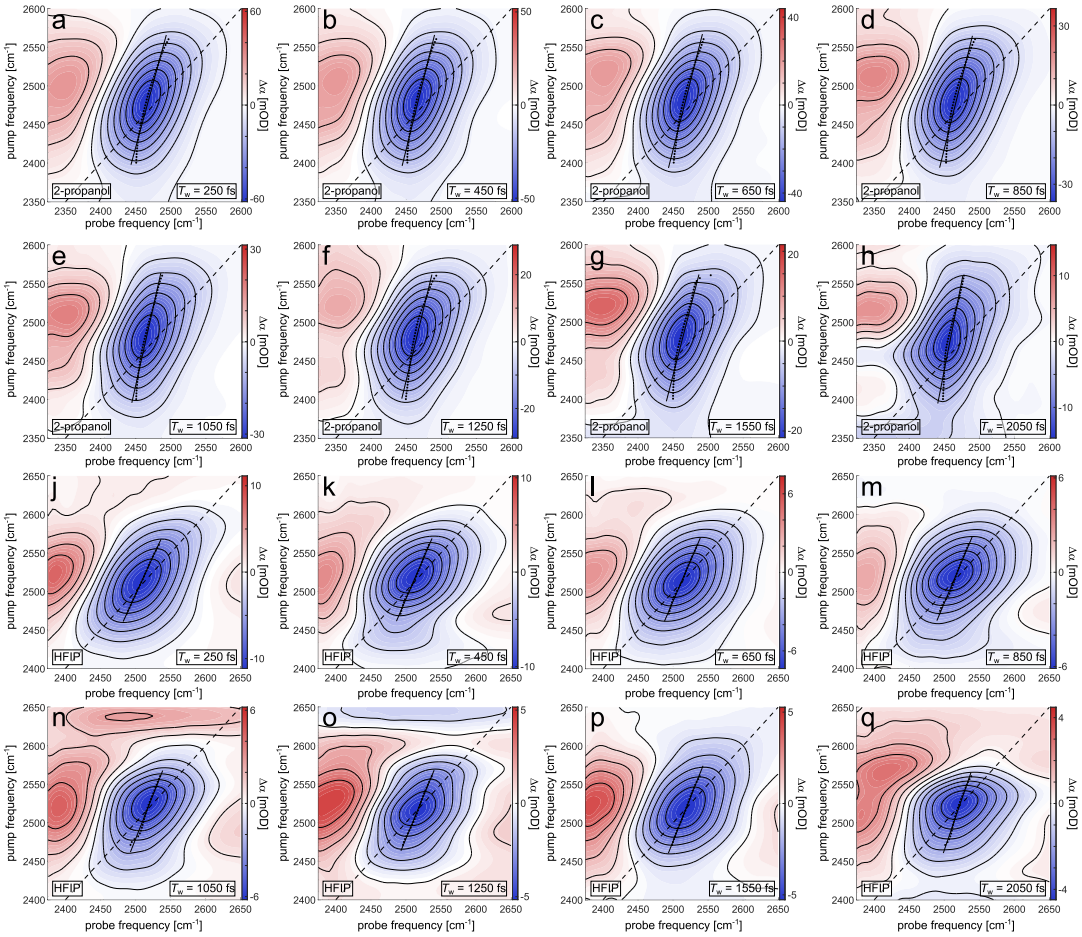

FIGURE 7.13: Additional 2D-IR spectra at different waiting times in $< ZZZZ >$ polarization (parallel) of a-h) isopropanol and j-o) HFIP with an isotope ratio D:H of 1:9. The minima parallel to the probe axis (center line points) are indicated with black symbols and the center line is displayed as solid line. Reproduced from [2].

7.6.5 Two-Dimensional Infrared Spectroscopy

Decay time maps

To explore frequency dependent vibrational relaxation dynamics in the alcohols we calculated decay time maps shown in Figure 7.14.[210] For this we integrated a 5x5 pixel grid for each pixel, and fit the decay of the integrated signal (from 250 fs to 2500 fs to exclude fast dynamics) with an monoexponential decay relaxing to a heated ground state[6] and display the decay times as a color map. We note that this approach neglects spectral diffusion dynamics, and spectral diffusion - as measured by the CLS dynamics (see main text) - will result in an apparent heterogeneity of the decay times. In this analysis we exclude pixels in the decay time maps that have less than 10% of the minimum signal at 250 fs waiting time as well as pixels with poor fit quality ($r^2 < 0.8$). Both HFIP and isopropanol show apparent frequency dependent vibrational lifetimes. Despite the slower spectral diffusion that should lead to less apparent lifetime heterogeneity (see Figure 3 of the main manuscript), HFIP shows

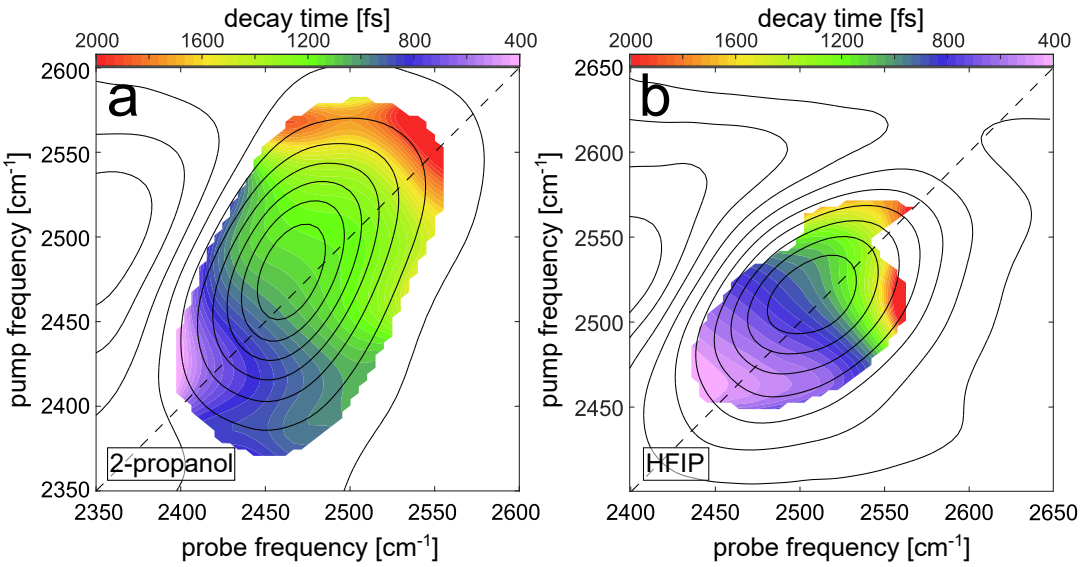

FIGURE 7.14: 2D-IR spectra at T_w = 100 fs in $< ZZZZ >$ polarization (parallel) of a) isopropanol and b) HFIP with an isotope ratio D:H of 1:9 (contour plot). Decay time maps are displayed as a color map. Reproduced from [2].

more inhomogeneous decay times than isopropanol (standard deviation of the decay times for isopropanol: 300 fs and HFIP 400 fs). The more pronounced heterogeneity is also consistent with a higher amplitude of the intermediate state in figure 7.8. The more pronounced heterogeneity of decay times in HFIP than in isopropanol can also be explained by a larger contribution of terminal OD groups of hydrogen-bonded HFIP chains than for isopropanol chains: Non-bonded, terminal OD groups (β) have a blue-shifted OD(OH) stretch frequency and do therefore not contribute to the main hydrogen-bonded IR bands (see SI Fig 7.6), however hydrogen-bonded molecules at the end (γ) of hydrogen-bonded chains are spectrally less shifted than OD groups in the middle (δ) of the chains as well as branching molecules (ϵ).[11, 238] These different subspecies therefore contribute to inhomogeneous broadening of the main, hydrogen-bonded OD peak. The ratio of these subspecies is linked to the size of the aggregates: longer chains are dominated by δ, while short chains have significant contributions from γ and more branched chains from ϵ and γ motifs. The vibrational lifetimes of these different species have been suggested to differ.[11, 238, 239] As such, different hydrogen-bonded chain lengths will results in differing heterogeneities in the signal decay times: The more heterogeneous decay times for HFIP support the notion that HFIP forms smaller clusters than isopropanol.

7.6.6 Hydrogen-bonding energies from DFT calculations

To computationally asses the differences in hydrogen-bond donor and acceptor strengths, we calculated the interaction energies of hydrogen-bonded dimers using DFT. Note that these energies are solely based on the electronic single point energies (see below for Cartesian coordinates and single point energies) and are not

corrected for zero point energies, vibrational, or entropic terms. As such, these calculations merely serve for qualitative comparison of trends in the hydrogen-bond donor and acceptor abilities of the alcohols. As apparent from these calculations in Figure 7.15, the hydrogen-bonding energies between two isopropanol and two HFIP molecules are comparable. These similar interaction energies are, however, a result of HFIP being a poorer hydrogen-bond donor (reduced interaction energy for isopropanol donating a hydrogen-bond to HFIP) and the enhanced hydrogen-bond donor strength (enhanced interaction energy of HFIP donating a hydrogen-bond to isopropanol) relative to isopropanol-isopropanol hydrogen-bonding. The enhanced hydrogen-bond donor strength of HFIP relative to isopropanol is further illustrated by the more favorable interaction with diethylether (Figure 7.15).

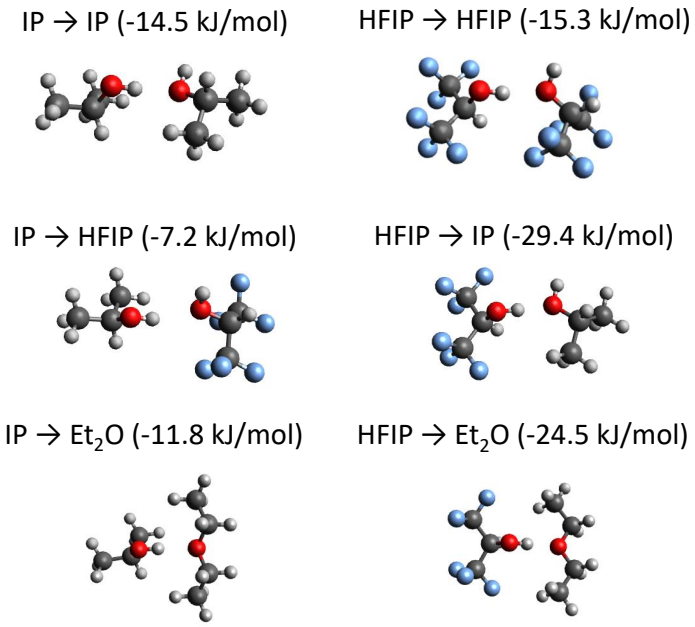

FIGURE 7.15: DFT-optimized geometries of hydrogen-bonded dimers of isopropanol (IP) and hexafluoroisopropanol (HFIP). Top row: homo-dimers; center row: hetero-dimers; bottom row: alcohol-diethylether dimers. Arrows indicate hydrogen-bond donation. Energies in parentheses refer to interaction energies as obtained from the DFT calculations (see text). Reproduced from [2].

7.6.7 Association constants obtained from linear IR spectra

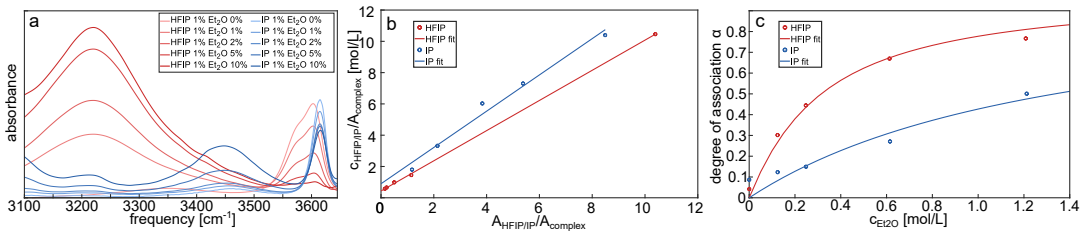

FIGURE 7.16: a) IR absorption spectra of 1 mol% HFIP (red)/isopropanol (blue) (IP) in chloroform with increasing amounts of diethylether as hydrogen-bond acceptor. Data show spectra with a scaled solvent background subtracted. b) Plot of $\frac{c^0_{\mathrm{HFIP/IP}}}{A_{\mathrm{complex}}}$ vs $\frac{A_{\mathrm{HFIP/IP}}}{A_{\mathrm{complex}}}$ with a linear regression according to equation 7.19 to obtain extinction coefficients. c) Degree of association as a function of diethylether concentration. Symbols show data extracted from spectral amplitudes and solid lines show fits with the bimolecular association model (Equation 7.15). Reproduced from [2].

Figure 1 in the main manuscript shows linear absorption spectra of HFIP (blue) and isopropanol (red) at 1, 2, 5, and 10 mol% in chloroform. For HFIP we observe a peak at 3600 cm^{-1}, which corresponds to the free OH peak. At higher HFIP concentrations a red shifted shoulder appears at about 3400 cm^{-1}, that is likely caused by self association of HFIP molecules. For low concentrations of isopropanol the spectrum is also dominated by the free OH peak at about 3615 cm^{-1} but with increasing concentration a bonded peak at about 3400 cm^{-1} grows in. Together the spectra show that self association is much more favourable for isopropanol compared to HFIP, where even at 10 mol% the free form still dominates. This can be explained with HFIP being a much weaker hydrogen bond acceptor.

To quantify the hydrogen-bonding of the alcohols to a representative interaction motif of a reactant we measured linear absorption spectra of HFIP and isopropanol with increasing concentrations of diehylether dissolved in chloroform (see Figure 7.16). From these spectra we calculate the association constants for alcohol-diethylether association using a bimolecular association model (Equation 7.15).[243]

$$K_{\mathrm{ass}} = \frac{[complex]}{[HFIP/IP][Et_2O]} \tag{7.15}$$

with the association constant K_{ass}, the equilibrium concentration of the alcohol-diethylether complex $[complex]$ and the equilibrium concentrations of the free alcohol, $[HFIP/IP]$, and free diethylether $[Et_2O]$. To relate the measured absorption A (average absorption for HFIP bonded: 3100-3500 cm^{-1}, HFIP free: 3520-3630 cm^{-1}, IP bonded: 3300-3570 cm^{-1} and IP free: 3570-3640 cm^{-1}) to the concentrations of free and complexed forms we use Beer-Lamberts law (see Equation 7.16 and 7.17).

$$A_{\mathrm{HFIP/IP}} = \epsilon_{\mathrm{HFIP/IP}} \cdot [HFIP/IP] \cdot d \tag{7.16}$$

$$A_{\mathrm{complex}} = \epsilon_{\mathrm{complex}} \cdot [complex] \cdot d \tag{7.17}$$

with the sample thickness $d = 200\ \mu$m. To obtain the extinction coefficients $\epsilon_{\mathrm{HFIP/IP}}$ and $\epsilon_{\mathrm{complex}}$ we substitute Equation 7.16 and 7.17 into the relation for the total alcohol concentration $c^0_{\mathrm{HFIP/IP}}$ Equation 7.18. To determine the total alcohol concentration we assume ideal mixing (volumes).

$$c^0_{\mathrm{HFIP/IP}} = [HFIP/IP] + [complex] \tag{7.18}$$

yielding Equation 7.19:

$$\frac{c^0_{\mathrm{HFIP/IP}}}{A_{\mathrm{complex}}} = \frac{1}{\epsilon_{\mathrm{HFIP/IP}} \cdot d} \cdot \frac{A_{\mathrm{HFIP/IP}}}{A_{\mathrm{complex}}} + \frac{1}{\epsilon_{\mathrm{complex}} \cdot d} \tag{7.19}$$

From linear regression of $\frac{c^0_{\mathrm{HFIP/IP}}}{A_{\mathrm{complex}}}$ vs $\frac{A_{\mathrm{HFIP/IP}}}{A_{\mathrm{complex}}}$ (Figure 7.16 b) we obtain the extinction coefficients from the slope and the intercept. Using these extinction coefficients we determine the equilibrium concentrations of free and complex species at each concentration.

To finally obtain the association constants K_{ass} we plot the degree of association α (see Equation 7.20) vs concentration of diethylether $c^0_{Et_2O}$

$$\alpha = \frac{[complex]}{c^0_{HFIP/IP}} \tag{7.20}$$

and fit

$$\alpha = \frac{1}{2 \cdot K_{\mathrm{ass}} \cdot c^0_{\mathrm{HFIP/IP}}} \left(K_{\mathrm{ass}} \cdot c^0_{\mathrm{HFIP/IP}} + K_{\mathrm{ass}} \cdot c^0_{\mathrm{Et_2O}} + 1 - \sqrt{K^2_{\mathrm{ass}} \cdot {c^0_{\mathrm{HFIP/IP}}}^2} \right.$$
$$\left. \frac{}{-2K^2_{\mathrm{ass}} \cdot c^0_{\mathrm{HFIP/IP}} \cdot c^0_{\mathrm{Et_2O}} + 2K_{\mathrm{ass}} \cdot c^0_{\mathrm{HFIP/IP}} + K^2_{\mathrm{ass}} \cdot {c^0_{\mathrm{Et_2O}}}^2 + 2K_{\mathrm{ass}} \cdot c^0_{\mathrm{Et_2O}} + 1} \right) \tag{7.21}$$

which is based on Equation 7.15 and 7.20 and mass conservation (Figure 7.16 c). Form these fits we obtain the association constants $K_{\mathrm{ass}}(\mathrm{IP}) = 0.8\ \frac{\mathrm{L}}{\mathrm{mol}}$ and $K_{\mathrm{ass}}(\mathrm{HFIP}) = 3.9\ \frac{\mathrm{L}}{\mathrm{mol}}$.

7.6.8 Optimized Cartesian coordinates obtained from DFT calculations

IP-IP dimer

```
IP-IP
FINAL SINGLE POINT ENERGY      -388.619213507818
  C   -0.69936655532737      1.07606519496207     -0.09622805530488
  C   0.78489238171738      0.78701168794454      0.08863420740594
  O   -1.17523930493686      1.64926212534575      1.13277625415041
  C   -1.49584653205521     -0.17617820716148     -0.46562742101847
  H   -0.81645985887085      1.81749659548525     -0.89997331556071
  H   0.93331541099217      0.05916807360746      0.89294664251117
  H   1.32607145813287      1.70118978945119      0.34664669194275
```

```
  H   1.21496765119488      0.37860536811464     -0.83005720698014
  H   -1.38941247255697     -0.93876832040834      0.31266098161560
  H   -1.14046575081378     -0.59492155215849     -1.41254600109740
  H   -2.55871917584989      0.05740624042420     -0.57784475242920
  H   -2.09959694170397      1.93541205123738      1.01310227694594
  O   -3.89858205355720      2.48066447641060      0.91871533713185
  C   -4.31674114241165      3.85084108447949      1.15181847999359
  H   -4.06964197452041      4.10940144594221      2.18941444390774
  C   -5.82118839086317      3.99094319468466      0.94360189222126
  C   -3.50140891262995      4.72443638936233      0.21057195296744
  H   -4.43240645881561      1.89763218462825      1.47292799451798
  H   -2.43108526313231      4.58263320480761      0.37917284726004
  H   -3.73832466946646      5.77851512493960      0.37665226104833
  H   -3.72695117020319      4.47899958186183     -0.83173899162535
  H   -6.37321795739653      3.32777166183926      1.61735829909176
  H   -6.09184431721580      3.74358451443778     -0.08738496173769
  H   -6.13922799970997      5.01711808976205      1.14985014304201

IP-IP constrained
FINAL SINGLE POINT ENERGY      -388.613688137588
  C   23.83564628933190    -10.60939752523594     -1.94286903133818
  C   25.24203896463911    -11.18022184729525     -1.83109662529407
  O   23.48054199700651    -10.12321417956266     -0.63018392250014
  C   22.81808815915103    -11.63422355679222     -2.43893150782209
  H   23.85061307224656     -9.75741372991140     -2.63656425996759
  H   25.25686695623476    -12.02584744031881     -1.13635990665671
  H   25.93916328083676    -10.42072881853356     -1.46798253692323
  H   25.58970476082298    -11.52857389035100     -2.80730230745933
  H   22.79020451173745    -12.50147205111321     -1.77186669429012
  H   23.07786779858375    -11.97739303263983     -3.44497505242807
  H   21.81480723074515    -11.19804162169246     -2.48210582075359
  H   22.58733729363151     -9.76168574600163     -0.67124943481967
  O   -3.68667892146827      2.53241767247209      0.70289070928730
  C   -4.19773555119415      3.83115369196195      1.07383947174472
  H   -3.79945422932807      4.09109211249886      2.06433291703520
  C   -5.72320358186750      3.81750414319126      1.14049981242012
  C   -3.65941348807919      4.81983923961759      0.04964694935222
  H   -4.00553572852136      1.88628991360863      1.34401435379321
  H   -2.56683360699579      4.79698607256706      0.02877279022294
  H   -3.97815821848831      5.83586381409042      0.29720094489766
  H   -4.03147761240843      4.57426424320252     -0.94992661123641
  H   -6.07497711131860      3.07786269888089      1.86701024792149
  H   -6.14742511335334      3.57091885645821      0.16223775906279
```

```
  H   -6.10318715194576      4.79657098089891      1.44773775575159
```

HFIP-HFIP dimer

```
HFIP-HFIP
FINAL SINGLE POINT ENERGY     -1579.518435370187
  C   -1.21977430062144      0.87168568339964     -0.22449485363802
  C   0.21322632316142      1.34570146632308     -0.53677461966691
  O   -1.47756987859573      1.10095252263753      1.12978733672660
  C   -1.45768951455938     -0.62049890477287     -0.53167198989732
  H   -1.88308912820445      1.43664131506583     -0.88642889969136
  F   1.14204554514102      0.70192177451243      0.19393727087255
  F   0.32291729571062      2.65964143805045     -0.26009095706923
  F   0.52714518085489      1.17997589229054     -1.83761042149995
  F   -0.69665315715443     -1.43255996153550      0.22463606987772
  F   -1.22089002185204     -0.92077918405583     -1.82385614163889
  F   -2.74722082921350     -0.92505563844992     -0.27770328512917
  H   -2.27106381154545      1.65562652340256      1.22442268203473
  O   -3.85517071009938      2.58174504684350      1.63832589576068
  C   -4.28483964911913      3.91066157932941      1.45667067389144
  H   -4.69780496994620      4.33894261390585      2.37405290543060
  C   -5.41256246846787      3.93771708858067      0.40356842095816
  C   -3.06074855183896      4.76741784709334      1.08072563119452
  H   -4.22220935986964      2.22673460885959      2.45859156278688
  F   -2.13174336773114      4.67115014565200      2.04853938698181
  F   -3.39026267920076      6.06525973454850      0.95355235593431
  F   -2.49036940800757      4.37224536497365     -0.07211005209974
  F   -6.43343289555767      3.17113677024478      0.83454157314540
  F   -5.02149959931389      3.45572797304961     -0.78882289147427
  F   -5.88722004396671      5.18229830004880      0.21366234620903

HFIP-HFIP constrained
FINAL SINGLE POINT ENERGY     -1579.512592590798
  C   16.66041009690571    -19.20335815874020      0.73045061354281
  C   16.66027872560048    -20.58884657361490      1.40818495800954
  O   16.33566054818867    -19.36445071392096     -0.62409466154296
  C   18.01044095590059    -18.46436694478075      0.82352349086348
  H   15.93285587017255    -18.59329552236888      1.27364163374089
  F   17.54595337116926    -21.43828018781074      0.85817806394806
  F   15.43768428234048    -21.14264232802039      1.28541930030836
  F   16.93505823004602    -20.50386978034437      2.72439585182861
  F   18.99792037810939    -19.10704128270426      0.17565168276430
  F   18.40152407272618    -18.28709895174277      2.10071859811523
```

```
  F   17.88803958975570   -17.24369399020625     0.26462207426217
  H   15.51358921612790   -18.89867317632465    -0.81793338694576
  O   -3.28265382108453     3.33074035943092    -0.40039175122118
  C   -3.79425635788471     3.97764497720586     0.73273749649698
  H   -3.69920877253608     5.06662610457327     0.68172241023811
  C   -2.95440447135381     3.52196046211452     1.93983530229162
  C   -5.30242537346299     3.67280598914801     0.86678540470443
  H   -3.22780961276004     3.95619925311973    -1.13289457762644
  F   -5.93040178376661     4.07204779590755    -0.25927710573135
  F   -5.86385718813287     4.33189141707142     1.89861874525800
  F   -5.55860834532717     2.36299590348052     1.02709122574296
  F   -1.67834356139069     3.92349518661698     1.77595852266438
  F   -2.94120783147716     2.18548956111795     2.08463635780277
  F   -3.40324821787847     4.05672060080689     3.09149975048330
```

IP-HFIP dimer

```
IP-HFIP
FINAL SINGLE POINT ENERGY      -984.065846174991
  C   -0.62312235970652     0.93413311682941    -0.27364869632303
  C   0.72737444781040      0.26613123131461    -0.05488346468402
  O   -0.91593619136553     1.68379426831313     0.92230562160235
  C   -1.73392955223948    -0.07016725313557    -0.57666592512935
  H   -0.54048369915374     1.63660237683560    -1.11470262451543
  H   0.67367704561888     -0.43792734279000     0.78172734682515
  H   1.49510577611466      1.01143365641079     0.16856371214305
  H   1.03111961366623     -0.28406290912315    -0.94956083423422
  H   -1.83148634849827    -0.79090016347149     0.24139921428507
  H   -1.51558602710336    -0.61865434928172    -1.49822255521262
  H   -2.69433334751510     0.43802955956664    -0.70741307432043
  H   -1.76342299808901     2.13655676153342     0.81162707152753
  O   -3.55130029193381     2.98446215537848     1.56004571000181
  C   -4.44783959685349     4.04557482545216     1.35234686316433
  H   -4.87925717313574     4.42029775784734     2.28461409745497
  C   -5.62265168687856     3.53813928412480     0.49251445488176
  C   -3.67096107919406     5.21984914263688     0.72420905036992
  H   -3.54228610061780     2.74009066525194     2.49364334858467
  F   -2.73197843396281     5.64483826043509     1.59204255546824
  F   -4.47203205224778     6.26639377765242     0.45061774724610
  F   -3.04559698639423     4.87145486647137    -0.41433524160899
  F   -6.24039001347196     2.52796726106479     1.13705914367982
  F   -5.22195064951639     3.07014067103126    -0.70315273720056
  F   -6.53921229533193     4.50011237965123     0.27531921599378
```

```
IP-HFIP constrained
FINAL SINGLE POINT ENERGY      -984.063109080579
  C   18.52016103599816    -18.05807429722210     -4.32553648231809
  C   19.66996485015529    -18.08643160297887     -3.32908840835925
  O   17.56885016367045    -17.09011244121816     -3.83178232645019
  C   17.86299054262343    -19.42412162803238     -4.51059845383638
  H   18.89832577579174    -17.70974913526479     -5.29659337749148
  H   19.31795183073667    -18.42315049813787     -2.34897018503560
  H   20.10797625980878    -17.09129367680191     -3.21736732598181
  H   20.45150328222338    -18.77078538256839     -3.66978982324911
  H   17.48387532430415    -19.79992479605318     -3.55517580906032
  H   18.58349971162621    -20.14596255338650     -4.90706329835559
  H   17.02718053443264    -19.36285735936337     -5.21509241023411
  H   16.82786657688522    -17.05035828238127     -4.44790750669768
  O   -3.14858415552753      3.86429709795134      1.79854926867189
  C   -4.45173303456334      4.20984477091422      1.41535784812217
  H   -5.14678819829733      4.24896162052245      2.25921063840686
  C   -4.99841378449443      3.14377113993957      0.44138412504636
  C   -4.40479479782814      5.63015192488101      0.81845283210095
  H   -3.15450966961653      3.52824617351991      2.70262935929274
  F   -4.01747184150117      6.50475280723089      1.76749288890614
  F   -5.61267574204974      6.02617535347456      0.37189346784774
  F   -3.53556474318125      5.73356816300788     -0.20141217358070
  F   -4.95377140601662      1.93366907037810      1.03534686029074
  F   -4.28211582502623      3.06240812613931     -0.69404522910445
  F   -6.28095269016048      3.37939540545522      0.10423552107085
```

HFIP-IP dimer

```
HFIP-IP
FINAL SINGLE POINT ENERGY      -984.074369320203
  C   -1.09065565238304      0.87947977561398     -0.05793176721708
  C   0.36863479506192      1.32056531586787     -0.27963943023953
  O   -1.48638740906151      1.29316616676160      1.21131067489145
  C   -1.29708388801232     -0.64410186314144     -0.20413703365644
  H   -1.67609749215834      1.34429515120168     -0.85883917051827
  F   1.20412950192653      0.85182653222878      0.66532554778780
  F   0.44069522118517      2.66702249432425     -0.24774066792434
  F   0.84422038333189      0.92125635795811     -1.47764847171889
  F   -0.53398500224393     -1.36381530261830      0.63996024826185
  F   -1.03705519928097     -1.07540151702637     -1.45583500718414
  F   -2.58486891806907     -0.94507621227480      0.06206794869141
  H   -2.34809677643249      1.77076320158340      1.14860012076108
```

```
  O   -3.89423298105449      2.48147446705118      0.96739319854648
  C   -4.27913500815622      3.86470451865496      1.21359357377365
  H   -4.35689357610091      4.00139121671844      2.29879497067357
  C   -5.62911155065311      4.15246858416655      0.56669079663063
  C   -3.15859146297690      4.73876314256217      0.67383198879833
  H   -4.59053753720089      1.89837275858283      1.29582402401530
  H   -2.20809770743792      4.49988183505545      1.15707397901250
  H   -3.38392433824501      5.79106904154257      0.86454595468366
  H   -3.04865295384973      4.59993906779774     -0.40592872291847
  H   -6.40092813767017      3.48046280169932      0.95488262734930
  H   -5.57029504544069      4.02679908091357     -0.51851853182653
  H   -5.93952926507743      5.17898338477619      0.78177314932659

HFIP-IP constrained
FINAL SINGLE POINT ENERGY      -984.063156029618
  C   15.84347739610987    -19.86125446468805     -5.33506584577116
  C   15.65401198893107    -20.11733749574924     -3.82443229989959
  O   14.88449837330096    -20.58811047384026     -6.05407215571630
  C   17.23170646745697    -20.26412794203553     -5.86704632365574
  H   15.75658880888548    -18.78068318856447     -5.48172171150560
  F   15.79080923101437    -21.41430716142465     -3.49680526001818
  F   14.40969233035113    -19.73812527708710     -3.46793108832471
  F   16.51814118410084    -19.40766316666872     -3.07410196471584
  F   17.45591637956782    -21.58661624206630     -5.77828691364702
  F   18.22158807955228    -19.63250914776136     -5.20614996794285
  F   17.33137732541031    -19.92387857462147     -7.16683201373114
  H   14.17202367053256    -19.99929230037722     -6.33085119922671
  O   -3.56597530439434      2.08057673670079      0.70689214985591
  C   -3.83976254914257      3.48938561488102      0.54300578404576
  H   -2.95756666013221      3.96415999760546      0.09193440168843
  C   -4.12493043381635      4.15065228310686      1.88954777002259
  C   -5.00873946840545      3.59799730755885     -0.42538249333270
  H   -2.81999454901678      1.98436306415931      1.31069701832332
  H   -4.77176372241929      3.10864296903098     -1.37356480626967
  H   -5.23867012569068      4.64758930958638     -0.62726600495812
  H   -5.90001096293711      3.12378457067088     -0.00264879591203
  H   -3.27642283537550      4.03125064091635      2.57096710096078
  H   -5.00896932177658      3.70501337057812      2.35621751252948
  H   -4.30305530211751      5.22259957010356      1.76056710720519
```

IP-Et_2O dimer

```
IP-Et2O
```

```
FINAL SINGLE POINT ENERGY      -427.898517826805
  C   -0.89284384738190      0.91701909682353     -0.14084997555989
  C   0.60699094407371       1.03788059606186     -0.37919430598540
  O   -1.23452845501866      1.86258813365892      0.88723811788765
  C   -1.30764593267027     -0.50127739546973      0.25266728134850
  H   -1.42037897357052      1.19522040863256     -1.06444904101852
  H   1.15858443499814       0.78119601158644      0.53102902279031
  H   0.87098593276020       2.05908319286273     -0.66636809346347
  H   0.92540128668503       0.36144579078092     -1.17716604147839
  H   -0.78481684855538     -0.81252955106784      1.16268796050561
  H   -1.06477125896752     -1.20923913006467     -0.54608198791442
  H   -2.38443456555382     -0.55591069515311      0.43703971285909
  H   -2.20356600835876      1.90184478983886      0.97841617153218
  H   -2.95727162151388      0.85876693788540      3.26040244965723
  H   -3.10169193642577      3.25254675313704     -1.03327382041750
  H   -4.09637706208062      3.10014089024825      3.13919147660379
  H   -4.16399326339993      4.29681512762909      0.99514809204526
  C   -4.04694780037980      0.93724457992327      3.27928133020931
  C   -4.51434833311869      2.22401271328307      2.62451198816309
  O   -4.09939180467994      2.23956078165782      1.25182306850187
  C   -4.18818512879950      3.28130714209659     -0.92000372565741
  C   -4.58271428462955      3.38790031771947      0.54157614821638
  H   -4.37308957396725      0.91679850273561      4.32296377845838
  H   -4.56514996579240      4.14993861972080     -1.46715773595533
  H   -4.46889525504496      0.06619862194189      2.77100769178921
  H   -4.61154295234536      2.38086583082704     -1.37300577576351
  H   -5.60904829512250      2.30295558066901      2.66395339991921
  H   -5.67504943113970      3.43424635203493      0.64505281272668

IP-Et2O constrained
FINAL SINGLE POINT ENERGY      -427.894019901879
   C   22.23852150619493     -9.82217359611176     -9.69485227720503
  C   23.75545322880639     -9.90099492543079     -9.78936329131254
  O   21.93883284415675     -8.90610819253626     -8.61931888690257
  C   21.58868641059225    -11.18198049260186     -9.44964644525703
  H   21.84405361431071     -9.40116554486828    -10.62993280754424
  H   24.17484404092586    -10.30750825490676     -8.86375930775382
  H   24.18355855242675     -8.90955407251162     -9.95804656220332
  H   24.05218979123300    -10.54981508370800    -10.61770951514230
  H   21.97124062091125    -11.62826858544183     -8.52646151582136
  H   21.79993322239795    -11.86346480068176    -10.27925922281995
  H   20.50156019680618    -11.08539532162254     -9.36324707649284
  H   20.98043059353737     -8.83622015859324     -8.53742395911800
```

```
  H   -2.80023274921429      0.87232866469991      3.11078475079322
  H   -3.18353119966985      3.06980595902708     -1.10165796548423
  H   -3.92247873706430      3.12003496921269      3.03919231736734
  H   -4.11559458815354      4.22306158070415      0.92753309655387
  C   -3.87826768844083      0.96653512461688      3.26702196570221
  C   -4.40885461856761      2.23000736277459      2.61358408656072
  O   -4.15031303487748      2.17122131547458      1.21171551239207
  C   -4.26284316725546      3.17514475824749     -0.96242752295291
  C   -4.60091337774186      3.32877976424257      0.50971237694625
  H   -4.06799677832664      0.99396831014359      4.34384675010344
  H   -4.59740081052715      4.05570229830867     -1.51815774930267
  H   -4.36799872273303      0.08019514616143      2.85478131835162
  H   -4.75509384261100      2.29486939924267     -1.38451528545109
  H   -5.49089206334030      2.33049831798668      2.78378670367568
  H   -5.68573324377635      3.44456605817175      0.64984051231763
```

HFIP-Et_2O dimer

```
HFIP-Et2O
FINAL SINGLE POINT ENERGY     -1023.352851163025
  C   -1.47642211292352      1.02125594229483      0.19465006554473
  C   0.03345435898455      1.31385655630836      0.34339012404000
  O   -2.09124221246915      1.15538347417714      1.43663124828372
  C   -1.77105939625690     -0.38708283202104     -0.36405856267769
  H   -1.85614051852696      1.72820804092600     -0.55070845270160
  F   0.59879511320928      0.61408919709600      1.34281592305322
  F   0.20746498177244      2.62372053909168      0.62408270215229
  F   0.72818177310840      1.05170826261847     -0.78273100504963
  F   -1.23243280517754     -1.37202619145145      0.38061512481911
  F   -1.31190494138992     -0.53407036646079     -1.62473917437778
  F   -3.10213265064943     -0.59112575413181     -0.39826784718479
  H   -2.67043420886327      1.95172346112169      1.45543086785331
  H   -1.22927141976710      4.35761728379878      2.08771686337866
  H   -4.71745549363389      2.14072232020190     -0.54902268895811
  H   -3.50809526951754      5.40264287416689      1.88650353066819
  H   -5.20389850192595      4.33227880238687      0.59375115837860
  C   -1.92213719420274      4.36479052642243      2.93188913026648
  C   -3.35948980084847      4.48045127318052      2.46304080566964
  O   -3.70047939322597      3.35934532053815      1.62849356062472
  C   -5.37076843275490      2.18994265861458      0.32609027581570
  C   -5.06260651091635      3.40993440065518      1.17198193080793
  H   -1.68020307927864      5.22347355173158      3.56441052740530
  H   -6.40492100537913      2.24438427965285     -0.02493245231767
```

```
  H   -1.76914961196024      3.45591080758584      3.51914871958577
  H   -5.25485566149292      1.26929060830855      0.90307566753305
  H   -4.04742596853197      4.50292137264816      3.31807298715797
  H   -5.72529003738183      3.45517359053839      2.04589897022878


HFIP-Et2O constrained
FINAL SINGLE POINT ENERGY     -1023.343517730692
  C   6.67848220506168    -10.69073148998833     -0.93949738773285
  C   8.14003654362411    -10.20305871659830     -0.84678529592435
  O   6.13155104209740    -10.76008092224776      0.34942194355856
  C   6.52007841741618    -12.07648301269001     -1.59430878223481
  H   6.15350570806159     -9.98236506054925     -1.58721842033761
  F   8.90509418102957    -10.99580494501726     -0.07596720188513
  F   8.15680268022777     -8.96926725045808     -0.30013920619636
  F   8.72387154988644    -10.11575071491773     -2.05693883734824
  F   7.11003742514084    -13.05636695241471     -0.88731445913508
  F   7.03293748727703    -12.10297152513420     -2.83923157915582
  F   5.21004298644117    -12.37733062185516     -1.68983261745818
  H   5.54514803928009    -10.00816466492121      0.49449751045311
  H   -8.06837192028043     14.85502171070458      3.62222329319940
  H   -11.58882743435081     12.77649939233651      1.10969234594562
  H   -10.28427910759036     16.03258110978140      3.46179217470307
  H   -12.04022542022132     14.99587963432502      2.20182385733524
  C   -8.73198024706948     14.92480672708242      4.48834559540402
  C   -10.17373306332983     15.11028727199021      4.05090047437674
  O   -10.57005269776776     13.99033923406838      3.26028676035751
  C   -12.24885573888424     12.85168303471080      1.97813308893140
  C   -11.91856321453558     14.08264801955997      2.80281027760646
  H   -8.41390542195167     15.77645994345587      5.09644889015089
  H   -13.28109349664985     12.90741891807151      1.62084089033174
  H   -8.62036602881671     14.01597218019350      5.08584612566331
  H   -12.14135164039756     11.94250758199635      2.57584784711548
  H   -10.83647533213919     15.19487640296591      4.92471908289853
  H   -12.59425750155781     14.16322471554852      3.66702362937677
```

Chapter 8

Deciphering Spectroscopic Signatures of Competing Ca^{2+} - Peptide Interactions

Krevert, C. S.; **Gunkel, L.**; Sutter, J.; Meyer, R.; Schneider, P.; Nagata, Y.; Hunger, J.
The Journal of Physical Chemistry B **2024**, *128*, 10688–10698.[3]
DOI: 10.1021/acs.jpcb.4c04760

C.S.K and J.H. designed the research project. C.S.K. prepared the samples. C.S.K. and P.S. measured the linear IR spectra; C.S.K. and L.G. measured the 2D IR data. C.S.K. analyzed and interpreted the spectroscopic data. J.S. performed the DFT calculations. R.M. prepared the 13C-labeled peptide sample. Y.N. performed the MD simulations. Y.N. and L.G. evaluated the simulation data. All authors discussed the results. C.S.K., L.G. and J.H. wrote the manuscript. C.S.K. and L.G. contributed equally.

8.1 Abstract

Calcium-protein interactions are of paramount importance in biochemistry. They are a key element in a number of biological processes, such as neuronal signaling. Therefore, an understanding of the interaction at the molecular level is highly desirable. Here, we study the zwitterionic model peptide L-alanyl-L-alanine (2Ala), which has two distinct and competing binding sites for Ca^{2+}: The carbonyl of the peptide bond and the C-terminus, the carboxylate group. We perform linear and two-dimensional IR spectroscopy experiments and find that the spectroscopic signatures of both moieties in the IR spectra change in amplitude and peak position upon the addition of $CaCl_2$: A blueshift of the asymmetric carboxylate band and a redshift for the amide I mode. *Ab initio* molecular dynamics simulations confirm the direct interaction of the Ca^{2+} ion at both the carboxylate and the amide CO site leading to different spectral responses. The blueshift of the asymmetric carboxylate band is caused by a localization of the charge, leading to a decoupling of the CO stretching modes of the carboxylate group. The slight redshift of the amide I mode

of 2Ala upon the addition of $CaCl_2$ contrasts the blueshift that has been observed for isolated amide motifs, such as *N*-methylacetamide (NMA). This difference is caused by the lower amount of water molecules being replaced by the Ca^{2+} ion for 2Ala's amide compared to less sterically hindered, isolated amide carbonyls, in conjunction with vibrational Stark effects. Our results highlight the importance of considering potential competing binding sites, such as the amide CO backbone, the termini and residues, as well as the nature of the hydration of both peptide and ion, when exploring ions' interacting with small peptides and larger proteins.

8.2 Introduction

Since the seminal work by Hofmeister in 1888[62] the interaction of ions with peptides and proteins in solution has been intensively studied. [4, 63, 65, 68, 69, 72, 125, 245–254] Among cations, bivalent cations have been shown to markedly interact with proteins and peptides.[72] Protein-cation interactions are utilized by nature in a plethora of biochemical processes, such as in signaling by ions or metal ions as enzymatic cofactors. [74–76] In particular, the ubiquitous divalent cation Ca^{2+} plays an important role in many biologically relevant processes.[255] Calcium ions bind to proteins, causing them to change in their three-dimensional structure. This alteration in protein conformation indirectly regulates cellular processes by affecting protein function, which is crucial for signaling pathways.[255, 256]
To understand the effect of Ca^{2+} on the conformation of proteins,[256] it is quintessential to understand the interaction of Ca^{2+} with proteins on a molecular level. However, the molecular details of such ion-protein interactions in aqueous environments are highly complex. These interactions involve pair-wise ion-peptide interactions and competing interaction with the solvent water (i.e., the hydration of the ion and the peptide). [257]
Vibrational spectroscopies have offered valuable insights into ion-protein interactions at elevated salt concentrations since the amide I (CO) vibration of the peptide/protein backbone has been shown to sensitively report on variations in its direct vicinity, such as binding of ions. [4, 68, 210, 254, 258] The vibrational response of amides or ketones in the presence of salts has indicated negligible[72, 259] or very moderate[4, 71, 260] effects of monovalent anions and cations on the CO moiety. Similarly, the CO groups of lipids have been shown to be little affected by salts, even for bivalent cations.[74, 75] These minimal ion-specific effects have been associated with weak interaction of these ions with the biomolecules.[72] Conversely, bivalent cations have been demonstrated to markedly shift the CO vibration of isolated CO groups. [68, 69, 71, 72, 254] Although these shifts are most pronounced at high salt concentrations - much higher than physiological concentrations - weak binding has also been inferred at low concentrations.[72] These spectral shifts in the presence of cations with a high surface charge density have been ascribed to a salt-induced variation of the hydration of the CO groups,[68, 69] contact ion-pair formation[72], or

to solvochromatic shifts due to the electric field of the ions exerted on the CO moiety.[71] Interestingly, in contrast to isolated amide moieties, the amide group of short model peptides with adjacent N- and C-termini is rather insensitive to the addition of salts.[4, 261] For instance, experiments studying the effect of $CaCl_2$ on a tripeptide have suggested that one of the two peptide's amide vibrations undergoes a minor redshift while for the other amide vibration, a weak, blueshifted shoulder - similar to the findings for isolated amides - appears.[261] Rather, the carboxylate vibrations of the peptides' C-terminus[4, 261] have been shown to be largely affected by the addition of salts, which can be rationalized by the marked interaction of carboxylates with cations with a high surface charge density.[262, 263] The salt-induced spectral response of the carboxylate resembles findings for oxalate, for which a blueshifted shoulder of the asymmetric stretching vibration is observed upon the addition of salt.[264]

However, the molecular-level origins of the markedly different response of the CO group for isolated CO moieties and peptides have remained elusive. Based on the knowledge for isolated CO groups, the insensitivity of peptides' amide bonds to salts may stem from weaker interaction of ions with the amide CO due to competing interaction sites at the charged termini,[4] differences in the local electric fields experienced by the CO due to the electric fields of the zwitterionic peptide,[71] or due to different hydration of the amide CO in peptides as compared to isolated amide groups.[68]

To elucidate the different behavior of amide groups for isolated amides and peptides, we investigate the effect of $CaCl_2$ (0-5 M) on the zwitterionic model peptide L-alanyl-L-alanine (2Ala) using infrared (IR) spectroscopy by studying the amide I (CO) vibration and the asymmetric carboxylate stretching vibration of 2Ala. With increasing $CaCl_2$ concentration, we find marked spectral changes to the carboxylate mode with a minor redshift at low salt concentrations and the emergence of a blueshifted carboxylate shoulder at high Ca^{2+} concentrations. These spectral changes are also reflected in the spectral dynamics observed by two-dimensional (2D) IR spectroscopy: In the presence of calcium, the carboxylate band becomes more heterogeneous. Conversely, the effect of $CaCl_2$ on the amide I band is less pronounced: We find a moderate redshift of the amide I band, which contrasts the blueshifted vibration observed for isolated amide moieties.[68, 69, 72] 2D IR experiments confirm weak, yet detectable effects of $CaCl_2$ on the vibrational dynamics of the amide CO, predominantly reflected in the vibrational lifetimes. To relate the observed spectral changes to the interaction of ions with 2Ala, we perform *ab initio* molecular dynamics (MD) simulations combined with single point density functional theory calculations. The simulations provide evidence for the direct interaction of Ca^{2+} with both, the CO and COO^- groups of 2Ala, yet with a higher probability for Ca^{2+} - carboxylate than for Ca^{2+} - amide CO interactions. MD simulations show that one or two Ca^{2+} ions bind to the carboxylate, which gives rise to a successive blueshift of the asymmetric

carboxylate mode due to Ca^{2+} lifting the degeneracy of the CO groups of the carboxylate moiety. Our results suggest that the $CaCl_2$-induced red-shift of the amide CO, as opposed to the blueshift of isolated amide motifs, can be attributed to less water molecules being replaced by a Ca^{2+} cation upon direct interaction for the peptide as compared to isolated amides, in conjunction with vibrational Stark effects. Our findings highlight the mutual interplay between ion binding at different binding sites of a peptide and the importance of considering these distinct binding sites within a peptide to understand specific ion effects on peptides and proteins.

8.3 Results and Discussion

8.3.1 Linear IR Spectroscopic Signatures of 2Ala - Ca^{2+} Interactions

To explore the effect of calcium on 2Ala, we study the infrared spectra of 2Ala in D_2O. The IR absorption spectrum of 2Ala (250 mM, black dashed line in Figure 8.1a) shows the asymmetric stretching vibration of the carboxylate group at 1590 cm^{-1} and the amide I (carbonyl stretching) vibration at 1660 cm^{-1}. Upon addition of $CaCl_2$, these spectral signatures undergo continuous variation in amplitude and resonance frequency: The carboxylate band decreases in amplitude, redshifts at low salt concentrations (1 - 3 M) (1) and a blueshifted shoulder emerges at $\sim$1620 cm^{-1} ((2)) at higher concentrations. The amide I band undergoes a small, yet detectable redshift (by about 7 cm^{-1}, (3)) and increases in amplitude. These spectral variations are further illustrated by the difference spectra in Supplementary Figure 4. We note that the spectra in Figure 8.1a have been corrected for a linear background absorption and normalized to the total peak integral to account for minor variations in the concentrations and optical path lengths, yet the observed spectral changes are also evident from the raw spectra (see Supplementary Figure 5, see Supplementary Information for details on the background correction and normalization). The spectral variations are similarly present at lower (50 mM) and higher (500 mM) 2Ala concentrations, indicating that self-aggregation of 2Ala does not contribute to the observed spectral changes (see Supplementary Figure 6). The $CaCl_2$ induced spectral changes are also distinctively different from the effect of pH on the 2Ala vibrations (Supplementary Figure 7), which excludes $CaCl_2$-induced changes of 2Ala's protonation state as cause for the spectral shifts observed in Figure 8.1a. In contrast to the effect of $CaCl_2$ and in line with earlier studies,[69, 72] 2Ala's infrared spectra are not affected by the addition of NaCl (see Supplementary Figure 8). As such, our data suggest that the $CaCl_2$ induced changes to the amide I and carboxylate vibrations in Figure 8.1a originate from the interaction of Ca^{2+} with zwitterionic 2Ala.
To elucidate the molecular origin of the Ca^{2+}-induced shoulder at 1620 cm^{-1}, we performed experiments using $^{13}COO^-$ labeled 2Ala. The IR spectra in Figure 8.1b show that upon isotope-labelling, both the band at 1590 cm^{-1} and the shoulder at

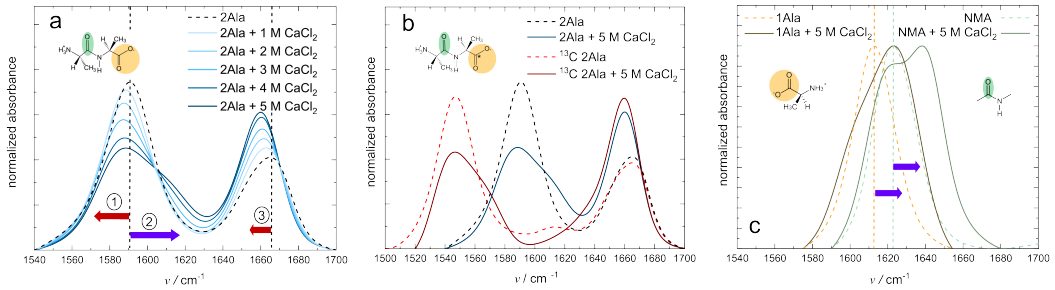

FIGURE 8.1: a) IR spectra of 2Ala in D_2O at frequencies characteristic for the amide I vibration ($\sim$ 1660 cm^{-1}) and for the asymmetric COO^- vibration ($\sim$ 1590 cm^{-1}) with increasing $CaCl_2$ concentration. Vertical dashed lines mark the peak positions in the absence of $CaCl_2$. Red arrows indicate the salt-induced redshift of the amide I band (③) and the asymmetric COO^- (①) at low salt concentrations and the purple arrow the emergence of the blueshifted shoulder of the carboxylate (②) at high salt concentrations. b) Comparison of the IR spectra of $^{13}COO^-$ and $^{12}COO^-$ 2Ala with and without 5 M $CaCl_2$. All spectral contributions at $< 1620\,cm^{-1}$ redshift upon isotopic substitution and are therefore assigned to the COO^- group. All spectra were corrected for a linear background and normalized to the integrated absorbance (see Supplementary Information) c) Linear IR spectra of 1Ala and NMA in D_2O with and without 5 M $CaCl_2$. For 1Ala and NMA addition of $CaCl_2$ blueshifts the COO^- and the amide I band, respectively. Reproduced from [3].

1620 cm^{-1} shift to lower wavenumbers.[265] As such, the isotope-labelling experiments demonstrate that both the band at 1590 cm^{-1} and the higher frequency shoulder can be assigned to the COO^- group, which is further supported by the increase of the shoulder at 1620 cm^{-1} with increasing $CaCl_2$ concentration (see fits of the linear IR spectra, Supplementary Figure 9).

The observed Ca^{2+}-induced spectral shifts for 2Ala contrast the effect of $CaCl_2$ on simpler molecules. Figure 8.1c demonstrates that the amide I mode of *N*-methylacetamide and the carboxylate mode of zwitterionic 1Ala both blueshift upon the addition of $CaCl_2$. The salt-induced blueshift of the amide I mode confirms earlier studies on NMA[68–70] and is in line with findings for N-ethylpropionamide [254], and butyramide.[72]

The observed $CaCl_2$ induced redshift of the amide I vibration for 2Ala is rather similar to the effect of $CaCl_2$ on one of the amide I modes of alanine tripeptide.[261] Such redshifts of amide I modes have been associated with Stark shifts, originating from the electric field due to cations and anions that accumulate at opposite ends of the CO oscillator.[71, 72, 266]

As such, our results show that the effect of $CaCl_2$ on 2Ala distinctively differs from the salt-induced changes to the amide vibrations of isolated amide groups, suggesting differing interactions. Yet, solely based on the IR absorption spectra it remains open whether the observed spectral changes are due to a gradual variation of the solvent environment (e.g. $CaCl_2$ induced dehydration of 2Ala[68, 267]) or due to a concentration-dependent variation of distinctively different molecular species with

different Ca^{2+} - 2Ala binding geometries.[261, 262, 268, 269]

8.3.2 2D IR Spectroscopy of 2Ala and 2Ala - $CaCl_2$ solutions

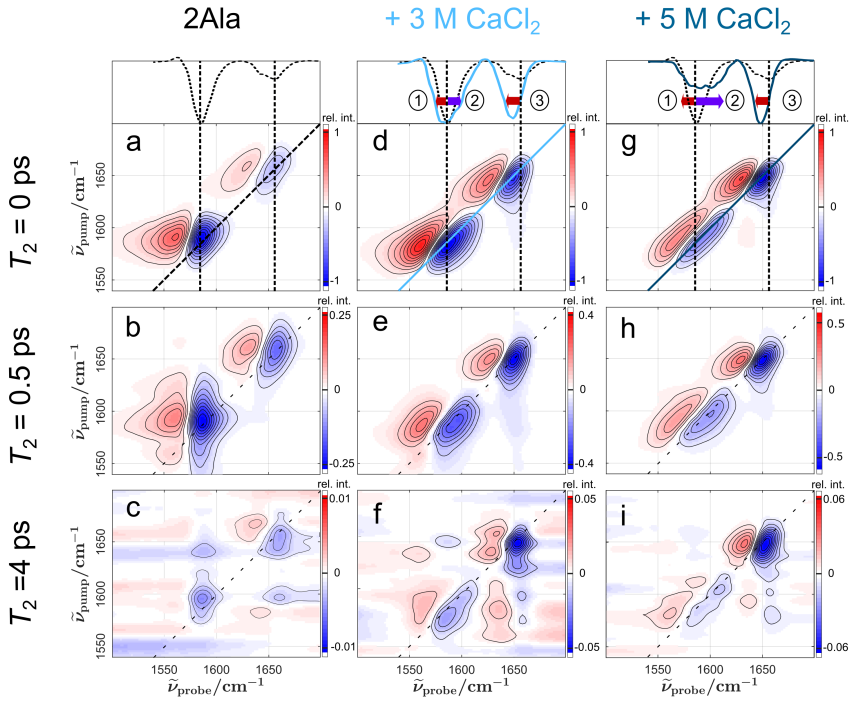

FIGURE 8.2: 2D IR spectra of 2Ala in D_2O (a, b, c) and with 3 M (d, e, f) and 5 M (g, h, i) $CaCl_2$ added at different waiting times T_2 (top to bottom). Top panels show the diagonal cuts of the 2D IR spectra at $T_2 = 0$ ps. The dashed line in the top panels corresponds to the diagonal cut in panel a (2Ala in D_2O). With increasing $CaCl_2$ concentration, the carboxylate band becomes more heterogeneous, as evidenced by the elongation of the carboxylate band at all waiting times. This heterogeneity persists up to $T_2 = 4$ ps (f, i), at which spectra are dominated by signals due to the heated ground state. Red arrows indicate the salt-induced redshift of the amide I band (③) and the asymmetric COO^- (①) at low salt concentrations and the purple arrow the emergence of the blueshifted shoulder of the carboxylate (②) at high salt concentrations. Reproduced from [3].

To spectroscopically decipher different molecular species contributing to the observed vibrational bands, we perform 2D IR experiments. In a 2D IR experiment, a subset of oscillators with a given instantaneous frequency is excited and the sample's response is probed over a broader detection frequency range. In this manner, the heterogeneity of vibrational bands due to inhomogeneous broadening, such as the distribution of molecular level oscillators with differing resonance frequency due to, e.g., differing environments, can be assessed. Probing the molecular response as a function of time can provide information on the dynamics of these differing molecular-level oscillators.[21]

Figure 8.2a shows a 2D IR spectrum of 250 mM 2Ala in D_2O at a waiting time $T_2 = 0$ ps with $< ZZZZ >$ (parallel) polarization combinations. For both vibrational modes, the amide I and the carboxylate band, two signal pairs are detected:

A negative signal at the diagonal due to depletion of the vibrational ground state and stimulated emission from the excited state and a redshifted positive signal due to the anharmonically shifted excited state absorption. The diagonal cut shown in the top panel of Figure 8.2a resembles the squared linear IR spectrum (see Figure 8.1).[21] With increasing time delay between excitation and probe pulse, the signal intensity decreases (Figure 8.2b, c) due to relaxation to the vibrational ground state. Due to the faster relaxation of the carboxylate mode relative to the amide I mode, the decrease in the signal intensity is more pronounced for the signal pair at $1590\,\mathrm{cm}^{-1}$. In addition to the decay of the signal intensity, the shape of the 2D IR signals varies with time: Both signals are elongated along the diagonal at 0 ps waiting time, with the amide I band exhibiting a more pronounced elongation. With increasing T_2 the signals become more vertical, evidencing a loss of correlation of the signal frequency to the excitation frequency. These dynamics are commonly referred to as spectral diffusion. At 4 ps waiting time, where the signals are dominated by thermally induced spectral signatures due to dissipation of the vibrational excess energy (Figure 8.2c), off-diagonal peaks can be observed.
Addition of 3 and 5 M $CaCl_2$ (Figure 8.2d, e, f and g, h, i; for other concentrations see Supplementary Figure 10) to solutions of 2Ala alters these signals: In line with the IR absorption spectra, the relative intensities of the amide I and carboxylate signals are altered. Also the diagonal slices at $T_2 = 0$ ps resemble the spectra in Figure 8.1 with an emerging shoulder at 1620 cm^{-1} (ⓒ) (Figure 8.2d, g) and a redshift of the amide I mode (ⓒ) with increasing $CaCl_2$ concentration.
Remarkably, for high $CaCl_2$ concentrations, in particular at 5 M, the loss of frequency-frequency correlations is slowed down (Figure 8.2 i): The carboxylate and to a lesser extent the amide I signal are markedly elongated along the diagonal at $T_2 = 0.5$ and 4 ps, which contrasts the spectra for 2Ala in D_2O (Figure 8.2a-c). Our data suggest that these changes to the vibrational structure and dynamics are specific to $CaCl_2$, as spectra of 2Ala in the presence of NaCl (Supplementary Figure 11) resemble the spectra of 2Ala in D_2O.

Spectral heterogeneity and dynamics from 2D IR

To further quantify the spectral heterogeneity and their dynamics, we evaluate the center line slope (CLS) for both, the amide I and carboxylate signals. We determine the CLS, a measure for the (time-dependent) spectral heterogeneity, from the minima of the bleaching signals parallel to the probe axis. The minima (center line points) are determined by Gaussian fits to the bleaching signals at frequencies for which the initial ($T_2 = 0$) bleaching signal is less than 10% of the maximum bleaching signal (for details, see Supplementary Figure 12). The slope of linear fits to the center line points as a function of excitation frequency represents the CLS. Here, a CLS of 1 means a perfect correlation between excitation and detection frequencies, while a CLS value of 0 corresponds to uncorrelated frequencies.
We evaluate the instantaneous heterogeneity by extracting the CLS value at T_2 =

0 fs (see Figure 8.3a). To determine spectral diffusion dynamics, we fit a mono-exponential decay with the rate constant k_{CLS} to the time-dependent CLS(T_2) at delay times with sufficiently intense signals ($T_2 \leq 800$ fs for the carboxylate and $T_2 \leq 1$ ps for the amide I mode, see also discussion of vibrational lifetimes below). The thus obtained k_{CLS} values are shown in Supplementary Figure 12.

When $CaCl_2$ is added, we initially observe a decrease in CLS for the amide I mode at T_2 = 0 fs, followed by a subsequent increase of approximately 15%. Yet, the $CaCl_2$-induced change is rather moderate and in line with observations for the interaction of 2Ala with monovalent ions (such as LiCl[4] or NaCl, see Supplementary Figure 13). As such, $CaCl_2$ does not alter the vibrational structure of the amide I mode significantly. However, the CLS(T_2 = 0 fs) for the anti-symmetric stretching vibration of the carboxylate mode shows a significant increase by a factor of $\sim$ 3.5 (from pure 2Ala to 5 M $CaCl_2$ solution). This increase is much more pronounced than for monovalent salts: For LiCl, the instantaneous heterogeneity of the carboxylate mode increases by a factor of $\sim$ 2.5,[4] for NaCl by a factor of 2 (see Supplementary Figure 13). These findings demonstrate a more pronounced spectral inhomogeneity for the carboxylate band in the presence of $CaCl_2$ as compared to NaCl and LiCl, which may point to a broader range of ion-carboxylate interaction motifs or to a stronger interaction and longer-lived binding of $CaCl_2$ to the carboxylate: The data suggest the presence of multiple molecular 2Ala-Ca^{2+} (or 2Ala-Cl^-) species.

To obtain information on the lifetime of the underlying molecular species, one can consider the spectral diffusion dynamics, i.e., the decay rates k_{CLS} of the carboxylate peak. We find that the decay rate decreases continuously upon the addition of $CaCl_2$ (see Supplementary Figure 12), and the decay time ($1/k_{CLS}$) parallels the variation of CLS(T_2 = 0 fs) with $CaCl_2$ concentration. The marked elongation of the signals at $T_2 = 4$ ps (Figure 8.2i) demonstrates that, even at waiting times for which the heated ground state dominates the signals (see also discussion of the vibrational relaxation below), the frequency response is still correlated to the excitation frequency, indicating that the underlying molecular-level species are long-lived and spatially separated: At 4 ps the excess energy (heat) is not transferred between initially excited and initially non-excited carboxylate groups. Interestingly, the slow-down of the spectral dynamics in the presence of $CaCl_2$ is comparable to our earlier findings for LiCl.[4] Conversely, for NaCl only minor changes in the rate constant k_{CLS} up to 20 % are observed (see Supplementary Figure 13).

The similarity for LiCl and $CaCl_2$ indicates slowed-down spectral diffusion dynamics for both highly viscous $\sim$ 5 M salt solutions,[270, 271] yet the altered dynamics do not simply reflect solution viscosity: While the viscosity for aqueous 5 M LiCl solutions increases by a factor of 2 (relative to neat water), the viscosity of a 5 M $CaCl_2$ solution increases by a factor of 5. The rate constants of the decay in CLS of the carboxylate mode decreases by a factor of $\sim$5 for $CaCl_2$, while $k_{COO^-,LiCl}$ decreases by a factor of $\sim$4. Hence, while the decrease in the spectral dynamics can be partly attributed to the increase in viscosity, the dynamics with which the COO^- groups

loose their frequency memory (i.e. the exchange of their environment) differs from macroscopic dynamics: Exchange of environments around COO^- are very similar for LiCl and $CaCl_2$, despite their differing viscosities. Again, the slowed down spectral dynamics evidence the presence of different molecular 2Ala-ion species, which barely inter-convert on the timescale of a few picoseconds.

Vibrational energy relaxation dynamics

To further elucidate different molecular-level species, we consider vibrational energy relaxation dynamics - i.e., the decay of the 2D IR signals with time - in more detail. The vibrational energy relaxation lifetime (τ_{VER}) of each molecular species is a result of the coupling of the vibrational mode to its microscopic environments and may thus differ for different molecular species, which have different environments. To explore whether $CaCl_2$ affects vibrational energy relaxation (the decay of the vibrationally excited state), we integrate the entire bleaching signals for the amide I and the carboxylate signals (for details on the integration, see Supplementary Figure 14). The characteristic relaxation time of the integrated signal is determined by fitting a kinetic model[6] (Equation 8.1) to the evolution of the signal. In this model, the exited state decays with relaxation time τ_{VER} and energy dissipation leads to a persistent modulation due to a heated ground state, with the peak integral of the excited state V_{exc} and the peak integral of the heated ground state V_{heat}:

$$V(T_2) = V_{exc} \cdot e^{\frac{-T_2}{\tau_{VER}}} + V_{heat} \cdot \left(1 - e^{\frac{-T_2}{\tau_{VER}}}\right) \tag{8.1}$$

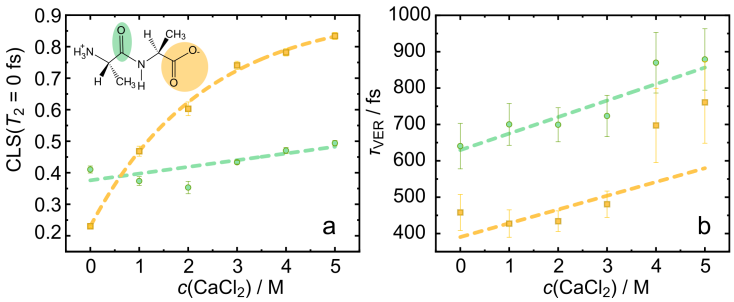

FIGURE 8.3: Concentration-dependence of a) CLS at 0 fs waiting time (instantaneous heterogeneity) and b) vibrational energy relaxation lifetimes τ_{VER} for the amide I (CO, green) and carboxylate peak (COO^-, yellow). Dashed lines serve to guide to the eye. Reproduced from [3].

This model describes the experimental data very well (see Supplementary Figure 14) with $\tau_{VER} \sim 0.46$ ps for the carboxylate mode and $\tau_{VER} \sim 0.67$ ps for the amide I mode[4] for 2Ala in D_2O.[4] With the addition of $CaCl_2$, the vibrational relaxation time increases, for both the amide I and the carboxylate peak (see Figure 8.3b). Interestingly, although the spectral signatures of the amide I peak are little affected by $CaCl_2$, its vibrational energy relaxation dynamics are altered and increase to τ_{VER} = 0.88 ps at 5 M $CaCl_2$. For the carboxylate mode, τ_{VER} nearly doubles from 0.46 ps

(0 M) to 0.76 ps at 5 M. Conversely, vibrational energy relaxation of both modes for 2Ala is virtually insensitive to the addition of NaCl (see Supplementary Figure 15). Although the overall relaxation time only provides the average effect of $CaCl_2$, this analysis demonstrates that $CaCl_2$ alters energy relaxation pathways and the relaxation dynamics have, as such, the potential to discriminate different molecular-level species that contribute to the observed vibrational bands.

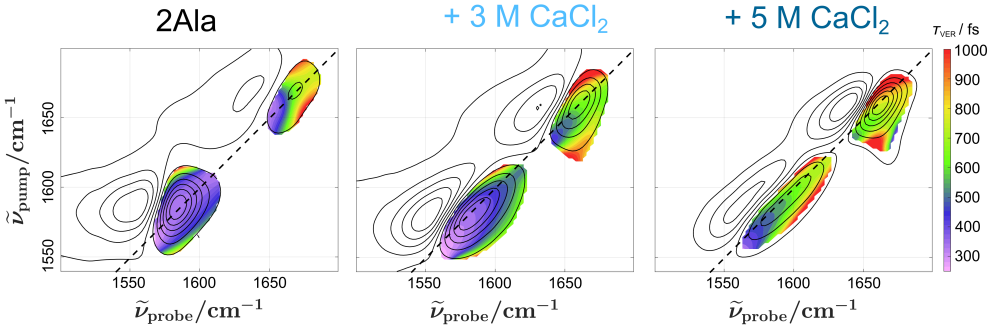

FIGURE 8.4: Decay time maps for 2Ala with 0 M(a), 3 M (b), and 5 M (c) $CaCl_2$ solutions. For each data point shown here, we integrate a 5×5 pixel grid of the 2D IR spectra and fit a mono-exponential decay to a heated ground state (see Equation 8.1) to the waiting-time dependent data. The decay time is shown as color map for all regions in the 2D IR spectra (contour lines) with a maximum bleaching signal exceeding 10% of the global maximum the bleaching signal at $T_2 = 0$ ps. Reproduced from [3].

To elucidate whether distinct molecular species with different vibrational lifetimes underlie the observed changes of the overall τ_{VER} values, we determine decay maps.[210] This is achieved by integrating the signal of a five-by-five pixel grid of the 2D IR spectra and determining the decay time of the signal analogously to the analysis above using Equation 8.1. The thus obtained decay times are shown for spectral regions where the bleaching signal is smaller than 10 % of the maximum bleach at $T_2 = 0$ ps in Figure 8.4 for pure 2Ala in D_2O (a), 3 M $CaCl_2$ (b), and 5 M $CaCl_2$ (c).

The decay time in these maps at a given spectral position can be affected by both, vibrational energy relaxation and spectral diffusion, and the heterogeneity in the decay times only represents heterogeneous energy relaxation dynamics if spectral diffusion dynamics are distinctively different from the energy relaxation dynamics. For the amide I signal, the timescales for spectral diffusion and energy relaxation are comparable and, as such, the decay time maps exhibit an apparent heterogeneity (Figure 8.4). Despite the similarity of the relaxation and spectral diffusion timescales, which prevents a more detailed interpretation, this heterogeneity becomes less pronounced with increasing $CaCl_2$ concentration, indicative of amide - Ca^{2+} interaction. Conversely, spectral diffusion and energy relaxation dynamics are distinctively different at low and high $CaCl_2$ concentrations for the carboxylate signal. At 0 M $CaCl_2$ the decay time map is rather homogeneous, and the observed decay time agrees well with the relaxation time in Figure 8.3b. At high $CaCl_2$ concentration, where the overall vibrational relaxation time is significantly faster than the spectral diffusion

dynamics, the decay time maps become heterogeneous: At the redshifted edge of the carboxylate signal, the decay time resembles the decay time of 2Ala in D_2O, while at higher frequencies where the shoulder in the linear IR spectra is observed (Figure 8.1) the decay time is significantly longer. As such, this analysis demonstrates that the observed increase in the overall τ_{VER} values (Figure 8.3b) is a result of the emergence of molecular species with blueshifted vibrational response and a longer vibrational lifetime in the presence of $CaCl_2$.
Again, the emergence of species with distinctively different vibrational lifetimes appears specific to $CaCl_2$ as the decay time maps for the carboxylate band in solutions of 2Ala and NaCl (see Supplementary Figure 15) remain homogeneous even at 5 M NaCl. For decay time maps for 1, 2 and 4 M $CaCl_2$-2Ala solutions see Supplementary Figure 16. Together, the vibrational lifetimes indicate the presence of at least two underlying molecular-level 2Ala species in the presence of $CaCl_2$ with different energy relaxation dynamics.

8.3.3 *Ab initio* MD simulations of 2Ala and 2Ala-$CaCl_2$ solutions

To better understand the molecular-level species that underlie the observed $CaCl_2$-induced spectral changes, we performed *ab initio* MD simulations. As different binding motifs can be readily separated from the trajectories, we limit the simulations to 2Ala in the presence of a high concentration of $CaCl_2$ (5 M), at which all relevant $CaCl_2$-2Ala species should be transiently formed. We investigate the distribution

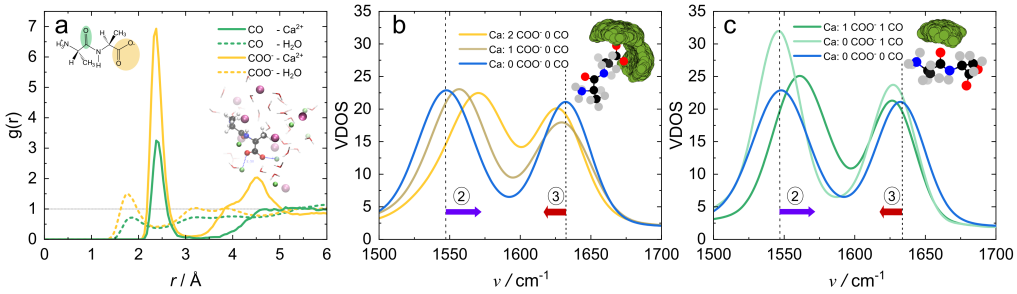

FIGURE 8.5: a) Oxygen-Ca^{2+} (solid lines) and oxygen-H_2O (dashed lines) radial distribution functions for carboxylate (yellow) and amide CO (green), with a simulation snapshot as inset b) Vibrational density of states (VDOS) of 2Ala in 5 M $CaCl_2$ with no direct Ca^{2+} interaction (blue), one Ca^{2+} at the carboxylate (dark yellow) and two Ca^{2+} at the carboxylate (yellow). Inset shows the distribution of $Ca^{2}+$ around the carboxylate group of 2Ala. c) VDOS of 2Ala in 5 M $CaCl_2$ solution with no direct Ca^{2+} interaction (blue), direct interaction at the amide CO but not at the carboxylate (bright green), and direct interaction at the carboxylate and the amide CO (dark green). Inset shows the distribution of Ca^{2+} around 2Ala's amide CO. Reproduced from [3].

of Ca^{2+} around 2Ala by calculating the radial distribution functions (RDFs) of Ca^{2+} next to 2Ala's oxygen atoms. The Ca^{2+}-O RDFs in Figure 8.5a, show intense peaks at 2.4 Å for all oxygens of 2Ala (solid lines). We find that this peak is about twice as intense for the carboxylate oxygens (solid yellow line) compared to the amide oxygen (solid green line), indicating a higher density of Ca^{2+} ions adjacent to the carboxylate

group than to the amide CO group. The RDF for the carboxylate group (solid yellow line) exhibits a second peak at ~ 4.5 Å, which is due to Ca^{2+} ions bound to the other oxygen atom of the carboxylate group, indicative of a monodentate binding being the predominant binding motif. Comparison of the Ca^{2+}-2Ala RDFs (solid lines) to the water-2Ala RDFs (dashed lines) shows that the first shell peaks of the Ca^{2+}-2Ala RDF are due to direct Ca^{2+}-2Ala interactions: The first peak in the carboxylate-water RDF (CO-H_{H_2O}) is located at 1.78 Åand for the amide oxygen at 1.88 Å. The slight difference in the location of both hydration peaks is also reflected in the oxygen-oxygen RDFs (COO-O_{H_2O}: 2.83 Å, CO-O_{H_2O}: 2.98 Å, see Supplementary Figure 17) and suggests somewhat stronger hydration of the carboxylate group as compared to the amide CO. The location of the first Ca^{2+} peak at shorter distances than the first water oxygen peak confirms that Ca^{2+} directly interacts with the CO oxygen. The RDFs for the chloride ion (see Supplementary Figure 18) suggest that Cl^- directly interacts with both, the amide NH and the N-terminus, and the occupancy is correlated to Ca^{2+} interaction with 2Ala. This correlation may enhance vibrational Stark effects upon binding of Ca^{2+} to 2Ala, albeit a high Cl^- concentration in NaCl solutions has negligible effect on the vibrational spectra (Supplementary Figure 8). To quantify the interplay between the interaction of 2Ala's oxygens with Ca^{2+} and water, we categorize simulation frames based on the interaction with Ca^{2+} (for more detail, see Supplementary Information) and determine the hydration numbers of the functional groups of 2Ala by integrating all water molecules within $d_{CO-H} \leq 2.4$ Å).

TABLE 8.1: Average number of water molecules present for categorized frames with a CO oxygen - water hydrogen distance $d_{CO-H} < 2.4$ Å as bonding criterion for water.

Category	Average number of water
0 Ca^{2+} at CO	0.73
1 Ca^{2+} at CO	0.01
0 Ca^{2+} at COO^-	1.64
1 Ca^{2+} at COO^-	0.38

Table 8.1 indicates that upon direct interaction of Ca^{2+} with the amide CO (1 Ca^{2+} at CO) the amide CO is fully dehydrated with Ca^{2+} replacing all water molecules. The same full dehydration of the carbonyl upon Ca^{2+} interaction has also been reported for NMA.[69] When Ca^{2+} binds to the oxygen of the carboxylate (1 Ca^{2+} at COO^-), on average about one water molecule is replaced, yet dehydration due to Ca^{2+} is incomplete. Thus, the analysis of the RDFs illustrates that, despite the very different spectral response observed in the IR experiments, Ca^{2+} ions directly interact with both, the carboxylate oxygens and the amide oxygen of 2Ala. For the amide oxygen, Ca^{2+} ions fully replace hydrating water molecules, while the carboxylate moiety remains partly hydrated.

In addition to the interplay between interaction of water and/or Ca^{2+} with the individual binding sites at 2Ala, we further consider the occurrence of Ca^{2+} at the different binding sites. In addition to simulation frames for which only one Ca^{2+} ion directly binds to only one of 2Ala's oxygens (26% only at COO^-; 2% only at CO), we find a significant fraction (26%) of configurations for which two Ca^{2+} ions bind (monodentate) to the two carboxylate oxygens, which is also referred to as a *bridging* binding configuration.[267] Also configurations with two Ca^{2+} ions binding to one of the carboxylate oxygens and to the amide CO are observed (13%). Yet, we find no evidence for all three oxygen sites (two carboxylate oxygens and one amide oxygen) being simultaneously occupied by Ca^{2+} at the same time or for bidentate coordination of both carboxylate oxygens to Ca^{2+}.

To further explore the spectral consequences of the interaction of calcium with 2Ala, we compute the vibrational density of states (VDOS) from the relative CO velocities for different binding states, categorized based on the interaction with Ca^{2+} (see Figure 8.5b and c). We categorized the frames from the simulation into five categories according to the number of Ca^{2+} bound to each interaction site (see Supplementary Information for more details).
Figure 8.5b illustrates the effect of 0, 1, and 2 Ca^{2+} binding to the carboxylate group on the VDOS, with the site at the amide oxygen not occupied by calcium, while Figure 8.5c shows the effect of Ca^{2+} binding to the amide CO group. The solid blue lines in Figure 8.5b and c represent the spectra for species for which 2Ala's amide I and asymmetric carboxylate vibration do not directly interact with Ca^{2+}. The computed spectral shifts upon binding of Ca^{2+} to 2Ala reproduce the experimentally observed trends with increasing $CaCl_2$ concentration very well:
Upon binding of one Ca^{2+} ion to the carboxylate, the carboxylate band shifts to higher wavenumbers (dark yellow line in Figure 8.5b) (2). Such blueshift is commonly observed for calcium binding to one oxygen atom of the carboxylate, with the other oxygen being hydrated by water. This coordination geometry is also often termed *pseudo-bridging* coordination.[261, 262, 267, 269] The blueshift of the carboxylate band upon the pseudo-bridging interaction can be rationalized by the localization of the charge at the interacting oxygen and, consequently, lifting of the degeneracy of the two CO bond potentials (see Supplementary Figure 19). Single point DFT calculations (see Supplementary Figure 20) show that the lifted degeneracy causes a spectral blueshift for the CO group of COO^- not interacting with Ca^{2+}, in contrast to the redshift for a bidentate binding geometry.[262, 263, 267]
Upon interaction of a second Ca^{2+} with the carboxylate, the VDOS exhibits an additional blueshift (yellow line in Figure 8.5b). Single point DFT calculations suggest that the asymmetry of the charge distribution at the carboxylate's oxygens for one and two Ca^{2+} interacting with the carboxylate is rather comparable (Supplementary Figure 19), and in both configurations the degeneracy of the two CO groups is lifted in a similar manner. The dissimilarity of the two CO groups interacting with two

Ca^{2+} ions is further supported by the MD simulations, which show that the oxygen-carbon distances of the two CO groups of COO^- differ for a trajectory with bridging Ca^{2+} interaction as opposed to the bond distances in the absence of Ca^{2+} (see Supplementary Figure 21). The additional blueshift upon interaction with a second calcium may be rationalized in analogy to the interaction of Ca^{2+} with isolated carbonyls: For the interaction of CO with water, electron density is transferred from the carbonyl to the σ^* orbital of water, weakening the CO bond and leading to a redshift. When water is replaced by Ca^{2+}, the transfer of electron density is no longer possible, leading to a blueshift, depending on the number of water molecules replaced by the ion.[69, 71, 72, 272, 273] Together, the gradual blueshift of the carboxylate band with additional Ca^{2+} ions (2) interacting with the carboxylate predicted by the MD simulations is in line with the gradual increase of the heterogeneity of the carboxylate band as concluded from the CLS (Figure 8.3a): The enhanced heterogeneity of the carboxylate vibration concluded from the 2D-IR spectra can be explained by a blueshift of the vibrational mode due to the successive binding of Ca^{2+} to the two oxygen sites at the carboxylate group with increasing $CaCl_2$ concentration.

The simulations at high $CaCl_2$ concentrations do not provide insights into the initial redshift of the carboxylate band (1) at low salt concentrations. Yet, for amide CO similar redshifts have been reported at low salt concentrations and ascribed to Stark shifts, which may also be the origin of the observed redshift for the carboxylate.[71, 266]

The experimentally observed weak redshift of the amide I mode (3) is also reproduced in the VDOS spectra (see Figure 8.5c, dark and bright green line). As such, also the simulations confirm that the spectral response of the amide I mode to Ca^{2+} interaction markedly differs from the response of isolated amide groups.[68, 69, 71, 72] To explore the molecular origins of this different behaviour, we disentangle the VDOS of the amide group for three different configurations: (i) One water molecule hydrating the amide oxygen, (ii) one Ca^{2+} ion bound to the amide oxygen, and (iii) neither water nor Ca^{2+} bound to the amide oxygen (see Supplementary Figure 22). The comparison of these three configurations shows that both, direct interaction between the amide and water (i) and the amide and Ca^{2+} (ii) induce a similar redshift as compared to the configurations with no interaction at the amide (iii). As such, the replacement of water by Ca^{2+} in the vicinity of the amide oxygen does not result in appreciable changes in the instantaneous frequency of the amide I mode: The simulated spectra explain the weak sensitivity of the amide I frequency to the presence of Ca^{2+}, as opposed to the response of isolated amide groups.[68, 69, 71, 72] This insensitivity of the amide I frequency to the molecular identity of its direct environment is in line with the experimentally observed insensitivity of the CLS to addition of $CaCl_2$ (Figure 8.3a). The moderate redshift of the amide I mode with increasing

$CaCl_2$ concentration (Figure 8.1a) is therefore likely related to a transition from an incompletely hydrated amide CO group at low concentrations to configurations with Ca^{2+} bound to the amide moiety at high $CaCl_2$ concentrations. Despite the insensitivity of the amide I mode frequency to Ca^{2+} interaction, the presence of a water molecule or a Ca^{2+} ion in the vicinity of the amide oxygen will most likely alter the density of states with lower energy and coupling of the amide I mode to those states, which is intimately connected to vibrational energy relaxation of the amide I mode. Therefore, the replacement of water molecules in the vicinity of the amide group by Ca^{2+} ions can explain the observed variation of the vibrational energy relaxation dynamics upon addition of $CaCl_2$ (Figures 8.4 and 8.3b).
The markedly different spectral response of more isolate amide groups to $CaCl_2$ (see Figure 8.1c and Refs. [68, 69, 71, 72]) can in turn be rationalized by the different hydration states of isolated amide groups and the sterically less accessible amide moiety of 2Ala: More sterically accessible amide groups like in NMA are hydrated by about two water molecules, which are nearly fully replaced by one Ca^{2+} ion[69] upon addition of $CaCl_2$. This replacement leads to a blueshift due to a reduction of electron transfer from the environment to the σ^* orbitals for Ca^{2+} bound to the amide as compared to the amide hydrated by two water molecules.[72, 272] Our results suggest that the spectral consequences for the sterically less accessible amide CO of 2Ala are similar since less than one hydrating water molecule is replaced by Ca^{2+}. Hence, the accessibility to hydration water of the amide group seems to be pivotal for the sensitivity to interaction with Ca^{2+}. Such steric arguments should also apply to amide groups in a protein backbone in general, suggesting that the amide I mode frequency is not an ideal probe for detecting amide-Ca^{2+} interactions. However, the altered energy relaxation pathways offer the potential to spectroscopically detect amide-Ca^{2+} interaction via the vibrational energy relaxation time scale.

8.4 Conclusion

Herein, we examined the interaction between the zwitterionic dipeptide L-alanyl-L-alanine (2Ala) and the physiologically relevant, strongly hydrated bivalent salt $CaCl_2$. Two distinct interaction sites at 2Ala have been examined with IR spectroscopy: The backbone CO (amide I mode) and C-terminus (asymmetric carboxylate mode). Linear IR spectra of 2Ala with increasing concentration of $CaCl_2$ show changes in peak position and amplitude for both modes and can be summarized in the following three major trends: (1) The asymmetric carboxylate stretching peak initially experiences a redshift, followed by (2) a blueshift at concentrations above 2 M $CaCl_2$. (3) The amide I mode, on the other hand, experiences a redshift with increasing salt concentration. Model systems that only contain either the amide I mode (NMA) or the carboxylate mode (zwitterionic alanine), both show a blueshift upon adding $CaCl_2$. 2D IR experiments reveal an increase in the vibrational relaxation lifetime of both amide I and carboxylate peak. Together with the enhanced

spectral heterogeneity of the carboxylate band in the presence of $CaCl_2$, these findings are indicative Ca^{2+} interaction at the amide CO and the carboxylate.
Ab initio MD simulations reveal that Ca^{2+} interacts with both of 2Alas binding sites, the amide CO group and the carboxylate group, but with a higher propensity at the negatively charged carboxylate. Computed VDOS align with the experimentally observed spectral shifts of both modes. The blueshift of the carboxylate (2) with increasing $CaCl_2$ concentration can be assigned to monodentate binding of not only one, but also two Ca^{2+} ions to the carboxylate, while a direct Ca^{2+}- amide CO interaction only leads to minor spectral shifts.
The spectral response of the amide contrasts what has previously been observed for NMA, where interaction with Ca^{2+} leads to the complete dehydration of the amide CO, which was initially hydrated by two water molecules.[69] Here, for 2Ala, the amide CO group is initially hydrated by (on average) less than one water molecule and the direct interaction with Ca^{2+} replaces one water molecule only. These differences in dehydration, together with vibrational Stark effects, can explain the differing spectral sensitivities to interaction with Ca^{2+}.
The computational spectra and experiments demonstrate the necessity to consider all potential interaction sites within a peptide and competing binding to these sites in order to fully rationalize specific ion effects on peptides using vibrational signatures. Furthermore, our results highlight that the accessibility and hydration of both the peptide's interaction sites and ions critically determine the sensitivity of amide modes to interaction with ions.

8.4.1 Acknowledgement

We are grateful to Maksmim Grechko and Mischa Bonn for insightful discussions. This project received funding from the European Research Council (ERC) under the European Union's Horizon 2020 research and innovation program (grant agreement no. 714691). We note that portions of this manuscript were first presented in the PhD thesis entitled "Spectroscopic Exploration of Protein and Peptide Systems: Unraveling Ion-Specific Interactions and H-Bond Dynamics" by Carola Sophie Krevert, published in July 2024 (University of Mainz).

8.5 Supporting Information

Synthesis of isotope-labeled 2Ala

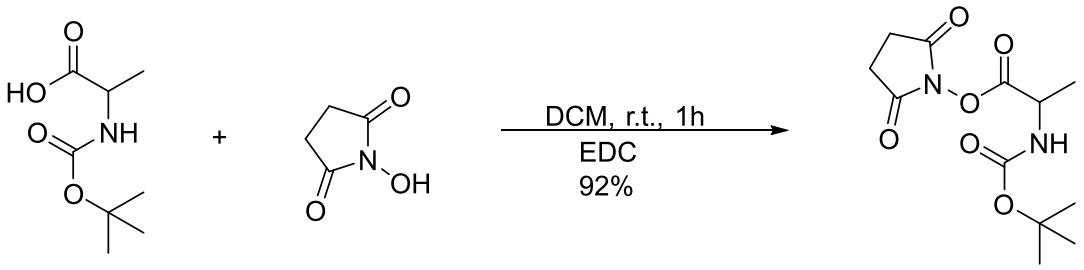

FIGURE 8.6: Step one in the reaction pathway for isotope-labeled 2Ala. Reproduced from [3].

Boc-alanine (500 mg, 2.64 mmol), N-hydroxysuccinimide (304 mg, 2.64 mmol) and 1-ethyl-3-(3-dimethylaminopropyl)carbodiimide (EDC) (507 mg, 2.64 mmol) were dissolved in dichloromethane (DCM) (15 mL) and stirred at room temperature for 1 hour. The solution was washed with saturated $NaHCO_3$-solution and the aqueous phase extracted with DCM. The combined organic phases were washed with brine and the solvent removed under reduced pressure. The product was gained as a slightly rose solid without further purification (692 mg, 2.43 mmol, 92%).

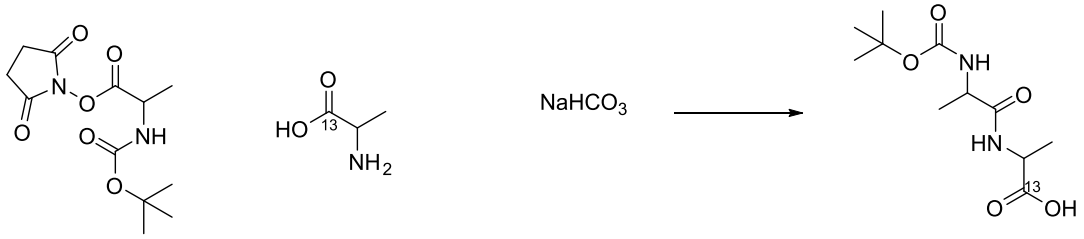

FIGURE 8.7: Step two in the reaction pathway for isotope-labeled 2Ala. Reproduced from [3].

^{13}C-labeled alanine (43 mg, 0.48 mmol) and sodium bicarbonate (80 mg, 0.95 mmol) were dissolved in 10 mL tetrahydrofuran (THF)/H_2O (1:1). Boc-Ala-OSu (150 mg, 0.52 mmol) in 5 mL THF was added drop-wise to that mixture and stirred overnight. THF was removed under reduced pressure and the solution was acidified to pH 2 with 1 M HCl and subsequently extracted with ethyl acetate. The product was gained as a colorless solid (120 mg, 0.46 mmol)

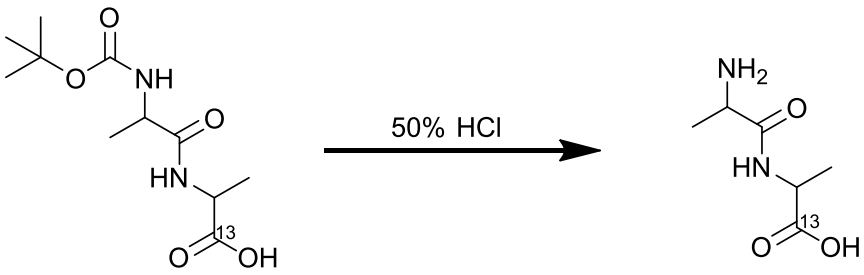

FIGURE 8.8: Step three in the reaction pathway for isotope-labeled 2Ala. Reproduced from [3].

Boc-Ala-Ala (24 mg, 92 µmol) was suspended in 10 ml semiconcentrated HCl and stirred overnight. The solvent was then removed under reduced pressure to yield the product as a colorless solid (14 mg, 87 µmol). Before the measurement, we neutralized the acidic ^{13}C 2Ala with NaOH.

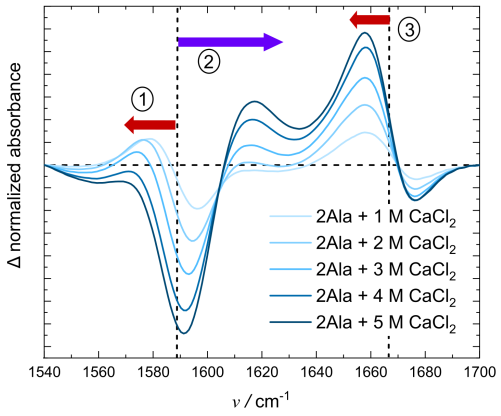

FIGURE 8.9: Difference spectra with the spectrum of 2Ala in D_2O subtracted from the 2Ala - $CaCl_2$ solutions at different salt concentrations to illustrate the three major trends with increasing salt concentration: At intermediate salt concentrations (1-3 M), a slight redshift can be observed for the carboxylate peak (1), while at higher salt concentrations (3-5 M) a significant blueshift is observed (2). The amide I mode redshifts as salt concentration is increased (3). The vertical dashed lines mark the peak positions of amide I and carboxylate in pure 2Ala solutions. Note that those difference spectra were obtained by subtracting area normalized spectra. Reproduced from [3].

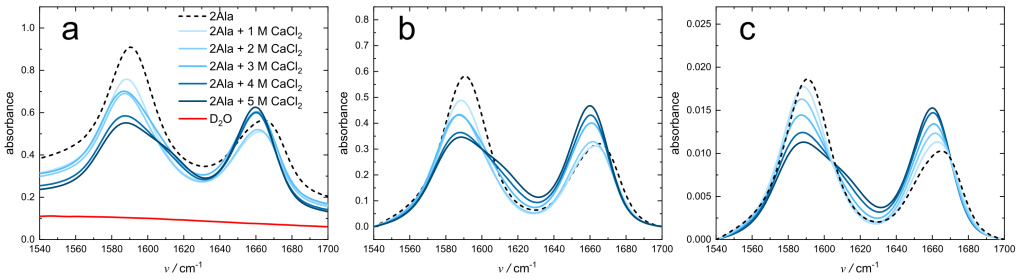

FIGURE 8.10: a) IR absorption spectra of 2Ala and 2Ala - $CaCl_2$ solutions as measured; b) linear background-subtracted spectra; c) linear background and area normalized spectra. Reproduced from [3].

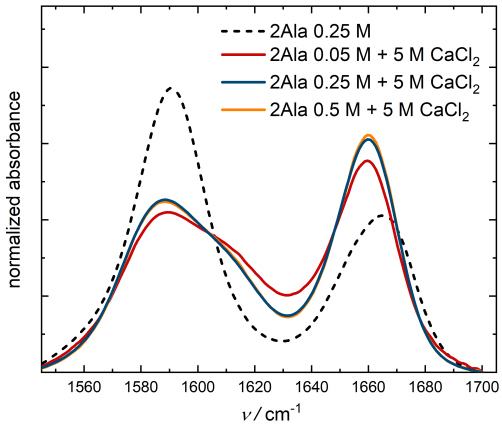

FIGURE 8.11: IR absorption spectra of 2Ala and 2Ala + 5 M $CaCl_2$ solution at 0.25 M 2Ala (dashed black line and solid blue line, respectively), as well as 0.05 M 2Ala, and 0.5 M 2Ala + 5 M $CaCl_2$ (solid red and orange lines). All spectra were background-subtracted and area-normalized. The spectra do not change significantly with altered 2Ala concentration even though the ratio peptide:salt changes significantly: At a wide range of 2Ala concentrations, the nature of interaction between peptide and ions is comparable. Reproduced from [3].

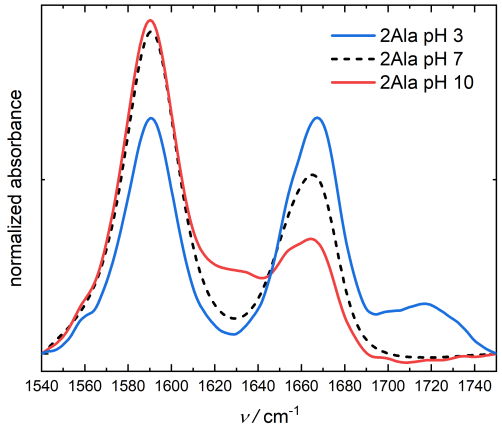

FIGURE 8.12: IR absorption spectra of 2Ala in D_2O at various pH values: pH 7 (black solid line), pH 3 (solid blue line) and pH 10 (solid red line). With increasing pH value, the NH_3^+ group is deprotonated, which changes the transition dipole moment of the amide I group significantly. A decrease in pH value results in a protonation of the carboxylate group, resulting in a decrease in signal of the asymmetric stretching vibration and the appearance of a mode due to the COOH group at 1710 cm^{-1}. Reproduced from [3].

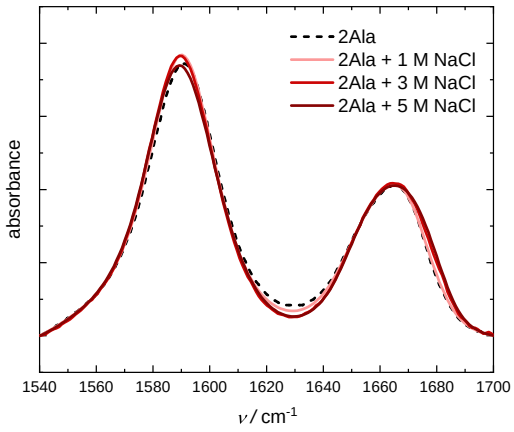

FIGURE 8.13: Linear, background subtracted and area-normalized IR spectra of 0.25 M 2Ala (black), 0.25 M 2Ala + 1 M NaCl (light red), 0.25 M 2Ala + 3 M NaCl (red), and 0.25 M 2Ala + 5 M NaCl (dark red). Reproduced from [3].

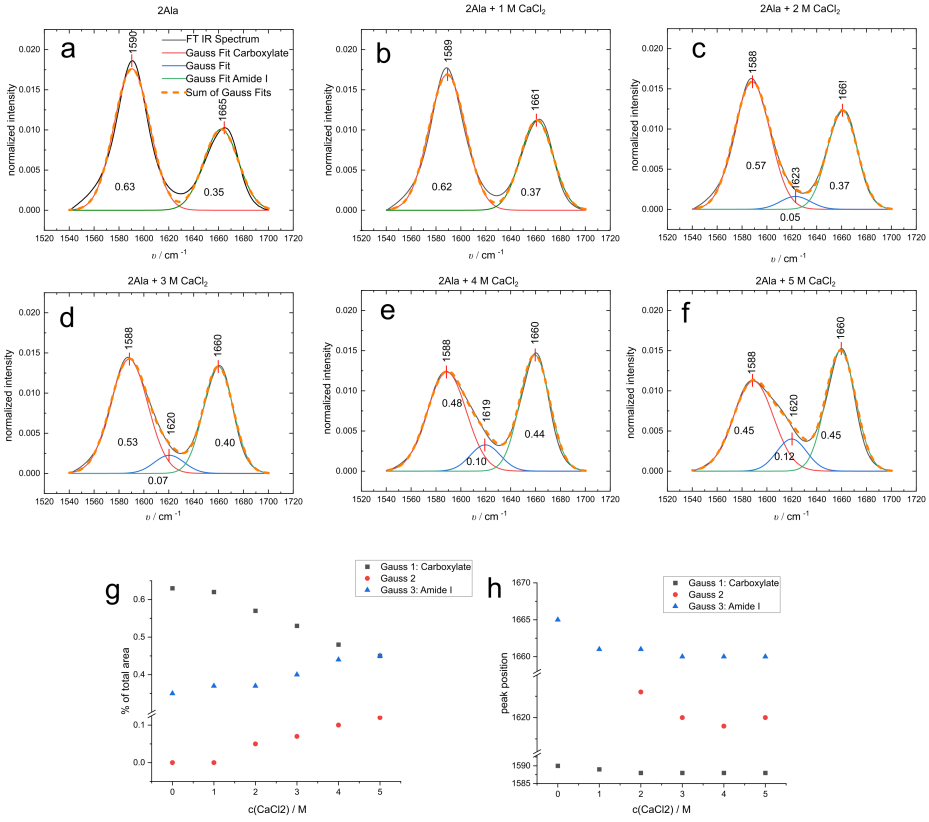

FIGURE 8.14: Linear IR spectra of 2Ala and 2Ala - $CaCl_2$ solutions with Gaussian fits (a-f). 0 M and 1 M $CaCl_2$ were fitted with two Gaussian functions, while 2-5 M $CaCl_2$ were fitted with a sum of three Gaussian functions. The concentration-dependent relative amplitudes (g) and peak positions (h) suggest that a third peak emerges with increasing $CaCl_2$ concentration. Reproduced from [3].

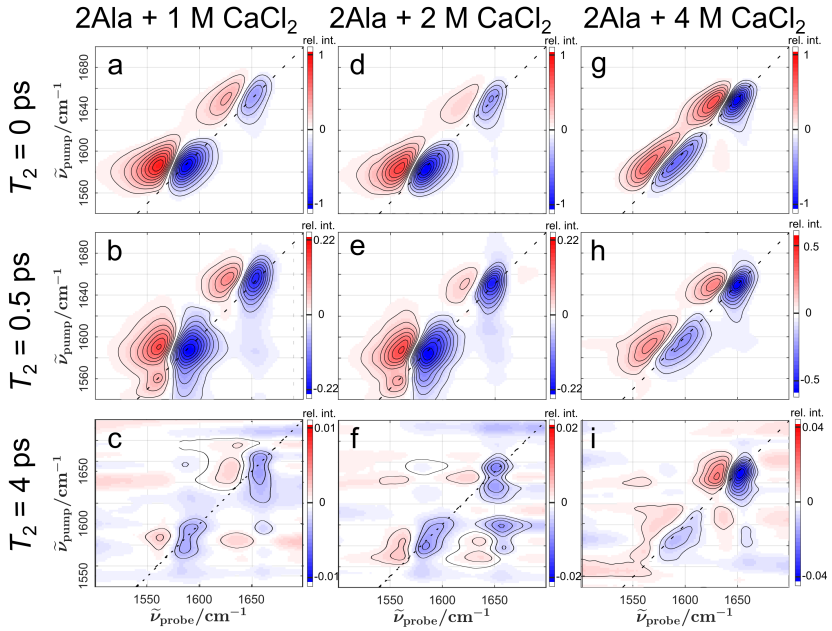

FIGURE 8.15: 2D IR spectra of 2Ala - $CaCl_2$ solutions at 1 M (a, b, c), 2 M (d, e, f), and 4 M (g, h i) $CaCl_2$ concentrations at 0 ps (a, d, g), 0.5 ps (b, e, h), and 4 ps (c, f, i) waiting time T_2. The observed trends resemble those shown in Figure 3 of the main manuscript. Reproduced from [3].

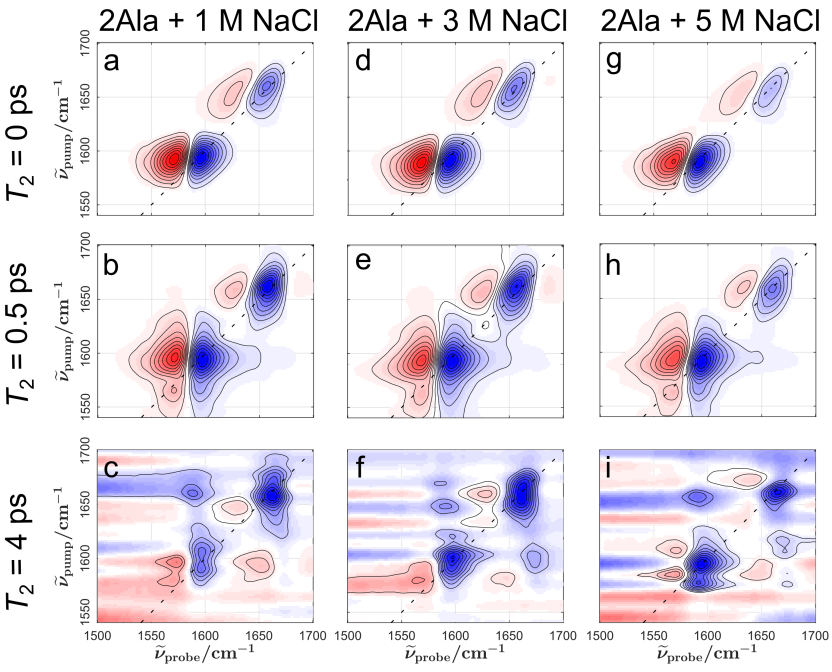

FIGURE 8.16: 2D IR spectra of aqueous 2Ala NaCl solutions at 1, 3 and 5 M NaCl concentration and 0 ps, 0.5 ps and 4 ps waiting time. The 2D spectra resemble the trends in the linear IR spectra of aqueous 2Ala-NaCl solutions: Only very moderate NaCl-induced changes in peak shape or vibrational dynamics can be observed. Reproduced from [3].

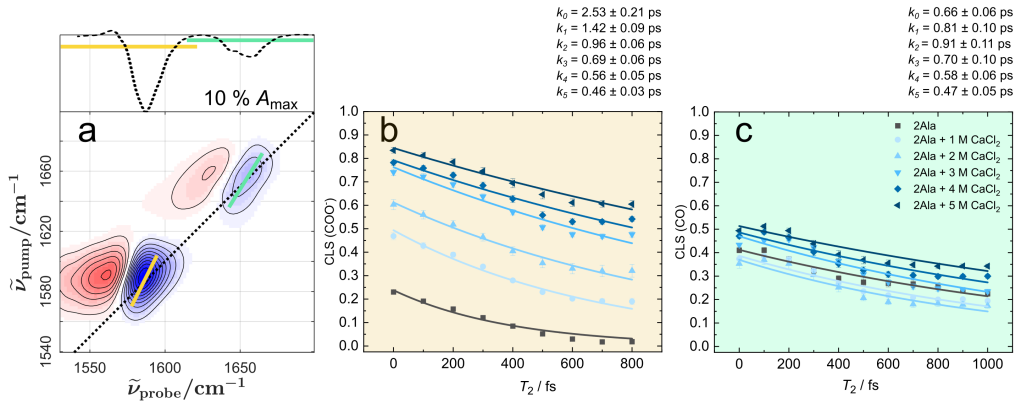

FIGURE 8.17: a) 2D IR spectrum of 2Ala at 0 fs waiting time with diagonal cut shown in the top panel. CLS were evaluated with the center line positions at frequencies for which the signal was less than 10 % of the bleach maximum (see yellow and cyan lines). The frequency range over which the CLS was evaluated was kept constant at all waiting times. The concentration- and waiting-time-dependent values for the CLS are displayed in b for amide I and c for carboxylate. The CLS decays were modelled with an exponential function ($CLS(T_2) = CLS(T_2 = 0) \cdot \exp(-k_{CLS} \cdot T_2)$). Reproduced from [3].

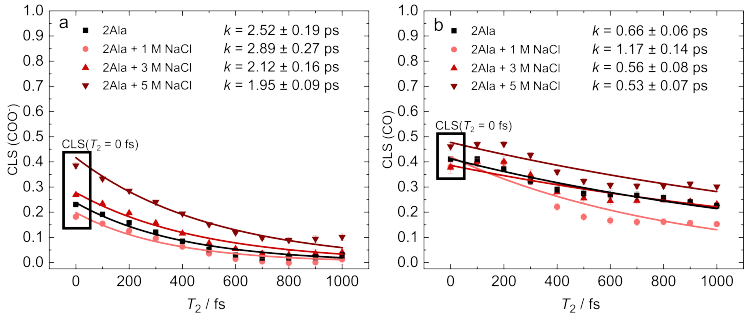

FIGURE 8.18: Waiting-time-dependent values for CLS of amide I (CO) and carboxylate mode (COO^-) in the presence of NaCl. Solid lines show the exponential fit (compare Figure 8.17). The respective values for the decay rates k are indicated in the Figure. The rate constant decreases by about 20 % for the case of the COO^- mode, while the rate constant of the amide I mode (CO) decreases by about 15 %. Reproduced from [3].

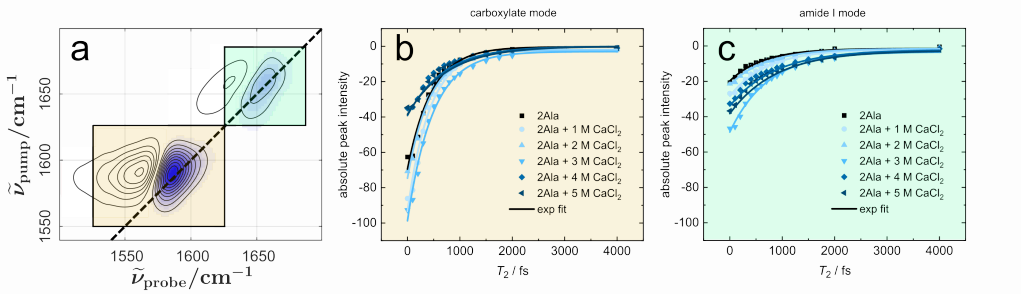

FIGURE 8.19: Vibrational relaxation lifetime determined via area integration of all negative values in the marked area (a) of both the carboxylate mode (b) and the amide I mode (c) and fitting them exponentially with Equation 1 (main manuscript). The vibrational energy relaxation times increase significantly with increasing concentration of $CaCl_2$ (Figure 4b). Reproduced from [3].

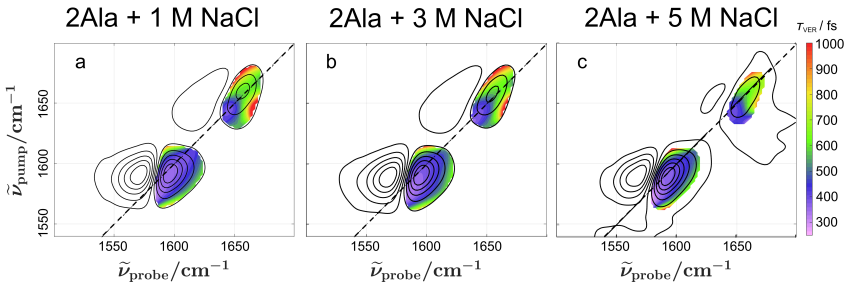

FIGURE 8.20: Decay time maps for 2Ala-NaCl solutions. The decay times determined for the entire peak (see Figure 8.19) gives relaxation lifetimes of: 1 M: amide I: 630 ± 40 fs; carboxylate: 480 ± 60 fs; 3 M: amide I: 610 ± 40 fs; carboxylate: 490 ± 60 fs; 5 M: amide I: 600 ± 40 fs; carboxylate: 510 ± 60 fs. Salt induced changes to the decay times are less pronounced for 2Ala-NaCl solutions, as compared to 2Ala-$CaCl_2$. Reproduced from [3].

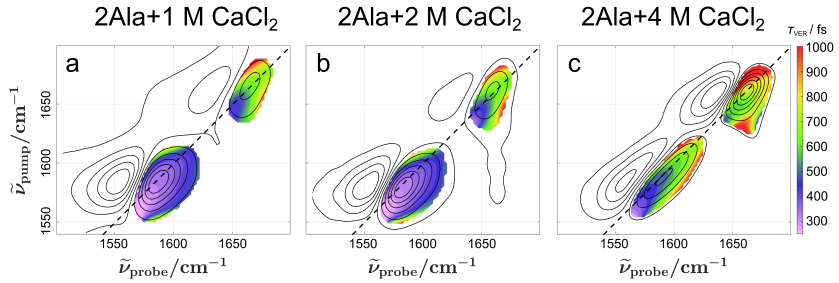

FIGURE 8.21: Decay time maps for 2Ala-$CaCl_2$ solutions for 1 M (a), 2 M (b) and 4 M $CaCl_2$ (c) solution (see also Figure 5 of the main manuscript). Reproduced from [3].

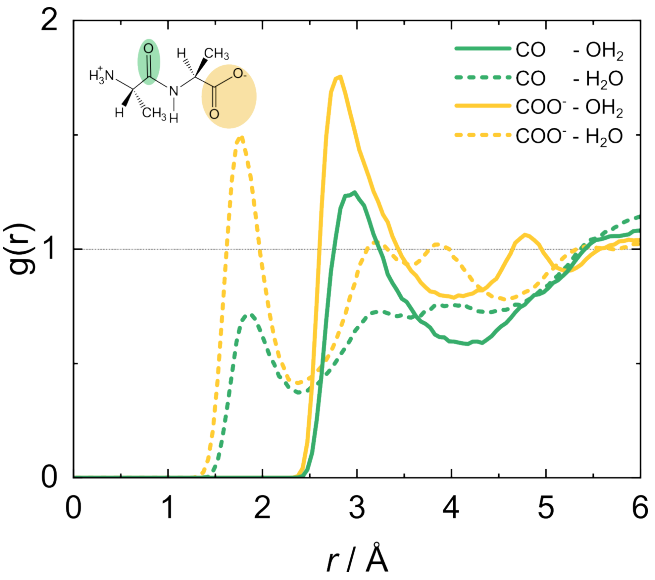

FIGURE 8.22: Radial distribution function of 2Ala carboxylate oxygen (yellow) and amide oxygen (green) with water hydrogen (dashed) and oxygen (solid) in the presence of 5 M $CaCl_2$. Reproduced from [3].

Categorization

For the calculation of the VDOS of different binding configurations we categorize simulation frames based on the interaction of the three oxygen atoms of 2Ala (COO1, COO2 and CO) with Ca^{2+}. We take the first minimum in the CO-Ca RDF (see Figure 6a) at 3.1 Å as a maximum value for being classified as direct interaction. Additionally, for a frame to count towards a certain category the Ca-CO distance has to be smaller than the threshold at this frame and a frame 1 ps later. We then check the occupation of the three binding sites and categorize frames accordingly. These categories together with their occurrence are listed below in Table 8.2. We display VDOS spectra for categories 1-3 in Figure 6b and for categories 4 and 5 in Figure 6c. We see no evidence for all interaction sites being occupied at the same time (category 6). Note that 1% of the frames are categorized as transitional frames where calcium -2Ala interactions are formed/broken.

TABLE 8.2: Categories for calculation of VDOS and their occurrence.

Category	number of Ca^{2+} at carboxylate	number of Ca^{2+} at amice CO	occurrence (%)
1	0	0	32
2	1	0	26
3	2	0	26
4	0	1	2
5	1	1	13
6	2	1	0

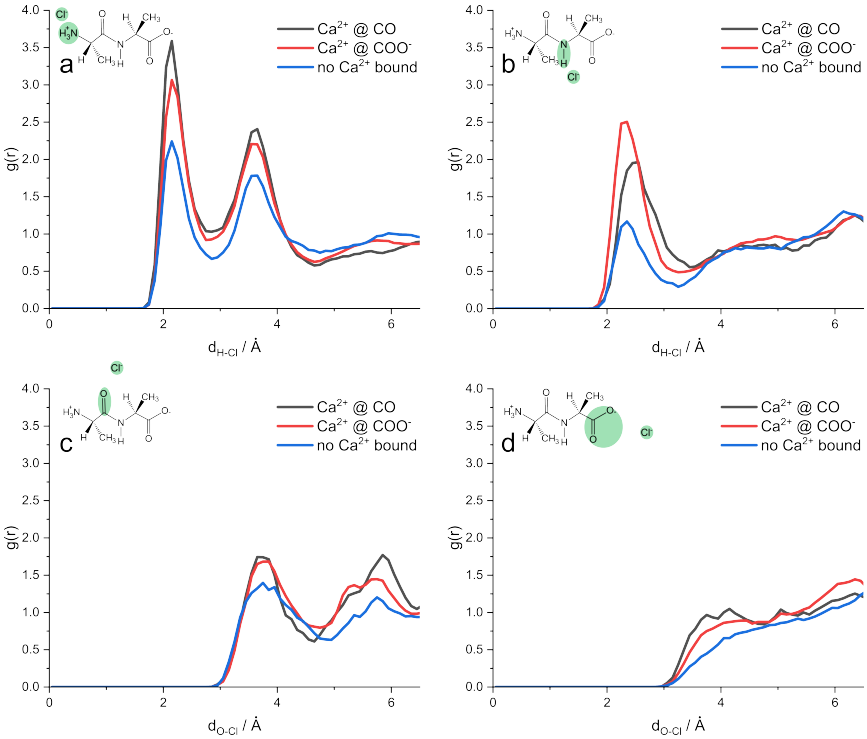

FIGURE 8.23: H-Cl$^-$ radial distribution functions for a) the N-terminus and b) the amide NH group. Panels c) and d) show the O-Cl$^-$ radial distribution functions for the amide CO and the C-terminus, respectively. To explore correlations of Cl$^-$ interaction to Ca^{2+} binding, we show RDFs separately for Ca^{2+} bound to the amide CO (black line), Ca^{2+} bound to the carboxylate (red line), and no Ca^{2+} bound to 2Ala (blue line). Cl$^-$ directly interacts with all NH protons and the occupancy increases when Ca^{2+} is bound to 2Ala, while no Cl$^-$ ions are in direct contact with 2Alas oxygens. Reproduced from [3].

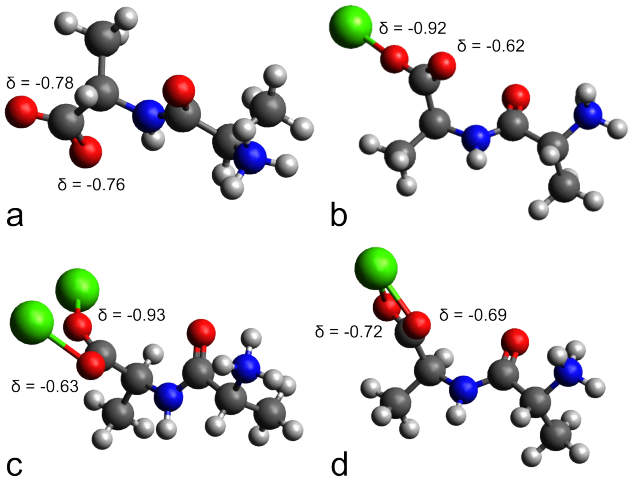

FIGURE 8.24: DFT optimized geometries of 2Ala with a) 0 Ca^{2+}, b) 1 Ca^{2+} monodentate, c) 2 Ca^{2+} monodentate, and d) 1 Ca^{2+} bidentate geometries together with calculated partial charges for carboxylate oxygens to illustrate the degeneracy of both CO groups. Reproduced from [3].

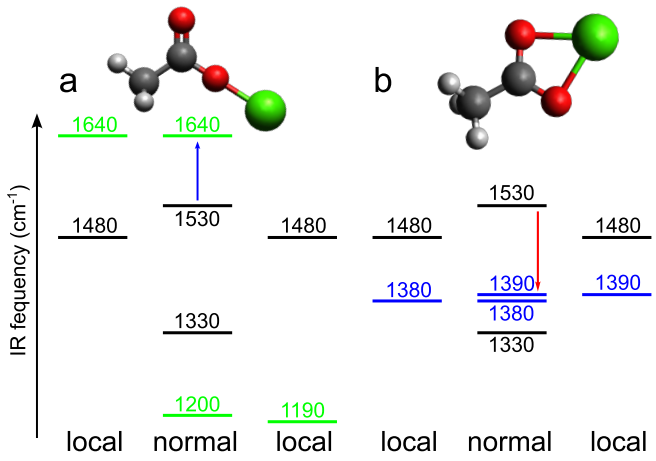

FIGURE 8.25: Energy level diagram for the carboxylate modes with a) pseudo bridging and b) bidentate binding of 1 Ca^{2+} to an acetate anion as obtained from single point DFT calculations. The harmonic, coupled normal modes are shown in the center for the acetate (black) and the acetate with Ca^{2+} (green in panel a) and blue in panel b)). Left and right energy levels correspond to the local (decoupled) CO stretching mode frequencies, which we obtained by artificially increasing the mass of one of the oxygens and the atoms of the methyl group to 100 u. Only for acetate in the absence of Ca^{2+} coupling of the two local CO modes results in an appreciable splitting into symmetric and anti-symmetric stretching modes. This splitting is not symmetric, presumably due to C-H mode contributions. [268] In the presence of Ca^{2+}, coupling is weak and the coupled harmonic frequencies resemble the local mode frequencies, demonstrating the lifting of the degeneracy. Reproduced from [3].

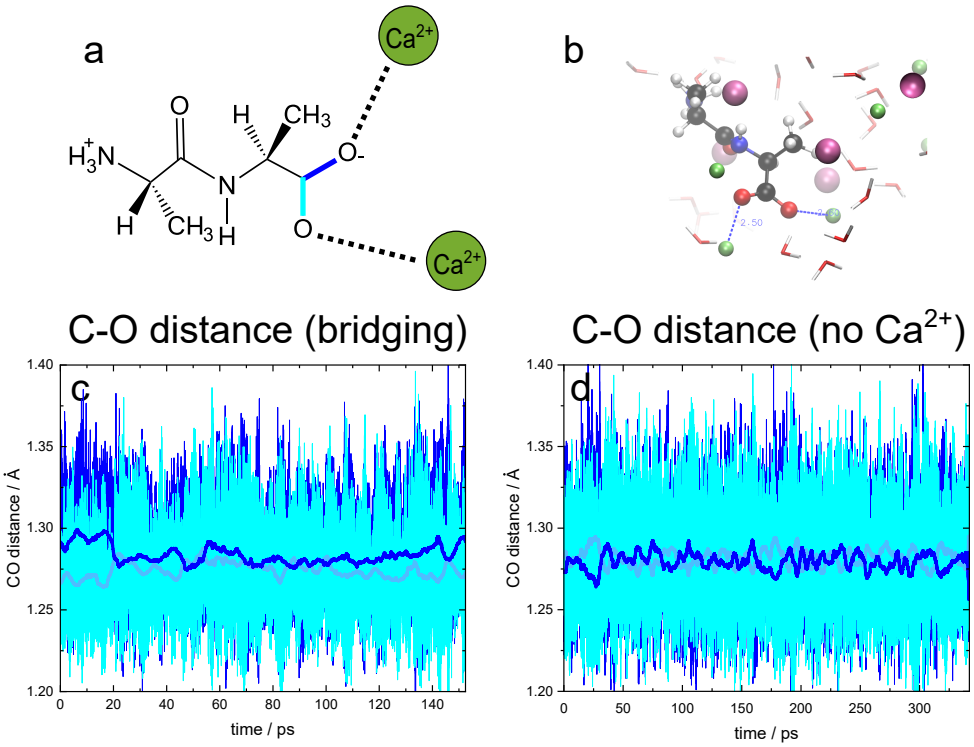

FIGURE 8.26: a) Schematic drawing of 2Ala interacting in a bridging configuration with the CO bonds color-coded. b) Simulation snapshot of 2Ala in a bridging geometry. CO distances versus time for a trajectory in bridging geometry c) and without direct Ca^{2+} interaction d). The colors of the solid lines in c) and d) represent the distances with the same color as in a). The solid lines mark the moving median distances. The mean difference between both CO distances of 0.01 for the bridging and of 0.002 in the absence of Ca^{2+} illustrates the absence of the degeneracy of both CO potentials for the bridging configuration. Reproduced from [3].

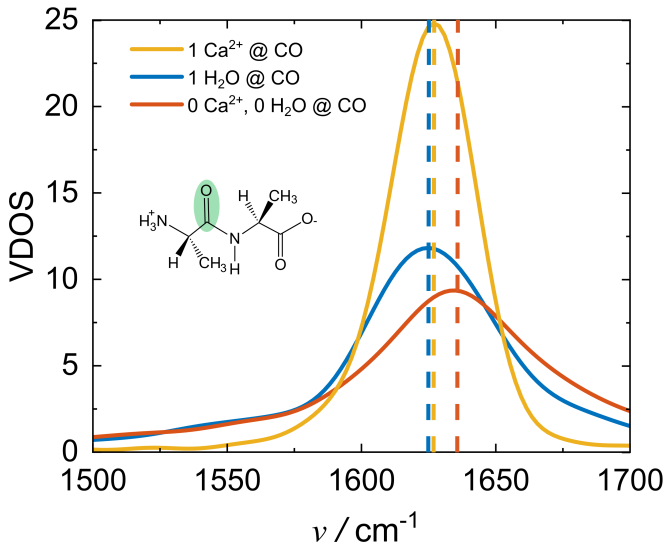

FIGURE 8.27: VDOS of the amide CO response for direct amide-Ca^{2+} interaction (yellow), direct amide-water interaction (blue), and no interaction of amide with water or Ca^{2+} (orange). Interaction with Ca^{2+} or water induces a redshift of similar magnitude. Reproduced from [3].

Chapter 9

Conclusion and Outlook

Understanding hydrogen bonds in liquids is a crucial in step gaining a deeper insight into bulk phenomena of liquids, such as water's anomal behaviors. Especially the dynamic nature of H-bonds and electrostatic bonds in general are not fully understood.

In chapter 6 we explored the correlation of water's donating hydrogen bonds. We employed linear IR and two dimensional infrared (2DIR) spectroscopy as well as density functional theory (DFT) calculations to study pure and isotopically dilute water, dissolved in dimethylformamide (DMF). We found a significant increase in line width for the decoupled HOD as compared to the coupled symmetric and asymmetric stretching modes in D_2O. With 2DIR spectroscopy we determine the respective homogeneous line shape, and subsequently deconvolve the diagonal line shape, so to obtain the pure inhomogeneous contribution. We found the inhomogenous distribution of frequencies to be about twice broader for HOD. Comparison with frequency maps, obtained from DFT calculations, reveal an anti-correlated H-bond distribution. This anti-correlation can also be seen directly from the coupling peak of D_2O. This reveals the transient nature of the anticorrelation, which decays in under 500 fs. We conducted similar experiments for urea-d6 and also found a less pronounced anti-correlation. This confirms that the anti-correlated H-bonds is not unique for water but is rather expected for all XH_2 like molecules.

In theoretical studies by Kühne and coworkers[14] on the correlations of Hydrogen bonds in liquid water and ice, these anti-correlations have been suggested to dependent on the temperature. Temperature dependent 2DIR measurements, could prove valuable to quantify the temperetaure dependence of these anti-correlations. Furthermore two color 2DIR (2C2DIR) could help to better resolve the coupling peak and therefore improve on the quantifiability of the anti-correlations. In 2C2DIR spectroscopy the probe and pump frequency are decoupled, and thus pumping the OH stretch and probing the OD stretch frequency would allow to see the coupling peak in isolation.

In chapter 7 we investigated the origin of the so called "booster effect" of hexafluoroisopropanol (HFIP) that was described by Berkessel and coworkers [10]. HFIP is a

perfluorinated alcohol that has been widely used in synthetic chemistry and chemical biology, due to its ability to enhance reaction speeds, to open novel reaction pathways and its unique solvent properties. We used polarization controlled time resolved IR spectroscopy (TRIR) to investigate the anisotropy decay and thus the reorientational dynamics of individual molecules in HFIP and its non fluorinated counterpart isopropanol (IP). We found a faster reorientation for IP even though linear IR spectroscopy showed weaker H-bonds for HFIP. 2DIR spectroscopy revealed slower H-bonding dynamics in HFIP suggesting longer lived H-Bonds. Dielectric relaxation spectroscopy (DRS) showed faster individual reorientation for IP but slower collective reorientation. Finally FTIR titration experiments with a substrate (diethylether) revealed that, while HFIP forms weak H-bonds with itself it forms much stronger H-bonds with the substrate. Our results suggest that HFIP consists of many small hydrogen-bonded clusters, which are sufficiently large and have a sufficiently long lifetime to efficiently boost chemical conversions, yet sufficiently small (smaller than in isopropanol) to posses a large number of available active terminal sites which can donate a hydrogen bond to a reactant molecule. These active terminal OH groups of HFIP can efficiently enhance chemical reaction rates by activating reactants via strong hydrogen-bond donation.

We thus far only studied the dynamics of the bulk alcohols, yet the interaction with a substrate revealed the largest difference. In the future measurements of a substrate dissolved in alcohol, directly measuring the dynamics of substrate solvent interactions using 2DIR spectroscopy could help deepening our understanding of the substrate solvent interactions for HFIP and other alcohols. Furthermore 2C2DIR spectroscopy could allow us to only study the terminal OH groups of H-bonded clusters bonded to a substrate. This would allow us to study the effects of cluster sizes on the hydrogen bonding dynamics.

In chapter 8 we investigated the specific ion interactions of Ca^{2+} with the model peptide L-alanyl-L-alanine (2Ala). Linear IR spectra show a pronounced blueshifted shoulder of the carboxylate peak. Furthermore we observe a small redshift of the amide CO band. Experiments with ^{13}C labeled 2Ala reveal that the shoulder indeed stems from interaction of the carboxylate with Ca^{2+}. 2DIR spectra show changes in the population lifetime for both peaks indicating that even though we do not see a blueshift (as seen for e.g. NMA) Ca^{2+} seems to interact with the amide CO. Using density functional theory (DFT) and Born-Oppenheimer molecular dynamics simulations (BOMD) we find that Ca^{2+} binds in a monodentate manner to the carboxylate group, localizing the charge on one of the COO^- oxygens, leading to a blueshift of the non-bonded CO group. Additionally we find a species of two monodentate Ca^{2+} binding to the carboxylate group, leading to an additional blueshift. Finally we find evidence for direct interaction of the Ca^{2+} with the amide CO. Contrary to the case of NMA, where the direct interaction with a Ca^{2+} leads to a blueshift, we see only see a small redshift. This difference is due to the different hydration states for NMA 2Ala.

The carbonyl in NMA is more accessible and is hydrated by on average two water molecules while for 2Ala the average number of water molecules is less than one. The Ca^{2+} replaces all water molecules and thus leads to different shifts depnending on how many water molecules were replaced. Our results highlight how the presence of multiple binding sites in a system changes the interactions as compared to the isolated cases such as NMA or alanine. Furthermore our research emphasizes the necessity of considering multiple techniques with different sensitivities as the absence of signal or shift, does not necessarily mean an absence of interaction.

Our results discuss the importance of considering the peptide interaction with water when discussing changes appearing due to ions. However we thus far only treat the peptide water interactions in the simulations. 2C2DIR measurements could provide valuable insights into water peptide interactions, because coupling peaks only appear for water molecules that directly interact with the peptide. Thus these experiments could help to take the hydration state of peptides into account when studying specific ion effects also for larger peptides.

Appendix A

Appendix

A.1 Usage of KI Tools

I hearby declare I used "DeepL Translate" to assist the translation of the "Abstract" section into german "Zusammenfassung". I declare that I did verify the translation to convey the same meaning as the english abstract.

Bibliography

(1) Gunkel, L.; Ehrhard, A. A.; Krevert, C. S.; Marekha, B. A.; Bonn, M.; Grechko, M.; Hunger, J. *Nature Communications* **2024**, *15*, 1–9.

(2) Caporaletti, F.; Gunkel, L.; Fernández-Ibáñez, M. Á.; Hunger, J.; Woutersen, S. *Angewandte Chemie - International Edition* **2024**, *63*.

(3) Krevert, C. S.; Gunkel, L.; Sutter, J.; Meyer, R.; Schneider, P.; Nagata, Y.; Hunger, J. *The Journal of Physical Chemistry B* **2024**, *128*, 10688–10698.

(4) Krevert, C. S.; Gunkel, L.; Haese, C.; Hunger, J. *Communications Chemistry* **2022**, *5*, 173.

(5) Seki, T.; Yu, X.; Zhang, P.; Yu, C. C.; Liu, K.; Gunkel, L.; Dong, R.; Nagata, Y.; Feng, X.; Bonn, M. *Chem* **2021**, *7*, 2758–2770.

(6) Ehrhard, A. A.; Gunkel, L.; Jäger, S.; Sell, A. C.; Nagata, Y.; Hunger, J. *ACS Catalysis* **2022**, *12*, 12689–12700.

(7) Wang, J.; Román-Pérez, G.; Soler, J. M.; Artacho, E.; Fernández-Serra, M. V. *Journal of Chemical Physics* **2011**, *134*.

(8) Kühne, T. D.; Krack, M.; Parrinello, M. *Journal of Chemical Theory and Computation* **2009**, *5*, 235–241.

(9) Elgabarty, H.; Kaliannan, N. K.; Kühne, T. D. *Scientific Reports* **2019**, *9*, 1–8.

(10) Berkessel, A.; Adrio, J. A.; Hüttenhain, D.; Neudörfl, J. M. *Journal of the American Chemical Society* **2006**, *128*, 8421–8426.

(11) Shinokita, K.; Cunha, A. V.; Jansen, T. L.; Pshenichnikov, M. S. *Journal of Chemical Physics* **2015**, *142*.

(12) Møller, K. B.; Rey, R.; Hynes, J. T. *Journal of Physical Chemistry A* **2004**, *108*, 1275–1289.

(13) Zhang, C.; Khaliullin, R. Z.; Bovi, D.; Guidoni, L.; Kühne, T. D. *Journal of Physical Chemistry Letters* **2013**, *4*, 3245–3250.

(14) Elgabarty, H.; Kühne, T. D. *Physical Chemistry Chemical Physics* **2020**, *22*, 10397–10411.

(15) Lawrence, C. P.; Skinner, J. L. *Journal of Chemical Physics* **2003**, *118*, 264–272.

(16) Lawrence, C. P.; Skinner, J. L. *Chemical Physics Letters* **2003**, *369*, 472–477.

(17) Auer, B. M.; Skinner, J. L. *Journal of Chemical Physics* **2008**, *128*.

(18) Perakis, F.; De Marco, L.; Shalit, A.; Tang, F.; Kann, Z. R.; Kühne, T. D.; Torre, R.; Bonn, M.; Nagata, Y. *Chemical Reviews* **2016**, *116*, 7590–7607.

(19) De Marco, L.; Carpenter, W.; Liu, H.; Biswas, R.; Bowman, J. M.; Tokmakoff, A. *Journal of Physical Chemistry Letters* **2016**, *7*, 1769–1774.

(20) Zhang, B. et al. *Proceedings of the National Academy of Sciences of the United States of America* **2020**, *117*, 15423–15428.

(21) Hamm, P.; Zanni, M. T., *Concepts and Methods of 2D Infrared Experiments*; Cambridge University Press: Oxford, UK, 2011.

(22) Seki, T.; Chiang, K.-Y.; Yu, C.-C.; Yu, X.; Okuno, M.; Hunger, J.; Nagata, Y.; Bonn, M. *The Journal of Physical Chemistry Letters* **2020**, *11*, 8459–8469.

(23) Kitadai, N.; Maruyama, S. *Geoscience Frontiers* **2018**, *9*, 1117–1153.

(24) Pettersson, L. G. M.; Henchman, R. H.; Nilsson, A. *Chemical Reviews* **2016**, *116*, 7459–7462.

(25) Röntgen, W. C. *Annalen der Physik* **1892**, *281*, 91–97.

(26) Finney, J. L. *Journal of Chemical Physics* **2024**, *160*.

(27) Chadwell, H. M. *Chemical Reviews* **1928**, *4*, 375–398.

(28) Eisenberg, D; Kauzmann, W, *The Structure and Properties of Water*; Oxford University Press: London, 1969.

(29) Poole, P. H.; Sciortino, F.; Essmann, U.; Stanley, H. E. *Nature* **1992**, *360*, 324–328.

(30) Poole, P. H.; Sciortino, F.; Grande, T.; Stanley, H. E.; Angell, C. A. *Physical Review Letters* **1994**, *73*, 1632–1635.

(31) Huang, C. et al. *Proceedings of the National Academy of Sciences of the United States of America* **2009**, *106*, 15214–15218.

(32) Clark, G. N.; Hura, G. L.; Teixeira, J.; Soper, A. K.; Head-Gordon, T. *Proceedings of the National Academy of Sciences of the United States of America* **2010**, *107*, 14003–14007.

(33) Nilsson, A.; Pettersson, L. G. M. *Nature Communications* **2015**, *6*, 8998.

(34) Faccio, C.; Benzi, M.; Zanetti-Polzi, L.; Daidone, I. *Journal of Molecular Liquids* **2022**, *355*, 118922.

(35) Pietzsch, A.; Niskanen, J.; da Cruz, V. V.; Büchner, R.; Eckert, S.; Fondell, M.; Jay, R. M.; Lu, X.; McNally, D.; Schmitt, T.; Föhlisch, A. *Proceedings of the National Academy of Sciences of the United States of America* **2022**, *119*, 2–7.

(36) Bragg, S. W. H. *Journal of the Franklin Institute* **1921**, *191*, 572.

(37) Barnes, W. H. *Proceedings of the Royal Society of London. Series A, Containing Papers of a Mathematical and Physical Character* **1929**, *125*, 670–693.

(38) Edoardo Amaldi *Physikalische Zeitschrift* **1931**, *32*, 914–919.

(39) Bernal, J. D.; Fowler, R. H. *The Journal of Chemical Physics* **1933**, *1*, 515–548.

(40) Wernet, P.; Nordlund, D.; Bergmann, U.; Cavalleri, M.; Odelius, N.; Ogasawara, H.; Näslund, L. Å; Hirsch, T. K.; Ojamäe, L.; Glatzel, P.; Pettersson, L. G.; Nilsson, A. *Science* **2004**, *304*, 995–999.

(41) Soper, A. K. *Journal of Physics Condensed Matter* **2005**, *17*.

(42) Head-Gordon, T.; Johnson, M. E. *Proceedings of the National Academy of Sciences* **2006**, *103*, 7973–7977.

(43) Tokushima, T.; Harada, Y.; Takahashi, O.; Senba, Y.; Ohashi, H.; Pettersson, L. G.; Nilsson, A.; Shin, S. *Chemical Physics Letters* **2008**, *460*, 387–400.

(44) Leetmaa, M.; Ljungberg, M.; Ogasawara, H.; Odelius, M.; Näslund, L. Å.; Nilsson, A.; Pettersson, L. G. *Journal of Chemical Physics* **2006**, *125*, 1–12.

(45) Kühne, T. D.; Khaliullin, R. Z. *Nature Communications* **2013**, *4*, 1–7.

(46) Kühne, T. D.; Khaliullin, R. Z. *Journal of the American Chemical Society* **2014**, *136*, 3395–3399.

(47) Fecko, C. J.; Eaves, J. D.; Loparo, J. J.; Tokmakoff, A.; Geissler, P. L. *Science* **2003**, *301*, 1698–1702.

(48) Fayer, M. D.; Moilanen, D. E.; Wong, D.; Rosenfeld, D. E.; Fenn, E. E.; Park, S. *Accounts of chemical research* **2009**, *42*, 1210–1219.

(49) Jansen, T. L.; Cringus, D.; Pshenichnikov, M. S. *Journal of Physical Chemistry A* **2009**, *113*, 6260–6265.

(50) Deàk, J. C.; Rhea, S. T.; Iwaki, L. K.; Dlott, D. D. *Journal of Physical Chemistry A* **2000**, *104*, 4866–4875.

(51) Fragiadakis, D.; Roland, C. M.; Casalini, R. *Journal of Chemical Physics* **2010**, *132*.

(52) Vrhovšek, A.; Gereben, O.; Jamnik, A.; Pusztai, L. *Journal of Physical Chemistry B* **2011**, *115*, 13473–13488.

(53) Gaffney, K. J.; Davis, P. H.; Piletic, I. R.; Levinger, N. E.; Fayer, M. D. *Journal of Physical Chemistry A* **2002**, *106*, 12012–12023.

(54) Colomer, I.; Chamberlain, A. E. R.; Haughey, M. B.; Donohoe, T. J. *Nature Reviews Chemistry* **2017**, *1*, 0088.

(55) Neimann, K.; Neumann, R. *Organic Letters* **2000**, *2*, 2861–2863.

(56) Berkessel, A.; Andreae, M. R. *Tetrahedron Letters* **2001**, *42*, 2293–2295.

(57) Berkessel, A.; Andreae, M. R. M.; Schmickler, H.; Lex, J. *Angewandte Chemie International Edition* **2002**, *41*, 4481–4484.

(58) Berkessel, A.; Adrio, J. A. *Journal of the American Chemical Society* **2006**, *128*, 13412–13420.

(59) Mohamadpour, F. *Results in Chemistry* **2024**, *9*, 101629.

(60) Giubertoni, G. et al. *Proceedings of the National Academy of Sciences of the United States of America* **2024**, *121*, 1–11.

(61) Reynolds, J. G. *Journal of Molecular Liquids* **2024**, *395*, 123824.

(62) Hofmeister, F. *Arch. Exp. Pathol. Pharmakol.* **1888**, *25*, 1–30.

(63) Collins, K. D.; Washabaugh, M. W. *Quarterly Reviews of Biophysics* **1985**, *18*, 323–422.

(64) Kunz, W.; Lo Nostro, P.; Ninham, B. W. *Current Opinion in Colloid and Interface Science* **2004**, *9*, 1–18.

(65) Jungwirth, P.; Cremer, P. S. *Nature Chemistry* **2014**, *6*, 261–263.

(66) Okur, H. I.; Hladílková, J.; Rembert, K. B.; Cho, Y.; Heyda, J.; Dzubiella, J.; Cremer, P. S.; Jungwirth, P. *Journal of Physical Chemistry B* **2017**, *121*, 1997–2014.

(67) Zhang, Y.; Cremer, P. S. *Current Opinion in Chemical Biology* **2006**, *10*, 658–663.

(68) Cracchiolo, O. M.; Geremia, D. K.; Corcelli, S. A.; Serrano, A. L. *Journal of Physical Chemistry B* **2020**, *124*, 6947–6954.

(69) Pluhařová, E.; Baer, M. D.; Mundy, C. J.; Schmidt, B.; Jungwirth, P. *Journal of Physical Chemistry Letters* **2014**, *5*, 2235–2240.

(70) Kashid, S. M.; Singh, R. K.; Kwon, H.; Kim, Y. S.; Mukherjee, A.; Bagchi, S. *Journal of Physical Chemistry B* **2019**, *123*, 8419–8424.

(71) Drexler, C. I.; Cracchiolo, O. M.; Myers, R. L.; Okur, H. I.; Serrano, A. L.; Corcelli, S. A.; Cremer, P. S. *Journal of Physical Chemistry B* **2021**, *125*, 8484–8493.

(72) Okur, H. I.; Kherb, J.; Cremer, P. S. *Journal of the American Chemical Society* **2013**, *135*, 5062–5067.

(73) Edington, S. C.; Baiz, C. R. *Journal of Physical Chemistry A* **2018**, *122*, 6585–6592.

(74) Magarkar, A.; Jurkiewicz, P.; Allolio, C.; Hof, M.; Jungwirth, P. *Journal of Physical Chemistry Letters* **2017**, *8*, 518–523.

(75) Bilkova, E.; Pleskot, R.; Rissanen, S.; Sun, S.; Czogalla, A.; Cwiklik, L.; Róg, T.; Vattulainen, I.; Cremer, P. S.; Jungwirth, P.; Coskun, Ü. *Journal of the American Chemical Society* **2017**, *139*, 4019–4024.

(76) Berridge, M.; Lipp, P.; Bootman, M. *Current Biology* **1999**, *9*, 157–159.

(77) Al-saad, K.; El-shafie, A. S., *Infrared Spectroscopy - Perspectives and Applications*, 2022.

(78) Hollas, J. M., *Modern Spectroscopy*, 4th ed.; John Wiley & Sons: Chichester, England, 2003, p 482.

(79) Atkins, P.; De Paula, J., *Atkins' physical chemistry*, 8th ed.; Oxford University Press: London, England, 2006, p 1096.

(80) Maxwell, J. C. *Philosophical Transactions of the Royal Society of London* **1865**, *155*, 459–512.

(81) Kremer, F.; Schönhals, A., *Broadband Dielectric Spectroscopy*; Kremer, F., Schönhals, A., Eds.; Springer Berlin Heidelberg: Berlin, Heidelberg, 2003, pp 41–73.

(82) Jackson, J. D., *Classical Electrodynamics*; Jackson, J. D., Ed.; John Wiley & Sons: New York, 1975, p 641.

(83) Cohen, M. L.; Louie, S. G., *Fundamentals of Condensed Matter Physics*; Cambridge University Press: Cambridge, 2016.

(84) Barthel, J.; Buchner, R. *Chemical Society Reviews* **1992**, *21*, 263.

(85) Marder, M. P., *Condensed Matter Physics*, Second Edi; Marder, M. P., Ed.; John Wiley & Sons, Inc: Hoboken, New Jersey, 2010, p 562.

(86) Parson, W. W., *Modern Optical Spectroscopy*, Secon Edit; Springer Berlin Heidelberg: Berlin, Heidelberg, 2015.

(87) Zhao, J.; Wang, J. *Journal of Physical Chemistry B* **2015**, *119*, 14831–14839.

(88) Hochstrasser, R. M. *Proceedings of the National Academy of Sciences of the United States of America* **2007**, *104*, 14190–14196.

(89) Kwak, K.; Park, S.; Finkelstein, I. J.; Fayer, M. D. *Journal of Chemical Physics* **2007**, *127*.

(90) Kubo, R. In *Stochastic Processes in Chemical Physics*; 1, 1969; Vol. 15, pp 101–127.

(91) Attig, N.; Binder, K.; Grubmueller, H.; Kremer, K., *Computational Soft Matter: From Synthetic Polymers to Proteins*; Attig, N., Binder, K., Grubmueller, H., Kremer, K., Eds., 2004; Vol. 23, p 440.

(92) Hansen, Jean-Pierre; McDonald, I. R., *Theory of Simple Liquids*, Fourth Edi; Hansen, Jean-Pierre; McDonald, I. R., Ed.; 9; Academic Press: Oxford, 2013, p 424.

(93) Verlet, L. *Physical Review* **1967**, *159*, 98–103.

(94) Verlet, L. *Physical Review* **1968**, *165*, 201–214.

(95) Hockney, R.; Eastwood, J., *Computer Simulation Using Particles*, 1st ed.; CRC Press: 1988.

(96) Swope, W. C.; Andersen, H. C.; Berens, P. H.; Wilson, K. R. *The Journal of Chemical Physics* **1982**, *76*, 637–649.

(97) Andersen, H. C. *The Journal of Chemical Physics* **1980**, *72*, 2384–2393.

(98) Evans, D. J.; Holian, B. L. *The Journal of Chemical Physics* **1985**, *83*, 4069–4074.

(99) Marx, D.; Hutter, J., *Ab Initio Molecular Dynamics*; Cambridge University Press: 2010.

(100) Levine, B. G.; Stone, J. E.; Kohlmeyer, A. *Journal of Computational Physics* **2011**, *230*, 3556–3569.

(101) Wang, J.; Wolf, R. M.; Caldwell, J. W.; Kollman, P. A.; Case, D. A. *Journal of Computational Chemistry* **2004**, *25*, 1157–1174.

(102) Ponder, J. W.; Case, D. A. *Advances in Protein Chemistry* **2003**, *66*, 27–85.

(103) Brooks, B. R.; Bruccoleri, R. E.; Olafson, B. D.; States, D. J.; Swaminathan, S.; Karplus, M. *Journal of Computational Chemistry* **1983**, *4*, 187–217.

(104) Brooks, B. R. et al. *Journal of Computational Chemistry* **2009**, *30*, 1545–1614.

(105) Jorgensen, W. L.; Maxwell, D. S.; Tirado-Rives, J. *Journal of the American Chemical Society* **1996**, *118*, 11225–11236.

(106) Born, M.; Oppenheimer, R. *Annalen der Physik* **1927**, *389*, 457–484.

(107) Copley, J. R.; Lovesey, S. W. *Reports on Progress in Physics* **1975**, *38*, 461–563.

(108) Karthick Kumar, S. K.; Tamimi, A.; Fayer, M. D. *Journal of Chemical Physics* **2012**, *137*.

(109) Neese, F.; Wennmohs, F.; Becker, U.; Riplinger, C. *Journal of Chemical Physics* **2020**, *152*.

(110) Lee, C.; Yang, W.; Parr, R. G. *Physical Review B* **1988**, *37*, 785–789.

(111) Becke, A. D. *Physical Review A* **1988**, *38*, 3098–3100.

(112) Grimme, S.; Antony, J.; Ehrlich, S.; Krieg, H. *Journal of Chemical Physics* **2010**, *132*.

(113) Grimme, S.; Ehrlich, S.; Goerigk, L. *Journal of Computational Chemistry* **2011**, *32*, 1456–1465.

(114) Weigend, F.; Ahlrichs, R. *Physical Chemistry Chemical Physics* **2005**, *7*, 3297–3305.

(115) Weigend, F. *Physical Chemistry Chemical Physics* **2006**, *8*, 1057–1065.

(116) Scalmani, G.; Frisch, M. J. *Journal of Chemical Physics* **2010**, *132*, 114110.

(117) Buczek, A.; Kupka, T.; Sauer, S. P.; Broda, M. A. *Journal of Molecular Modeling* **2012**, *18*, 2471–2478.

(118) Cowan, M. L.; Bruner, B. D.; Huse, N; Dwyer, J. R.; Chugh, B; Nibbering, E. T. J.; Elsaesser, T; Miller, R. J. D. *Nature* **2005**, *434*, 199–202.

(119) Jansen, T. L.; Auer, B. M.; Yang, M.; Skinner, J. L. *Journal of Chemical Physics* **2010**, *132*.

(120) Yang, M.; Li, F.; Skinner, J. L. *Journal of Chemical Physics* **2011**, *135*.

(121) Krevert, C. S.; Chavez, D.; Chatterjee, S.; Stelzl, L. S.; Pütz, S.; Roeters, S. J.; Rudzinski, J. F.; Fawzi, N. L.; Girard, M.; Parekh, S. H.; Hunger, J. *J. Phys. Chem. Lett.* **2023**, *14*, 11224–11234.

(122) Blackham, D. V.; Pollard, R. D. *IEEE Trans. Instrum. Meas* **1997**, *46*, 1093–1099.

(123) Kaatze, U. *Measurement Science and Technology* **2013**, *24*, 012005.

(124) Ensing, W; Hunger, J; Ottosson, N; Bakker, H. J. *Journal of Physical Chemistry C* **2013**, *117*, 12930–12935.

(125) Balos, V.; Kim, H.; Bonn, M.; Hunger, J. *Angewandte Chemie - International Edition* **2016**, *55*, 8125–8128.

(126) Schrödle, S.; Hefter, G.; Kunz, W.; Buchner, R. *Langmuir* **2006**, *22*, 924–932.

(127) Becke, A. D. *J. Chem. Phys.* **1993**, *98*, 5648–5652.

(128) Vosko, S. H.; Wilk, L; Nusair, M *Canadian Journal of Physics* **1980**, *58*, 1200–1211.

(129) Stephen, P. J.; Devlin, F. J.; Chabalowski, C. F.; Frisch, M. J. *The Journal of Physical Chemistry* **1994**, *98*, 11623–11627.

(130) Krishnan, R.; Binkley, J. S.; Seeger, R.; Pople, J. A. *The Journal of Chemical Physics* **1980**, *72*, 650–654.

(131) Klamt, A.; Schüürmann, G. *Journal of the Chemical Society, Perkin Transactions 2* **1993**, 799–805.

(132) Andzelm, J.; Kölmel, C.; Klamt, A. *The Journal of Chemical Physics* **1995**, *103*, 9312–9320.

(133) Barone, V.; Cossi, M. *Journal of Physical Chemistry A* **1998**, *102*, 1995–2001.

(134) Cossi, M.; Rega, N.; Scalmani, G.; Barone, V. *Journal of Computational Chemistry* **2003**, *24*, 669–681.

(135) Middleton, C. T.; Woys, A. M.; Mukherjee, S. S.; Zanni, M. T. *Methods* **2010**, *52*, 12–22.

(136) Strasfeld, D. B.; Middleton, C. T.; Zanni, M. T. *New Journal of Physics* **2009**, *11*.

(137) Hutter, J.; Iannuzzi, M.; Schiffmann, F.; Vandevondele, J. *Wiley Interdisciplinary Reviews: Computational Molecular Science* **2014**, *4*, 15–25.

(138) Zhang, Y.; Yang, W. *Physical Review Letters* **1998**, *80*, 890.

(139) Vandevondele, J.; Krack, M.; Mohamed, F.; Parrinello, M.; Chassaing, T.; Hutter, J. *Computer Physics Communications* **2005**, *167*, 103–128.

(140) Goedecker, S.; Teter, M. *Physical Review B - Condensed Matter and Materials Physics* **1996**, *54*, 1703–1710.

(141) Bussi, G.; Donadio, D.; Parrinello, M. *Journal of Chemical Physics* **2007**, *126*.

(142) Humphrey, W.; Dalke, A.; Schulten, K. *Journal of molecular graphics* **1996**, *14*, 33–38.

(143) Li, K.; Luo, L.; Zhang, Y.; Li, W.; Hou, Y. *ACS Applied Materials and Interfaces* **2018**, *10*, 41525–41534.

(144) Zhang, J.; Lu, T. *Physical Chemistry Chemical Physics* **2021**, *23*, 20323–20328.

(145) Lu, T.; Chen, F. *Journal of Computational Chemistry* **2012**, *33*, 580–592.

(146) Glasser, L. *Journal of Chemical Education* **1987**, *64*, A228.

(147) Prabhu, K. M. M., *Window Functions and Their Applications in Signal Processing*; CRC Press: Boca Raton, London, New York, 2014.

(148) Clark, G. N.; Cappa, C. D.; Smith, J. D.; Saykally, R. J.; Head-Gordon, T. *Molecular Physics* **2010**, *108*, 1415–1433.

(149) Stillinger, F. H. *Science* **1980**, *209*, 451–457.

(150) Russo, J.; Tanaka, H. *Nature Communications* **2014**, *5*, 3556.

(151) Liu, J.; He, X.; Zhang, J. Z. *Physical Chemistry Chemical Physics* **2017**, *19*, 11931–11936.

(152) Russo, J.; Akahane, K.; Tanaka, H. *Proceedings of the National Academy of Sciences of the United States of America* **2018**, *115*, E3333–E3341.

(153) Neophytou, A.; Chakrabarti, D.; Sciortino, F. *Nature Physics* **2022**, *18*, 1248–1253.

(154) Duboué-Dijon, E.; Laage, D. *Journal of Physical Chemistry B* **2015**, *119*, 8406–8418.

(155) Kim, K. H.; Späh, A.; Pathak, H.; Perakis, F.; Mariedahl, D.; Amann-Winkel, K.; Sellberg, J. A.; Lee, J. H.; Kim, S.; Park, J.; Nam, K. H.; Katayama, T.; Nilsson, A. *Science* **2017**, *358*, 1589–1593.

(156) Yun, Y.; Khaliullin, R. Z.; Jung, Y. *Journal of the American Chemical Society* **2022**, *144*, 13127–13136.

(157) Møller, K. B.; Rey, R.; Hynes, J. T. *Journal of Physical Chemistry A* **2004**, *108*, 1275–1289.

(158) Ramasesha, K.; De Marco, L.; Mandal, A.; Tokmakoff, A. *Nature Chemistry* **2013**, *5*, 935–940.

(159) Yu, C. C.; Chiang, K. Y.; Okuno, M.; Seki, T.; Ohto, T.; Yu, X.; Korepanov, V.; Hamaguchi, H. o.; Bonn, M.; Hunger, J.; Nagata, Y. *Nature Communications* **2020**, *11*, 5977.

(160) Matt, S. M.; Ben-Amotz, D. *Journal of Physical Chemistry B* **2018**, *122*, 5375–5380.

(161) Koverga, V.; Juhász, Á.; Dudariev, D.; Lebedev, M.; Idrissi, A.; Jedlovszky, P. *Journal of Physical Chemistry B* **2022**, *126*, 6964–6978.

(162) Lotze, S.; Groot, C. C.; Vennehaug, C.; Bakker, H. J. *Journal of Physical Chemistry B* **2015**, *119*, 5228–5239.

(163) Wulf, A.; Ludwig, R. *ChemPhysChem* **2006**, *7*, 266–272.

(164) Biliškov, N.; Baranović, G. *Journal of Molecular Liquids* **2009**, *144*, 155–162.

(165) Tokmakoff, A.; Fayer, M. D. *The Journal of Chemical Physics* **1995**, *103*, 2810–2826.

(166) Kim, Y. S.; Hochstrasser, R. M. *Journal of Physical Chemistry B* **2009**, *113*, 8231–8251.

(167) Cundiff, S. T.; Mukamel, S. *Physics Today* **2013**, *66*, 44–49.

(168) Van Hoozen, B. L.; Petersen, P. B. *Journal of Chemical Physics* **2018**, *148*.

(169) Kuroda, D. G.; Abdo, M.; Chuntonov, L.; Smith, A. B.; Hochstrasser, R. M. *Journal of Chemical Physics* **2013**, *139*.

(170) Kumar, K.; Sinks, L. E.; Wang, J.; Kim, Y. S.; Hochstrasser, R. M. *Chemical Physics Letters* **2006**, *432*, 122–127.

(171) Rubtsov, I. V.; Wang, J.; Hochstrasser, R. M. *Proceedings of the National Academy of Sciences of the United States of America* **2003**, *100*, 5601–5606.

(172) Hoffman, D. J.; Fayer, M. D. *Journal of Physical Chemistry A* **2020**, *124*, 5979–5992.

(173) Wong, D. B.; Giammanco, C. H.; Fenn, E. E.; Fayer, M. D. *Journal of Physical Chemistry B* **2013**, *117*, 623–635.

(174) Duan, R.; Mastron, J. N.; Song, Y.; Kubarych, K. J. *Journal of Chemical Physics* **2021**, *154*.

(175) Marroux, H. J.; Orr-Ewing, A. J. *Journal of Physical Chemistry B* **2016**, *120*, 4125–4130.

(176) Bakker, H. J.; Woutersen, S; Nienhuys, H.-K. *Chem. Phys.* **2000**, *258*, 233–245.

(177) Kandratsenka, A.; Schroeder, J.; Schwarzer, D.; Vikhrenko, V. S. *Journal of Chemical Physics* **2009**, *130*.

(178) Vaz da Cruz, V. et al. *Nature Communications* **2019**, *10*, 1–9.

(179) Vaz da Cruz, V.; Ertan, E.; Couto, R. C.; Eckert, S.; Fondell, M.; Dantz, M.; Kennedy, B.; Schmitt, T.; Pietzsch, A.; Guimarães, F. F.; Ågren, H.; Gel'Mukhanov, F.; Odelius, M.; Föhlisch, A.; Kimberg, V. *Physical Chemistry Chemical Physics* **2017**, *19*, 19573–19589.

(180) Van Der Post, S. T.; Hsieh, C. S.; Okuno, M.; Nagata, Y.; Bakker, H. J.; Bonn, M.; Hunger, J. *Nature Communications* **2015**, *6*.

(181) De Marco, L.; Ramasesha, K.; Tokmakoff, A. *Journal of Physical Chemistry B* **2013**, *117*, 15319–15327.

(182) Tokmakoff, A.; Urdahl, R. S.; Zimdars, D.; Francis, R. S.; Kwok, A. S.; Fayer, M. D. *The Journal of Chemical Physics* **1995**, *102*, 3919–3931.

(183) Saito, Y.; Machida, K.; Uno, T. *Spectrochimica Acta Part A: Molecular Spectroscopy* **1971**, *27*, 991–1002.

(184) Keuleers, R; Desseyn, H. O.; Rousseau, B.; Van Alsenoy, C. *Journal of Physical Chemistry A* **1999**, *103*, 4621–4630.

(185) Motiwala, H. F.; Armaly, A. M.; Cacioppo, J. G.; Coombs, T. C.; Koehn, K. R.; Norwood, V. M.; Aubé, J. *Chemical Reviews* **2022**, *122*, 12544–12747.

(186) Cai, S.; Tang, H.; Li, B.; Shao, Y.; Zhang, D.; Zheng, H.; Qiao, T.; Chu, X.; He, G.; Xue, X. S.; Chen, G. *Journal of the American Chemical Society* **2024**, *146*, 5952–5963.

(187) Bhattacharya, T.; Ghosh, A.; Maiti, D. *Chemical Science* **2021**, *12*, 3857–3870.

(188) Sukowski, V.; van Borselen, M.; Mathew, S.; Fernández-Ibáñez, M. Á. *Angewandte Chemie - International Edition* **2022**, *61*.

(189) Hirota, N.; Mizuno, K.; Goto, Y. *Protein Science* **1997**, *6*, 416–421.

(190) Schaal, H.; Häber, T.; Suhm, M. A. *Journal of Physical Chemistry A* **2000**, *104*, 265–274.

(191) Czarnik-Matusewicz, B.; Pilorz, S.; Zhang, L. P.; Wu, Y. *Journal of Molecular Structure* **2008**, *883-884*, 195–202.

(192) Zeng, X.; Li, J.; Ng, C. K.; Hammond, G. B.; Xu, B. *Angewandte Chemie* **2018**, *130*, 2974–2978.

(193) Ramos-Villaseñor, J. M.; Rodríguez-Cárdenas, E.; Barrera Díaz, C. E.; Frontana-Uribe, B. A. *Journal of The Electrochemical Society* **2020**, *167*, 155509.

(194) Yoneda, N.; Iyama, H.; Nagata, T.; Katahira, M.; Ishii, Y.; Tada, K.; Matsumoto, K.; Hagiwara, R. *Journal of Physical Chemistry Letters* **2024**, *15*, 1677–1685.

(195) Oswald, S.; Seifert, N. A.; Bohle, F.; Gawrilow, M.; Grimme, S.; Jäger, W.; Xu, Y.; Suhm, M. A. *Angewandte Chemie - International Edition* **2019**, *58*, 5080–5084.

(196) Hibbert, F.; Emsley, J. In Bethell, D, Ed.; Advances in Physical Organic Chemistry, Vol. 26; Academic Press: 1990, pp 255–379.

(197) Ensing, B.; Tiwari, A.; Tros, M.; Hunger, J.; Domingos, S. R.; Pérez, C.; Smits, G.; Bonn, M.; Bonn, D.; Woutersen, S. *Nature Communications* **2019**, *10*, 1–8.

(198) Tros, M.; Zheng, L.; Hunger, J.; Bonn, M.; Bonn, D.; Smits, G. J.; Woutersen, S. *Nature Communications* **2017**, *8*, 1–7.

(199) Lawrence, C. P.; Skinner, J. L. *Journal of Chemical Physics* **2003**, *118*, 264–272.

(200) Ramasesha, K.; Roberts, S. T.; Nicodemus, R. A.; Mandal, A.; Tokmakoff, A. *The Journal of Chemical Physics* **2011**, *135*.

(201) Mazur, K.; Bonn, M.; Hunger, J. *Journal of Physical Chemistry B* **2015**, *119*, 1558–1566.

(202) Elsaesser, T. *Accounts of Chemical Research* **2009**, *42*, 1220–1228.

(203) Marekha, B. A.; Hunger, J. *Physical Chemistry Chemical Physics* **2019**, *21*, 20672–20677.

(204) Czurlok, D.; Von Domaros, M.; Thomas, M.; Gleim, J.; Lindner, J.; Kirchner, B.; Vöhringer, P. *Physical Chemistry Chemical Physics* **2015**, *17*, 29776–29785.

(205) Hume, S.; Greetham, G. M.; Donaldson, P. M.; Towrie, M.; Parker, A. W.; Baker, M. J.; Hunt, N. T. *Analytical Chemistry* **2020**, *92*, 3463–3469.

(206) Johnson, C. A.; Parker, A. W.; Donaldson, P. M.; Garrett-Roe, S. *Journal of Chemical Physics* **2021**, *154*.

(207) Caporaletti, F.; Bonn, D.; Woutersen, S. *Journal of Physical Chemistry Letters* **2021**, *12*, 5951–5956.

(208) Lorenz-Ochoa, K. A.; Baiz, C. R. *Journal of the American Chemical Society* **2023**, *145*, 27800–27809.

(209) Hunt, N. T. *Accounts of Chemical Research* **2024**, *57*, 685–692.

(210) Feng, C. J.; Tokmakoff, A. *J. Chem. Phys.* **2017**, *147*, 85101.

(211) Williams, G. *Chemical Reviews* **1972**, *72*, 55–69.

(212) Buchner, R. *Pure and Applied Chemistry* **2008**, *80*, 1239–1252.

(213) Böhmer, R.; Gainaru, C.; Richert, R. *Physics Reports* **2014**, *545*, 125–195.

(214) Patil, S.; Sun, R.; Cheng, S.; Cheng, S. *Physical Review Letters* **2023**, *130*, 098201.

(215) D. Hadži, S. B. In *The Hydrogen Bond, Vol II*, P. Schuster, G. Zundel, C. S., Ed.; Elsevier: Amsterdam, 1976; Chapter 12.

(216) Woutersen, S; Bakker, H. J. *Nature* **1999**, *403*, 507–509.

(217) Czarnik-Matusewicz, B.; Pilorz, S.; Bieńko, D.; Michalska, D. *Vibrational Spectroscopy* **2008**, *47*, 44–52.

(218) Futami, Y.; Kudoh, S.; amd Munetaka Nakata, M. T. *Chem. Phys. Lett.* **2002**, *3–4*, 209–216.

(219) Biswas, B.; Singh, P. C. *Journal of Fluorine Chemistry* **2020**, *235*, 109414.

(220) Liddel, U; Becker, E *Spectrochim. Acta* **1957**, *10*, 70–84.

(221) Huerta-Viga, A.; Shaw, D. J.; Woutersen, S. *J. Phys. Chem. B* **2010**, *114*, 15212–15220.

(222) Cota, R.; Van Dam, E. P.; Woutersen, S.; Bakker, H. J. *Journal of Physical Chemistry B* **2020**, *124*, 8309–8316.

(223) Laage, D.; Stirnemann, G.; Sterpone, F.; Rey, R.; Hynes, J. T. *Annu. Rev. Phys. Chem.* **2011**, *62*, 395–416.

(224) Mesele, O. O.; Vartia, A. A.; Laage, D.; Thompson, W. H. *Journal of Physical Chemistry B* **2016**, *120*, 1546–1559.

(225) Tamm, K. *Berichte der Bunsengesellschaft für physikalische Chemie* **1980**, *84*, 1190–1191.

(226) Wieth, P; Vogel, M *Journal of Chemical Physics* **2014**, *140*.

(227) Barthel, J.; Bachhuber, K.; Buchner, R.; Hetzenauer, H. *Chemical Physics Letters* **1990**, *165*, 369–373.

(228) Fukasawa, T.; Sato, T.; Watanabe, J.; Hama, Y.; Kunz, W.; Buchner, R. *Phys. Rev. Lett.* **2005**, *95*, 1–4.

(229) Gainaru, C.; Meier, R.; Schildmann, S.; Lederle, C.; Hiller, W.; Rössler, E. A.; Böhmer, R. *Physical Review Letters* **2010**, *105*, 1–4.

(230) Gabriel, J.; Pabst, F.; Blochowicz, T. *Journal of Physical Chemistry B* **2017**, *121*, 8847–8853.

(231) Xu, D.; Feng, S.; Wang, J. Q.; Wang, L. M.; Richert, R *Journal of Physical Chemistry Letters* **2020**, *11*, 5792–5797.

(232) Bolle, J.; Bierwirth, S. P.; Požar, M.; Perera, A.; Paulus, M.; Münzner, P.; Albers, C.; Dogan, S.; Elbers, M.; Sakrowski, R.; Surmeier, G.; Böhmer, R.; Tolan, M.; Sternemann, C. *Physical Chemistry Chemical Physics* **2021**, *23*, 24211–24221.

(233) Pabst, F.; Gabriel, J. P.; Böhmer, T.; Weigl, P.; Helbling, A.; Richter, T.; Zourchang, P.; Walther, T.; Blochowicz, T. *Journal of Physical Chemistry Letters* **2021**, *12*, 3685–3690.

(234) Koperwas, K.; Paluch, M. *Physical Review Letters* **2022**, *129*, 25501.

(235) Böhmer, T.; Pabst, F.; Gabriel, J. P.; Blochowicz, T. *Physical Review Letters* **2024**, *132*, 206101.

(236) Laage, D.; Hynes, J. T. *Journal of Physical Chemistry B* **2008**, *112*, 14230–14242.

(237) Cabaço, M. I.; Besnard, M.; Cruz, C.; Morgado, P.; Silva, G. M.; Filipe, E. J.; Coutinho, J. A.; Danten, Y. *Journal of Physical Chemistry B* **2022**, *126*, 1992–2004.

(238) Asbury, J. B.; Steinel, T.; Fayer, M. D. *Journal of Luminescence* **2004**, *107*, 271–286.

(239) Knop, S.; Jansen, T. L. C.; Lindner, J.; Vöhringer, P. *Physical Chemistry Chemical Physics* **2011**, *13*, 4641–4650.

(240) Middleton, W. J.; Lindsey, R. V. *Journal of the American Chemical Society* **1964**, *86*, 5712.

(241) Vuluga, D.; Legros, J.; Crousse, B.; Slawin, A. M.; Laurence, C.; Nicolet, P.; Bonnet-Delpon, D. *Journal of Organic Chemistry* **2011**, *76*, 1126–1133.

(242) Spange, S.; Weiß, N.; Schmidt, C. H.; Schreiter, K. *Chemistry-Methods* **2021**, *1*, 42–60.

(243) Ehrhard, A. A.; Jäger, S.; Malm, C.; Basaran, S.; Hunger, J. *Journal of Molecular Liquids* **2019**, *296*.

(244) Rezus, Y. L. A.; Bakker, H. J. *J. Phys. Chem. A* **2008**, *112*, 2355–2361.

(245) Neurath, H.; Greenstein, J. P.; Putnam, F. W.; Erickson, J. O. *Chemical Reviews* **1944**, *34*, 157–265.

(246) Pinna, M. C.; Bauduin, P; Touraud, D; Monduzzi, M; Ninham, B. W.; Kunz, W *Journal of Physical Chemistry B* **2005**, *109*, 16511–16514.

(247) Jungwirth, P.; Winter, B. *Annual Review of Physical Chemistry* **2008**, *59*, 343–366.

(248) Kastelic, M.; Kalyuzhnyi, Y. V.; Hribar-Lee, B.; Dil, K. A.; Vlachy, V. *Proceedings of the National Academy of Sciences of the United States of America* **2015**, *112*, 6766–6770.

(249) Balos, V.; Marekha, B.; Malm, C.; Wagner, M.; Nagata, Y.; Bonn, M.; Hunger, J. *Angewandte Chemie - International Edition* **2019**, *58*, 332–337.

(250) Balos, V; Bonn, M; Hunger, J *Physical Chemistry Chemical Physics* **2017**, *19*, 9724–9728.

(251) Pasquier, C.; Vazdar, M.; Forsman, J.; Jungwirth, P.; Lund, M. *Journal of Physical Chemistry B* **2017**, *121*, 3000–3006.

(252) De Oliveira, D. M.; Zukowski, S. R.; Palivec, V.; Hénin, J.; Martinez-Seara, H.; Ben-Amotz, D.; Jungwirth, P.; Duboué-Dijon, E. *Physical Chemistry Chemical Physics* **2020**, *22*, 24014–24027.

(253) Hladílková, J.; Heyda, J.; Rembert, K. B.; Okur, H. I.; Kurra, Y.; Liu, W. R.; Hilty, C.; Cremer, P. S.; Jungwirth, P. *Journal of Physical Chemistry Letters* **2013**, *4*, 4069–4073.

(254) Shi, J.; Wang, J. *Journal of Physical Chemistry B* **2014**, *118*, 12336–12347.

(255) Bo, T.; Pawliszyn, J. *Analytica Chimica Acta* **2006**, *559*, 1–8.

(256) Strynadka, N. C.; James, M. N. *Current Opinion in Structural Biology* **1991**, *1*, 905–914.

(257) Lutter, J. C.; Wu, T. Y.; Zhang, Y. *Journal of Physical Chemistry B* **2013**, *117*, 10132–10141.

(258) Kim, Y. S.; Wang, J.; Hochstrasser, R. M. *Journal of Physical Chemistry B* **2005**, *109*, 7511–7521.

(259) Heyda, J.; Vincent, J. C.; Tobias, D. J.; Dzubiella, J.; Jungwirth, P. *Journal of Physical Chemistry B* **2010**, *114*, 1213–1220.

(260) Balasubramanian, D; Shaikh, R. *Biopolymers* **1973**, *12*, 1639–1650.

(261) Zhao, J.; Dong, T.; Yu, P.; Wang, J. *Journal of Physical Chemistry B* **2022**, *126*, 161–173.

(262) Vazquez de Vasquez, M. G.; Wellen Rudd, B. A.; Baer, M. D.; Beasley, E. E.; Allen, H. C. *Journal of Physical Chemistry B* **2021**, *125*, 11308–11319.

(263) Denton, J. K.; Kelleher, P. J.; Johnson, M. A.; Baer, M. D.; Kathmann, S. M.; Mundy, C. J.; Wellen Rudd, B. A.; Allen, H. C.; Choi, T. H.; Jordan, K. D. *Proceedings of the National Academy of Sciences of the United States of America* **2019**, *116*, 14874–14880.

(264) Kuroda, D. G.; Hochstrasser, R. M. *Physical Chemistry Chemical Physics* **2012**, *14*, 6219–6224.

(265) Shim, S. H.; Gupta, R.; Ling, Y. L.; Strasfeld, D. B.; Raleigh, D. P.; Zanni, M. T. *Proceedings of the National Academy of Sciences of the United States of America* **2009**, *106*, 6614–6619.

(266) Edington, S. C.; Flanagan, J. C.; Baiz, C. R. *Journal of Physical Chemistry A* **2016**, *120*, 3888–3896.

(267) Nara, M.; Torii, H.; Tasumi, M. *Journal of Physical Chemistry* **1996**, *100*, 19812–19817.

(268) Mitra, S.; Werling, K.; Berquist, E. J.; Lambrecht, D. S.; Garrett-Roe, S. *Journal of Physical Chemistry A* **2021**, *125*, 4867–4881.

(269) Edington, S. C.; Baiz, C. R. *Journal of Physical Chemistry A* **2018**, *122*, 6585–6592.

(270) Abdulagatov, I. M.; Zeinalova, A. B.; Azizov, N. D. *Journal of Molecular Liquids* **2006**, *126*, 75–88.

(271) Wahab, A.; Mahiuddin, S. *Canadian Journal of Chemistry* **2002**, *80*, 175–182.

(272) Drexler, C. I.; Koehler, S. J.; Myers, R. L.; Lape, B. A.; Elacqua, E.; Cremer, P. S. *The Journal of Physical Chemistry B* **2021**, *125*, 477–478.

(273) Gruenbaum, S. M.; Tainter, C. J.; Shi, L; Ni, Y; Skinner, J. L. *Journal of Chemical Theory and Computation* **2013**, *9*, 3109–3117.